Energie & Umwelt
Energy & Environment

316

Oxidation Mechanisms of Metallic Carrier Materials

Martin Schiek

Member of the Helmholtz Association

Oxidation Mechanisms of Metallic Carrier Materials for Gas Separation Membranes

Martin Schiek

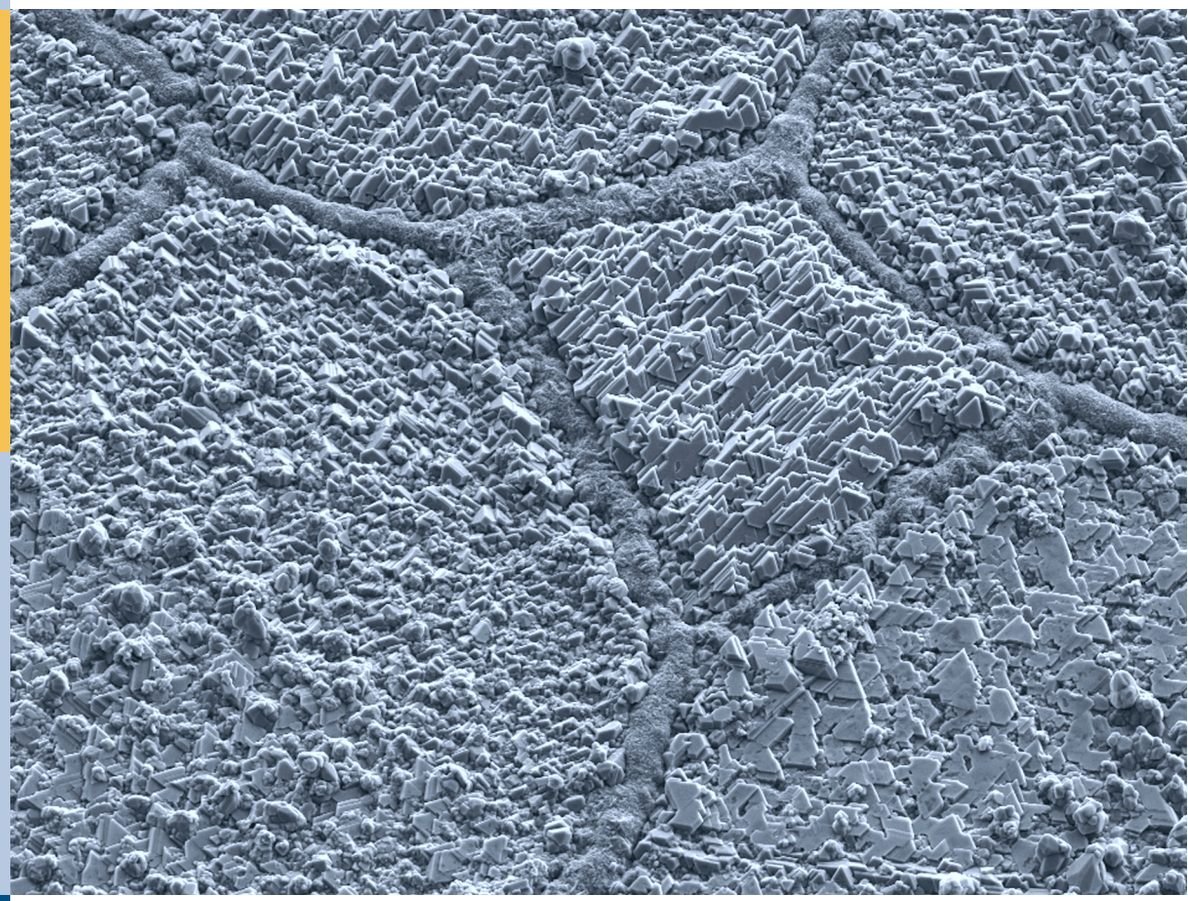

Energie & Umwelt /
Energy & Environment
Band / Volume 316
ISBN 978-3-95806-138-5

JÜLICH
FORSCHUNGSZENTRUM

Energie & Umwelt /
Energy & Environment
Band / Volume 316
ISBN 978-3-95806-138-5

JÜLICH
FORSCHUNGSZENTRUM

Schriften des Forschungszentrums Jülich
Reihe Energie & Umwelt / Energy & Environment Band / Volume 316

Forschungszentrum Jülich GmbH
Institute of Energy and Climate Research (IEK)
Microstructure and Properties of Materials (IEK-2)

Oxidation Mechanisms of Metallic Carrier Materials for Gas Separation Membranes

Martin Schiek

Schriften des Forschungszentrums Jülich
Reihe Energie & Umwelt / Energy & Environment Band / Volume 316

ISSN 1866-1793 ISBN 978-3-95806-138-5

Bibliographic information published by the Deutsche Nationalbibliothek.
The Deutsche Nationalbibliothek lists this publication in the Deutsche
Nationalbibliografie; detailed bibliographic data are available in the
Internet at http://dnb.d-nb.de.

Publisher and Distributor: Forschungszentrum Jülich GmbH
Zentralbibliothek
52425 Jülich
Tel: +49 2461 61-5368
Fax: +49 2461 61-6103
Email: zb-publikation@fz-juelich.de
www.fz-juelich.de/zb

Cover Design: Grafische Medien, Forschungszentrum Jülich GmbH

Printer: Grafische Medien, Forschungszentrum Jülich GmbH

Schriften des Forschungszentrums Jülich
Reihe Energie & Umwelt / Energy & Environment, Band / Volume 316

D 294 (Diss., Bochum, Univ., 2016)

ISSN 1866-1793
ISBN 978-3-95806-138-5

The complete volume is freely available on the Internet on the Jülicher Open Access Server (JuSER)
at www.fz-juelich.de/zb/openaccess.

Abstract

A major goal of research worldwide is the development of new concepts for reducing CO_2 emissions in power plants and other industry sectors. Very promising concepts are the "carbon capture and storage" (CCS) technologies. These contain gas separation units requiring the use of gas separation membranes. The need to reduce membrane thickness in combination with a high susceptibility for mechanically-induced failure of the ceramic membrane material makes the use of a metallic support structure for the membranes necessary. The requirements for the supports can be fulfilled by α-Al_2O_3 forming NiCrAl-base alloys. The membrane carriers have to withstand different aggressive atmospheres at temperatures up to 1000°C. As the formation of a protective Al_2O_3 surface scale is crucial for the operation of the membrane carrier, the present study deals with the influence of temperature and gas atmosphere on the selective oxidation of aluminum thereby using the commercially available alloys 602 CA and Haynes 214 with different aluminum contents of 2.4 wt.-% and 4.5 wt.-%, respectively. As these amounts are far below the high aluminum contents of MCrAlY alloys (10 – 13 wt.-% Al) considered as promising materials for the use as support structure, the investigation of possible effects of gas composition and/or temperature on the protective Al_2O_3 scale formation was possible in relatively short-term experiments (up to 1000 h). The studies were focused on the temperature range 800 – 1100°C in different atmospheres.

During 800°C exposure Alloy 602 CA formed a protective external Al_2O_3 scale independent of the test gas used mainly due to the beneficial effect of surface cold work while Haynes 214 showed initially Al_2O_3 formation but after 1000 h exposure in Ar-20%O_2 significant internal oxidation of aluminum due to the formation of γ'-precipitates. It was suggested that the aluminum concentration in γ is crucial for the formation of an Al_2O_3 layer and not the bulk alloy concentration. In addition, also the concentration of other alloying elements affects the formation of an external Al_2O_3 scale. In contrast to the behavior at 800°C, Alloy 602 CA exhibited at 900 – 1100°C internal Al_2O_3 nodules, whose amount increased with increasing exposure temperature, whereas Haynes 214 formed after initial internal oxidation of aluminum a continuous Al_2O_3 layer in Ar-20%O_2. A mechanism describing the oxidation processes in Haynes 214 at 800 – 1100°C in Ar-20%O_2 was proposed. Exposure of Haynes 214 in different H_2O containing gases revealed an increased tendency to internal oxidation of aluminum in the absence of O_2 in the test gas possibly due to hydrogen diffusion into the alloy. Furthermore, a lower pO_2 was proposed to suppress or decrease the growth rate of NiO to a larger extent than that of Al_2O_3 and therefore promote the formation of an external Al_2O_3 scale. Investigations on Haynes 224 showed that, despite its lower aluminum content compared to Haynes 214 the material exhibited after 72 h oxidation at 800 – 1100°C always an external Al_2O_3 formation with different amounts of Cr-rich transient oxide. It was proposed that the addition of iron, results in a lower amount of Al-rich γ'-precipitates in Haynes 224 compared to Haynes 214 thus increasing the tendency to external Al_2O_3 formation.

Kurzfassung

Ein zentrales Forschungsziel ist die Entwicklung neuer Konzepte zur Reduzierung der CO_2 Emissionen von Kraftwerken und Industrieanlagen. Eine sehr aussichtsreiche Technologie hierzu ist „Carbon Capture and Storage“ (CCS), welche u. a. Prozessschritte zur Gastrennung mittels Gastrennmembranen beinhaltet. Die notwendige Reduzierung der Membrandicke zusammen mit einer erhöhten Anfälligkeit der keramischen Membranen für mechanisch induziertes Versagen erfordert die Verwendung von metallischen Trägerstrukturen. Deren Anforderungen können von α-Al_2O_3 bildenden NiCrAl-basis Legierungen erfüllt werden. Die Membranträger müssen verschiedenen aggressiven Atmosphären bei Temperaturen bis 1000°C standhalten. Da die Bildung einer schützenden Al_2O_3-Schicht entscheidend für den Betrieb des Membranträgers ist, werden in der vorliegenden Arbeit die Einflüsse von Temperatur und Atmosphäre auf die selektive Oxidation von Aluminium untersucht. Dafür wurden die kommerziellen Legierungen Alloy 602 CA und Haynes 214 mit 2.4 Masse-% bzw. 4.5 Masse-% Aluminimum verwendet. Da diese Mengen weit unterhalb der hohen Aluminiumkonzentrationen von typischen Membranträgermaterialien (MCrAlY Legierungen mit 10 – 13 Masse-% Al), liegen, war die Untersuchung der Einflüsse von Gaszusammensetzung und Temperatur in relativ kurzen Versuchszeiten (bis zu 1000 h) möglich. Es wurden Versuche im Temperaturbereich 800 – 1100°C in verschiedenen Atmosphären durchgeführt.

Alloy 602 CA bildete nach isothermer Auslagerung bei 800°C unabhängig von der Atmosphäre eine schützende Al_2O_3-Schicht. Dies wird maßgeblich von durch Schleifen eingebrachte Kaltverformung der Probenoberfläche beeinflusst. Aufgrund der Bildung von Al-reichen γ′-Ausscheidungen wies Haynes 214 jedoch deutliche interne Oxidation von Aluminium bei 800°C nach 1000 h auf. Die Versuchsergebnisse legten nahe, dass der Aluminiumgehalt in der γ-Phase kritisch für die Bildung einer Al_2O_3 Schicht ist und nicht primär der Gehalt in der Legierung. Weiter beeinflussen auch die Legierungszusätze Chrom und Eisen deren Bildung. Im Gegensatz zu 800°C, bildeten sich bei 900 – 1100°C in Alloy 602 CA interne Al_2O_3 Ausscheidungen, deren Anteil mit steigender Temperatur zunahm, während Haynes 214 nach längeren Zeiten in Ar-20%O_2 eine geschlossene Al_2O_3-Schicht aufwies, was anhand eines entwickelten Mechanismus beschrieben werden konnte. Auslagerungen von Haynes 214 in verschiedenen wasserdampfhaltigen Gasen zeigten eine erhöhte Tendenz zur internen Oxidation von Aluminium in der Abwesenheit von O_2 im Gas. Weiter wurde angeregt, dass ein niedriger pO_2 die Bildung von NiO unterdrückt bzw. dessen Wachstumsrate stärker herabsenkt als die von Al_2O_3 und somit die Al_2O_3-Schichtbildung begünstigt. Versuche mit Haynes 224 zeigten, dass, obwohl der Aluminiumgehalt geringer ist als in Haynes 214, das Material nach 72 h Oxidation bei 800 – 1100°C immer eine geschlossene Al_2O_3-Schicht mit unterschiedlichen Gehalten an Cr-reichem Oxid bildete. Hierfür ist der höhere Cr- und Fe-Gehalt verantwortlich. Letzterer bewirkt einen geringeren Gehalt an Al-reichen γ′-Ausscheidungen in Haynes 224 im Vergleich zu Haynes 214 und erhöht somit die Tendenz zur Bildung einer externen Al_2O_3 Schicht.

Acknowledgements

This doctoral thesis was written by me at the Institute for Energy and Climate Research, Microstructure and Properties (IEK-2), at the Forschungszentrum Jülich GmbH. I would like to express my gratitude to Prof. Dr. R. Vaßen from Institute for Energy and Climate Research, Materials Synthesis and Processing (IEK-1), for the supervision of my work and his excellent support.

I would like to thank a lot Prof. Dr. G. H. Meier from University of Pittsburgh for giving me the opportunity to gain new experience by working in his group and his support during my stay. Fruitful discussions about my studies and very valuable comments on the results were essential for this thesis. Also many thanks to the other colleagues at University of Pittsburgh for a great time.

I would like to thank my supervisor at IEK-2 Prof. Dr.-Ing. W. J. Quadakkers a lot for his continuous excellent support during my work. Many of the very valuable discussions about my studies were a substantial support for interpreting my results and extensively broadened my technical knowledge. I am very grateful to Dr.-Ing. L. Niewolak for the daily support during my work, his patience and assistance with his scientific and experimental know-how.

This work would not have been possible without the support of my colleagues at IEK-2. I would like to thank H. Cosler, R. Mahnke and A. Kick for carrying out the oxidation experiments, M. Borzikov for SNMS analyses, V. Gutzeit and J. Bartsch for metallographic investigations, M. Ziegner for XRD analyses, Dr. E. Wessel and Dr. D. Grüner for SEM analysis and Dr.-Ing. W. Nowak for GDOES measurements.

I express my sincere gratitude to all the colleagues in the High Temperature Corrosion group: D. Naumenko, V. Shemet, J. Zurek, A. Jalowicka, E. Hejrani, P. Huczkowski, R. Duan, M. Hänsel, T. Galiullin, A. Chyrkin and R. Pillai for fruitful discussions, motivating coffee breaks ☺ and a great time in the institute.

The continuous support and patience of my parents and especially my girlfriend Sabine Kurth were essential for my successful work. Thanks to Lukas Durmich for helping me to train my presentation skills.

The financial support of “Deutsche Forschungsgemeinschaft” (DFG) is gratefully acknowledged under grant no. QU 78/7-1.

Parts of the results presented in this thesis have already been published in the following article:

M. Schiek, L. Niewolak, W. Nowak, G. H. Meier, R. Vaßen, W. J. Quadakkers
Scale Formation of Alloy 602 CA During Isothermal Oxidation at 800-1100°C in Different Types of Water Vapor Containing Atmospheres
Oxidation of Metals, Vol. 84, 661-694 (2015)

Index

Nomenclature

Abbreviations:

BOS	Basic oxygen steelmaking process
CCS	Carbon Capture and Storage
CFZ	Carbide-free zone
CO_2-EOR	CO_2-enhanced oil recovery
DFG	Deutsche Forschungsgemeinschaft
EDX	Energy dispersive X-ray spectroscopy
FCC	Face-centered cubic
GD-OES	Glow discharge optical emission spectroscopy
IOZ	Internal oxidation zone
MIEC	Mixed ionic and electronic conductor
OTM	Oxygen transport membrane
PFZ	Precipitate-free zone
RTO	Regenerative thermal oxidizer
SC	Super critical
SEM	Scanning electron microscopy
SNMS	Secondary neutrals mass spectrometry
TG	Thermogravimetry
USC	Ultra super-critical
XRD	X-ray diffraction

Symbols:

A	Surface area $[cm^2]$
A_{Sample}	Surface area of the sample $[cm^2]$
a_i	Activity of substance i
a, b, c, d	Number of moles of different substances form a chemical reaction
C_0	Initial concentration of the scale forming element $[wt.-\%]$
C_B	Breakaway concentration of the scale forming element $[wt.-\%]$
D_i	Diffusivity of substance i $[cm^2/s]$
d_{sheet}	Sheet diameter $[cm]$
d_{sphere}	Sphere diameter $[cm]$
G'	Gibbs free energy $[J/mol]$
$g^*_{AlO_{1.5}}$	Critical value of the volume fraction of $AlO_{1.5}$
$g_{BO_{vB}}$	Molar volume fraction of oxide BO_{vB} in the IOZ
$g_{BO_{vB}}$ *	Critical molar volume fraction of oxide BO_{vB} in the IOZ

H'	Enthalpy $[J/mol]$
iO_{vi}	Oxide of element i
J_i	Flux of substance i $[mol/cm^2 \times s]$
$J_i^{(S)}$	Flux of substance i at the surface $[mol/cm^2 \times s]$
K	Equilibrium constant
K_{pO2}	Equilibrium reaction constant for the dissolution of oxygen
k'_C	Parabolic rate constant for the recession of the oxide/metal interface $[cm^2/s]$
k_p	Parabolic rate constant in respect to specimen thickness $[cm^2/s]$
k_w	Parabolic rate constant in respect to area specific weight gain $[mg^2/cm^4 \times s]$
k_W'	Instantaneous apparent parabolic rate constant $[mg^2/cm^4 \times s]$
M_{gas}	Molar mass of the respective gas $[g/mole]$
M_i	Molar mass of substance i
m_i	Weight of substance i $[mg]$
$N_B^{(0)}$	Initial solute concentration of B [mole fraction]
$N_{B\,critical,1}^{(0)}$	Initial concentration of B necessary for the transition from internal to external formation of oxide BO_{vB} [mole fraction]
$N_{B\,critical,2}^{(0)}$	Initial concentration of B necessary to maintain an external scale of oxide BO_{vB} [mole fraction]
N_i	Concentration of substance i [mole fraction]
$N_i^{(S)}$	Concentration of substance i at the surface [mole fraction]
$n_O^{(IOZ)}$	Amount of oxygen in the IOZ $[mol/cm^2]$
p_i	Partial pressure of gas i $[bar]$
p_i^0	Partial pressure of gas i for standard state $[bar]$
p_0	Standard pressure $= 1.01325 \times 10^5 \frac{N}{m^2}$
$pO_{2,iO_{vi}}$	Dissociation pressure of the respective oxide iO_{vi} $[bar]$
R	Ideal gas constant $= 8.314 J/mol \cdot K$
S'	Entropy $[J/mol \times K]$
T	Temperature $[K]$
t	Time $[s]$
t_B	Time to breakaway $[s]$

V_m^{A-B}	Molar volume of the alloy A-B $\left[cm^3 / mol\right]$
$V_m^{BO_{vB}}$	Molar volume of the oxide BO_{vB} $\left[cm^3 / mol\right]$
V_{Sample}	Volume of the sample $\left[cm^3\right]$
X	Oxide thickness $\left[cm\right]$
X_{IOZ}	Width of the IOZ $\left[cm\right]$
X_{IOZ^*}	Width of the IOZ without counter-diffusion of B $\left[cm\right]$
$X_{IOZ,1}$	Width of the IOZ for limiting condition 1 $\left[cm\right]$
$X_{IOZ,2}$	Width of the IOZ for limiting condition 2 $\left[cm\right]$
x	Distance from the original surface into the respective alloy $\left[cm\right]$
γ	Time dependent kinetic parameter
ΔG^0	Change in Gibbs free energy for standard state of all reactants $\left[J / mol\right]$
$\Delta G^0{}_i$	Change in Gibbs free energy for standard state of substance i $\left[J / mol\right]$
$\Delta G'$	Change in Gibbs free energy $\left[J / mol\right]$
ΔH_O	Enthalpy change for the dissolution of oxygen $\left[J / mol\right]$
Δm	Area specific weight change $\left[mg / cm^2\right]$
Δm_A	Area specific weight gain difference caused by buoyancy effect $\left[mg / cm^2\right]$
ΔS_O	Entropy change for the dissolution of oxygen $\left[J / mol \times K\right]$
ε	Very small increment in x
μ	Metal / oxide mass ratio (Al_2O_3: 1.125)
v_{gas}	Molar volume of the respective gas $\left[m^3 / mole\right]$
ν_i	Specific factor of the respective oxide iO_{vi}
$\rho_{gas,Ti}$	Density of the respective gas environment at temperature T_i $\left[mg / cm^3\right]$
ρ_i	Density of substance i

1 Introduction

Since its beginning, the electricity production worldwide is undergoing continuous development and improvement. A large number of different techniques is available. Nowadays, fossil fuel fired power plants produce the biggest part of electric energy [1]. The combustion of fossil resources is largely dependent on their reserves. Figure 1 shows how long the regional fossil fuel reserves will still be available, assuming a constant consumption equal to that at the end of 2014. The worldwide explored reserves of coal will meet the demands for more than 100 years, which is the largest reserve-to-production ratio for any fossil fuel [2].

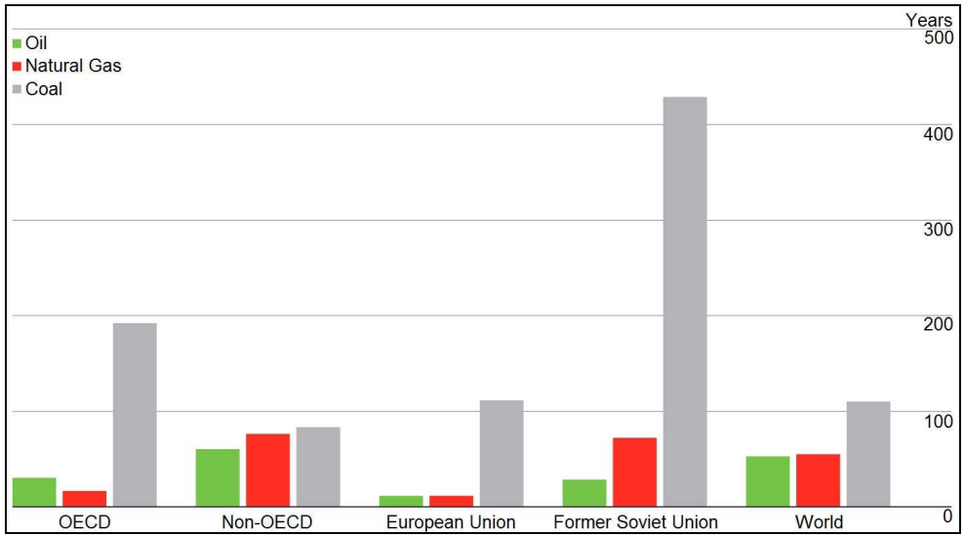

Figure 1: Reserve to production ratio of fossil fuel by region at the end of 2014 [2]

As the largest part of electric energy is produced by combusting fossil fuel, these plants emit also a major part of the global CO_2 emissions (Figure 2) [3]. As initially pointed out by Arrhenius in 1896 [4], an increase of CO_2 in the atmosphere is connected to an increase in global equilibrium temperature (greenhouse effect) [5]. To reduce these emissions and counteract their adverse effects, different techniques can be applied. Figure 3 [6] shows the roadmap of the International Energy Agency from 2013 for the reduction of CO_2 emissions between 2009 and 2050.

A major goal of research worldwide in the field of fossil fuel combustion is the development of new power plant concepts for reducing CO_2 emissions [7]. The most promising concepts in this field are the “carbon capture and storage” (CCS) technologies [6, 8]. Not only in the energy sector but also in other industry sectors CCS is considered as the only available large-scale option to decrease the CO_2 emissions of the respective process [6, 9].

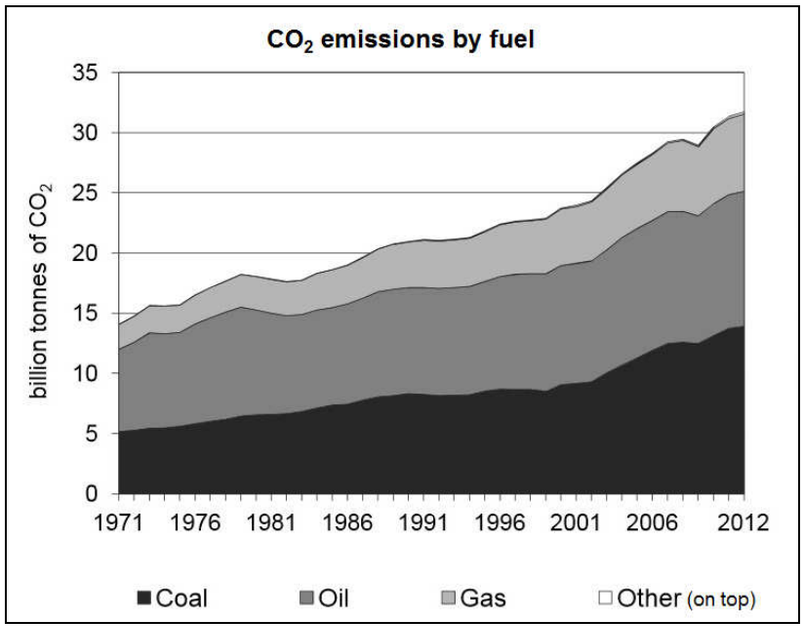

Figure 2: Global CO_2 emissions between 1971 and 2012 separated by type of fuel [3]

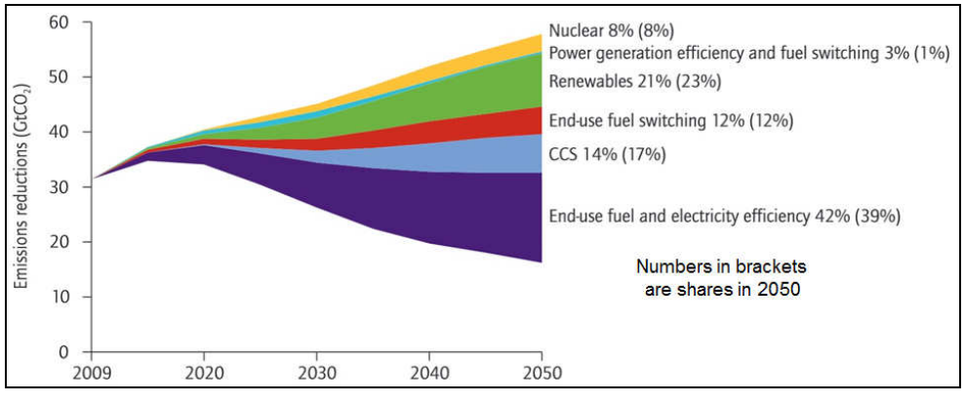

Figure 3: Reduction of CO_2 emissions by different measures [6]
14% is the share of CCS in cumulative emission reduction through 2050 and 17% is the share in 2050

The key-points of CCS are the extraction of CO_2 from the traditional fuel combustion process, the CO_2 transportation and its storage in saline aquifers or empty oil deposits [6]. Due to the extra energy needed for operating a CCS facility it is proposed that retrofitting CCS technologies is only useful in power plants with super-critical (SC) or ultra-super-critical (USC) steam conditions. These plants with a net efficiency of 40-45% require about 25% less CO_2 capture compared to a sub-critical plant with about 35% net efficiency [7]. To offset some of the additional costs associated with the CCS process, using CO_2 to extract oil from oil fields by the CO_2 enhanced oil recovery (CO_2-EOR) process is considered [10].

The main methods of CCS to extract CO_2 from the traditional power plant process are described below [6, 11, 12]:

- Post-combustion capture [11]:

The CO_2 is separated from the exhaust gas of the combustion process by a membrane which separates CO_2 and N_2 (Figure 4). The disadvantage of this membrane is the very high gas flow, namely the whole exhaust gas of the combustion process, which has to pass the membrane. To cover this high flow rate the membrane area has to be very large or has to have a very high gas permeation rate [11]. Potentially suitable membranes are zeolite, different types of polymer membranes [13, 14] and microporous membranes [15].

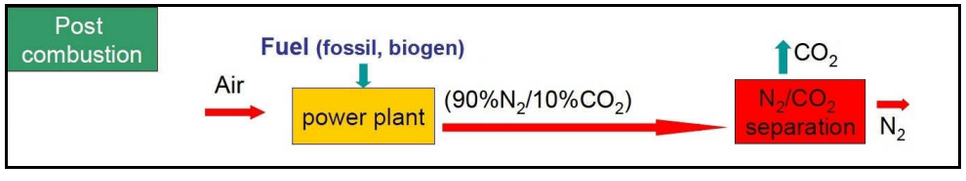

Figure 4: Post combustion process [11]

- Oxyfuel combustion [11]:

Pure oxygen is used instead of air for the combustion of fossil fuel to yield a flue gas containing mainly CO_2 and H_2O which can be separated by condensation of H_2O (Figure 5). The oxygen is obtained by separating it from air via an oxygen transport membrane (OTM). Possible candidates for the membrane material are mixed ionic and electronic conducting (MIEC) materials [11].

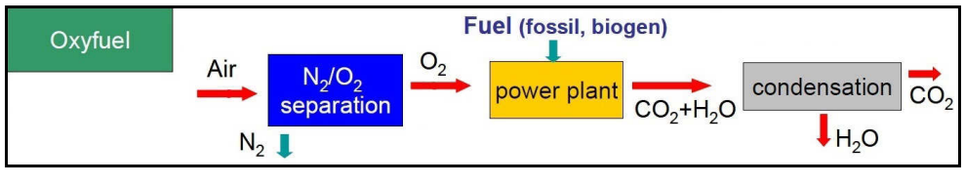

Figure 5: Oxyfuel process [11]

- Pre-process capture [11, 16]:

Oxygen separated from air via an oxygen transport membrane (OTM) is used for partial oxidation of fossil fuel (Figure 6). The subsequent CO-Shift reaction yields CO_2 and H_2, which can be separated afterwards by a membrane. H_2 is then used as a fuel, which has as result that the flue gas of the combustion will consist mainly of H_2O. The main drawback of this process is the need to construct new power plants, as it cannot be applied in existing plants [11].

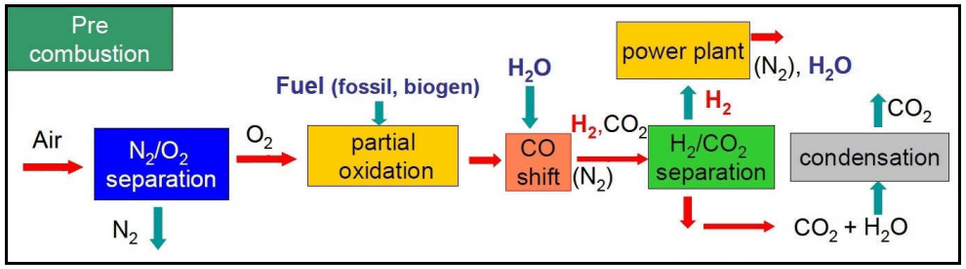

Figure 6: Pre-Combustion process [11]

All three mentioned CO_2 capture processes contain gas separation tasks (Table 1) requiring the use of gas separation membranes to keep the efficiency loss by the separation units as small as possible [12]. Basically, there are polymeric and ceramic membranes available for these purposes. Due to disadvantages of polymeric membranes in respect to their chemical and thermal stability ceramic membranes are preferred [12]. For instance, for the air separation into nitrogen and oxygen, perovskite materials are in use as oxygen transport membranes (OTM). The following perovskites are potentially suitable for the separation of oxygen and nitrogen [12, 17, 18]:

- $La_{1-X}Sr_XFe_{1-Y}Co_YO_{3-\delta}$ (LSFC)
- $Ba_{0,5}Sr_{0,5}Co_{0,8}Fe_{0,2}O_{3-\delta}$ (BSFC)
- $SrCo_{0,8}Fe_{0,2}O_{3-\delta}$ (SCF)
- $La_{0,6}Ca_{0,4}CoO_{3-\delta}$

Another application for perovskite type membranes is the production of synthesis gas and the decomposition of nitrous oxide (N_2O) [19]. Beside the energy sector, air separation is also needed in other industries, for instance in concrete and steel production [20, 21]. In the latter, the basic oxygen steelmaking process (BOS, in German called “Linz-Donawitz Verfahren”) is a broadly used technology [22]. Via a lance pure oxygen is blown into the metal melt to oxidize some specific species, such as C and Ca. The classical method to produce pure oxygen is the cryogenic air separation (Linde-Fränkl Process) [21], which can reach a minimum energy consumption of about 0.36 kWh_{el}/m_N^3 O_2 [20]. As air separating ceramic MIECs typically operate at temperatures above 800°C, their energy consumption is mainly connected to the heat recovery rate in the overall process [20]. For a heat recovery rate of about 92% the minimum energy consumption of MIECs is lower than that of cryogenic air separation. As by the use of regenerative thermal oxidizers (RTO) for flue gas cleaning in steel production [23] a heat recovery rate of up to 98% is state of the art [20], the usage of gas separating ceramic membranes for production of pure oxygen is reasonable.

Process	Separation	Additional gases	Temperature range
Oxyfuel Pre-Combustion	O_2 / N_2	CO_2, H_2O	600 – 1000°C
Pre-Combustion	H_2 / CO_2	H_2O, CO	400 – 900°C
Post-Combustion	CO_2 / N_2	H_2O	Ca. 200°C

Table 1: Gas separation processes in the three CCS technologies [11]

The main drawback of the fully ceramic gas separation membranes is their inherent brittleness. Consequently, they are prone to mechanically-induced failure, especially in large-scale facilities [24]. To overcome this problem, a porous metallic structure might be applied for supporting the ceramic membranes [24]. Since the gas separation membranes are operated at relatively high temperatures (up to 1000°C) in various gas environments, they require an oxidation resistant metallic material as a support structure (Table 1) [12]. Further requirements to the support material are [12]:

1. A thermal expansion coefficient close to that of the membrane material
2. A slow reaction rate with the membrane material
3. Limited evaporation of Cr species, because of Cr poisoning of the membrane material

These requirements can principally be fulfilled by α-Al_2O_3 forming Ni-base alloys [24], e. g. of the type MCrAlY (M = Ni, Co, Fe). These materials are known to form slowly growing alumina scales if the aluminum contents are sufficiently high (approximately 3 – 6 wt.-% depending on alloy type, temperature and gas composition [25]). Thereby it should be borne in mind that in spherical particles, used in the porous substrates, the alumina growth results in consumption of the aluminum in the particle. This will eventually result in aluminum depletion to such a level that alumina scale growth can no longer be sustained. For practical applications it is obviously of great importance to have quantitative information on the times at which this type of change from protective to non-protective oxidation occurs as function of temperature, gas composition and detailed alloy composition.

2 Fundamentals of Alumina-forming NiCrAl-base Alloys

Ni-base alloys exhibit an FCC (face centered cubic) structure with a typical density between 7.8 and 8.9 g/cm³ [26]. Conventional Ni-base superalloys can be used in wrought or cast form depending on melting procedures, forging and working processes, casting techniques and predominantly on the heat treatment as well as the type and amount of alloying elements [26, 27]. Generally, the number of controlled alloying elements in a Ni-base superalloy may be up to 14 including, beside Cr and Al also e. g. Ti, Co, B, Zr, Mg and C [26]. The wrought Ni-base materials have commonly a low alloyed composition [27] and are used up to about 800°C [26]. Above that temperature cast Ni-base alloys are preferred as they are intrinsically stronger at elevated temperatures. Additionally, their compositions can be adjusted more effectively for obtaining optimal high temperature strength [26]. On the other hand, wrought alloys exhibit higher yield strength and better low cycle fatigue resistance at intermediate temperatures [26].

Cast materials often have an Al content of about ≥5 wt.-% [28], which results in the formation of intermetallic strengthening phase γ'-Ni_3Al. Other strengthening mechanisms are solid-solution hardening, e. g. by W, Mo and/or Nb additions, and carbide formation, mainly at grain boundaries [29]. Ni-base superalloys are generally used at temperatures above about 540°C and possess a very good combination of high-temperature corrosion resistance and stress-rupture strength (Figure 7) [26, 27]. They can be used at temperatures up to 80% of their melting points, which is much higher compared to other commercially available alloys [26, 30].

The good corrosion resistance of Ni-base superalloys at high temperatures depends on the formation of a slow growing protective oxide scale, consisting of Cr_2O_3 and/or Al_2O_3 [25, 29, 31]. While a Cr_2O_3 layer provides adequate oxidation resistance at intermediate temperatures [28], superior oxidation resistance up to very high temperatures is only obtained by the formation of a very slow growing Al_2O_3 surface scale [32]. The formation of Al_2O_3 on NiCrAl-base materials is a complex process and was investigated by several authors [25, 31, 33, 34, 35, 36].

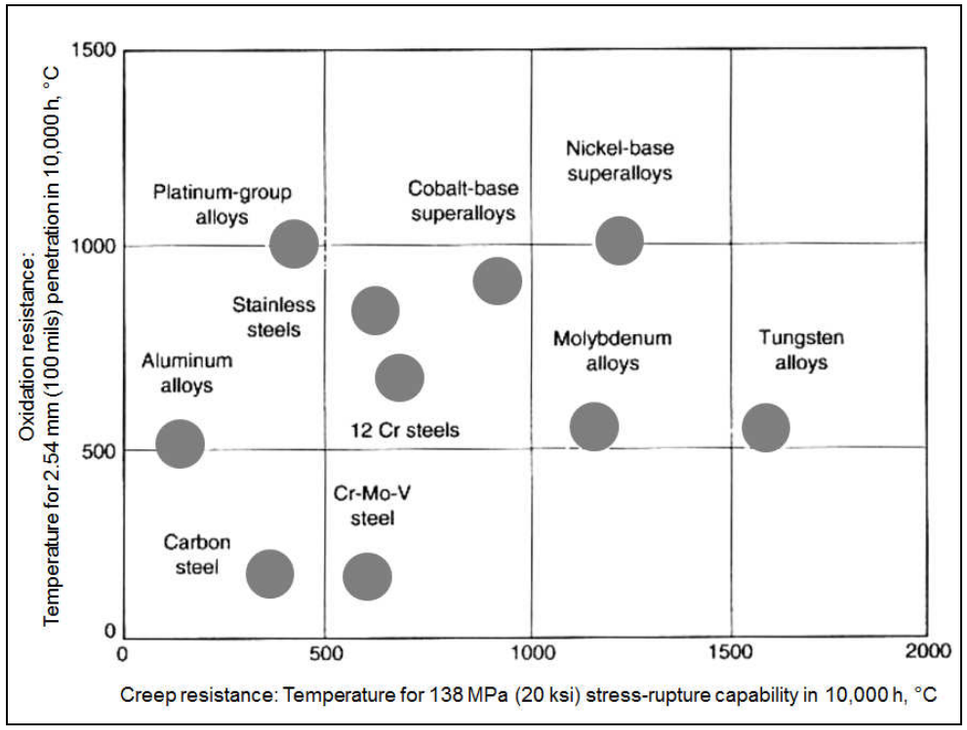

Figure 7: Relative oxidation/stress-rupture capabilities of various alloy systems [37]

3 Aims of the Studies

For different gas separation tasks in the CCS processes as well as in other industry fields, e. g. synthesis gas and steel production (see chapter 1), the use of gas separation membranes is reasonable. Compared to other gas separation processes, like cryogenic air separation, an efficiency increase, related to the overall plant process, can be achieved. A high susceptibility for mechanically-induced failure of ceramic membrane materials especially in large-scale facilities makes the use of a metallic support structure for the membranes necessary. As described in chapter 1, the requirements to such a metallic support structure can be fulfilled by α-Al_2O_3 forming NiCrAl-base alloys.

Alloys of the MCrAlY type with a high Al content are considered as promising materials for the use as membrane support structure [11, 12]. The membrane carriers have to withstand different aggressive atmospheres at temperatures up to 1000°C (see Table 1). MCrAlY alloys commonly have aluminum contents of 10 – 13 wt.-%. However, after long-term operation, aluminum in the porous membrane supports becomes severely depleted after which protective alumina scale formation can no longer be maintained. Studies dealing with critical depletion processes resulting in a change from protective to non-protective oxidation are available in literature for selected alumina forming materials [31, 36]. However, no systematic studies prevail in which the effect of the practically important service parameters temperature and gas composition on the transition from protective to non-protective scale formation has been evaluated.

Aim of the present study is the estimation of the effect of gas composition and temperature on the critical aluminum contents for obtaining protective alumina scale formation. This was realized using two alloys with typical Chromium contents for MCrAlY material and different Aluminum contents in the range of 2.4-4.5 wt.-%. As these amounts are far below the high Al contents of the MCrAlY alloys mentioned above (10-13 wt.-% Al), the investigation of possible effects of gas composition and/or temperature on the protective Al_2O_3 scale formation was possible in relatively short-term experiments (up to 1000 h).

The studies are focused on experiments with the wrought Ni-base alloys 602 CA (2.43 wt.-% Al) and Haynes 214 (4.46 wt.-% Al), to investigate the effects of alloy composition on the oxidation behavior.

This thesis is part of the research project “Oxidation Mechanisms of Metallic Carrier Materials for Gas Separation Membranes in Power Generation Systems with CO_2 Capture”, funded by Deutsche Forschungsgemeinschaft (DFG).

4 Theory of High Temperature Corrosion

In the following sections the thermodynamical background relevant to high temperature oxidation processes is presented. Special emphasis was put on the description of oxidation mechanisms of alloy systems. These fundamental aspects are the basis for analysis and evaluation of the results of material testing as well as the modelling approaches used in the discussion of the own experiments.

4.1 Thermodynamics

The oxidation processes of a metallic material obviously depend on the environment to which it is exposed. These environments are characterized by temperature, chemical composition and pressure of the gas, in which the material is exposed and the duration of the impact of this environment.

4.1.1 Fundamentals

The reaction of metal (M) and oxygen forming one mole of metal oxide (M_aO_b) can be described by the following chemical equation [38]:

$$aM + \left(\frac{b}{2}\right)O_2 \rightarrow M_aO_b \qquad (1)$$

Whether a chemical reaction, like oxidation, takes place under certain conditions depends on its change in free Gibbs energy G'. The Gibbs energy of a certain state is explained by the second law of thermodynamics [31].

$$G' = H' - T \cdot S' \qquad (2)$$

H' = Enthalpy $[J/mol]$

T = Temperature $[K]$

S' = Entropy $[J/mol \cdot K]$

From this equation it results for the change in Gibbs free energy:

$\Delta G' < 0$ ➔ Reaction proceeds from left to right in equation (1)

$\Delta G' = 0$ ➔ Thermodynamic equilibrium, no reaction

$\Delta G' > 0$ ➔ Reaction proceeds from right to left in equation (1) [25]

For a chemical reaction of the type $aA + bB \rightarrow cC + dD$ with a, b, c and d as different numbers of moles and different substances A, B, C and D, ΔG' is defined as [25]:

$$\Delta G' = \Delta G° + R \cdot T \cdot \ln\left(\frac{a_C^c \cdot a_D^d}{a_A^a \cdot a_B^b}\right) \tag{3}$$

$\Delta G°$ = Change in Gibbs free energy for standard state of all reactants $[J/mol]$

R = Ideal gas constant = $8{,}314 J/mol \cdot K$

a_i = Activity of substance i

a, b, c, d = Number of moles of the different substances from the chemical reaction

The change in Gibbs free energy for standard state of all reactants $\Delta G°$ is calculated as [25]:

$$\Delta G° = c \cdot \Delta G°_C + d \cdot \Delta G°_D - a \cdot \Delta G°_A - b \cdot \Delta G°_b \tag{4}$$

$\Delta G°_i$ = Change in Gibbs free energy for standard state of the substance i $[J/mol]$

The activity a_i of the different substances is defined as [25]:

$$a_i = \frac{p_i}{p_i^0} \tag{5}$$

p_i = Partial pressure of gas i

p_i^0 = p_i for standard state of gas i

4.1.2 Dissociation Pressure

The dissociation pressure describes the oxygen partial pressure which marks the limiting p_{O_2} for oxide formation. Beyond this value the metal forms its respective oxide and beneath it the oxide will not be formed or existing oxide will be dissociated. If the oxygen partial pressure is equal to the dissociation pressure of a metal, the metal and its respective oxide coexist [25]. The reaction is in thermodynamic equilibrium, hence equation (3) changes to:

$$\Delta G' = \Delta G° + R \cdot T \cdot \ln\left(\frac{a_C^c \cdot a_D^d}{a_A^a \cdot a_B^b}\right) = 0 \tag{6}$$

Rearranging leads to [25]:

$$-\Delta G° = R \cdot T \cdot \ln\left(\frac{a_C^c \cdot a_D^d}{a_A^a \cdot a_B^b}\right) = R \cdot T \cdot \ln(K) \tag{7}$$

$$=> \frac{-\Delta G^\circ}{R \times T} = \ln(K) = 2.303 \times \log(K)$$

$$=> \log(K) = \frac{-\Delta G^\circ}{2.303 \times R \times T} \tag{8}$$

K = Equilibrium constant

The value of K is constant for each metal/oxide pair at one temperature and can be taken from thermodynamic data bases, e. g. FACTSAGE. For the reaction of metal (M) and oxygen forming one mole of metal oxide (equation 1) the logarithm of the equilibrium constant $\log K$ can be derived as:

$$\log K = \log\left(\frac{a_{Oxide}}{p_{O_2}^{\frac{b}{2}} \times a_{Metal}^{a}}\right) \tag{9}$$

a_{Oxide} = Activity of the oxide

a_{Metal} = Activity of the metal

p_{O_2} = Oxygen partial pressure $[bar]$

If oxide and metal are pure substances, their activities can be assumed as 1. This simplifies equation (9) to:

$$\log K = \log\left(\frac{1}{p_{O_2}^{\frac{b}{2}}}\right) \tag{10}$$

Combining equation (8) and (10) leads then to the following expression for the oxygen partial pressure for the case that metal and oxide coexist [38, 39]:

$$\log\left(pO_2^{-\frac{b}{2}}\right) = \frac{-\Delta G^\circ}{2.303 \times R \times T}$$

$$=> pO_2 = \exp\left(\frac{2 \times \Delta G^\circ}{b \times R \times T}\right) \tag{11}$$

The dissociation pressure is temperature dependent and differs for every element. Figure 8 shows the calculated dissociation pressures of some metal oxides as function of reciprocal temperature.

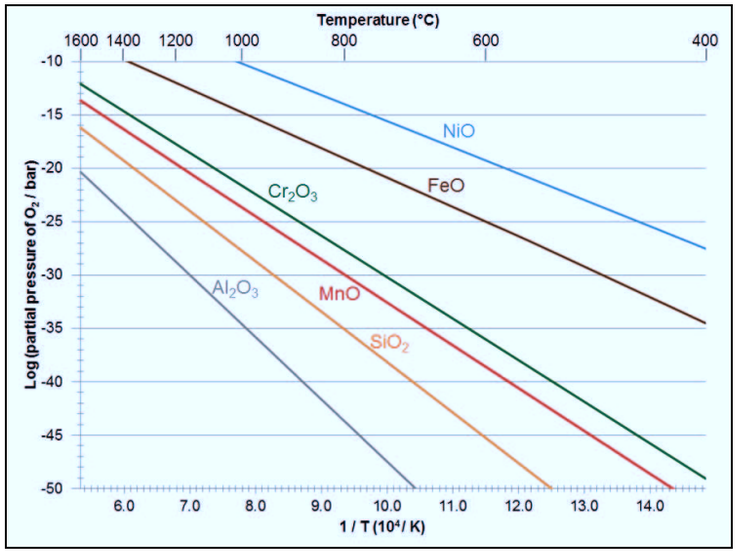

Figure 8: Dissociation pressures of different metal/oxide systems as function of temperature calculated with FACTSAGE assuming unit activities for metals and oxides

4.1.3 Oxidation in H_2O/H_2 and CO_2/CO Mixtures

As shown in Figure 8 the dissociation pressures are for most of the relevant oxides very low compared to the oxygen partial pressure in air (0.21 bar). Lower oxygen partial pressures can prevail in gas mixtures, such as e. g. H_2O/H_2 or CO_2/CO. Considering a mixture of water vapor and hydrogen at high temperature, the equilibrium in the gas phase will be established given by the following reaction [40].

$$2H_2O(g) \Leftrightarrow 2H_2(g) + O_2 \tag{12}$$

Applying the same procedure as described for equation (11), using $K = \left(\frac{(pH_2)^2 \times pO_2}{(pH_2O)^2} \right)$ leads to [41]:

$$pO_2 = \frac{\exp\left(\frac{2 \times \Delta G^\circ}{b \times R \times T} \right)}{\left(\frac{pH_2}{pH_2O} \right)^2} \tag{13}$$

The equilibrium oxygen partial pressure in the gas mixture thus depends on the H_2O/H_2 ratio and not on the absolute partial pressures of the individual species. In pure steam or in Ar-H_2O mixtures the equilibrium hydrogen and oxygen partial pressures derived from equation (13)

have similar values, but in the calculations the change in water vapor content due to formation of H_2, O_2 and other gas species such as HO_2 and OH has to be taken into account [41]. The equilibrium oxygen partial pressures in gases with various H_2O/H_2 ratios as well as in pure steam in the temperature range 500-1100°C are shown in Figure 9. The equilibrium oxygen partial pressure in CO_2/CO mixtures can be calculated in the same way as for H_2O/H_2 mixtures and is thus not shown here. In addition, Figure 10 shows the oxygen partial pressure of the test gases used in the present study compared with the dissociation pressures of the relevant oxides.

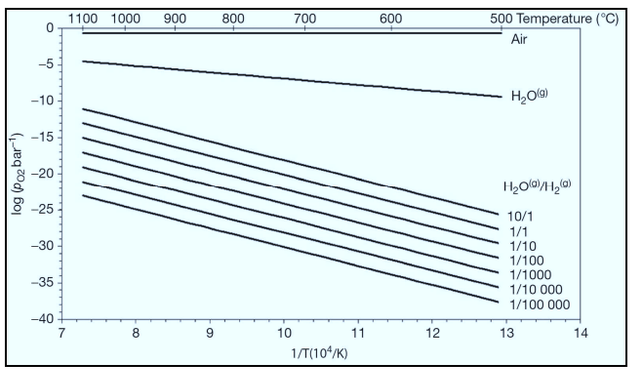

Figure 9: Equilibrium oxygen partial pressure as function of temperature in various gas atmospheres calculated with FACTSAGE [41]

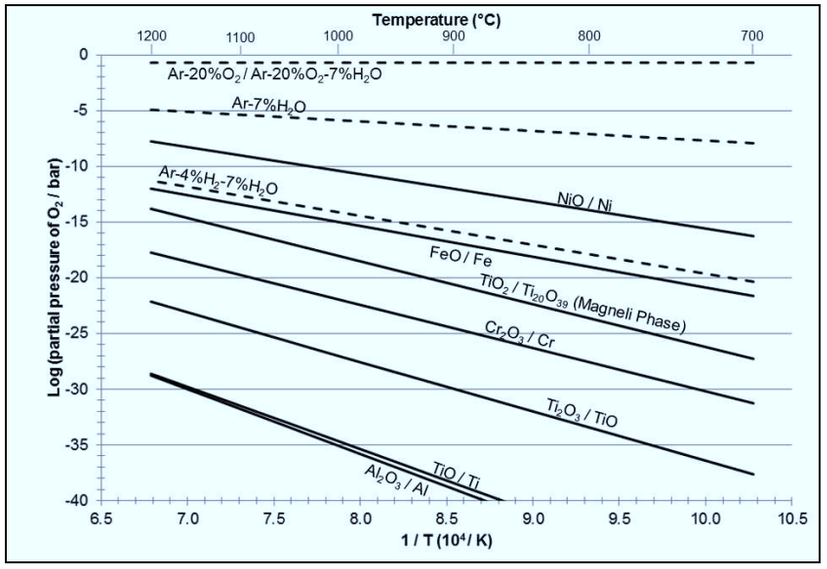

Figure 10: Equilibrium oxygen partial pressure of gas mixtures (dashed lines) and dissociation pressures of selected oxides (solid lines) calculated with FACTSAGE. For the metal/oxide equilibria unit activities for the respective metals and oxides were assumed

4.1.4 Ellingham Diagram

The change in Gibbs free energy for standard state $\Delta G°$ as a function of temperature and the corresponding dissociation pressure can be derived from the Ellingham diagram (Figure 11), originally developed by Ellingham in 1944 [42]. The values of $\Delta G°$ refer to the standard free energies of formation of the oxides per one mole of oxygen (O_2). In addition to the corresponding dissociation pressures of the various oxides, also the corresponding ratios of H_2O/H_2 and CO_2/CO can be derived from the diagram.

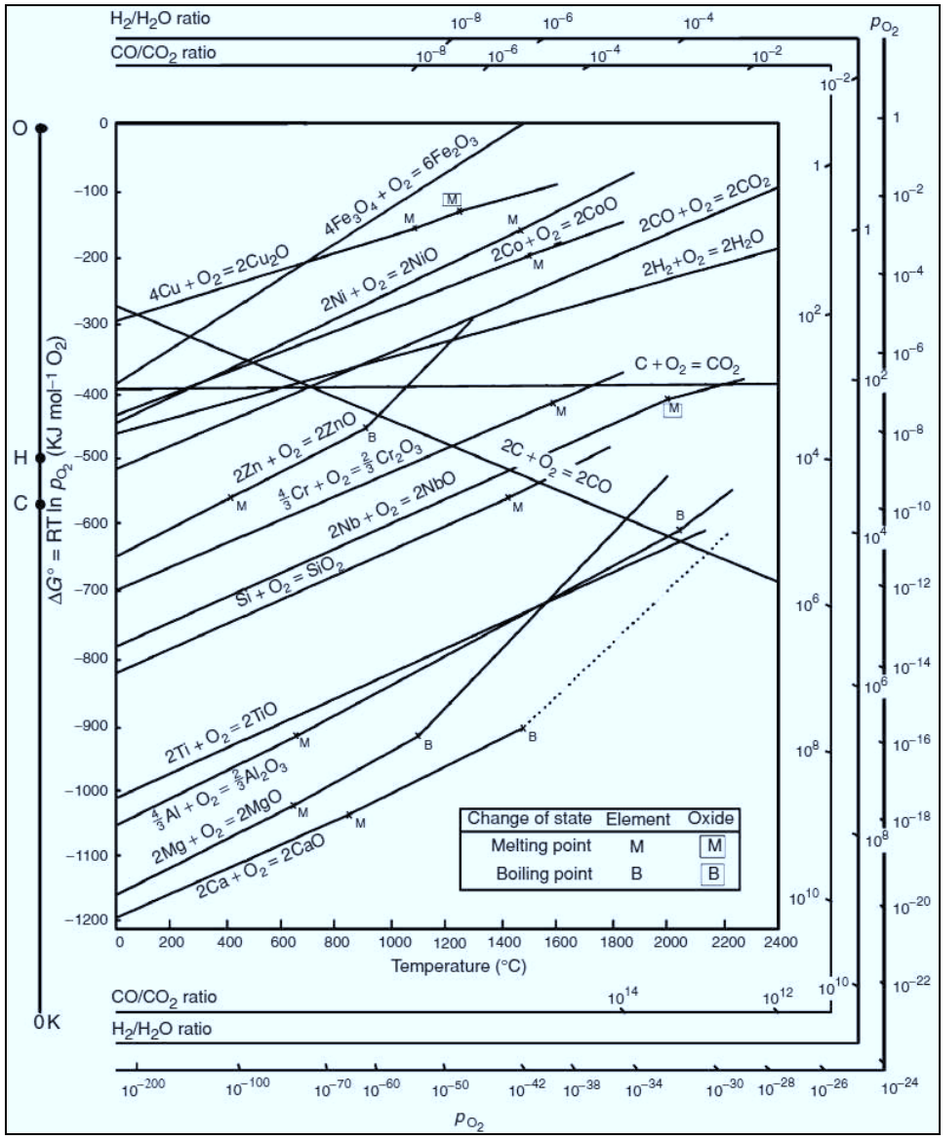

Figure 11: Ellingham diagram for various metal oxidation reactions [25]

4.2 Oxidation Kinetics

4.2.1 Oxide Growth

If a metal is exposed in an atmosphere whose oxygen partial pressure is higher than the dissociation pressure of the oxide, the metal begins, according to equation (1), to form oxide. This means, metal atoms in contact with the gas react with the oxygen contained in the gas and form oxide on the metal surface. This oxide formation continues until a dense oxide layer has formed which separates the metal from the oxidizing gas. For further oxidation to proceed it is necessary, that either metal diffuses through the oxide layer to the oxide/gas interface or oxygen diffuses to the metal/oxide interface to form new oxide at the respective location. That implies, that the kinetics of further oxidation are not governed by the thermodynamics of equation (1), but depend on the transport of metal and/or oxygen through the existing oxide layer [31].

At high temperature the majority of the metals form very rapidly a dense oxide layer on the metal surface, the kinetics of oxidation depends mainly on the diffusion through this oxide layer [25, 31]. In classical oxidation theory it is assumed that diffusion occurs via point defects in the oxide. Figure 12 shows the schematic structure of an oxide and illustrates the types of major point defects.

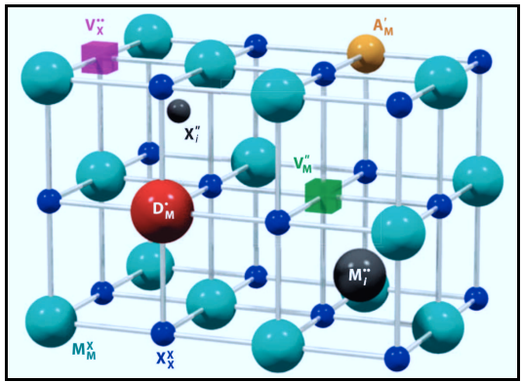

Figure 12: Possible point defects in the ionic structure of an oxide [43]

Figure 12 uses the Kröger-Vink notation [38] for description of the different point defects (X = Anion/Oxygen; M = Cation/Metal). Using this notation, possible point defects are:

$V_X^{\bullet\bullet}$ = Anion vacancy, a lack of one oxygen ion

V_M^{II} = Cation vacancy, a lack of one metal ion

X_i^{II} = Interstitial anion, an oxygen ion

$M_i^{\bullet\bullet}$ = Interstitial cation, a metal ion

$D_M^{\bullet}$ = Donor substitutional impurity

A_M^{I} = Acceptor substitutional impurity

The latter two will not be further discussed and for the theoretical approach the assumption of an impurity-free metal oxide is reasonable [25, 31, 38, 44]. In high-stoichiometric ionic compounds, which have a fixed metal to non-metal ratio [25] the remaining four types of point defects form commonly in pairs [45] to maintain stoichiometry and electrical charge neutrality. These pairs can be divided into three groups:

Schottky defects pairs = V_M^{II} - $V_X^{\bullet\bullet}$

Describes a pair of anion and cation vacancy

Frenkel defect pairs = V_M^{II} - $M_i^{\bullet\bullet}$

Describes a combination of a cation vacancy and a cation interstitial

Anti-Frenkel defect pairs = $V_X^{\bullet\bullet}$ - X_i^{II}

Describes a combination of an anion vacancy and an anion interstitial

Non-stoichiometric ionic compounds consist of anions or cations with variable atomic charges, although their metal to non-metal ratio varies [25]. In metal oxides mostly the cations have variable atomic charges [25].

The four possible defects in the ionic lattice of a metal oxide, as displayed in Figure 12 (except the substitutional impurities), enable metal and/or oxygen ions to diffuse through the oxide and the oxide layer is continuously growing. However the flux of the metal and/or oxygen ions decreases with increasing oxide thickness. The oxide thickening rate at a given time $\left(dx/dt\right)$ is inversely proportional to the thickness of the oxide (X) at time t [38]:

$$\frac{dx}{dt} = \frac{k_P}{X} \qquad (14)$$
$$\Rightarrow X \times dx = k_P \times dt$$

X = Oxide thickness $[cm]$

k_P = Parabolic rate constant $[cm^2/s]$

t = Time $[s]$

Integration yields:

$$X^2 = 2 \times k_P \times t + C \qquad (15)$$

Thus the oxide thickness obeys a parabolic time dependence. Assuming that the oxide thickness X = 0 at t = 0 [25] yields to:

$$X^2 = 2 \cdot k_P \cdot t \tag{16}$$

From this it follows that a change in oxidation time by a factor z, results in a change of the oxide thickness by the factor $z^{1/2}$. The parabolic rate constant k_P may be determined by experimental measurement of the oxide thickness X as function of time. However these measurements in the range of µm are frequently inaccurate and time consuming [31].

4.2.2 Correlation between Oxide Thickness and Weight Change

Another way to determine the kinetics of an oxide layer, in addition to the measurement of the oxide thickness X, is the measurement of the oxygen uptake as function of time. This value can be determined much more accurate than the oxide thickness. It can also be applied during isothermal exposure and therefore this method is applied more frequently in practice for measuring oxidation kinetics [31]. Analogous to the determination of the oxide layer thickness the area specific weight change as a function of time is given by:

$$\Delta m^2 = 2 \cdot k_W \cdot t \tag{17}$$

Δm = Area specific weight change $\left[mg / cm^2\right]$

k_W = Parabolic rate constant $\left[mg^2 / cm^4 \cdot s\right]$

The parabolic rate constants of different oxides may differ by several orders of magnitude. The higher the point defect concentration in the oxide, the faster the oxide grows. Thus, the oxides with the highest defect concentration exhibit, according to section 4.2.1, the highest parabolic rate constants. Figure 13 shows parabolic rate constants for different oxides as function of reciprocal temperature, revealing the well-established Arrhenius type temperature dependence.

In contrast to most other oxides, the oxidation of Al may result in different types of Al_2O_3 polymorphs after different exposure times, as shown by several authors [25, 31, 46, 47]. The thermodynamically stable form of Al_2O_3 is corundum type α-Al_2O_3. However, a number of metastable alumina phases exist, i. e. γ-, δ- and/or θ-Al_2O_3 [25, 31]. The transition from metastable phases to corundum is time and temperature dependent. Figure 13 shows the parabolic oxidation rates of different types of Al_2O_3 (here γ, θ and α) as a function of temperature.

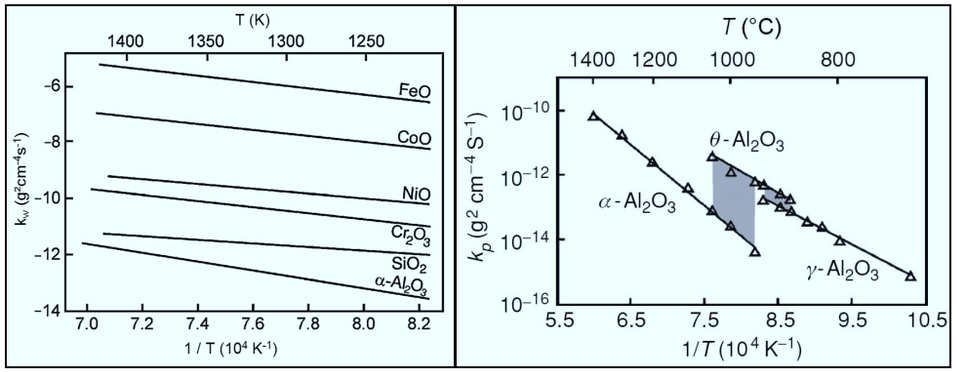

Figure 13: Parabolic rate constants for different oxides (left, [25]) and for different types of Al_2O_3 formed during oxidation of pure NiAl (right, [48])

The correlation between the area specific weight change Δm and the oxide thickness X is given by the following equation:

$$X = \frac{\Delta m}{\rho_{Oxide}} \times \frac{M_{Oxide}}{M_{Oxygen}} \tag{18}$$

ρ_{Oxide} = Density of the respective Oxide $\left[mg / cm^3\right]$

M_{Oxide} = Molar mass of oxide $\left[mg / mol\right]$

M_{Oxygen} = Molar mass of oxygen $\left[mg / mol\right]$

4.3 Oxidation of Alloys

The oxidation of alloys is more complex than that of pure metals. This results mainly from [25, 31]:

1. Different oxidation rates of oxides formed from different alloying elements
2. Different dissociation pressures of the respective oxides
3. Ternary and higher oxides can be formed
4. Diffusion processes in the alloy
5. Depletion of one or more elements in the subsurface zone
6. Different diffusivities of the elements in the oxide phases
7. Time and temperature dependent formation of different phases
8. Dissolution of oxygen into the alloy can lead to internal oxidation of one or more elements

The following chapters will show the theory describing the different processes relevant to alloy oxidation at high temperatures.

4.3.1 Transient Oxidation Stage

Both, alloys and pure metals, show during the very first moments of the oxidation process, when no external oxide scale is present, the formation of transient oxides. After a certain time, if parabolic kinetics are assumed like described in 4.2 for pure metals, the parabolic rate constant k_p will reach a steady-state [31]. The time period before the oxide growth reaches steady-state conditions is designated as "Transient Oxidation Stage" [31]. The initial oxidation can be divided into three main stages [38]:

1. Adsorption of oxygen on the alloy surface
2. Formation of oxide islands which grow laterally, forming a continuous film
3. Further growth of the formed oxide film normal to the alloy surface

During the steady-state, before an oxide layer with a critical thickness is formed, the oxide growth is mainly governed by the reactions at the scale/alloy interface, as these are much slower than the reactions at the scale/gas interface [31]. However, in the transient stage the scale/gas interaction processes contribute to the scaling rate [49, 50], resulting in an approximately linear behavior of the oxidation kinetics. As soon as the interface reactions become faster than the transport processes in the scale due to scale thickening, this will result in parabolic oxide growth.

If the experimental conditions allow the formation of more than one stable oxide of the alloy constituents, the transient oxidation stage may contain the oxidation of all the respective elements. For the transient oxidation of alloys consisting of Ni, Cr and Al there are three different mechanisms proposed in literature. All three mechanisms assume that Ni, Cr and Al can form thermodynamically stable oxides and that after the transient stage a three-layered oxide morphology is formed (see Figure 14).

Mechansim A – The Giggins and Pettit model [25, 33]:
Exposure of several NiCrAl alloys (0-30 wt.-% Cr, 0- 6 wt.-% Al) at 1000 – 1200°C in oxygen at 0.1 bar revealed that in the first step NiO and spinel form externally and Cr and Al oxidize beneath. Subsequently, Cr_2O_3 starts to form an external scale between the NiO/spinel layer and the internal Al_2O_3 precipitates. If the Al_2O_3 precipitates are connected among themselves, a three-layered structure is formed.

Mechanism B – The Nijdam, Jeurgens and Sloof model [51]:
During exposure of γ-Ni-27Cr-9Al (at.-) at 1100°C in one high- and one low pO_2 gas ($2 \cdot 10^4$ Pa, 0.1 Pa) the oxidation of Al is preferred initially, as this element forms a thermodynamically more stable oxide than Ni and Cr, and a thus thin Al_2O_3 scale is formed. Due to the rapid growth in the early stages of the oxidation process the concentration of Al beneath the scale is depleted to virtually zero. The mole fraction of Al drops to a value, where Al_2O_3 and Cr_2O_3 are in equilibrium with the alloy, namely $pO_2(Al_2O_3) = pO_{2,Diss}(Cr_2O_3)$. Cr_2O_3 can be formed, additionally to Al_2O_3. As due to Cr_2O_3 formation the Cr concentration at the surface decreases rapidly, Al_2O_3, Cr_2O_3 and NiO are in equilibrium with the alloy at the scale/alloy interface, namely $pO_2(Al_2O_3) = pO_2(Cr_2O_3) = pO_{2,Diss}(NiO)$. NiO is formed but its amount is relatively small. At 1100°C the formation of all three phases occurs within the first 10 min. of oxidation. Subsequently, the decreasing oxidation rate in combination with the oxide/alloy interface recession enables Cr enrichment beneath the scale and NiO formation is stopped. After approx. 4 h oxidation the overall oxidation rate has decreased to such an extent that Cr_2O_3 formation also stops and Al_2O_3 is formed exclusively. As a disadvantage, this model does not address the morphology and distribution of the formed oxide phases within the scale, as shown in point 3 in Figure 14.

Mechanism C – The Hu, Hovis, Heuer model [52]:
In the first minutes of exposure of γ-Ni-28Cr-11Al (at.-%) at 1100°C in air a continuous external Cr_2O_3 layer forms and Al oxidizes internally. Ni particles are included between the two oxide phases. Subsequently, the volume increase by transformation from metastable- to α-Al_2O_3 causes extrusion of Ni particles towards the surface and NiO forms rapidly. The NiO and the Cr_2O_3 layer continue to grow until a continuous inner α-Al_2O_3 layer has formed.

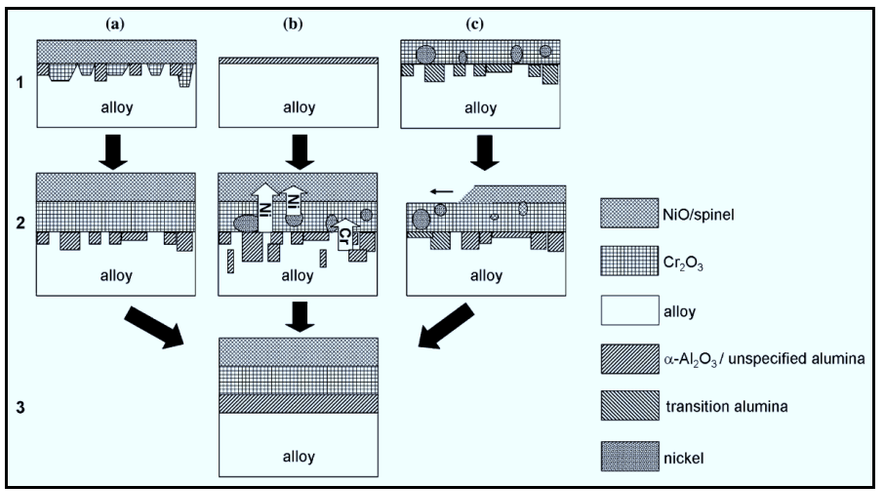

Figure 14: Scheme of the different mechanisms (a, b, c) proposed for the transient oxidation of single-phase γ-NiCrAl alloys [52]

All three mechanisms describe a different sequence for the formation of the various oxides. Mechanism A starts with NiO formation, mechanism B with Al_2O_3 formation and mechanism C with the formation of a Cr_2O_3 layer. However, all proposed mechanisms show after the transient stage a three-layered oxide scale.

4.3.2 Internal Oxidation

A homogeneous binary alloy with parent metal A and alloying element B is assumed, whereby the dissociation pressure of the oxide AO_{vA} is higher than that of BO_{vB}. Exposing this alloy to conditions where B can form a thermodynamically stable oxide but A cannot be oxidized will lead to diffusion of B atoms in the solid solution to the surface [25]. If the solubility of oxygen in A exceeds a certain value, the formation of BO_{vB} will take place inside the alloy by reaction of B with inward diffusing oxygen [53]. This is called internal oxidation [53, 54, 55, 56, 57]. The necessary conditions for internal oxidation are [25]:

1. ΔG^0 for the solute metal oxide BO_{vB} must be smaller than ΔG^0 for the base metal oxide AO_{vA}
2. ΔG for the formation of BO_{vB} must be smaller than zero
3. The solute concentration of B in the alloy must be lower than that required for the transition from internal to external oxidation
4. At the start of oxidation no surface layer prevents the dissolution of oxygen into the alloy

4.3.2.1 Internal Oxidation in the Absence of an External Oxide Scale

When the environmental oxygen partial pressure is below the dissociation pressure of AO_{vA} but above that of BO_{vB}, then the environmental conditions allow the formation of a stable oxide of BO_{vB} and prevent the formation of AO_{vA} [25]. Thus, the internal formation of BO_{vB} without an external oxide scale of A is possible. Figure 15 shows the simplified concentration profiles of oxygen and element B through the zone of internal oxidation (IOZ) in the absence of an external oxide scale of A. The oxygen flux into the IOZ is defined as J_O and the growing width of the IOZ as X_{IOZ}.

J_O = Oxygen flux $[mol/cm^2 \times s]$

X_{IOZ} = Width of the IOZ $[cm]$

$N_O^{(S)}$ = Oxygen solubility at the surface [mole fraction]

$N_B^{(0)}$ = Initial solute concentration of B [mole fraction]

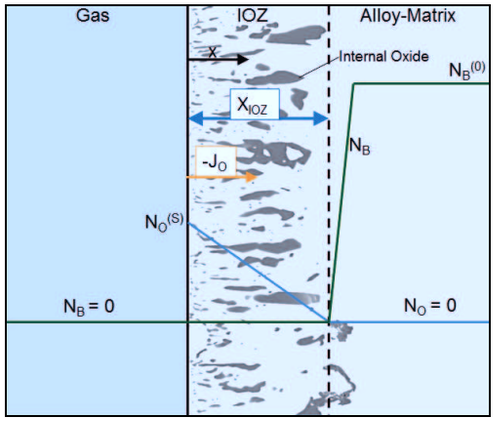

Figure 15: Simplified concentration profiles in and beneath the internal oxidation zone (IOZ) without external oxide scale formation [25]

A quasi-steady state approximation requires the assumption that the dissolved oxygen concentration changes linearly across the IOZ [25]. Hence, the oxygen flux can be calculated using Fick's first law [25]:

$$-J_O = \frac{dn_O}{dt} = D_O \times \frac{N_O^{(S)}}{V_m^{A-B} \times X_{IOZ}} \tag{19}$$

$n_O^{(IOZ)}$ = Amount of oxygen in the IOZ $\left[mol / cm^2\right]$

D_O = Diffusivity of oxygen $\left[cm^2 / s\right]$

V_m^{A-B} = Molar volume of the alloy A-B $\left[cm^3 / mol\right]$

If the counter-diffusion of B towards the IOZ is neglected (Figure 16, left) and assuming the formation of $BO_{\nu B}$, the amount of oxygen in the IOZ can be calculated by [25]:

$$n_O = \frac{N_B^{(0)} \times \nu_B \times X_{IOZ^*}}{V_m^{A-B}} \tag{20}$$

ν_B = Specific factor of oxide $BO_{\nu B}$

X_{IOZ^*} = Width of the IOZ without counter-diffusion of B $\left[cm\right]$

Combining equation (19) with equation (20) yields:

$$\frac{dn_O}{dt} = \frac{N_B^{(0)} \times \nu_B}{V_m^{A-B}} \times \frac{dX_{IOZ^*}}{dt} = D_O \times \frac{N_O^{(S)}}{V_m^{A-B} \times X_{IOZ^*}}$$

$$X_{IOZ^*} \times dX_{IOZ^*} = \frac{N_O^{(S)} \times D_O}{N_B^{(0)} \times \nu_B} \times dt \tag{21}$$

Integration, assuming $X_{IOZ^*} = 0$ at t = 0, yields the expression for calculation of the depth of the IOZ, X_{IOZ^*}, without considering diffusion of element B [25]:

$$\frac{1}{2} X_{IOZ^*}^{\ 2} = \frac{N_O^{(S)} \times D_O}{N_B^{(0)} \times \nu_B} \times t$$

$$\Rightarrow X_{IOZ^*} = \left[\frac{2 \times N_O^{(S)} \times D_O}{N_B^{(0)} \times \nu_B} \times t \right]^{\frac{1}{2}} \tag{22}$$

Equation (22) assumes no counter-diffusion of B. If the diffusion of B towards the IOZ is taken into account, the dissolution of oxygen and B in the IOZ and the alloy can be determined by Fick's second law [58, 59]:

$$\frac{\partial N_i}{\partial t} = D_i \times \frac{\partial^2 N_i}{\partial x^2} \qquad \text{with } i = O \text{ or } i = B \tag{23}$$

If it is assumed that the molar volume of the alloy A-B is constant and the formed oxide particles $BO_{\nu B}$ do not affect the oxygen diffusion in the material, equation (22) can be solved for the following limiting conditions [57]:

$N_O = N_O^{(S)}$ for x = 0 , t > 0

$N_O = 0$ for $x > X_{IOZ}$, t > 0

$N_B = N_B^{(0)}$ for $x \geq 0$, t = 0

$N_B = 0$ for $x \leq X_{IOZ}$, t > 0

The solutions of equation (23) are [57]:

$$N_O = N_O^{(S)} \times \left(1 - \frac{erf\left(\frac{x}{2 \times \sqrt{D_O \times t}} \right)}{erf(\gamma)} \right) \qquad \text{for } 0 \leq x \leq X_{IOZ} \tag{24}$$

$$N_B = N_B^{(0)} \times \left(1 - \frac{erfc\left(\frac{x}{2 \times \sqrt{D_B \times t}} \right)}{erfc\left(\gamma \times \sqrt{\frac{D_O}{D_B}} \right)} \right) \qquad \text{for } X_{IOZ} \leq x \tag{25}$$

γ = Time dependent kinetic parameter [59], defined in equation (31)

Assuming that BO_{vB} is only formed at the reaction front, $x = X_{IOZ}$, then the fluxes of oxygen from the surface and of B from the bulk material towards this interface have to be equal. Using equation (19) leads to [57, 59]:

$$\begin{aligned} &\left(J_O\right)_{x=X_{IOZ}} = -\nu_B \times \left(J_B\right)_{x=X_{IOZ}} \\ &\Rightarrow -D_O \times \left(\frac{\partial N_O}{\partial x} \right)_{x=X_{IOZ}} = \nu_B \times D_B \times \left(\frac{\partial N_B}{\partial x} \right)_{x=X_{IOZ}} \end{aligned} \tag{26}$$

From substitution of the equations (24) and (25) into equation (26) it follows [57]:

$$\frac{N_O^{(S)}}{\nu_B \times N_B^{(0)}} = \frac{\exp\left(\gamma^2\right) \times erf\left(\gamma\right)}{\sqrt{\frac{D_O}{D_B}} \times \exp\left(\gamma^2 \times \frac{D_O}{D_B} \right) \times erfc\left(\gamma \times \sqrt{\frac{D_O}{D_B}} \right)} \tag{27}$$

If the mole fractions of oxygen at the surface $N_O^{(S)}$ and B in the bulk alloy $N_B^{(0)}$ as well as the diffusion coefficients D_O and D_B are known, γ can be determined by numerical calculations of equation (27). For the permeabilities of oxygen and element B, defined as the product of mole fraction and diffusion of the respective element, two limiting conditions can be defined [57, 59]:

I. The permeability of oxygen is much higher than that of B, thus $N_O^{(S)} \times D_O >> N_B^{(0)} \times D_B$
II. The permeability of B is much higher than that of oxygen, thus $N_B^{(0)} \times D_B >> N_O^{(S)} \times D_O$

For the limiting condition I, it was shown that $\gamma << 1$ and $\gamma \times \sqrt{\frac{D_O}{D_B}} >> 1$ [57]. Then equation (27) can be approximated as:

$$\frac{N_O^{(S)}}{\nu_B \times N_B^{(0)}} = 2 \times \gamma^2 \tag{28}$$

In contrast to this, the limiting condition II implies that $\gamma << 1$ and thus $\gamma \times \sqrt{\frac{D_O}{D_B}} << 1$ [57]. For this case equation (27) can be approximated as:

$$\frac{N_O^{(S)}}{\nu_B \times N_B^{(0)}} = \frac{2 \times \gamma}{\sqrt{\pi} \times \left(\frac{D_O}{D_B}\right)^{\frac{1}{2}}} \tag{29}$$

The two limiting cases have different effects on the concentration profiles of oxygen and element B in the alloy as illustrated in Figure 16 [25].

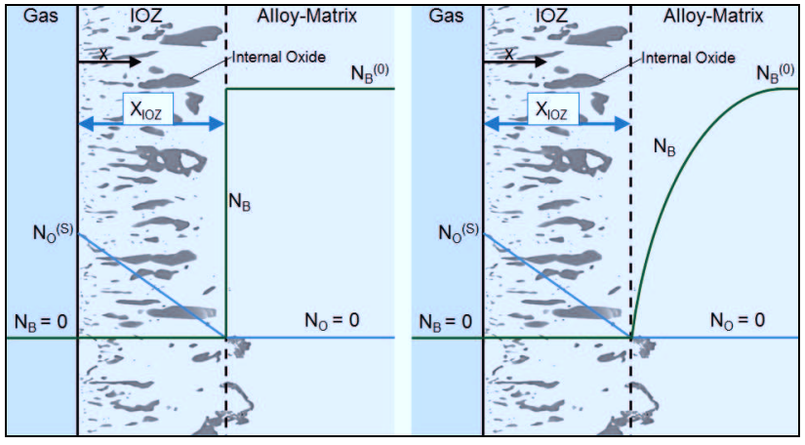

Figure 16: Schematic concentration profiles of oxygen and alloying element B during internal oxidation for limiting condition I (left) and limiting condition II (right)

As the concentration of oxygen is in both cases equal to zero at the reaction front, $x = X_{IOZ}$, (see Figure 16) equation (24) can for this location be rewritten as:

$$0 = N_O^{(S)} \times \left(1 - \frac{erf\left(\frac{X_{IOZ}}{2 \times \sqrt{D_O \times t}}\right)}{erf(\gamma)}\right) \tag{30}$$

From considering $N_O^{(S)} > 0$, as shown in Figure 16, it follows:

$$0 = 1 - \frac{erf\left(\frac{X_{IOZ}}{2 \times \sqrt{D_O \times t}}\right)}{erf(\gamma)}$$

Rearranging then leads to:

$$X_{IOZ} = 2 \times \gamma \times \sqrt{D_O \times t} \tag{31}$$

Assuming limiting condition I ($N_O^{(S)} \times D_O >> N_B^{(0)} \times D_B$), and substituting equation (28) into equation (31), leads to the same result for X_{IOZ}, as obtained by neglecting the diffusion of B, shown in equation (22):

$$X_{IOZ,1} = \left[\frac{2 \times N_O^{(S)} \times D_O}{N_B^{(0)} \times \nu_B} \times t\right]^{\frac{1}{2}} \qquad \text{for limiting condition I} \tag{32}$$

As the permeabilities in the limiting cases are very small [59], namely $N_O^{(S)} \times D_O << 1$ and $N_B^{(0)} \times D_B << 1$, it holds that $X_{IOZ,1}$ equals X_{IOZ^*}

In case of limiting condition II ($N_B^{(0)} \times D_B >> N_O^{(S)} \times D_O$), the substitution of equation (28) into equation (30) yields for the depth of the internal oxidation zone X_{IOZ}:

$$X_{IOZ,2} = \frac{N_O^{(S)} \times D_O}{\nu_B \times N_B} \times \left(\frac{\pi \times t}{D_B}\right)^{\frac{1}{2}} \qquad \text{for limiting condition II} \tag{33}$$

Equation (32) and (33) can be used to estimate the depth of the zone affected by internal oxidation. However, many alloy systems show deviations from these simplified calculations. These deviations are based e. g. on [25, 55]:

1. Accelerated diffusion along the internal oxide/alloy interfaces, allowing deeper penetrations than calculated
2. Preferential formation of internal oxide on alloy grain boundaries
3. Alternating bands of internal oxide formed parallel to the alloy surface
4. Extrusions of the parent element A from the IOZ forming pure metal nodules on the alloy surface
5. Formation of areas containing more than the stoichiometric amount of oxygen

In spite of these deviations, it follows from equations (32) and (33) that there is a limiting initial concentration of element B for which the internal oxidation is stopped [25]. If this is the case, a transition from internal to external oxidation of B takes place.

4.3.2.2 Internal Oxidation in the Presence of an External Oxide Scale

When the environmental oxygen partial pressure is above the dissociation pressure of oxide AO_{vA}, then BO_{vB} and AO_{vA} can be stable [59]:

$$pO_2 > pO_{2,AO_{vA}} > pO_{2,BO_{vB}} \tag{34}$$

$pO_{2,iO_{vi}}$ = Dissociation pressure of the respective oxide iO_{vi} $[bar]$

Values for dissociation pressures of several oxides as function of temperature may be calculated with FACTSAGE (see Figure 8). Figure 17 shows the concentration profiles for oxygen and element B in the IOZ in the presence of an external oxide scale of AO_{vA} [59]. In comparison to the internal oxidation of element B without the external formation of AO_{vA}, there are two main differences to note [59]:

1. Recession of the scale/alloy interface, due to formation of AO_{vA}
2. The oxygen partial pressure at the interface between AO_{vA} scale and the IOZ is not governed by the oxygen partial pressure of the gas but equals the dissociation pressure of AO_{vA}

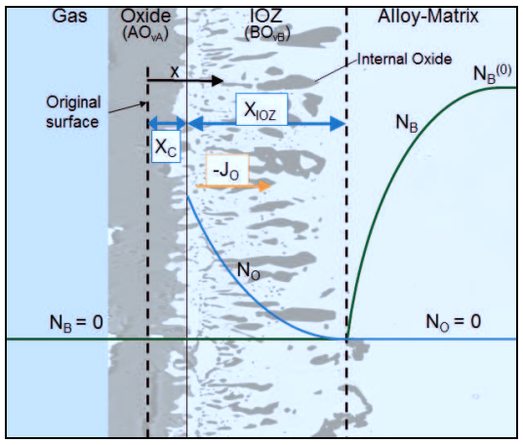

Figure 17: Simplified concentration profiles in the internal oxidation zone (IOZ) for the case that an external oxide scale is formed based on reference [59]

Both effects were investigated by Nesbitt [60]. To consider the recession of the scale/alloy interface in a binary Ni-Al alloy at 1200°C a modified form of equation (27) from F. Maak [61] can be used:

$$\frac{N_O^{(S)}}{\nu_B \times N_B^{(0)}} = \frac{\left(erf(\gamma) - erf\left(\frac{k'_C}{2 \times D_O} \right)^{\frac{1}{2}} \right) \times \exp(\gamma^2)}{\sqrt{\frac{D_O}{D_B}} \times \exp\left(\gamma^2 \times \frac{D_O}{D_B} \right) \times erfc\left(\gamma \times \sqrt{\frac{D_O}{D_B}} \right)} \tag{35}$$

k'_C = parabolic rate constant for the recession of the oxide/metal interface $\left[\frac{cm^2}{s} \right]$

To consider effect number 2 (see page 27) the oxygen partial pressure at the scale/IOZ interface has to be considered to be equal to the dissociation pressure of AO_{vA}. Compared to the conditions without formation of an external scale (pO_2 < dissociation pressure of AO_{vA}), this will result in a pO_2 increase at the interface, affecting the formation of the IOZ by the oxygen solubility N_O. The relation between pO_2 and oxygen solubility N_O is given by Sieverts' law [62] in which the equilibrium reaction constant K_{pO2} is related to the standard Gibbs free energy change ΔG^0 of the reaction $\frac{1}{2} O_2(g) = \underline{O}$ [31] by equation (7):

$$N_O^{(S)} = K_{pO2} \times (pO_2)^{\frac{1}{2}} \tag{36}$$

K_{pO2} = Equilibrium reaction constant for the dissolution of oxygen

Substitution of equation (7) into equation (36) yields to [31]:

$$K_{pO2} = \exp\left(\frac{-\Delta G^\circ}{R \times T} \right) = \exp\left(\frac{-\Delta H_O + T \times \Delta S_O}{R \times T} \right) \tag{37}$$

$$N_O^{(S)} = K_{pO2} \times (pO_2)^{\frac{1}{2}} = \exp\left(\frac{-\Delta H_O + T \times \Delta S_O}{R \times T} \right) \times (pO_2)^{\frac{1}{2}} \tag{38}$$

ΔH_O = Enthalpy change for the dissolution of oxygen $\left[\frac{J}{mol} \right]$

ΔS_O = Entropy change for the dissolution of oxygen $\left[\frac{J}{mol \times K} \right]$

Values for ΔH_O and ΔS_O differ depending on the respective base metal and can be found from various sources in literature [63, 64]. By calculations, considering interface recession and a pO_2 equal to the dissociation pressure of AO_{vA}, it was found by Nesbitt for binary NiAl alloys that the surface recession has only a marginal effect on the calculation of concentrations of element B (here Al), whereas a higher pO_2 at the scale/alloy interface will promote the internal oxidation of B [60]. However, if the initial concentration of B exceeds a certain value a transition from internal to external oxidation of B occurs.

4.3.3 Transition from Internal to External Oxidation

Equation (32) and (33) show that the width of the IOZ decreases with increasing $N_B^{(0)}$ and decreasing $N_O^{(S)}$. If, for a given oxygen solubility $N_O^{(S)}$, the initial concentration of B is sufficiently high, the outward diffusion of B will cause the formation of a continuous layer of BO_{vB} and internal oxidation is stopped. The binary alloy A-B will then be covered by an external BO_{vB} scale [25]. It is assumed that no external scale of AO_{vA} is present. The transition from internal to external oxidation of one alloying element in a binary alloy system was firstly investigated by Wagner in the late 1950s [56, 57].

The mole concentration of BO_{vB} per unit volume in the IOZ is defined as $N_{BO_{vB}} / V_m^{A-B}$, if V_m^{A-B} is the molar volume of the alloy A-B [25]. During time increment *dt* the internal oxidation front, with the area A, moves a distance step dX_{IOZ}. Hence, the number of moles of BO_{vB} in a volume element can be defined as $\frac{N_{BO_{vB}}}{V_m^{A-B}} \times A \times dX_{IOZ}$. This amount has to be equal to the number of moles of B arriving from the bulk alloy at the reaction front [25]. Using equation (19) yields then to [25]:

$$\left(\frac{N_{BO_{vB}}}{V_m^{A-B}}\right) \times A \times dX_{IOZ} = \left(-A \times J_B\right) dt$$

$$\Rightarrow \left(\frac{N_{BO_{vB}}}{V_m^{A-B}}\right) \times A \times dX_{IOZ} = A \times \frac{D_B}{V_m^{A-B}} \times \left(\frac{\partial N_B}{\partial x}\right) dt \tag{39}$$

Substituting the derivatives of equation (25) and (31) into equation (39) leads to [25]:

$$\frac{N_{BO_{vB}}}{N_B^{(0)}} = \frac{1}{\sqrt{\pi} \times \gamma \times \sqrt{\frac{D_0}{D_B}} \times \exp\left(\gamma^2 \times \frac{D_O}{D_B}\right) \times erfc\left(\gamma \sqrt{\times \frac{D_O}{D_B}}\right)} \tag{40}$$

The molar volume fraction of BO_{vB} in the IOZ can be defined as [59]:

$$g_{BO_{vB}} = \frac{N_{BO_{vB}} \times V_m^{BO_{vB}}}{V_m^{A-B}} \tag{41}$$

Thus, by combining equation (40) and (41) it follows:

$$N_B^{(0)} = g_{BO_{vB}} \times \frac{V_m^{A-B}}{V_m^{BO_{vB}}} \times \sqrt{\pi} \times \gamma \times \sqrt{\frac{D_0}{D_B}} \times \exp\left(\gamma^2 \times \frac{D_O}{D_B}\right) \times erfc\left(\gamma \sqrt{\times \frac{D_O}{D_B}}\right) \tag{42}$$

A critical molar volume fraction $g^*_{BO_{vB}}$ for which the transition from internal to external oxidation takes place is assumed. This critical volume fraction $g^*_{BO_{vB}}$ is defined as the minimum volume fraction of the oxide BO_{vB} in the IOZ necessary to form a continuous scale of BO_{vB} instead of precipitates separated by the base alloy matrix A [25]. Connecting the critical molar volume fraction $g^*_{BO_{vB}}$ to limiting condition II ($N_B^{(0)} \times D_B >> N_O^{(S)} \times D_O$) [59] will simplify equation (42) to [59]:

$$N_{B\ critical,1}^{(0)} = g^*_{BO_{vB}} \times \frac{V_m^{A-B}}{V_m^{BO_{vB}}} \times \sqrt{\pi} \times \gamma \times \sqrt{\frac{D_O}{D_B}} \tag{43}$$

Substitution of equation (29) into equation (43) and rearrangements yield to the general criterion for the transition from internal to external oxidation, defined originally by Wagner [25, 57]:

$$N_{B\ critical,1}^{(0)} = \left(\frac{g^*_{BO_{vB}} \times \pi \times V_m^{A-B} \times N_O^{(S)} \times D_O}{2 \times \nu_B \times V_m^{BO_{vB}} \times D_B} \right)^{\frac{1}{2}} \tag{44}$$

It has to be taken into account that equation (44) holds when the concentrations of oxygen (N_O) and alloying element B (N_B) at the reaction front of the internal oxidation zone are virtually zero [59]. If $N_B^{(0)}$ exceeds $N_{B\ critical,1}^{(0)}$ then the oxidation process will change from internal to external oxide formation of B, as the critical molar volume fraction $g^*_{BO_{vB}}$ is reached [25]. In 1961 Rapp determined experimentally the value $g^*_{BO_{vB}}$ to 0.3 for In_2O_3 in Ag-In alloys [65]. For experiments with binary Ni-Al alloys Nesbitt [60] identified an average critical volume fraction $g^*_{BO_{vB}}$ of 0.2. However, by comparing calculations with the experiments of Giggins and Pettit [33] it was found that for Ni-Al alloys, oxidized at 1200°C, a critical volume fraction of 0.3 corresponds much better to the experiments than the value of 0.2 does [60]. In the present work a calculation of Zhao et al [66] is used to determine the critical

volume fraction $g^{*}_{BO_{vB}}$ for the formation of external Al_2O_3 on NiCrAl alloy. It calculates as [66]:

$$g^{*}_{BO_{vB}} = \frac{2 \times \left(\frac{V_m^{BO_{vB}}}{V_m^{A-B}} \right)^{\frac{1}{2}}}{6^{\frac{1}{2}} + 2 \times \left(\frac{V_m^{BO_{vB}}}{V_m^{A-B}} \right)^{\frac{1}{2}}} \tag{45}$$

Using equation (45) leads to a critical volume fraction for the materials of the present study of 0.53, which is higher compared to the value of 0.3 determined by Rapp [65]. The authors of the applied quantitative approach leading to equation (45) mention a certain overestimation of $g^{*}_{BO_{vB}}$, arising from missing consideration of supersaturation affecting the volume fraction $g_{BO_{vB}}$ and of the oxide particles geometry in the IOZ [66]. The latter can be affected by different environmental conditions, particularly different gas species and temperatures [67, 68].

4.3.4 Maintenance of External Oxide Scale Growth

Formation of an external oxide scale BO_{vB} results in a depletion of the scale forming element B beneath that scale. To maintain an existing external oxide scale BO_{vB} the concentration of element B beneath the scale after its formation has to be high enough to sustain the scale growth [25, 56]. The time dependent change of the concentration profile of B in alloy A-B can be described by equation (46) and is illustrated in Figure 18 [25].

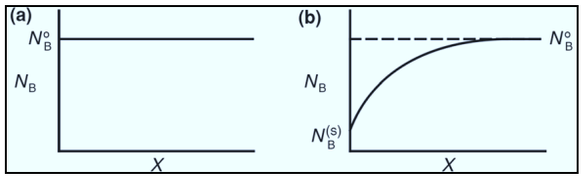

Figure 18: Schematic concentration of B in alloy A-B at t = 0 (a) and at t > 0 (b) in case of external BO_{vB} formation [25]

$$N_B = N_B^{(S)} + \left(N_B^{(0)} - N_B^{(S)} \right) \times erf\left(\frac{x}{2 \times \sqrt{D_B \times t}} \right) \tag{46}$$

The concentration of B beneath the external scale is connected to the outward flux of B. Similar to equation (19), the flux of B at the surface $J_B^{(S)}$ (x = 0) can be calculated by Fick's first law [58]:

$$J_B^{(S)} = \frac{dn_B}{dt} = -\frac{D_B}{V_m^{A-B}} \times \left(\frac{\partial N_B}{\partial x} \right)_{x=0} \tag{47}$$

Deriving equation (46) and assuming $N_B^{(S)}$ to be zero [25] results for x = 0 in:

$$\left(\frac{\partial N_B}{\partial x} \right)_{x=0} = -N_{B\ critical,2}^{(0)} \times \frac{2}{\sqrt{\pi \times D_B \times t}}$$

$$\Rightarrow J_B^{(S)} = -\frac{D_B}{V_m^{A-B}} \times \left(\frac{\partial N_B}{\partial x} \right)_{x=0} = \left(\frac{D_B}{\pi \times t} \right)^{\frac{1}{2}} \times \frac{2 \times N_{B\ critical,2}^{(0)}}{V_m^{A-B}} \tag{48}$$

Where $N_{B\ critical,2}^{(0)}$ is the minimum initial concentration of B for the outward flux $J_B^{(S)}$. The change in molar volume of B per surface area can be written as [31]:

$$\frac{dn_B}{dt} = \frac{d\left(\frac{X}{V_m^{BO_{vB}}} \right)}{dt} \tag{49}$$

Substitution of equation (16), calculating oxide scale thickness X, into (49) yields to [31]:

$$J_B^{(S)} = \frac{dn_B}{dt} = \frac{d\left(\frac{X}{V_m^{BO_{vB}}} \right)}{dt} = \frac{1}{V_m^{BO_{vB}}} \times \frac{dX}{dt} = \frac{1}{V_m^{BO_{vB}}} \times \left(\frac{2 \times k_p}{t} \right)^{\frac{1}{2}} \tag{50}$$

Combining equation (48) and (50) leads to [59]:

$$J_B^{(S)} = \left(\frac{D_B}{\pi \times t} \right)^{\frac{1}{2}} \times \frac{2 \times N_{B\ critical,2}^{(0)}}{V_m^{A-B}} = \frac{1}{V_m^{BO_{vB}}} \times \left(\frac{2 \times k_p}{t} \right)^{\frac{1}{2}}$$

$$\Rightarrow N_{B\ critical,2}^{(0)} = \frac{V_m^{A-B}}{V_m^{BO_{vB}}} \times \left(\frac{\pi \times k_p}{2 \times D_B} \right)^{\frac{1}{2}} \tag{51}$$

Thus, the growth of an external scale of BO_{vB} on a binary alloy A-B will be maintained if the initial concentration of B ($N_B^{(0)}$) is higher than $N_{B\ critical,2}^{(0)}$, i. e. diffusion is fast enough to supply sufficient B for the scale growth.

5 Experimental

5.1 Studied Materials

The requirements on a construction material for support structures of gas separation membranes can be fulfilled by α-Al_2O_3 forming Ni-base alloys, as mentioned in section 1. During operation at elevated temperatures these components have to withstand different corrosive atmospheres, containing e. g. O_2, H_2O and CO_2 (Table 1). In these conditions, the formation of a protective Al_2O_3 surface scale is crucial for the operation of the membrane carrier. To determine the influences of temperature, exposure time and gas atmosphere on the selective oxidation of Al, the "borderline" NiCrAl-base alloys Haynes 214 and Alloy 602 CA were investigated. The expression "borderline" here means, that the alloy Al contents are close to the value given by equations (44) and (51) and may thus change from external to internal Al_2O_3 formation upon changes of experimental conditions, e. g. temperature and gas composition.

The materials were provided by Haynes International (Haynes 214) and VDM Metals (Alloy 602 CA) in the form of 2 mm thick sheets. The chemical analysis of the materials was performed by inductively coupled plasma optical emission spectroscopy (ICP-OES) for most of the elements. The carbon analysis was performed by combustion in an oxygen flow with subsequent quantitative infrared spectroscopy. In addition, the boron concentration was determined by ICP mass spectrometry (ICP-MS), as its concentration is <0.01. The results (Table 2) show only small variations between the analyzed batch of Haynes 214 and the nominal composition from the manufacturer.

Haynes 214	Ni	Cr	Al	Fe	Mn	C	Si	Zr	Co	B
Analyzed (at.-%)	69.93	16.68	8.96	3.49	0.19	0.401	0.058	0.0143	0.0147	0.0144
Analyzed (wt.-%)	75.7	16.0	4.46	3.6	0.19	0.0895	0.030	0.024	0.016	0.00287
Nominal (wt.-%)	Bal.	16	4.5	3	<0.5	0.05	<0.2	<0.1	-	<0.01

Table 2: Nominal and analyzed chemical composition of Haynes 214

Alloy 602 CA with a lower Al content was chosen in addition to Haynes 214 to investigate effects of composition, especially Al content, on external alumina scale formation. Table 3 gives the exact chemical composition, determined the same way as for Haynes 214.

Alloy 602 CA	Ni	Cr	Al	Fe	Ti	Mn	Co	Si	Mo	C	Zr	Y	B
at.-%	58.59	24.8	4.9	10.1	0.16	0.05	0.044	0.08	0.006	0.840	0.043	0.038	0.004
wt.-%	62.8	23.6	2.43	10.4	0.38	0.35	0.35	0.32	0.24	0.0997	<0.01	<0.01	0.0008

Table 3: Analyzed chemical composition of Alloy 602 CA

5.2 Sample Preparation

Specimens with a size of 20 x 10 x 2 mm were machined by laser cutting of all two test materials. For the oxidation studies the specimens were ground to p1200 grit surface finish and ultrasonically cleaned with ethanol prior to exposure. Figure 19 shows the sample dimensions and a photo of the sample in the post preparation state.

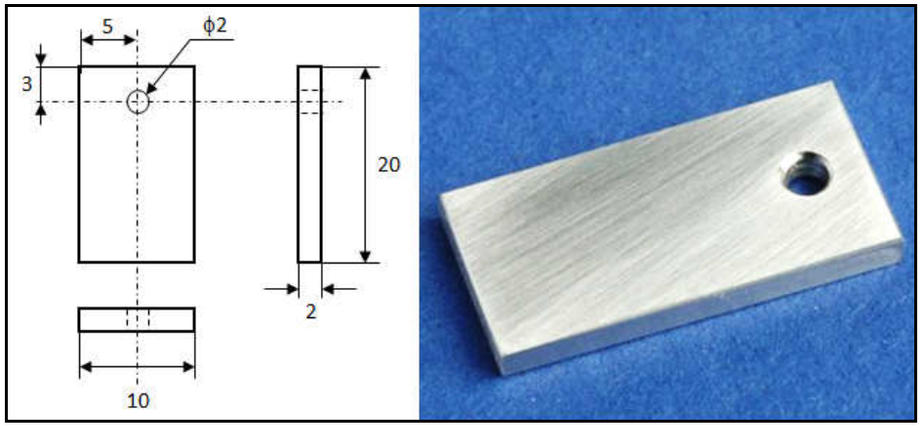

Figure 19: Dimensions and photo of a ground sample before oxidation

5.3 Oxidation Experiments

The oxidation of the different samples was carried out in furnaces with controlled atmosphere. Two types of test rigs were used:

1. Thermogravimetric analysis facility
2. Tube furnace

For isothermal experiments up to 72 h a thermogravimetry facility was used for continuous recording of the mass change during exposure [69]. The experiments were carried out using a Setaram TGA 92 microbalance. The specimens were heated to the test temperatures at a rate of 90 K/min in the respective test gas, kept at temperature for 72 h, and subsequently furnace cooled at approximately 10 K/min. The volume flow of the respective gas was set to 2 l/h, which corresponds to a linear velocity of 0.2 cm/s. The accuracy of this measurement technique is limit by the drift of the device (0.1 µm/h), the resolution (0.002 µg), which is not dependent on sample size, and the accuracy of the measurement of the sample dimensions (10 µm). Figure 20 shows the setup of the thermogravimetry facility.

For long-term experiments up to 1000 h a tube furnace was used for the oxidation tests. The heating and cooling rate of the furnace were 10 K/min and 2 K/min, respectively. The gas

flow rate was set to be equal to that of the thermogravimetric furnace, thus 2 l/h. Figure 21 shows the setup of the tube furnace, including the gas supply device.

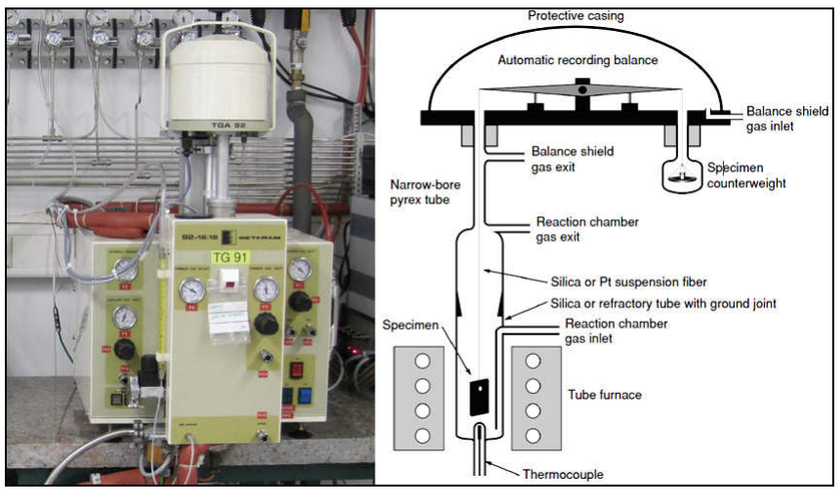

Figure 20: Photo and layout of a thermogravimetry facility (drawing from [25])

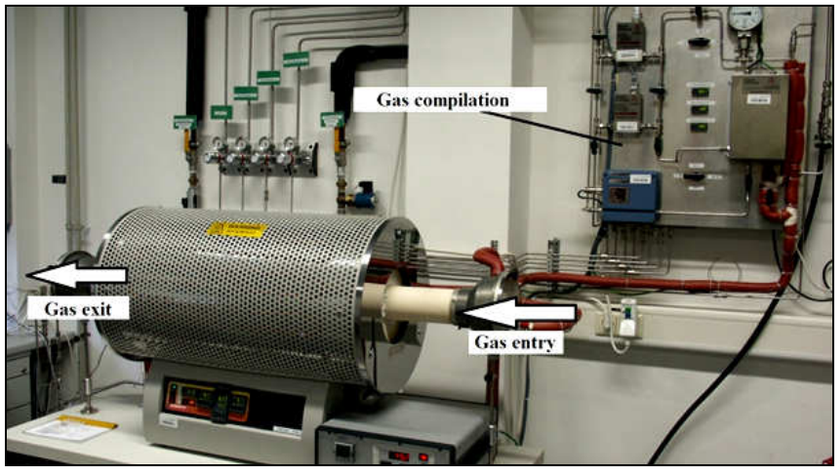

Figure 21: Photo of a tube furnace used for oxidation testing up to 1000 h exposure

5.4 Test Parameters

The separation of O_2 from air has a big relevance for industrial applications (electricity, concrete, and steel production (see section 1)). Thus, main emphasis was put on oxidation studies in Ar-20%O_2 atmosphere. The test temperatures are:

800°C
900°C
1000°C
1100°C

Thermogravimetric (TG) experiments were carried out for 8 h and 72 h. In addition, at 800°C and 900°C tests were performed in a tube furnace for 1000 h.

One set of specimens of Haynes 214 was aged in vacuum at 800°C for 100 h and subsequently, after surface preparation, exposed to Ar-20%O_2 for 72 h at every test temperature to investigate the effects of microstructural changes on the oxidation behavior. In addition, as all gas separation processes in CCS contain H_2O (Table 1), the effect of different H_2O-containing gases on oxidation behavior was investigated using the following test gases in 72 h TG exposures, beside Ar-20%O_2:

Ar-20%O_2-7%H_2O
Ar-7%H_2O
Ar-4%H_2-7%H_2O

5.5 Sample Characterization

After the oxidation process the samples were analyzed by a variety of techniques. The microscope Leica MF4 was used for investigations by light optical microscopy. The other characterization methods are described in the following sections.

For cross-section analyses with light optical microscopy and SEM/EDX after oxidation the specimens were prepared according to the following steps:

1. The sample is coated with a very thin gold layer (approx. 10 nm in thickness) to obtain an electrically conductive surface ready for nickel plating
2. A nickel plating is applied electrochemically from a $NiSO_4$ bath to obtain a better contrast between oxide scale and epoxy resin during light and electron optical microscopy
3. The sample is embedded in epoxy resin to protect the oxide layer against possible damages during grinding/polishing and to allow easier handling
4. A series of grinding (SiC paper) and polishing steps (diamond paste) is performed with a final polishing using 0.25 µm granulation SiO_2 solution

5.5.1 SEM/EDX

Analyses to determine the compositions of the respective specimen surfaces are carried out with the scanning electron microscopes (SEM) Zeiss Merlin and Zeiss Supra 50VP (Zeiss Microscopy, Oberkochen, Germany) equipped with energy dispersive X-Ray spectroscopy (EDX) X-Max (Oxford Instruments). The working principle of SEM is illustrated in Figure 22 [70].

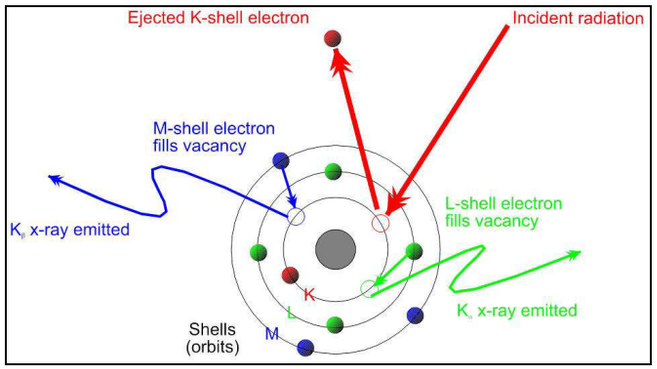

Figure 22: Illustration of the working principle of SEM [70]

The surface which has to be analysed in the device is bombarded with electrons. This causes the electrons on the inner shells to leave their original orbital. These leaving electrons are called secondary electrons and are measured with a detecting device to obtain an image of the samples surface [71]. Other signals are backscattered electrons, namely primary electrons reflected by the sample, and X-rays [71].

The EDX method works by measuring the X-rays, emitted by shell changes of electrons. Basically, the empty places on the inner shell, resulting from the leaving electrons, are immediately filled up with more energy-rich electrons from a higher orbital. This change induces an energy difference and the X-rays of this energy difference can be analysed by a detector. Thereby, each electron change, each atom and each element has its own characteristic X-rays [71]. Therefore, in each location of the surface all elements can be characterized.

5.5.2 XRD

With X-Ray diffraction (XRD) it is possible to determine the crystal structure of solid objects. The D4 Endeavor Diffractometer from Bruker AXS GmbH (Karlsruhe, Germany) was used in the present studies. Figure 23 illustrates the principle of the X-Ray diffraction schematically [72].

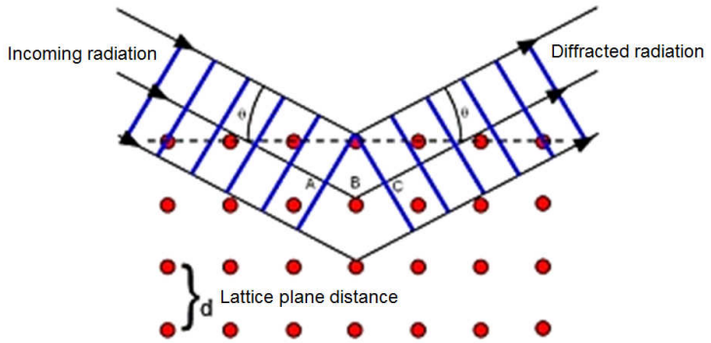

Figure 23: Principle of the X-ray diffraction [72]

The incoming X-rays are partly diffracted at the atoms of the crystal structure and partly transmitted. The wave length of the X-rays in this case has to be smaller than the distance of the atoms to get a characteristically X-ray diffraction picture of the analysed solid object [73].

5.5.3 GD-OES

The so-called glow discharge optical emission spectroscopy (GD-OES) allows not only to determine the chemical composition of the sample surfaces (like SEM), but also to analyse the element composition in the deeper layers. In the present study GD Profiler HR from Horiba Jobin Yvon (France) was used. The working principle of a GD-OES device is shown in Figure 24 [74].

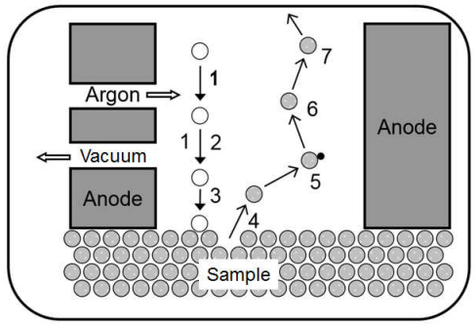

Figure 24: Illustration of the working principle of GD-OES [74]

Between the sample and a glow-discharge lamp, which is used as anode, a direct voltage is applied in the way that the sample works as cathode. Argon ions, which are present around the sample and the anode, are ionised by the voltage and accelerated towards the sample. By hitting the sample surface the argon ions remove the surface atoms layer by layer. The single

sample particles are now stimulated with ion push processes and other interactions and the light, which they emit, is decomposed in spectral lines by a spectrometer. Photomultipliers analyse the intensity of the single spectral lines [74]. In addition, the values received from the multiplier have to be quantified with the aid of the exact bulk alloy concentration. The method of quantification is described in [75, 76]. In this way it is possible to determine the composition of the sample as function of the penetration depth, which is of prime importance to interpret the corrosion mechanisms.

5.5.4 SNMS

In the present studies INA-5 SNMS Analyzer from SPECS GmbH (Berlin, Germany) was used for secondary neutral mass spectrometry (SNMS). The working principle is similar to GD-OES (see Figure 24), but in SNMS measurements the neutral particles coming from the sample are analysed using mass spectrometry. The method of quantification is the same as for GD-OES [75, 76].

5.5.5 Fluorescence Spectroscopy

Fluorescence optical spectroscopy can be used for identification of various crystallographic modifications of alumina scales and their mechanical stresses arising from thermal mismatch between oxide and alloy [77]. For prevailing investigations the device Labram HR 800 from Horiba Jobin Yvon (France) was used.

The fluorescence is excited using an Ar-ion laser with a wavelength of 514.5 nm or a He-Ne laser with a wavelength of 623.8 nm. Substitution of the native oxide cation in octahedral coordination by Cr^{3+} ions produces Cr^{3+} luminescence lines (so-called R-lines) [77] which are measured at specific wavelengths.

Estimation of mechanical stresses in the Al_2O_3 scale can be made by measuring shifts between the R-lines of the respective specimen and of a stress free reference sample, e. g. sapphire [77, 78, 79].

6 Results and Discussion

Oxidation tests on alloy 602 CA were carried out in different H_2O-containing atmospheres and compared to those in Ar-20%O_2 to investigate possible effects of H_2O on the oxidation behavior. The effects of exposure time, temperature and alloy microstructure on the formation of an external Al_2O_3 layer were investigated by oxidation tests in Ar-20%O_2 on Haynes 214. Subsequently, the results obtained in Ar-20%O_2 were compared with those in Ar-7%H_2O, Ar-4%H_2-7%H_2O and Ar-20%O_2-7%H_2O. In addition, to study effects of alloy composition, especially changing aluminum concentrations, on the formation of a continuous Al_2O_3 layer, the results of the oxidation tests on Haynes 214 and alloy 602 CA are compared.

6.1 Oxidation Behavior of Alloy 602 CA

The isothermal exposures were performed in Ar-7%H_2O, Ar-4%H_2-7%H_2O, and Ar-20%O_2-7%H_2O atmospheres at 800, 900, 1000, and 1100°C respectively (see section 5.3). For selected experimental conditions, the results were compared with the behavior in dry Ar-20%O_2.

6.1.1 Phase Composition and Microstructure of Alloy 602 CA

The detailed chemical composition of the investigated batch of alloy 602 CA is shown in Table 3. Figure 25 shows the backscattered electron (BSE) image of cross-sections of the investigated alloy in the as-received condition. The alloy exhibits a recrystallized microstructure consisting of equi-axed γ-phase grains with evenly distributed precipitates of $Cr_{23}C_6$ and Y-, Zr-, Ti-rich nitrides. The $Cr_{23}C_6$ precipitates have round shapes with a mean diameter of 5-10 µm. Furthermore, small amounts of Y-, Zr-rich oxides were found in the γ-matrix.

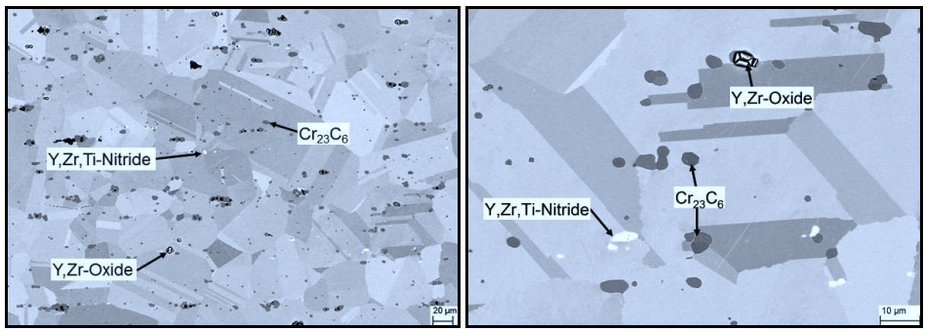

Figure 25: Bulk alloy microstructure (BSE image) of alloy 602 CA in the as-received condition

6.1.2 Results of the Behavior in Ar-20%O_2 and H_2O-Containing Gases

6.1.2.1 Oxidation Kinetics

Figure 26 - Figure 28 show area specific weight gain kinetics for alloy 602 CA measured by continuous TGA (section 5.3) during 72 h of exposure in Ar-7%H_2O, Ar-4%H_2-7%H_2O, and Ar-20%O_2-7%H_2O between 800°C and 1100°C. The weight gains increase with increasing oxidation temperature for all specimens. Specimens oxidized at 800°C show very similar weight changes after 72 h oxidation, independent of test gas used. Increasing the oxidation temperature to 900°C, results in differentiation of recorded weight gains between the test environments. The specimen exposed for 72 h in Ar-20%O_2-7%H_2O shows approximately two times smaller weight gain than that measured in Ar-7%H_2O. For specimens oxidized at 1000°C and 1100°C the highest weight gains were recorded in Ar-7%H_2O. The weight gains during exposure in Ar-20%O_2-7%H_2O and Ar-4%H_2-7%H_2O are very similar and approximately 14 % smaller than those obtained in Ar-7%H_2O. Results in dry Ar-20%O_2 revealed a qualitatively similar temperature dependence of oxidation kinetics (Figure 29).

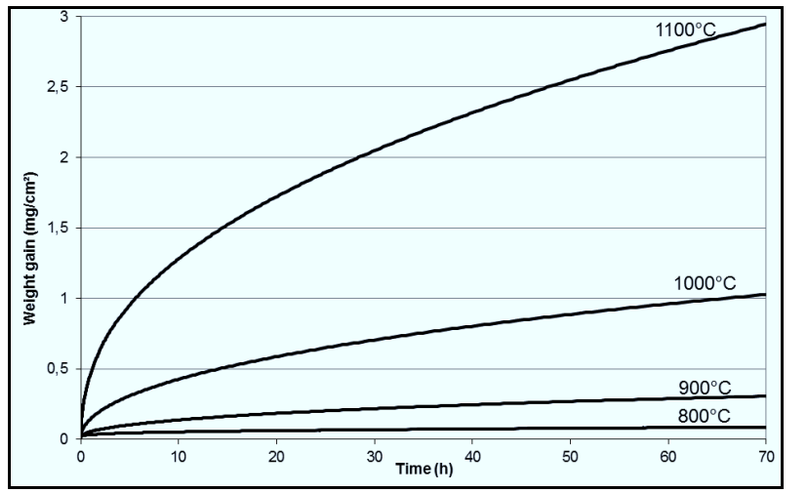

Figure 26: Area specific weight gain during isothermal oxidation of alloy 602 CA in Ar-7%H_2O at different temperatures

The oxidation kinetics of the material exposed in all four test gases exhibit sub-parabolic oxidation behavior and could therefore not be described using the classical parabolic rate description, shown in equation (17). Therefore Figure 30 shows an example of the instantaneous, apparent parabolic rate constant as function of time using the procedure described in appendix B. A constant value of k'_w would relate to ideal parabolic oxidation. However, the curves exhibit k'_w-values which are steadily decreasing with increasing exposure time. No sudden change in apparent k'_w-value occurred during exposure, thus

indicating that the oxidation mechanism at a given temperature did not fundamentally change during exposure. This tendency was found for all test atmospheres, as already indicated by the shape of the TGA curves.

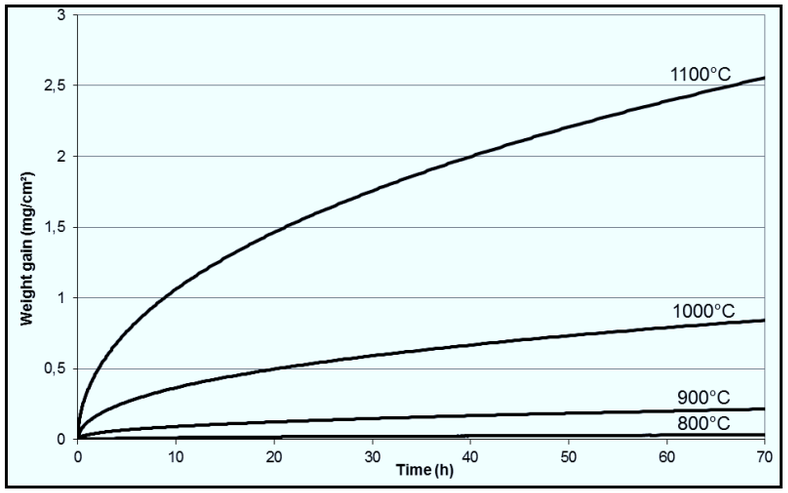

Figure 27: Area specific weight gain during isothermal oxidation of alloy 602 CA in Ar-4%H_2-7%H_2O at different temperatures

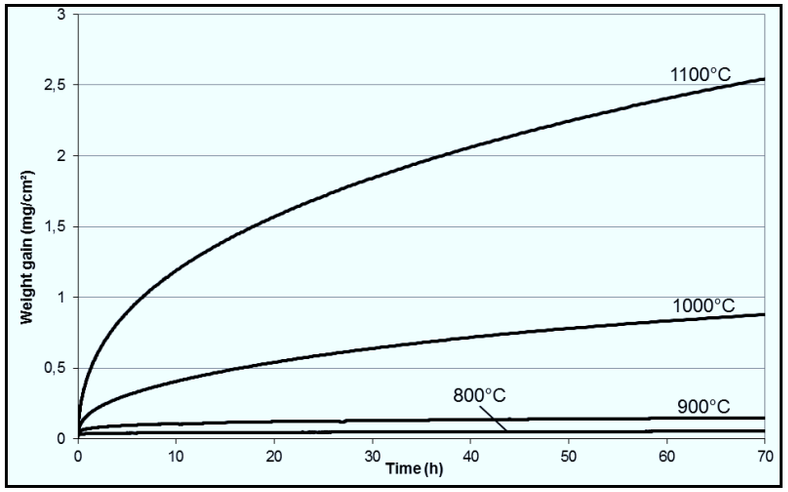

Figure 28: Area specific weight gain during isothermal oxidation of alloy 602 CA in Ar-20%O_2-7%H_2O at different temperatures

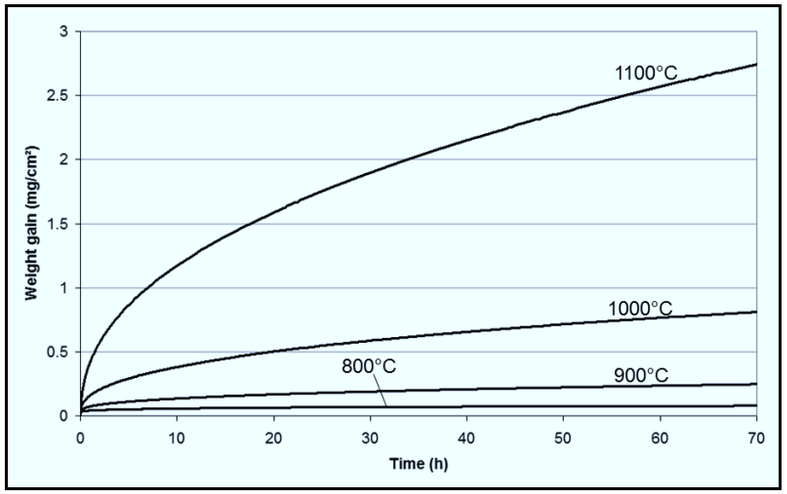

Figure 29: Area specific weight gain during isothermal oxidation of alloy 602 CA in Ar-20%O_2 at different temperatures

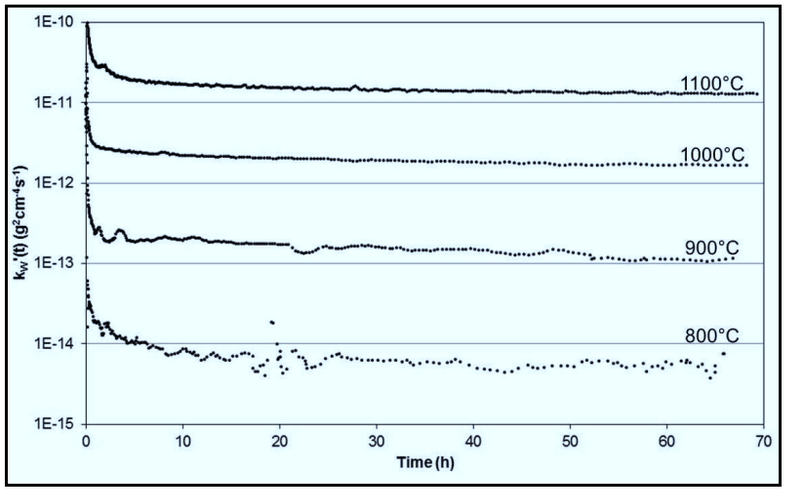

Figure 30: Time dependence of the instantaneous apparent parabolic oxidation rate constant of alloy 602 CA during isothermal oxidation in Ar-7%H_2O

6.1.2.2 Oxide Scale Formation

Figure 31 shows the SEM/BSE images of the oxide scale formed on alloy 602 CA exposed for 72 h at 800°C. The oxide scales consist predominantly of a thin external Al_2O_3 layer with a thickness up to approximately 200 nm. Chromium rich transient oxides with a thickness of up to 0.5 µm are locally present on top of the alumina scale. Since the oxide scales formed on the investigated specimen possess thicknesses below 1µm the XRD measurement in Bragg-Brentano geometry only shows the phases present in the metal matrix, which are γ-NiCr and chromium rich carbides of the type $M_{23}C_6$ (Figure 32). The grazing incidence XRD

measurements at 1° show that the phases present at detectable levels in the oxide scale are spinel (probably $NiCr_2O_4$), Cr_2O_3 and α-Al_2O_3. The average amount and composition of the transient oxides can hardly be estimated from SEM or XRD measurements. Additional information can be obtained from GDOES or Plasma-SNMS measurements which give an average element concentration from a circular area of 3-5 mm diameter. Exact quantitative interpretation of the elemental depth distribution is, however, difficult due to lateral inhomogeneity of the oxide scales formed on the investigated specimens (see Figure 31).

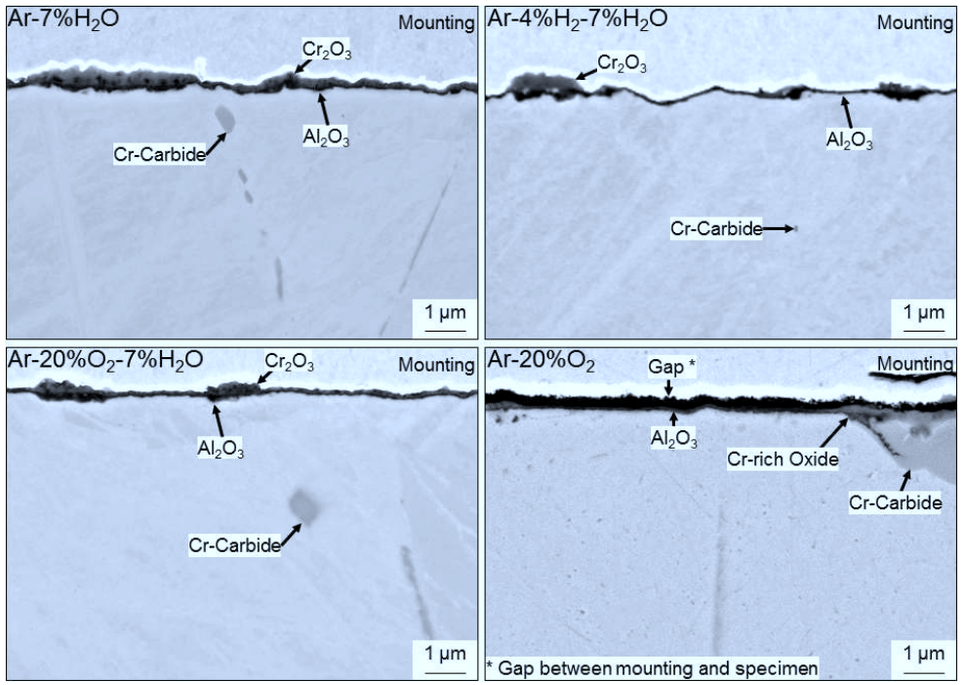

Figure 31: Metallographic cross sections (BSE images) of alloy 602 CA after isothermal oxidation at 800°C in Ar-7%H_2O, Ar-4%H_2-7%H_2O and Ar-20%O_2-7%H_2O for 72 h, results are compared with those for a specimen exposed in Ar-20%O_2

Figure 33 shows GDOES depth profiles from the oxide scale formed at 800°C in Ar-20%O_2-7%H_2O. The signals related to the absolute outer part of the scale are affected by adsorbed species, especially oxygen, and therefore do not exactly represent the composition of the oxide corresponding to the sputter time of t = 0 s. The surface oxide scale is clearly enriched in chromium and aluminum. Figure 31 shows the scale to be laterally inhomogeneous. Thus, the distribution of chromium and aluminum in Figure 33 does not exactly describe the real distribution as a function of depth. The metal matrix in the direct vicinity of the oxide scale is very slightly depleted of aluminum by approximately 0.5 at.-%, whereas chromium shows no depletion. Additionally, a relatively small titanium enrichment was found in the oxide scale. From Figure 31 it appears that the transient oxide in this case seems to consist mainly of

Cr_2O_3. The nickel concentration in the oxide scale is quite small. The borderlines between the transient oxide and the alumina layer are not very well defined in the Plasma-SNMS profiles for the reason mentioned above. The lateral inhomogeneity of the scale is, to some extent, caused by the presence of partially oxidized chromium carbides located in the direct vicinity of the specimen surface (Figure 31).

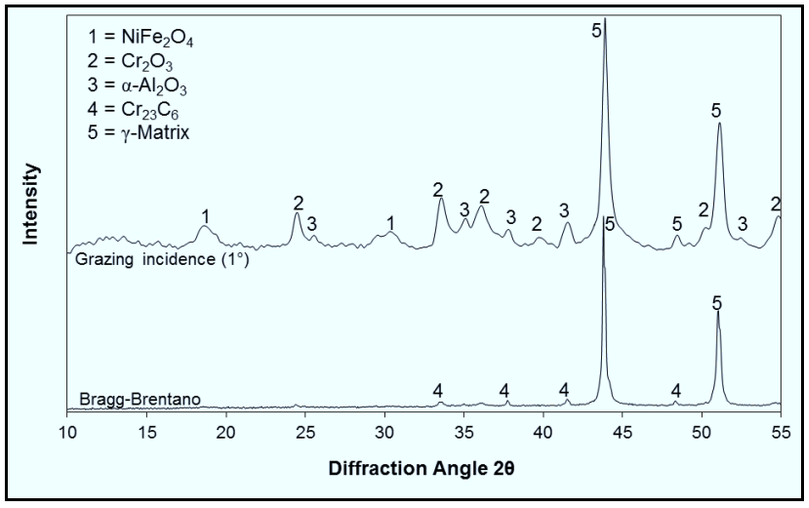

Figure 32: XRD analysis of alloy 602 CA exposed to Ar-20%O_2-7%H_2O at 800°C for 72 h

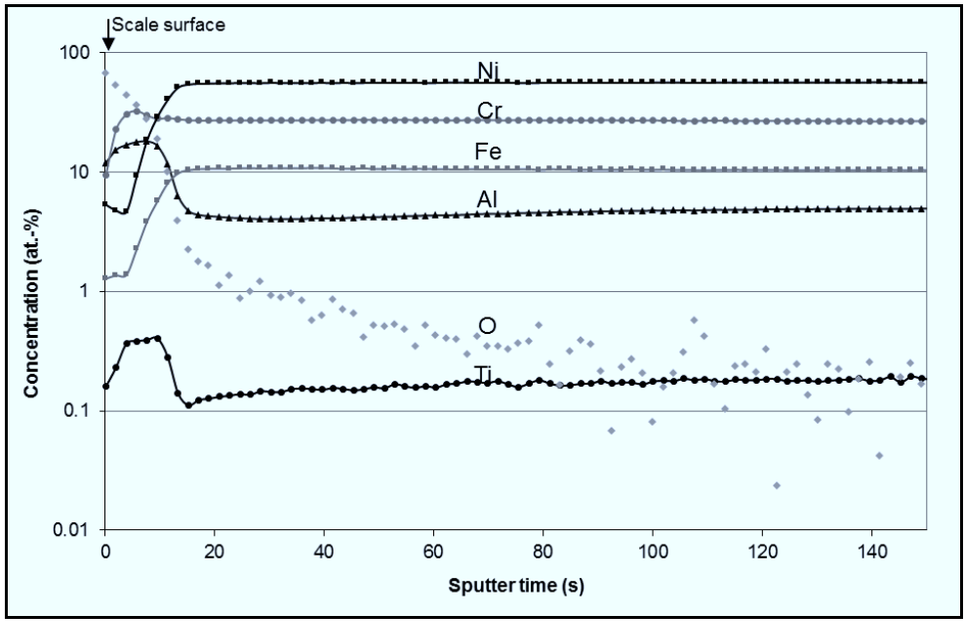

Figure 33: GDOES depth profiles of alloy 602 CA exposed in Ar-20%O_2-7%H_2O at 800°C for 72 h

In contrast, the Plasma-SNMS elemental concentration profiles from the specimen exposed in Ar-7%H_2O (Figure 34) show three clearly distinguishable regions in the oxide scale. The outer region is enriched in nickel, aluminum and to lesser extent in iron. In the second region chromium is the main metallic element. The third inner region, in which aluminum is the main metallic component, corresponds to the external alumina scale. Moreover, enrichment of titanium can be seen in this region. These results correlate well with those of SEM and XRD measurements (Figure 31, Figure 32). The outer part of the oxide scale thus consists of transient Ni- and Cr-rich oxides such as e.g. spinel and/or Cr_2O_3. An alumina layer was formed beneath the transient oxide.

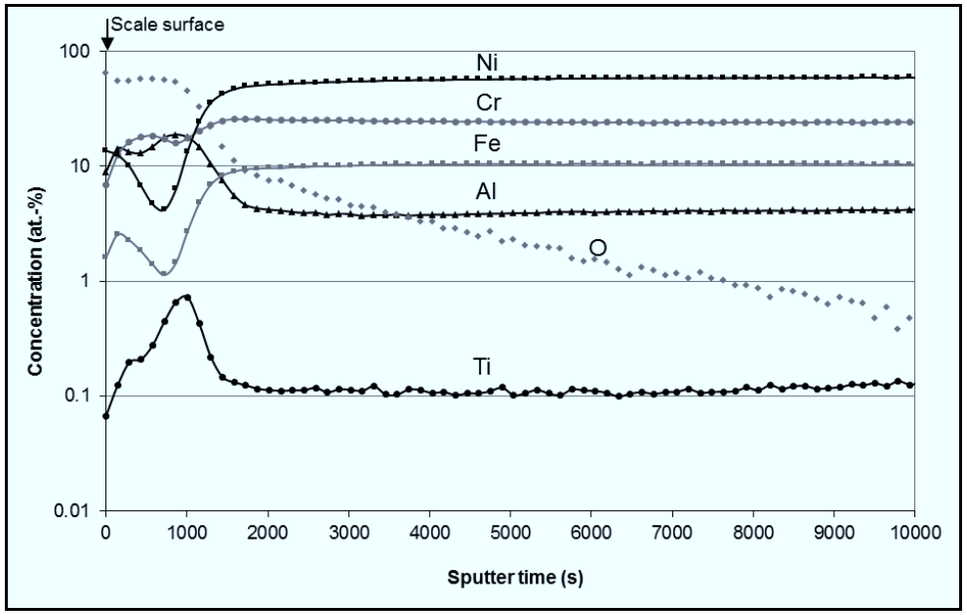

Figure 34: Plasma-SNMS depth profiles of alloy 602 CA exposed in Ar-7%H_2O at 800°C for 72 h

The SNMS depth profiles for the various elements in the oxide scale formed during oxidation in Ar-4%H_2-7%H_2O at 800°C were quite similar to those measured in the specimen exposed to Ar-7%H_2O and are therefore not shown here. The nickel enrichment present on the surface of the oxide scale formed in Ar-4%H_2-7%H_2O does, however, relate to evenly distributed fine particles consisting of nickel rather than Ni-containing oxide (Figure 35), since NiO is not thermodynamically stable in this atmosphere (Figure 10). Formation of such metallic nickel was not observed in the other test atmospheres.

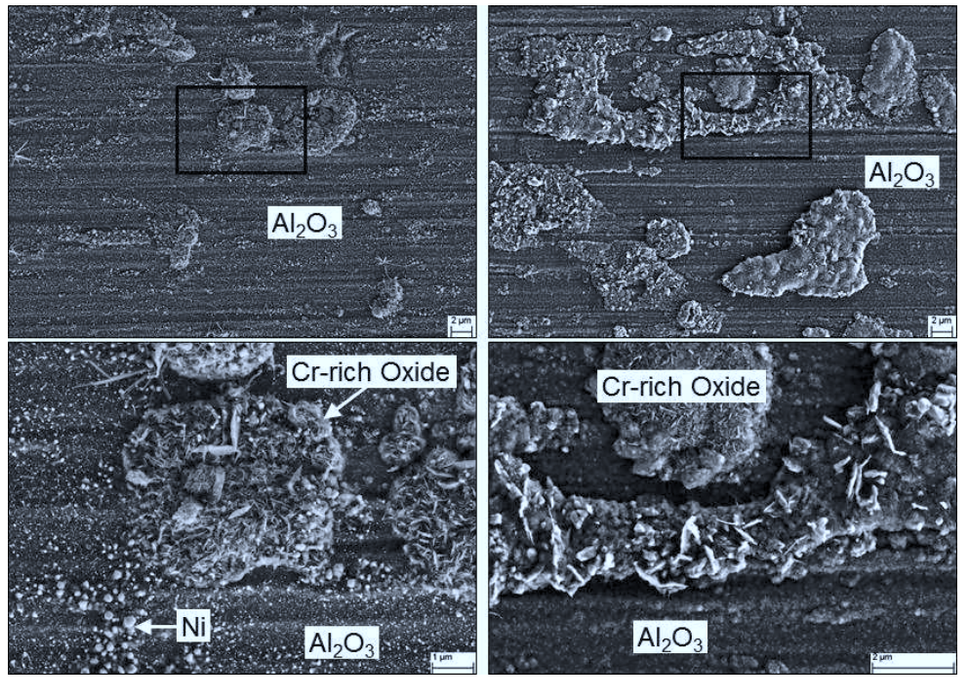

Figure 35: Secondary electron (SE) image of surface oxide morphology for alloy 602 CA after isothermal oxidation in Ar-4%H_2-7%H_2O (left) and Ar-7%H_2O (right) at 800°C for 72 h

Optical fluorescence measurements of Cr^{3+} ions were performed in a number of random locations on the specimen surfaces to obtain more detailed information about the type of Al_2O_3 formed on the specimens exposed at 800°C. A typical example of these measurements is shown in Figure 36. The results show that the alumina consisted of significant amounts of α-Al_2O_3 and smaller amounts of metastable alumina (probably θ-Al_2O_3) (Note that the fluorescence intensity for α is approximately ten times larger than that for an equivalent amount of θ [78]). The amount of metastable alumina formed during oxidation at 800°C was too small to be detected by XRD. The positions of the R1 and R2 fluorescence lines for Cr^{3+} ions in α-Al_2O_3 differ from those of the stress-free sapphire reference. This suggests the presence of residual compressive stresses in the oxide scales formed in the investigated test gases. According to the literature [79], these stresses arise from a thermal expansion mismatch between oxide scale and alloy during cooling to room temperature and from oxide growth stresses. Calculating the average in-plane stresses of the alumina-based scales, using the procedure described in reference [79], gives approximate values in the range of 2.6 to 3.8 GPa. These values are lower than those reported for the oxidation of a 45Ni-25Cr-25Fe-5Al alloy in air at 1100°C (6.4-6.7 GPa) [79] and those found after oxidation at the same temperature on a NiCrAl base γ-matrix (7-8 GPa) [80]. Although the calculations give an estimation rather than exact values, indications were found that the residual stresses after

exposure at 800°C for 72 h in Ar-4%H_2-7%H_2O were slightly higher than those in the other atmospheres. The relative amounts of θ-Al_2O_3 formed were not significantly affected by the gas composition (Figure 36).

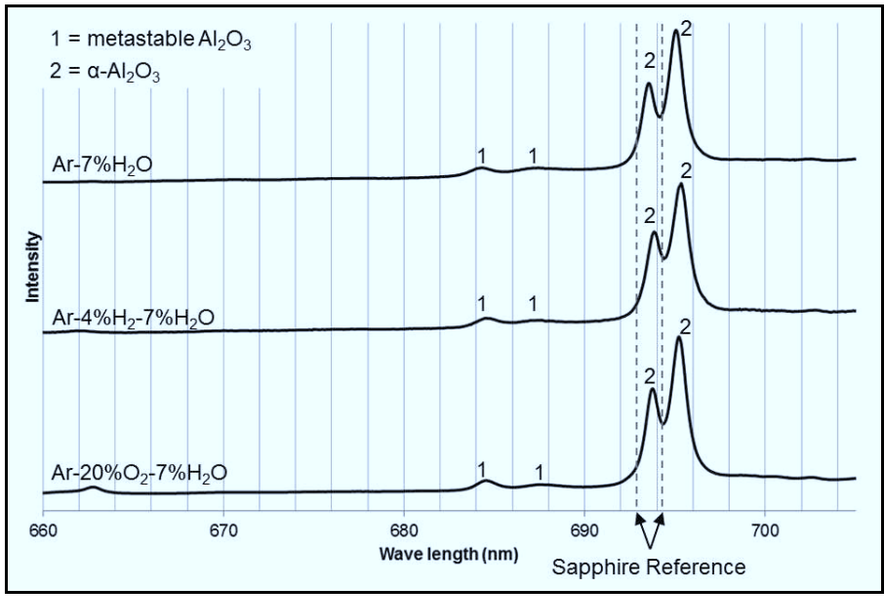

Figure 36: Fluorescence of Cr^{3+} of the oxide surfaces of alloy 602 CA after oxidation in Ar-7%H_2O, Ar-4%H_2-7%H_2O and Ar-20%O_2-7%H_2O at 800°C for 72 h

After exposure in the low pO_2 gases Ar-7%H_2O and Ar-4%H_2-7%H_2O at 900°C the specimen surfaces are predominantly covered by external chromia. However, some local areas are still covered by an external alumina scale (Figure 37). A similar scale formation mechanism is also found after exposure in Ar-20%O_2. Formation of an internal oxidation zone (IOZ) containing alumina precipitates was observed in the sub-surface zone beneath the external chromia. In contrast to this, the surface of the specimen exposed in Ar-20%O_2-7%H_2O at 900°C is covered by an external Al_2O_3 scale, which correlates with the lower weight gain recorded for this specimen (Figure 28).

A similar oxide formation is found after exposure at 1000°C, independent of the gas composition (Figure 39). All specimens oxidized at 1100°C formed external chromia scales on their surfaces (Figure 40). Detailed GDOES analyses (Figure 42 - Figure 44) show that the oxidation affected zone consists of three regions. The first region is a relatively thin outer layer exhibiting enrichment in titanium (3 - 10 at.%) and manganese (1 – 2 at.%). The maximum titanium enrichment was observed for the sample oxidized in Ar-7%H_2O. The second region, in which the main metallic element is chromium corresponds to an approximately 10 µm thick external chromia scale. On all specimens an enrichment in

titanium of 0.3 – 0.5 at.-% was found within the chromia. The third region with clearly visible aluminum enrichment corresponds to the internal oxidation zone.

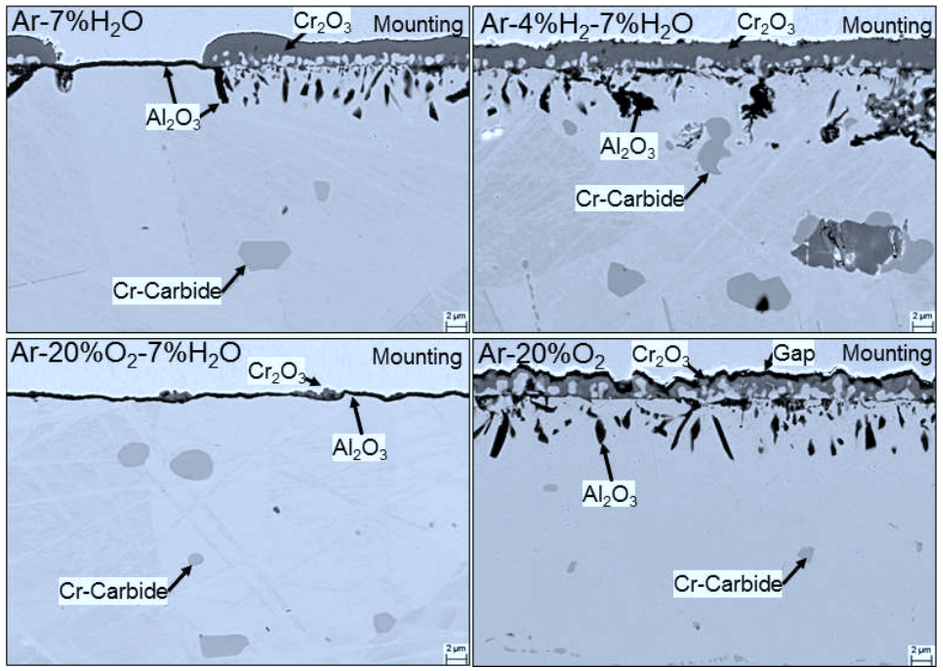

Figure 37: Metallographic cross sections (BSE images) of alloy 602 CA after isothermal oxidation at 900°C in Ar-7%H_2O, Ar-4%H_2-7%H_2O and Ar-20%O_2-7%H_2O for 72 h, results are compared with those for a specimen exposed in Ar-20%O_2

Comparison of the microstructures of the oxide scales formed at 1000 and 1100°C in various test gases (Figure 39 - Figure 40) illustrate that the chromia scales grown in Ar-20%O_2-7%H_2O or Ar-20%O_2 contains more voids and cracks than those grown in Ar-7%H_2O or Ar-4%H_2-7%H_2O (Figure 40). After oxidation at 1100°C the Cr_2O_3 scale formed in the low pO_2 gases, especially Ar-7%H_2O, are thicker than the scales formed in Ar-20%O_2-7%H_2O (as well as in Ar-O_2). This is in agreement with the higher weight gain at 1100°C in Ar-7%H_2O (Figure 26 - Figure 29), although it should be borne in mind that this is affected by oxygen uptake by internal oxidation and thus does not represent a direct correlation with chromia growth kinetics. Figure 41 shows BSE images of the oxide scales with lower magnification to provide a better overview especially over the internal oxidation zone.

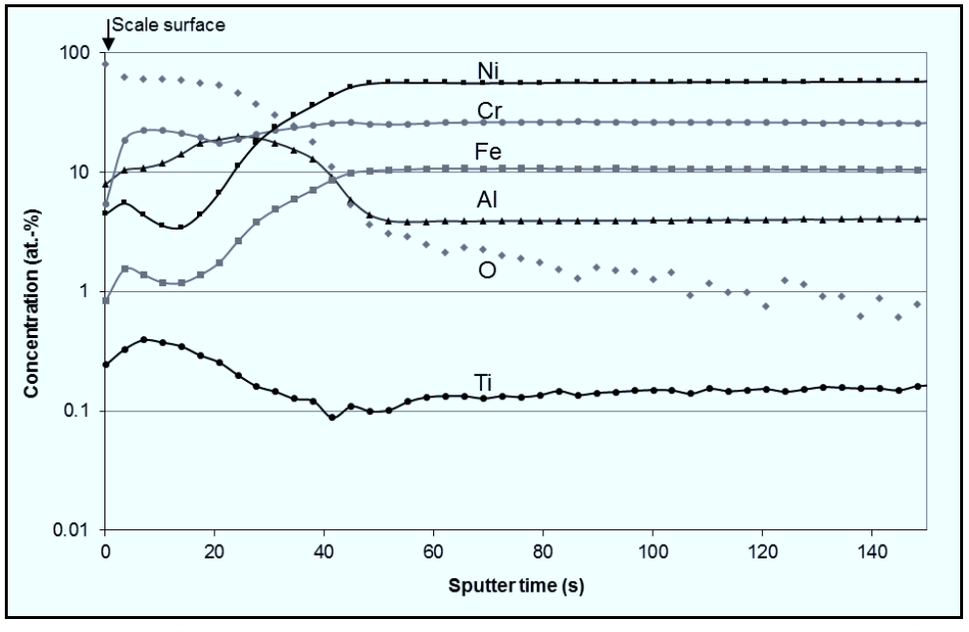

Figure 38: GDOES depth profiles of alloy 602 CA exposed in Ar-20%O_2-7%H_2O at 900°C for 72 h

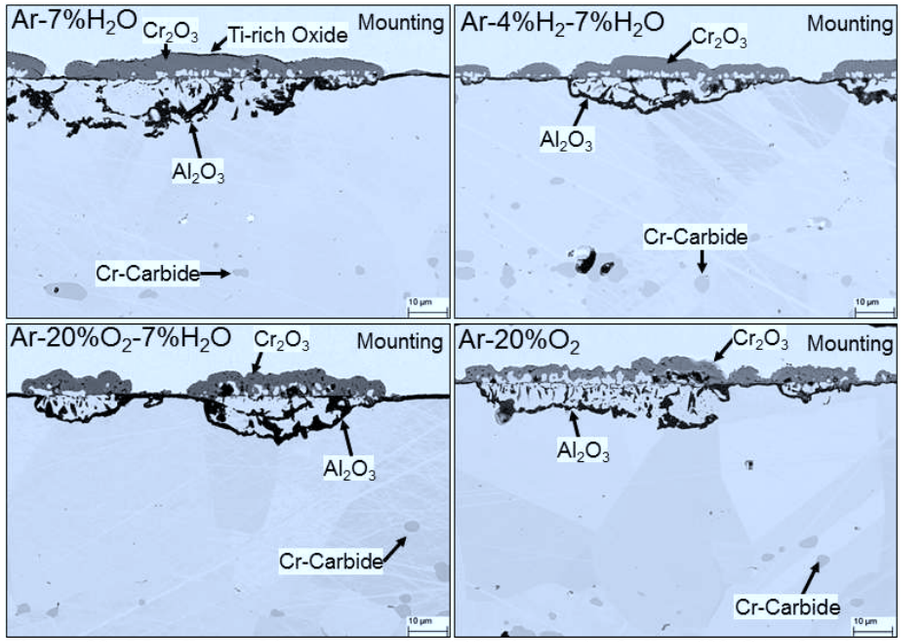

Figure 39: Metallographic cross section (BSE images) of alloy 602 CA after isothermal oxidation at 1000°C in Ar-7%H_2O, Ar-4%H_2-7%H_2O and Ar-20%O_2-7%H_2O for 72 h. Results are compared with those for a specimen exposed in Ar-20%O_2

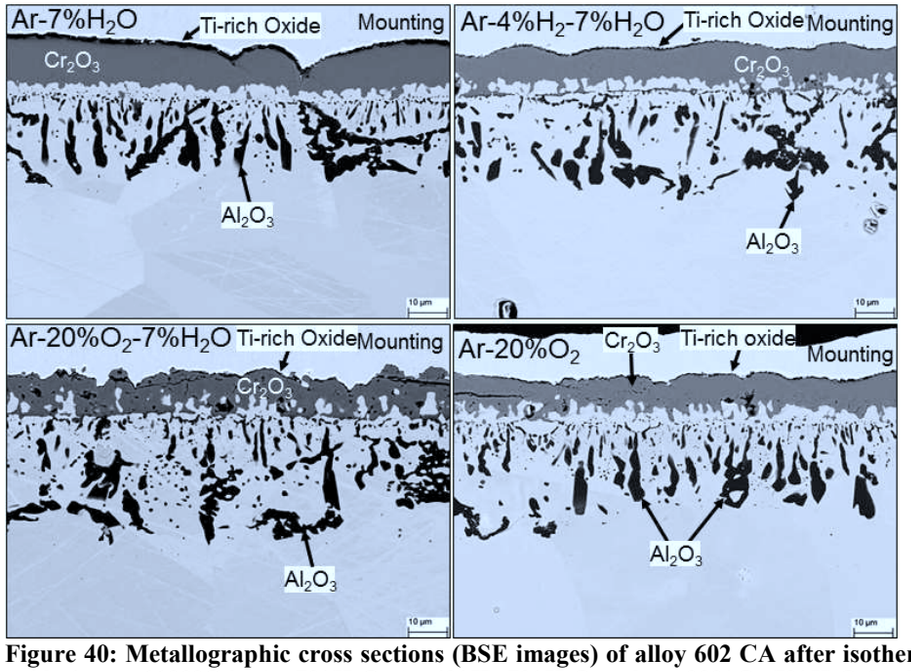

Figure 40: Metallographic cross sections (BSE images) of alloy 602 CA after isothermal oxidation at 1100°C in Ar-7%H_2O, Ar-4%H_2-7%H_2O and Ar-20%O_2-7%H_2O for 72 h. Results are compared with those for a specimen exposed in Ar-20%O_2

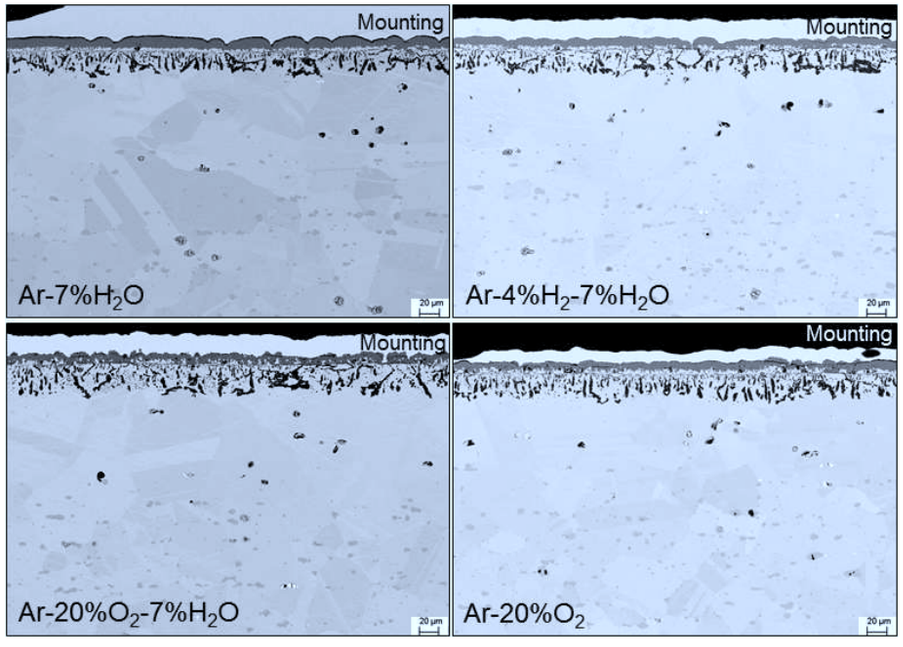

Figure 41: Metallographic cross sections (BSE images) of alloy 602 CA after isothermal oxidation at 1100°C in Ar-7%H_2O, Ar-4%H_2-7%H_2O and Ar-20%O_2-7%H_2O for 72 h. Results are compared with those for a specimen exposed in Ar-20%O_2

The detailed SEM/EDX investigations revealed that, in spite of relatively small concentrations of manganese (0.05 at.-%) and titanium (0.16 at.-%) in the alloy, these elements are enriched on top of the chromia scales, as confirmed by the GDOES profiles (Figure 42 - Figure 44). This enrichment is more pronounced in Ar-7%H_2O than in the other gases, and more pronounced at 1100°C than at 1000°C (Figure 42, Figure 45). The GDOES depth profiles confirm that the observed enrichments in the scale correlate well with the extent of depletion of the two elements in the sub-scale zone in the alloy matrix (Figure 42 - Figure 44). Increasing the oxidation temperature from 1000°C to 1100°C increases predominantly the concentration of titanium on the oxide surfaces up to 3 at.% and 10 at.% for specimens exposed in Ar-20%O_2-7%H_2O and Ar-7%H_2O respectively (Figure 42, Figure 44). Furthermore, the GDOES analyses show the presence of titanium in the inner part of the Cr_2O_3 scale (Figure 42 - Figure 44). The effect is more pronounced after oxidation in Ar-20%O_2-7%H_2O than in Ar-7%H_2O. The EDX-mapping performed on the cross section of the specimens oxidized in Ar-20%O_2-7% H_2O confirms the presence of titanium within the Cr_2O_3 scale (Figure 46, Figure 47).

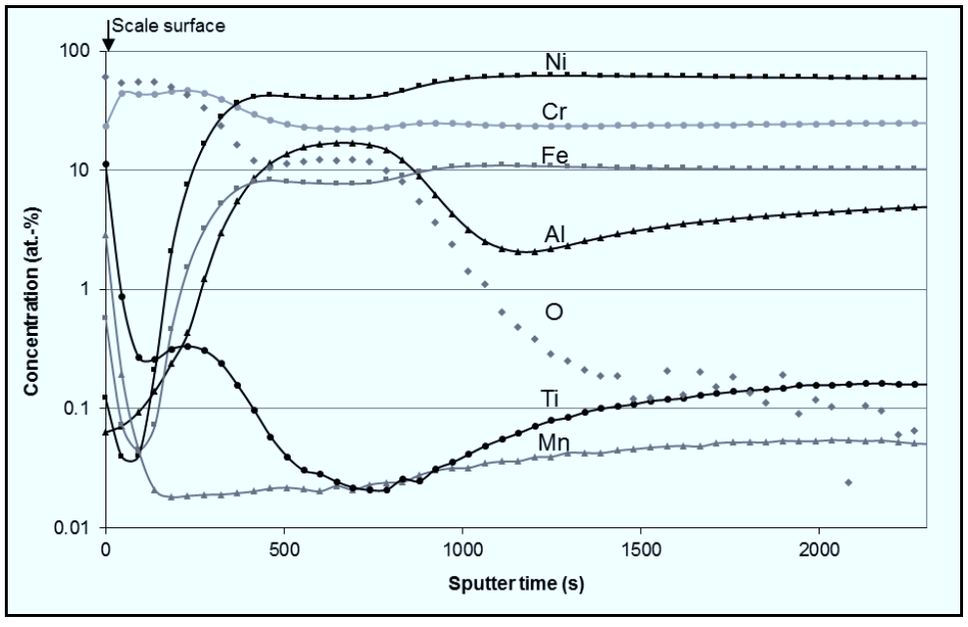

Figure 42: GDOES depth profiles of Alloy 602 CA exposed in Ar-7%H_2O at 1100°C for 72 h

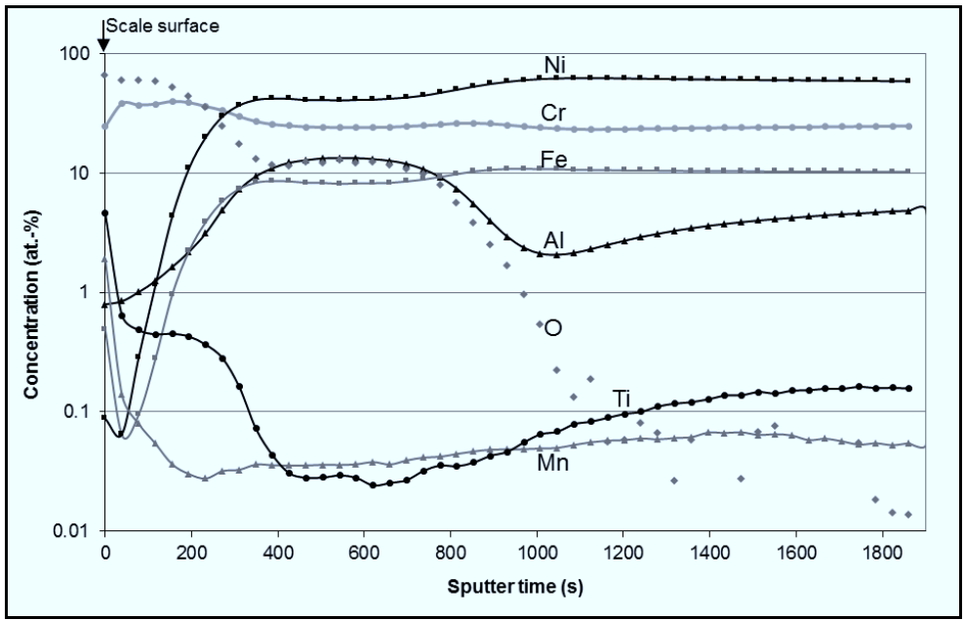

Figure 43: GDOES depth profiles of Alloy 602 CA exposed in Ar-4%H_2-7%H_2O at 1100°C for 72 h

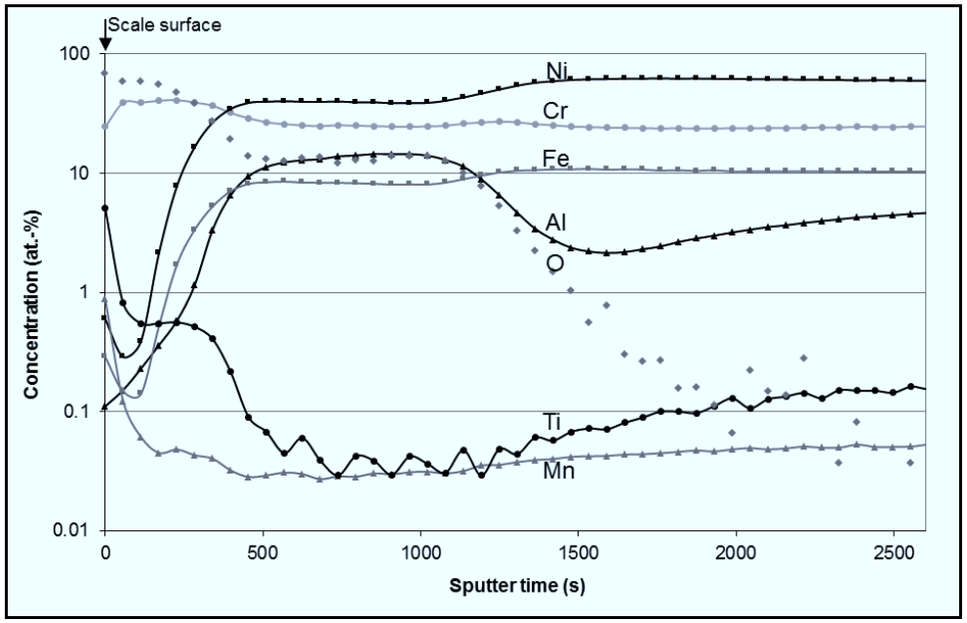

Figure 44: GDOES depth profiles of Alloy 602 CA exposed in Ar-20%O_2-7%H_2O at 1100°C for 72 h

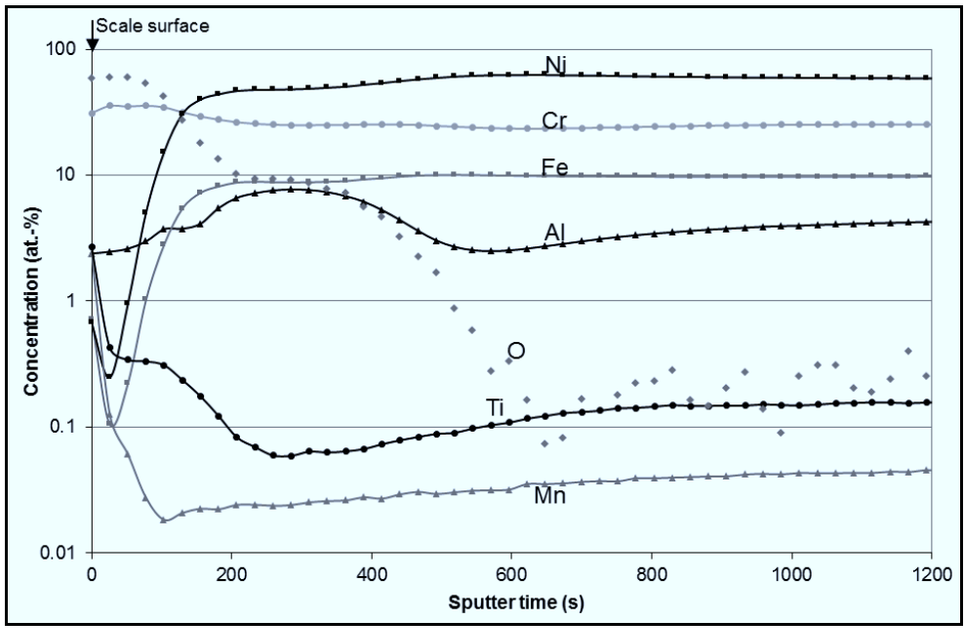

Figure 45: GDOES depth profiles of Alloy 602 CA exposed in Ar-7%H_2O at 1000°C for 72 h

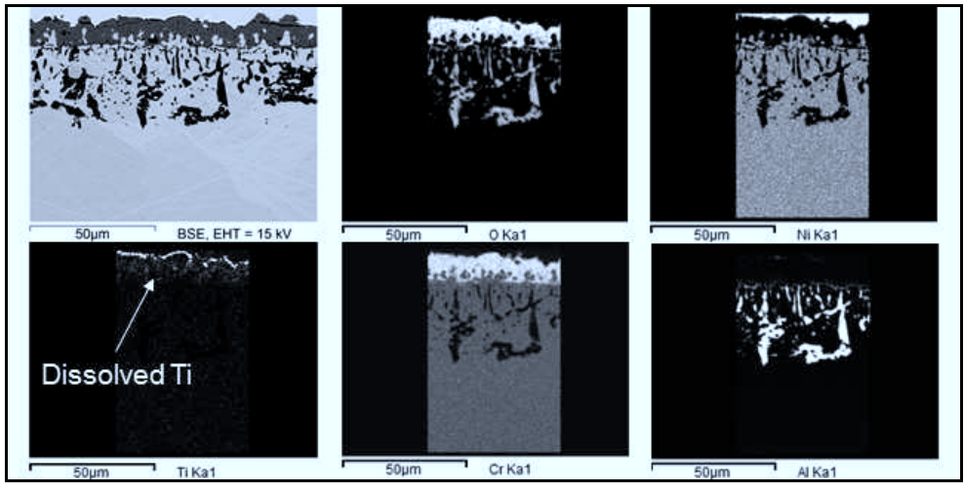

Figure 46: BSE image and X-ray-mapping of alloy 602 CA after isothermal oxidation at 1100°C in Ar-20%O_2-7%H_2O for 72 h

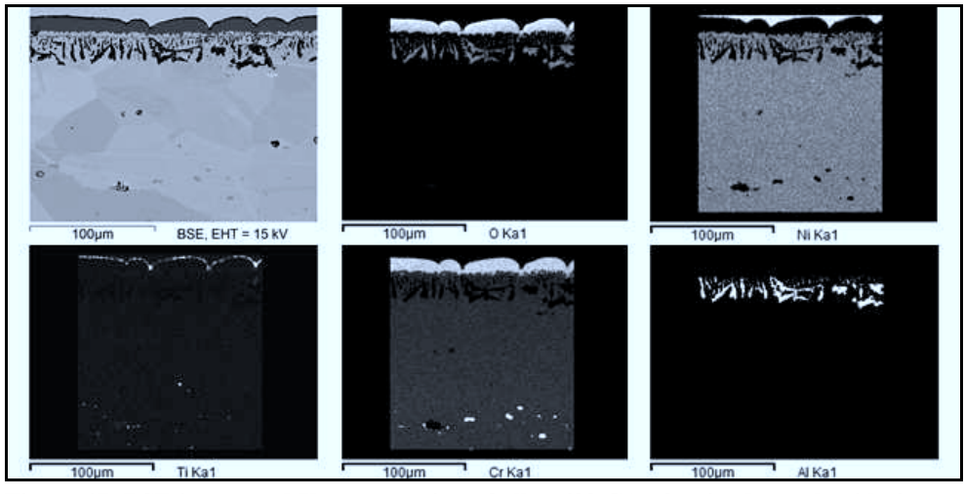

Figure 47: BSE image and X-ray-mapping of alloy 602 CA after isothermal oxidation at 1100°C in Ar-7%H_2O for 72 h

In spite of the relatively high concentration of titanium in the outer parts of the oxide scales it was not possible to unequivocally identify by SEM or XRD the type of titanium rich phase. Micro-Raman spectroscopy measurements (Figure 48) of the specimen oxidized in Ar-7%H_2O at 1100°C confirm the presence of Cr_2O_3, $MnCr_2O_4$ and a phase which is probably rutile (TiO_2) with disordered crystallographic structure. Figure 10 shows that in all test gases the pO_2 is sufficiently high for TiO_2 to be formed.

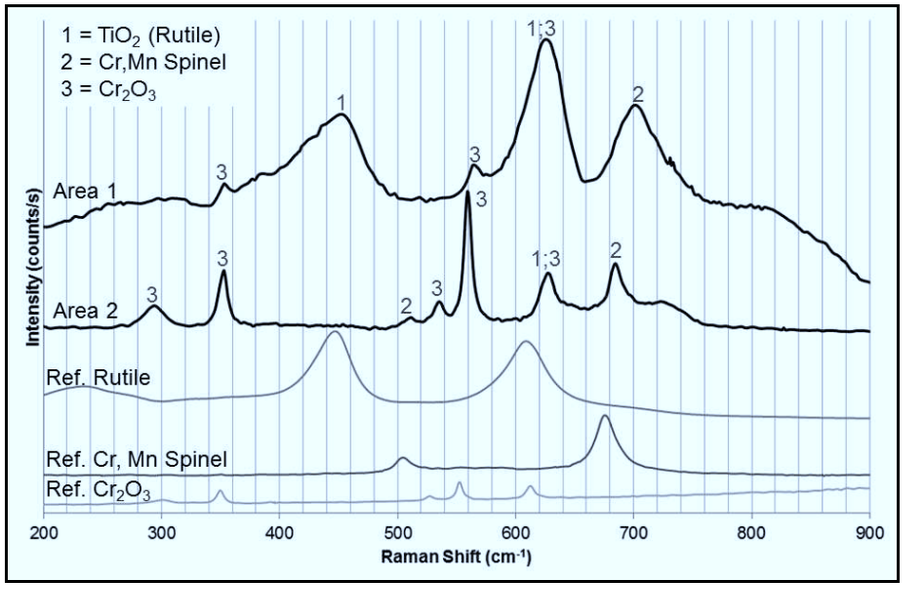

Figure 48: Raman spectra of two areas on the oxide surface on alloy 602 CA after isothermal oxidation in Ar-7%H_2O at 1100°C for 72 h

6.1.2.3 Internal Oxidation and Carbide Depleted Zones

When an external chromia scale is formed, in all cases an internal oxidation zone (IOZ) containing Al_2O_3 precipitates is present. Table 4 shows that the average widths of the IOZ increases with increasing oxidation temperature in all investigated test gases. Furthermore, the morphology of the internal alumina precipitates changes with oxidation temperature and environment. The internal oxide particles, in most cases, increase in size with increasing distance from the scale-alloy interface, in agreement with previous observations [31, 81].

The internal alumina precipitates formed have predominantly a needle- or plate-like shape, elongated perpendicular to the specimen surface (see Figure 37, Figure 39 - Figure 41); although Figure 39 indicates that at 1000°C the precipitates seem to grow more parallel to the specimen surface.

The composition of the oxidizing environment has much less effect on the width and morphology of the IOZ than does temperature. At a given temperature the depths of the internal oxidation zones were similar in all four test environments. Figure 40 indicates that the coarsening of the precipitates in the vicinity of the IOZ/alloy interface is less pronounced in Ar-20%O_2 than in the other three environments.

	Depths (µm)					
	IOZ			CFZ		
Atmosphere	900°C	1000°C	1100°C	900°C	1000°C	1100°C
Ar-7%H_2O	5.0	12.5	24.4	3.7	17.0	72.0
Ar-4%H_2-7%H_2O	5.4	12.44	26	4.0	16.5	71.5
Ar-20%O_2-7%H_2O	0	9.8	33.3	3.9	11.1	84.9

Table 4: Average depths of internal oxidation zone (IOZ) and carbide free zone (CFZ) of alloy 602 CA after oxidation in Ar-7%H_2O, Ar-4%H_2-7%H_2O, and Ar-20%O_2-7%H_2O at 900-1100°C for 72 h measured with analySIS Pro

It is interesting to note that formation of an external chromia layer accompanied by internal alumina precipitates results in a depletion profile of aluminum in the metallic matrix whereas no significant subscale Cr concentration depletion profile is observed (Figure 42 - Figure 44). EDX analyses revealed that, as expected, the alloy matrix in the zone of internal oxidation is almost completely depleted of aluminum (Figure 49, Figure 50). This has the result that the aluminum concentration in the metallic matrix in the direct vicinity of the chromia scale is virtually zero but the chromium concentration remains at a level of 22.5 wt.-%, i.e. only slightly lower than the original value of 23.6 wt.-%. Also of interest is that the metallic protrusions in the oxide scale, which are surrounded to a large extent by Cr_2O_3, exhibit virtually no depletion of chromium. Its content measured by EDX analysis is 23.7 wt.-%.

As indicated in the experimental section, the microstructure of alloy 602 CA shows a substantial amount of evenly distributed $Cr_{23}C_6$ precipitates in the as-received microstructure (Figure 25). Formation of an external chromia scale at 900°C and above results not only in formation of an IOZ but also in formation of a carbide free region (CFZ) in the subscale zone (Figure 37). Table 4 shows the average depths of the CFZ measured in the investigated samples. Figure 37, Figure 39, Figure 40 and Table 4 illustrate that the width of the CFZ increases with increasing oxidation temperature but seems not to be substantially affected by the used test gas. The depth of the aluminum depleted zone (see Figure 50) correlates well with the depth of the CFZ. In the region where chromium carbides are still present, the aluminum concentration is close to the bulk concentration of 2.4 wt.-%.

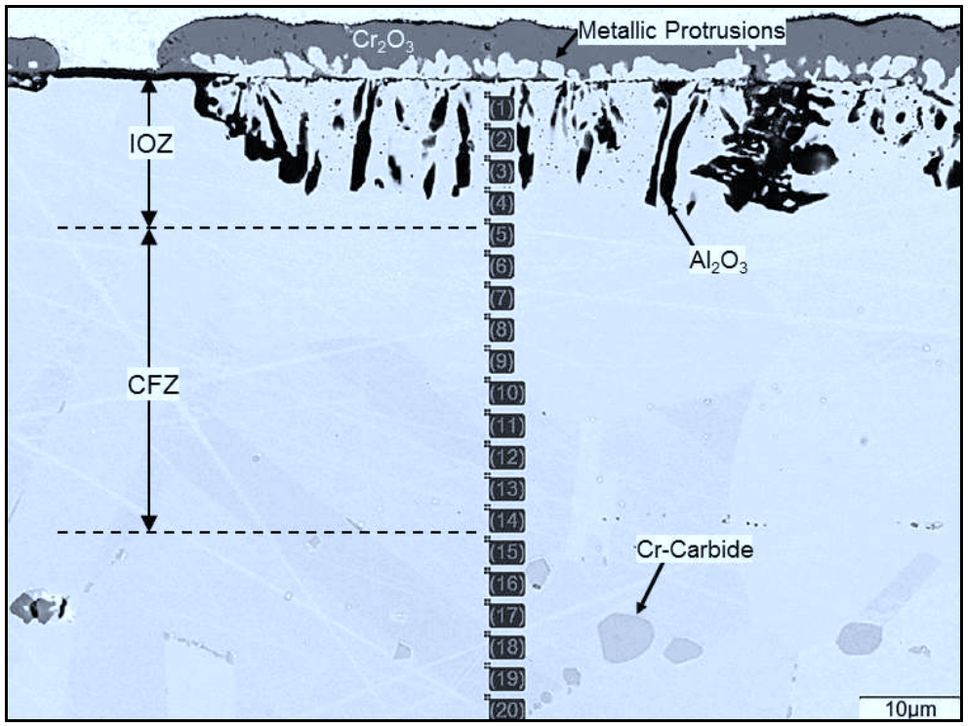

Figure 49: BSE image showing metallographic cross section of alloy 602 CA exposed in Ar-7%H_2O at 1000°C for 72 h. Points 1 – 20 illustrate locations of EDX point analyses given in Figure 50

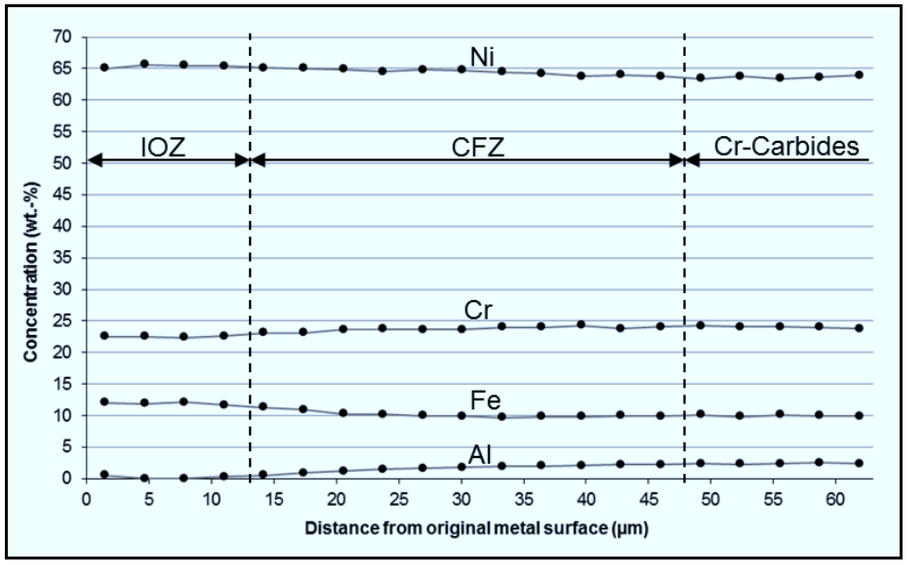

Figure 50: Element concentrations measured in alloy matrix by EDX at points marked in Figure 49 (Specimen of alloy 602 CA after oxidation in Ar-7%H_2O at 1000°C for 72 h)

6.1.3 Discussion of the Behavior in Ar-20%O_2 and H_2O-Containing Gases

6.1.3.1 External Chromia Scale Formation in Different Environments

The experimental results have shown that alloy 602 CA oxidized at 800°C and to some extent at 900°C forms external alumina scales. At higher temperatures however, an external chromia scale is formed accompanied by formation of a carbide depleted region and an internal oxidation zone. The chromia scales grown at 1000 and 1100°C in the low pO_2 gases Ar-H_2O and Ar-H_2-H_2O are more compact and "crack free" than those formed in Ar-O_2(H_2O) (Figure 39, Figure 40). This is in agreement with results from Zurek et al [82] comparing the behavior of a binary Ni-25%Cr alloy in Ar-20%O_2 and Ar-4%H_2-7%H_2O. The authors attributed the greater compactness and better adherence of the scales formed in the low-pO_2 gas to a substantial contribution of inward oxygen grain boundary diffusion to the overall scale growth process and to formation of so-called H_2O/H_2 bridges. The inward growth in combination with H_2O/H_2 bridges within in-scales voids prevents vacancy condensation and void growth at the scale/alloy interface, which occurs in high-pO_2 gases [82].

The present results showed that the chromia growth rates were higher in the low pO_2 gases than in the oxygen rich gases (Figure 40). This is in qualitative agreement with findings from

binary Ni-Cr model alloys during exposure in Ar-H_2O or Ar-H_2-H_2O and Ar-O_2(-H_2O) [82, 83]. However, the differences in chromia growth rates in the prevailing experiments were substantially smaller than those reported in the literature for Ni-Cr alloys. For instance, the thickness of the chromia scales formed on a Ni-25 wt.% Cr model alloy during 72 h isothermal oxidation at 1050°C in Ar-7%H_2O and Ar-20%O_2 were approx. 20 µm and 4 µm, respectively [83], whereas the chromia scale thicknesses in the present studies at 1100°C only varied from approximately 10 to 12 µm. This may be related to the fact that in the case of Alloy 602 CA the external chromia scale growth is affected by the internal oxidation of aluminum. The volume increase accompanying the extensive internal oxidation has the result, that protrusions of Al depleted alloy are pushed outward and are visible as metal protrusions in the external chromia scale, as described in previous publications (see e.g. [84]). Outwardly protruding alloy nodules will cause micro damage of the scale. This has as result that the scale growth process will not solely be governed by solid state diffusion processes in the scale but additionally to some extent by molecular gas transport. As the latter will occur in all test gases, the effect of gas composition on the growth rate of the external chromia on Alloy 602 CA is qualitatively similar to that found for a model alloy Ni-25 wt.% Cr but the effects are less pronounced.

It is interesting that for alloy 602 CA the growth of the external chromia scales does not result in steep chromium depletion profiles in the subscale regions (Figure 50), in contrast to numerous findings for other NiCr base alloys [82, 84]. For instance, the exposure of a Ni-25 wt.-%Cr model alloy in laboratory air at 1100°C for 100 h results in a chromium concentration at the scale-alloy interface which is 7 wt.-% lower than the original value [84]. In reference [84] it was illustrated that the flat subscale chromium profiles in Alloy 602 CA are related to the thermodynamic interaction of aluminum and chromium in the nickel matrix. They result from the enhanced chromium diffusion in the aluminum-depleted zone as caused by the internal oxidation of aluminum. The subscale alumina precipitation creates aluminum depletion in a zone deeper into the alloy. Due to the thermodynamic interaction of aluminum and chromium in the γ-Ni matrix [34, 84] this provides an additional driving force for chromium to diffuse from the bulk alloy towards the surface. From the flat concentration chromium profile in the metal matrix it may not be concluded that no chromium depletion occurred. As illustrated by Pillai et al [85] a substantial amount of chromium in the bulk alloy is tied up in chromium-rich carbides due to the relatively high carbon content of the material (Table 3). The EDX data (Figure 50) relate to point analyses in the γ-Ni matrix without any Cr-carbides measured and therefore do not take into account the chromium tied up in carbides. The flat chromium profiles measured by EDX thus give the erroneous impression that no chromium is consumed by formation of the external chromia scale, but in fact Cr-carbide dissolution in the CFZ compensates chromium consumption by chromia scale formation.

6.1.3.2 Incorporation of Titanium into Chromia Scales

As shown in section 3.1 titanium is present in the alloy in relatively small amounts (0.16 at.-%) but exhibits a substantial enrichment on the surface of the chromia scale. The effect was reported previously by various authors [86, 87, 88, 89]. The driving force for titanium diffusion in chromia scales is the oxygen activity gradient between the metal/scale and scale/gas interfaces [86]. Thus, titanium diffusion and, as a result, titanium enrichment is expected to increase with increasing pO_2 in the surrounding gas. The present results demonstrate that the effect exhibits an apparent maximum for the atmosphere with intermediate oxygen partial pressure (Ar-7%H_2O). This finding is in good agreement with results from Essuman et al [90] for a Ni-Cr base oxide dispersion strengthened (ODS) alloy. The authors discussed two possible mechanisms resulting in the observed atmosphere dependent titanium distribution. The more likely mechanism seems to be a pO_2 dependent solubility of titanium in chromia [91].

Holt and Kofstad [92] showed that in a pO_2 region corresponding approximately to the equilibrium oxygen partial pressure in Ar-7%H_2O the electrical conductivity of titanium-doped chromia as well as the titanium solubility in Cr_2O_3 exhibits a local minimum. They proposed two different mechanisms of titanium dissolution in Cr_2O_3. At low pO_2 ($< 10^{-5}$ bar) the amount of titanium dissolved in chromia decreases with increasing pO_2, whereas at higher pO_2 values ($> 10^{-4}$ bar) increasing pO_2 results in increasing titanium solubility. Therefore, the most pronounced titanium enrichment, formed in Ar-7%H_2O, may result from the combined large pO_2 gradient and low titanium solubility in the outer part of the chromia scale. Since the diffusing titanium cannot remain dissolved in the outer part of the chromia scale it precipitates in the form of a titanium enriched oxide layer on the scale surface. The titanium enrichment formed in Ar-4%H%-7H_2O is less pronounced due to a lower pO_2 gradient and higher solubility of titanium in chromia [92]. In the high pO_2 gas Ar-20%O_2-7%H_2O the solubility of titanium in the inner chromia increases again, so that outwardly diffusing titanium stays partially dissolved in chromia. This explanation is confirmed by the results of the GDOES (Figure 42 - Figure 44) and SEM/EDX measurements (Figure 40), where the highest concentration of titanium within the chromia scale at 1100°C was measured for the specimen oxidized in Ar-20%O_2-7%H_2O gas.

6.1.3.3 External Alumina Scale Formation

Due to its relatively low aluminum content of only 2.5 wt.% Alloy 602 CA is expected to be a “marginal alumina former” [31]. This indicates that formation of a protective outer alumina scale on the alloy surface is likely affected by factors such as temperature, time, test environment and/or surface treatment. This is probably the reason that literature data about the type of external scale formation of Alloy 602 CA in the temperature range relevant to the present studies, are contradictory (Table 5).

In the present studies alloy 602 CA was found to form an external alumina scale for at least 72 h of oxidation at 800°C in all test gases used (Figure 31). Increasing the oxidation temperature to 900°C resulted in (partial) replacement of the external alumina by external chromia in the case of specimen oxidized in Ar-7%H_2O and Ar-4%H_2-7%H_2O atmospheres (Figure 37).

When mentioning that external alumina formation occurred at 800°C, it should be born in mind, that the alumina is present at the scale / alloy interface (see e. g. Figure 31) but is covered with Ni- and Cr-rich oxide originating from the transient stages of oxidation (Figure 31) [25]. An exception to this sequence was the specimen exposed at 800°C in Ar-4%H_2-7%H_2O. For that specimen finely distributed metallic nickel particles were found in the outer part of the scale. A similar type of nickel particle morphology on top of the oxide scale was previously observed when a NiCr(Al) base alloy was first oxidized in air and subsequently in Ar-H_2-H_2O [93]. The initially formed outer NiCr-base spinel then changed into Cr_2O_3 and finely distributed nickel particles. In the present case formation of the nickel particles would be theoretically possible if during specimen heating initially a mixed Ni-containing oxide would form which becomes unstable at or near the actual oxidation temperature of 800°C. This seems, however, to be unlikely considering the temperature dependence of the equilibrium pO_2 in Ar-4%H_2-7%H_2O and that of the dissociation pressures for the various oxides (Figure 10). A further possibility would be that in the very early stages of oxidation, aluminum oxidizes initially internally and starts to form after this step a closed layer near the interface between inner oxidation zone and alloy. This means that the metallic regions between the initially formed internal oxide precipitates are no longer in contact with the metallic matrix. The chromium and nickel in the metallic regions will thus completely oxidize forming Cr- and Ni-rich oxides if the oxygen partial pressure in the gas is sufficiently high. However, in Ar-4%H_2-7%H_2O this process can only result in Cr-oxidation leaving the remaining nickel unaffected. Further studies are necessary to verify whether this mechanism is correct.

The papers quoted in Table 5 give no clear indications regarding influence of atmosphere and/or temperature on formation of external scales on alloy 602 CA. Giggins and Pettit [33] performed isothermal experiments on model Ni-Cr-Al alloys in static oxygen between 1000 and 1200°C. The authors used 600 grit ground specimens of 0.13 mm thickness in their experiments. According to the classification in [33] alloy 602 CA (when considering it as an alloy merely containing Ni.Cr and Al) is a borderline case, changing between external chromia and alumina formation. The classical paper by Giggins and Pettit [33], however, gives no information regarding the oxidation behavior of Ni-Cr-Al alloys below 1000°C.

Source	Test type	Surface treatment	Temperature (°C)	Gas	Time (h)	Type of oxide scale
Brill [94]	Discontinuous	Ground P120	750 - 1200	Air	1000	Alumina
Joshi [96]	Isothermal	1µm polished	700 - 900	Air	Up to 24	Chromia
Pillai [86]	Isothermal	As received	977 - 996	N_2-O_2-CO_2-H_2O	Up to 5470	Chromia
Stanislowski [95]	Isothermal	Ground P1200	800	Air + 1.8H_2O	500	Alumina
Stanislowski [97]	Isothermal	Ground P1200	1200	Air	24	Chromia
Chyrkin [84]	Discontinuous	Ground P1200	1000 - 1200	Lab. air	Up to 1000	Chromia
Teneva-Kosseva [98]	Burner Rig	Not defined	Up to 1000	CO-CO_2-N_2-NO_X-O_2-H_2O-SO_2-SO_3	50	Chromia
Ackerman [87]	Burner Rig	Not defined	1000	Combustion gas	Up to 3000	Chromia

Table 5: Scale formation on alloy 602 CA as reported in the literature [84, 86, 94, 95, 96, 97, 98]

Kvernes and Kofstad investigated several Ni-(4-14)%Cr-(2.5-9)%Al alloys at temperatures between 800 and 1300°C in 1 atm oxygen or air [99]. The conclusion of their work was that increasing oxidation temperature generally favors external alumina scale formation. The authors pointed out that the temperature region of transition from internal to external alumina is placed between 1000 and 1200°C. This statement seems to be in contradiction to the present results, which clearly show that external alumina formation is favored at lower temperatures in the case of alloy 602 CA.

When discussing conditions for external (alumina) scale formation, many authors use the expressions defined by Wagner [57], shown in chapter 4.3.3. For external alumina formation on an aluminum containing alloy, equation (44) can be written as:

$$N_{Al}^{(1)} = \left(\frac{g_{AlO_{1.5}}^{*} \times \pi \times V_m^{Alloy} \times N_O^{(S)} \times D_O}{3 \times V_m^{AlO_{1.5}} \times D_{Al}} \right)^{\frac{1}{2}} \quad (52)$$

$g_{AlO_{1.5}}^{*}$ = Critical value of the volume fraction of $AlO_{1.5}$ ($g_{AlO_{1.5}}^{*} = f\left(\frac{V_m^{Oxide}}{V_m^{Alloy}}\right)$ [65])

D_{Al} = Al diffusion coefficient [cm²/s] (Rigorously, the interdiffusion coefficient should be used here but it is nearly equal to the intrinsic diffusivity because of the low Al concentration)

Equation (52) was derived assuming that only one reactive metallic element (here Al) is dissolved in an inert (non oxidizing) metallic matrix. This condition is not obeyed for the investigated alloy 602 CA, since virtually all elements present in the alloy matrix might be oxidized in the used test gases, with the exception of nickel in Ar-4%H_2-7%H_2O (Figure 10). In spite of this limitation, equation (52) may be used for qualitative approximation of the temperature and pO_2 dependence of $N_{Al}^{(1)}$ for known temperature dependencies of D_O, D_{Al} and N_O, the latter additionally depending on pO_2 [60]. The critical volume fraction of the oxide $g_{AlO_{1.5}}^{*}$ can be calculated according to equation (45). For a rough estimation of $N_{Al}^{(1)}$ in the present work the critical volume fraction of the oxide $g_{AlO_{1.5}}^{*}$ is set to 0.3, as described in chapter 4.3.3.

For binary Ni-Al alloys Nesbitt [60] calculated values for $N_{Al}^{(1)}$ using values for the diffusivities D_O and D_{Al} from references [31, 63]. The oxygen solubility values N_O were calculated according to the procedure described in chapter 4.3.2.2. The author distinguished between the case when oxidation occurred in a gas with an equilibrium oxygen partial pressure lower as well as higher than the dissociation pressure of NiO. In the latter case he calculated N_O using Sievert's law on the basis of the equilibrium partial pressure of oxygen prevailing at the scale/alloy interface. The author found for $N_{Al}^{(1)}$ values of 0.07 - 0.09 whereby the mole fractions were found to decrease with increasing temperature. In gases, in which no external NiO could be formed, a pO_2 dependence of $N_{Al}^{(1)}$ by using Sievert's law was found in qualitative agreement with equation (52) [60].

For alloy 602 CA, however, the external alumina formation is not competing with external NiO but with Cr_2O_3, as illustrated by the numerous metallographic cross sections (see e.g. Figure 37, Figure 39 and Figure 40). The value of N_O should thus be governed by the dissociation pressure of chromia in equilibrium with the chromium activity at the chromia/alloy interface at the respective temperature. The oxygen partial pressure of the gas phase should thus have no direct effect on $N_{Al}^{(1)}$ as long as it does not substantially affect the

scale growth rate and thus the subscale chromium depletion. $N_{Al}^{(1)}$ is affected by the dissociation pressure of Cr_2O_3. As this is e.g. at 1000°C approximately 10 - 12 orders of magnitude (depending on element activities and exact subscale chromium depletion) smaller than that of nickel oxide, application of Sieverts law reveals that the value of $N_{Al}^{(1)}$ should be a few orders of magnitude smaller than in case of binary Ni-Al alloys. Calculations revealed for the investigated temperature range 800-1100°C values of $N_{Al}^{(1)}$ in the range 0.00011 and 0.00033, which is equal to 0.011 and 0.033 at.-% Al. This limit for the transition from internal to external Al_2O_3 formation is clearly exceeded by the Al concentration of alloy 602 CA (4.9 at.-%) and should thus at all studied temperatures in all used test gases result in external alumina scale formation.

The fact that this is apparently not the case, might find its cause in the second criterion defined by Wagner, i.e. the condition for maintaining the growth of an existing external Al_2O_3 scale, described in chapter 4.3.4. The corresponding equation (51) can be adapted for the maintenance of an external Al_2O_3 according to:

$$N_{Al}^{(2)} = \frac{V_m^{A-B}}{V_m^{AlO_{1.5}}} \times \left(\frac{\pi \times k_p}{2 \times D_{Al}} \right)^{\frac{1}{2}} \tag{53}$$

The temperature dependent value D_{Al} can be calculated from reference [31, 63]. The oxidation rate of the respective Al_2O_3 scale k_p is dependent on temperature and the type of Al_2O_3 formed. To determine the possible range of $N_{Al}^{(2)}$ typical oxidation rates of metastable- and stable α-Al_2O_3 on NiCrAl alloys [48] are used for calculations similar to the work of Gheno et al [100]. Figure 51 shows the calculated values of $N_{Al}^{(2)}$ as a function of temperature for both Al_2O_3-types compared with the bulk Al concentration of alloy 602 CA. The used values are given in Table 6. Due to inaccuracies arising from the uncertainties in estimation of the inserted values, the fact that equation (53) was determined for a binary alloy [56] and α-Al_2O_3 growth frequently obeys subparabolic kinetics [69], calculation of $N_{Al}^{(2)}$ (Figure 51) gives approximated values rather than exact numbers. However, as the calculation revealed values in the same range as the calculations of Gheno et al [100] and as the differences between $N_{Al}^{(2)}$-values for θ- and α-Al_2O_3 and the Al concentration in the alloy differ by a factor of 1.6-2 at 1100°C and 2-5 at 800°C the following order for the present experiments is assumed to be correct:

$$N_{Al}^{(2)}(\theta - Al_2O_3) > N_{Al}(602CA) > N_{Al}^{(2)}(\alpha - Al_2O_3) \tag{54}$$

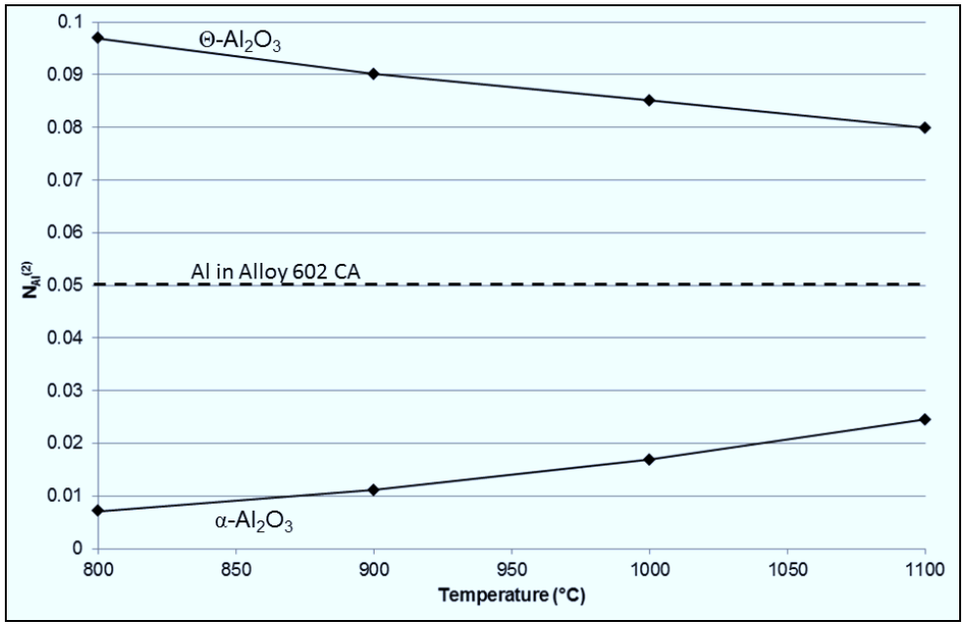

Figure 51: $N_{Al}^{(2)}$ values for alloy 602 CA as a function of temperature calculated according to equation (53)

Temperature	°C	800	900	1000	1100
V_m^{A-B}	cm³/ mol	6.93			
$V_m^{AlO_{1.5}}$	cm³/ mol	12.81			
k_p (α-Al_2O_3)	cm²/s	2.4E-17	7.1E-16	1.3E-14	1.7E-13
k_p (θ-Al_2O_3)	cm²/s	6.7E-15	6.9E-14	5.0E-13	2.6E-12
D_{Al}	cm²/s	2.2E-13	2.7E-12	2.2E-11	1.3E-10
$N_{Al}^{(2)}$ (α-Al_2O_3)	Mole fraction	0.0071	0.0111	0.0169	0.0245
$N_{Al}^{(2)}$ (θ-Al_2O_3)	Mole fraction	0.0969	0.0901	0.0851	0.0799

Table 6: Values used for the calculation of $N_{Al}^{(2)}$ according to equation (53) and displayed in Figure 51 [31, 33, 63]

The transformation from θ-Al_2O_3 to α-Al_2O_3 is reported to accelerate with increasing exposure temperature [31]. On NiAl θ-Al_2O_3 is reported to persist for more than 100 h at 800°C [31]. This was in the present studies not found to occur in the case of alloy 602 CA; after 72 h exposure at 800°C the material forms mainly α-Al_2O_3 (Figure 36).

As the material is covered by an external Al_2O_3 scale at this temperature (Figure 31), according to the calculations of $N_{Al}^{(2)}$, α-Al_2O_3 seems to be the phase governing the maintenance of the external scale after 72 h exposure at 800°C. From the assumption that the rate of transformation from θ-Al_2O_3 to α-Al_2O_3 increases with increasing temperature, after 72 h exposure at higher temperatures (>800°C) the amount of α-Al_2O_3 increases. Thus, after 72 h exposure α-Al_2O_3 seems to govern the scale maintenance in the whole investigated temperature range (800-1100°C). In that case the ratio between K_p and D_{Al} should be very small and no steep aluminum concentration gradient should establish beneath an existing external alumina scale. This is in agreement with the GDOES data for the 800°C specimens (Figure 33, Figure 34). It also agrees with results from Chyrkin et al [36] related to studies on alloy 214 with a substantially higher aluminum content (4.5 wt.-%) than alloy 602 CA. In the temperature range 1100-1200°C the alloy 214 exhibited external alumina formation after a period of transient oxidation. The aluminum depletion profiles beneath the surface scales appeared to be virtually flat, clearly showing that the ratio K_p / D_{Al} is extremely small and thus in the case of α-alumina formation equation (53) seems to be always fulfilled.

In addition, the fact that the actually observed value for $N_{Al}^{(1)}$ strongly differs from that calculated on the basis of the above-mentioned calculations may find its cause in the fact that for the prevailing case, in the Wagner treatment leading to equation (52), a number of experimentally observed facts are neglected:

- Equation (52) does not take into account interface recession as a result of the external chromia scale growth
- The formation of metallic protrusions in the chromia scale due to volume increase resulting from internal Al_2O_3 formation is neglected
- Oxygen and aluminum diffusion are assumed to occur in a single phase matrix without the presence of grain boundaries or other interfaces

Consequently, the limiting factor regarding the question whether aluminum oxidizes externally or internally seems to be $N_{Al}^{(1)}$.

In reference [101] it was shown that the interfaces between the metallic matrix and the internal oxide precipitates act as rapid diffusion paths for oxygen. This has the result that, especially in case of rod like precipitates arranged perpendicular to the alloy surface, oxygen permeability may be substantially larger than the values calculated assuming only bulk alloy diffusion. This seems a likely explanation for the fact that the real value of $N_{Al}^{(1)}$ is, at temperatures of 900 – 1100°C, larger than the actual mole fraction of aluminum in alloy 602 CA. Based on the treatments in the literature, it is, as far as known to the authors, hardly

possible to estimate a temperature dependent permeability to explain the experimentally observed temperature dependence of external alumina scale formation.

A further factor, which is not considered in deriving equation (52), is that diffusion of aluminum in the alloy matrix is affected by the presence of alloy grain boundaries. It has frequently been found, that in the temperature range considered, the diffusivities of metallic elements along alloy grain boundaries are substantially larger than in the bulk alloy grains. This effect is e.g. the reason that external scale formation is promoted by fine alloy grain size and/or introducing cold work in the specimen surface [102]. The latter results in an increased number of grain boundaries and dislocations, which act as rapid diffusion paths for the scale forming elements in the alloy. In fact, grain boundaries in the alloy also promote transport of oxygen but it is well established that the difference between grain and grain boundary transport is less pronounced for interstitially dissolved elements. The specimens in the present study were ground prior to oxidation testing. It is well established that this surface treatment is sufficient to produce a surface layer in the µm range [103] in which an increased density of grain boundaries and dislocations are formed. These may be able to enhance diffusion of the scale forming element to such an extent that external scale formation may be obtained.

To check this hypothesis, two alloy 602 CA specimens were prepared for 24 h TGA tests in Ar-20%O_2 at 800°C. One specimen was p1200 grit ground, as in the previous experiments, the other was prepared to a mirror like surface using diamond paste. Figure 52 shows that the area specific weight gain of the ground specimen is in very good agreement with the data shown in Figure 29; the weight gains after 24 h are 0.052 mg/cm² and 0.047 mg/cm² respectively, illustrating the reproducibility of the results. The weight gain of the polished specimen is substantially larger than that of the ground specimen after 24 h oxidation at 800°C, i.e. 0.096 mg/cm². Figure 53 compares metallographic cross sections of the diamond polished specimen and the p1200 grit ground specimen. The latter exhibits external alumina scale formation as found for the oxidation tests in the various test gases at 800°C described in the previous sections (Figure 29). However, the specimen, which was diamond polished prior to exposure, exhibits a scale morphology which is typical of that observed at the higher temperatures in the previous sections: aluminum is internally oxidized accompanied by outwardly moved metallic protrusions which are covered by a chromia scale.

An etched metallographic cross section of the ground specimen clearly reveals even after 72h exposure at 800°C, formation of a thin near surface zone (approx. 10 µm wide) in which the grain size is substantially smaller than in the bulk material (Figure 25, Figure 54). These observations strongly indicate that the external alumina scale formation at 800°C described in the previous sections is affected by the surface treatment. The latter will also affect the behavior at the higher temperatures. However, recovery and recrystallization are known to

accelerate with increasing temperature [104]. Therefore it seems likely that the beneficial effect of the cold work introduced by grinding will rapidly vanish upon heating the specimen to oxidation temperatures in the range 900 – 1100°C as the time required to alleviate the effect decreases with increasing temperature [102]. If the temperature dependence of the effect of cold work introduced by specimen grinding is a crucial effect for the observed temperature dependence of protective alumina scale formation, it explains why hardly any effect of gas composition on this temperature dependence was observed. Even when changing the equilibrium oxygen partial pressure of the gas by approximately 15 orders of magnitude (upon changing from Ar-O_2(H_2O) to Ar-H_2-H_2O), hardly any effect on external alumina scale formation was found. This strongly indicates that the pronounced effect of gas composition on external alumina scale formation in the case of NiCrAl alloys e.g. described in references [68, 105] is related to the low chromium content (< 10 wt.-%) in the alloys used in the mentioned studies. In these cases the transient oxide of the more noble element competing with the external alumina scale formation is NiO and/or nickel-rich mixed oxides. Taking into account the presence of an external scale of a more noble element has been shown to increase the critical aluminum content for obtaining external alumina scale $N_{Al}^{(1)}$ [60]. Thereby the latter value increases with increasing growth rate of the external scale formed by the more noble element, essentially as a result of a decrease of the enrichment of Al in the internal oxidation zone (IOZ) [106]. As the nickel oxide growth rate is strongly affected by variations in pO_2 [83] and presence of water vapor at constant pO_2 [67], it is understandable that the external alumina scale formation in low chromium NiCrAl alloys is strongly affected by the exact composition of the test gas.

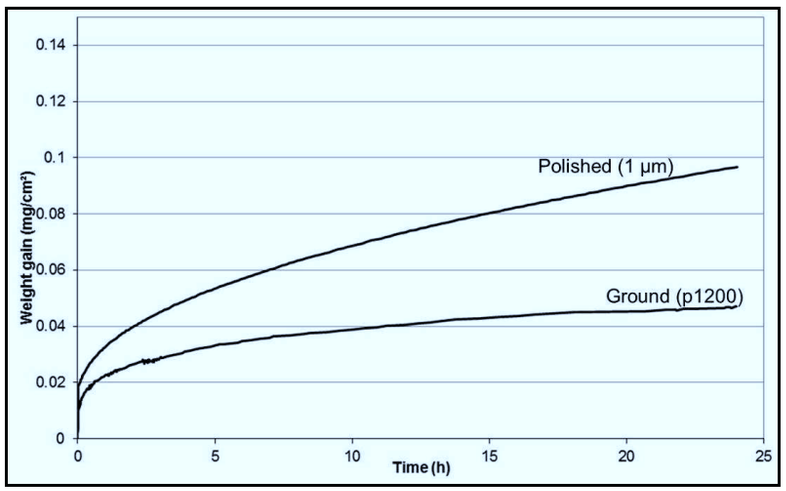

Figure 52: Area specific weight gain during isothermal oxidation of alloy 602 CA in Ar-20%O_2 at 800°C showing effect of surface treatment on oxidation kinetics

Also in the case of alloy 602 CA external alumina scale formation is competing with formation of an external scale of a more noble element, here chromium. Thus, variations in chromia growth rate are expected to affect $N_{Al}^{(1)}$ in a qualitatively similar manner as described above for growth rate variations of nickel-rich oxides. However, as discussed in section 6.1.2.1, the observed variation in growth rate in the various gases was small. Because of this limited variation in growth rate of the external chromia scales, the changes in the values of $N_{Al}^{(1)}$ due to presence of the external scale of a more noble element (here chromium) have only a minor effect on the value of $N_{Al}^{(1)}$. However, these considerations cannot explain the formation of an external alumina scale during 900°C oxidation in Ar-20%O_2-7%H_2O, whereas in Ar-7%H_2O, Ar-4%H_2-7%H_2O and Ar-20%O_2 the material mainly exhibits external Cr_2O_3 at this temperature. An effect which is well known to occur in Ar-O_2-H_2O to a much larger extent than in the other gases is the formation of volatile chromium oxy-hydroxide [107, 108]. Under the same experimental conditions, i.e. gas flow rate, as used in the present studies, Michalik et al [109] observed for pure chromia scales at 1000°C in air with 7%H_2O a volatilization rate of $2 \cdot 10^{-3}$ mg·cm^{-2}·h^{-1}. Extrapolation of the data reveals for 800°C a value of approximately $4 \cdot 10^{-4}$ mg·cm^{-2}·h^{-1}. In reference [110] it was found that in air with 3%H_2O and a flow rate of 5 cm³/s a temperature increase from 850°C to 950°C increased the evaporation rate of alloy 602 CA approximately by a factor of five. Whether this increased chromium evaporation promotes external Al_2O_3 formation is, as far as known by the authors, not clearly apparent from other studies. Further investigations are necessary to estimate whether this is indeed the case.

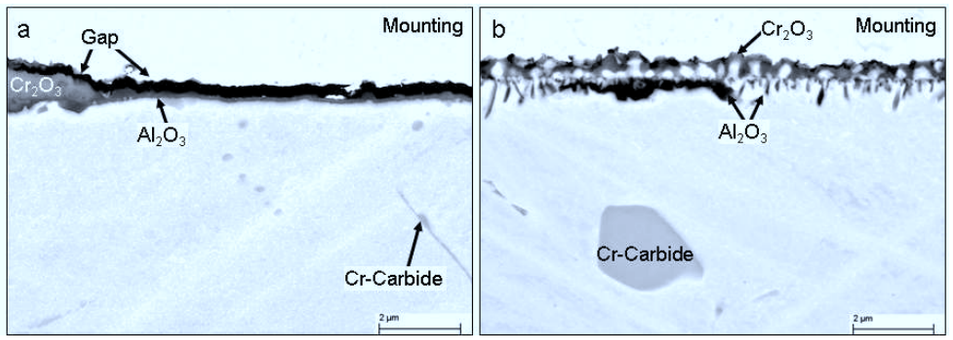

Figure 53: Metallographic cross section (BSE image) of alloy 602 CA after isothermal oxidation at 800°C in Ar-20%O_2 for 24 h. a) specimen ground (b) diamond polished prior to exposure

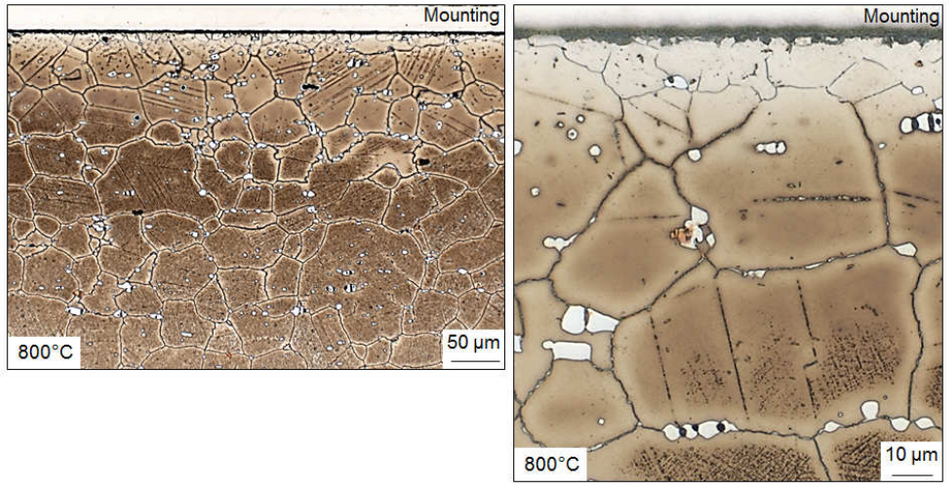

Figure 54: Etched metallographic cross sections of ground alloy 602 CA specimen after isothermal oxidation at 800°C in Ar-20%O_2 for 72 h

6.2 Oxidation Behavior of Haynes 214

The detailed chemical composition of the investigated batch of Haynes 214 is shown in Table 2. The isothermal exposures for 8 h and 72 h were performed in Ar-20%O_2 atmosphere at 800, 900, 1000 and 1100°C respectively. For long-term experiments at 800°C and 900°C up to 1000 h a tube furnace was used for the oxidation tests. In addition, specimens were exposed for 72 h in different H_2O-containing test gases at 800, 900, 1000 and 1100°C. Due to the higher aluminum content of Haynes 214 compared to Alloy 602 CA, γ´-formation is expected to occur in the envisaged temperature range, which may affect oxide scale formation. Therefore, in the following section, first results of aging studies for estimating the formation of γ´ as a function of time and temperature will be described.

6.2.1 Phase Composition and Microstructure of Haynes 214

Haynes 214 was supplied in the solution annealed condition. The solution annealing was conducted at 1095°C followed by rapid cooling to room temperature to suppress formation of γ´-precipitates [111]. As a consequence, the material can be formed by cold-working. Figure 55 shows the microstructure of as-received Haynes 214. The matrix of Haynes 214 consists of equiaxed γ-Ni grains with an average size of 40 µm determined according to DIN EN ISO 643:2003 [112].

Exposure of the alloy at temperatures between 800°C and 1000°C changes the initial alloy microstructure due to precipitation or dissolution of γ´-phase and recrystallization of the γ-matrix [111]. Figure 56 shows BSE images of the cross-sections of Haynes 214 after annealing for 1 h, 10 h, 100 h and 500 h in static vacuum at 800°C. Prior to SEM analysis the specimens were etched (5ml HNO_3 + 2 ml HF + 93 ml H_2O) to improve the contrast between γ´-precipitates and γ-matrix.

After 1 h annealing the γ`-precipitates had a diameter smaller than 100 nm and were evenly distributed within the γ-matrix. The size of γ´-precipitates increases as expected with time so that after 500 h annealing at 800°C the average diameter is approximately 250 nm. The microstructure of the specimens annealed for 100 h and 500 h were used for estimation of γ´-phase fraction with AnalysisPro software. The estimated fractions of γ´ were 34 vol.-% and 29 vol.-% after 100 h and 500 h, respectively. Similar amounts of γ´-phase indicate that the alloy annealed for 100 h is near the equilibrium phase composition. Unfortunately, the size of γ´-precipitates and the spacing were too small to allow EDX measurements of the γ-matrix and γ´-precipitates compositions.

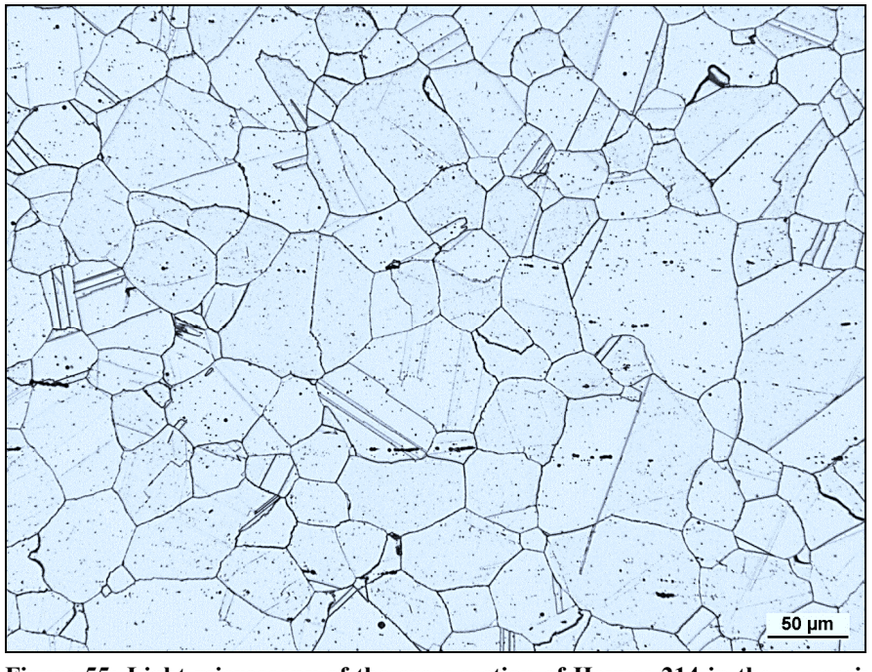

Figure 55: Light microscopy of the cross-section of Haynes 214 in the as-received state after etching with 5% H_2SO_4 aqueous solution

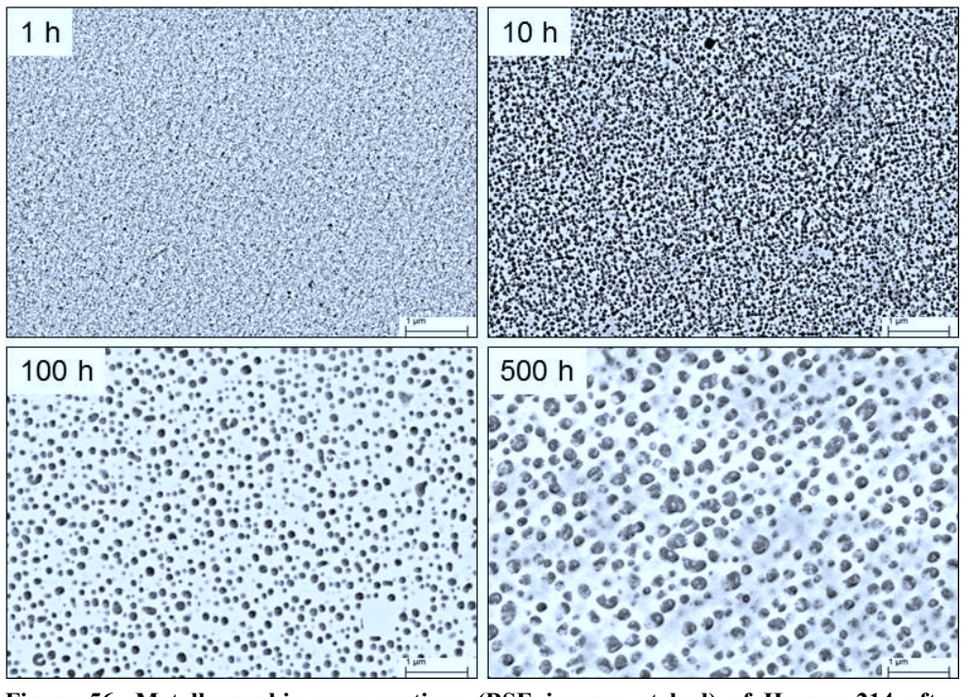

Figure 56: Metallographic cross sections (BSE images, etched) of Haynes 214 after isothermal exposure in vacuum at 800°C

Figure 57 shows the BSE images of the cross-sections of Haynes 214 after annealing for 1 h, 10 h, 100 h and 500 h in static vacuum at 900°C. Increasing the annealing temperature to 900°C reduces significantly the amount of γ´-phase formed in the alloy. The fractions of γ´ estimated with AnalysisPro were 14 vol.-% and 13 vol.-% after 100 h and 500 h, respectively. Moreover, coarsening proceeds, as expected, at 900°C faster than at 800°C, resulting in the formation of a smaller number of larger γ´-precipitates (compare Figure 56 and Figure 57). The mean diameter of the γ´-particles after 500 h exposure at 900°C is with approximately 0.5 µm twice as large as that formed during 800°C exposure. The size of γ´-precipitates formed at 900°C was still too small to allow quantitative EDX measurements. However, the spacing between the precipitates was large enough to measure the composition of the γ-matrix. Its composition was 74.5%Ni – 18.1%Cr – 4%Fe – 3.5%Al (wt.-%).

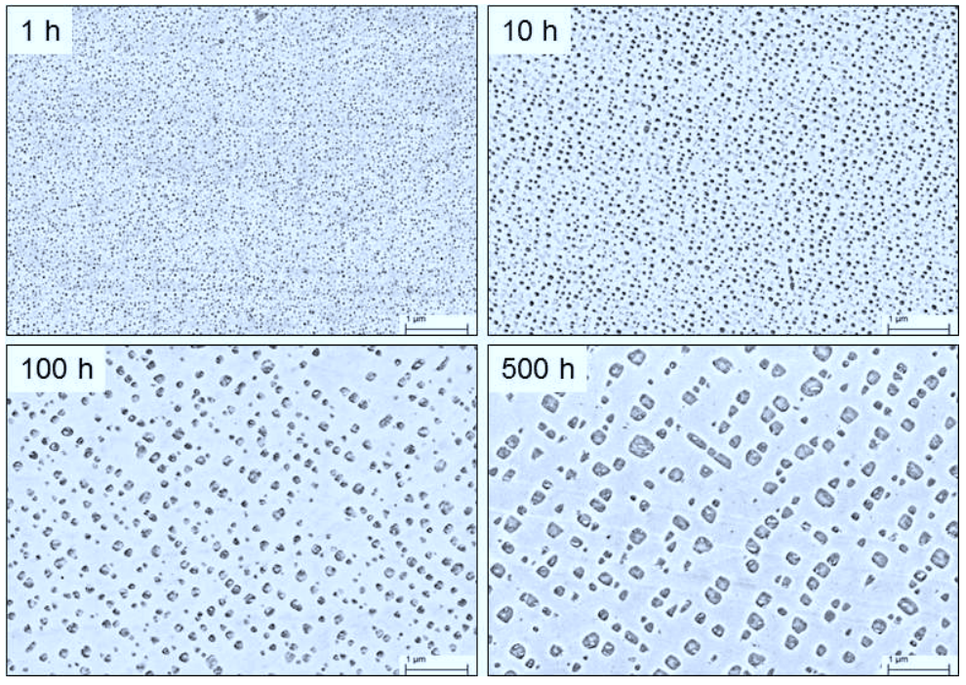

Figure 57: Metallographic cross sections (BSE images, etched) of Haynes 214 after various times of isothermal exposure in vacuum at 900°C

Figure 58 shows the BSE images of the cross-sections of Haynes 214 after annealing for 1 h, 10 h, 100 h and 500 h in static vacuum at 1000°C. The average size of γ´-precipitates is comparable to those found after annealing for 1 h at 900°C. Furthermore, the size and number of γ´-precipitates formed at 1000°C seems to be not affected by annealing time. The same effect was observed for specimens annealed at 1100°C. This is a strong indication that the γ´-precipitates observed after annealing at 1000°C and 1100°C were formed exclusively during

cooling but not during high temperature exposure. After exposure all specimens were cooled in a water bath.

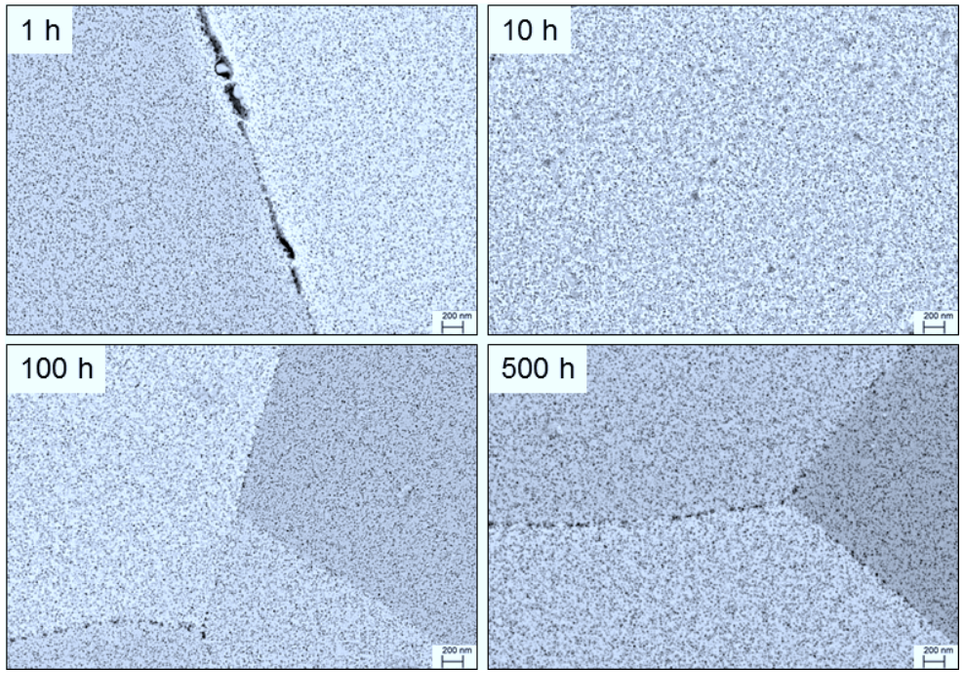

Figure 58: Metallographic cross sections (BSE images, etched) of Haynes 214 after various times of isothermal exposure in vacuum at 1000°C; specimens were water cooled after the isothermal exposure

6.2.2 Oxidation Behavior in Ar-20%O_2

6.2.2.1 Oxidation Kinetics

Figure 59 shows the area specific weight gains of Haynes 214 during isothermal exposure at 800°C, 900°C, 1000°C and 1100°C in Ar-20%O_2 for 72 h (see section 5.3). The oxidation kinetics of the material exposed at the four test temperatures could not be described using the classical parabolic rate description, shown in equation (17). Therefore Figure 60 shows the instantaneous, apparent parabolic rate constant as function of time, calculated using the procedure described in reference [113, 114]. The curves do not exhibit values which are steadily decreasing with increasing exposure time, as frequently observed for alumina forming FeCrAl alloys [69]. Sudden changes in time dependence of the apparent k_w-values, occurring during exposure, indicate a change in oxidation mechanisms. This behavior was found for all test temperatures, but especially at 900°C and 1000°C. The rapid decrease in apparent k_w-values by about three orders of magnitude was observed in the first 1 – 3 h of exposure in all oxidation experiments. After that time the apparent k_w-values for the specimen

oxidized at 1100°C virtually stabilize on a level of approximately $2 \cdot 10^{-13}$ $g^2cm^{-4}s^{-1}$. For specimens oxidized at 900°C and 1000°C the apparent k_w-values after the initial stages increase with prolonged exposure time to reach a local maximum. The time required to reach these local maxima was approximately 3 h for the specimen oxidized at 1000°C and 20 h for the specimen oxidized at 900°C. For the specimen oxidized at 800°C such a relative maximum was not observed during the 72 h TGA experiment. To overcome possible time limitations of the TGA experiments two additional 1000 h discontinuous oxidation tests were performed. Figure 61 shows the area specific weight gains during discontinuous exposure at 800°C and 900°C in Ar-20%O_2 compared with the 72 h TGA results. The discontinuously recorded weight changes fit reasonable well with these from respective isothermal TGA experiments. The slope of the 900°C weight change curve shows clearly that the oxidation rate decreases continuously between 100 h and 300 h of exposure. After this time the weight change remains virtually constant. In contrast, the 800°C curve shows an increase of the specific weight gain between approximately 200 h and 600 h of exposure. The acceleration of specific weight gain clearly shows that the apparent k_w-values increase in this time period. The data points between 600 h and 1000 h do not show clearly whether the oxidation rate increases or remains constant.

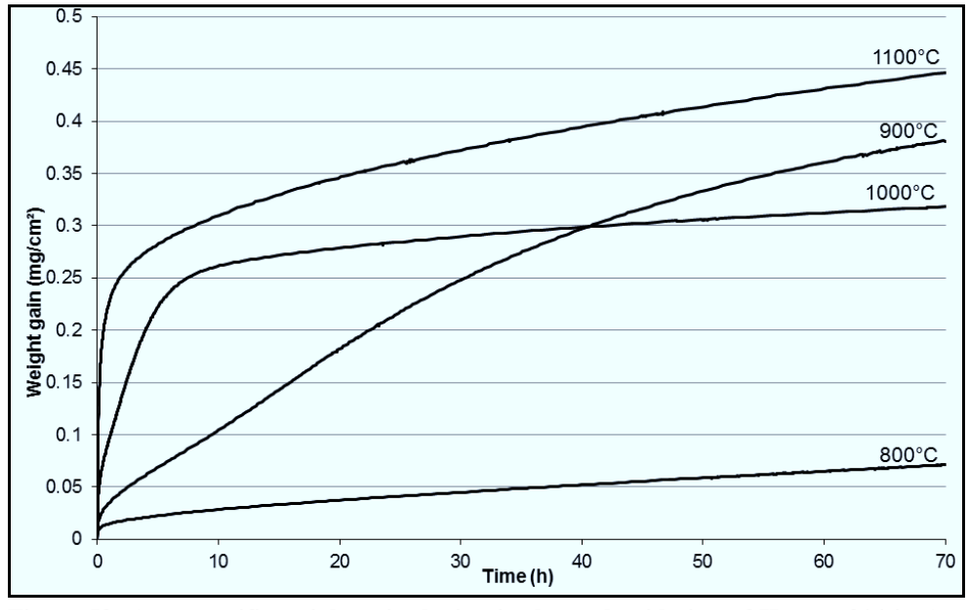

Figure 59: Area specific weight gain during isothermal oxidation of Haynes 214 in Ar-20%O_2 at different temperatures

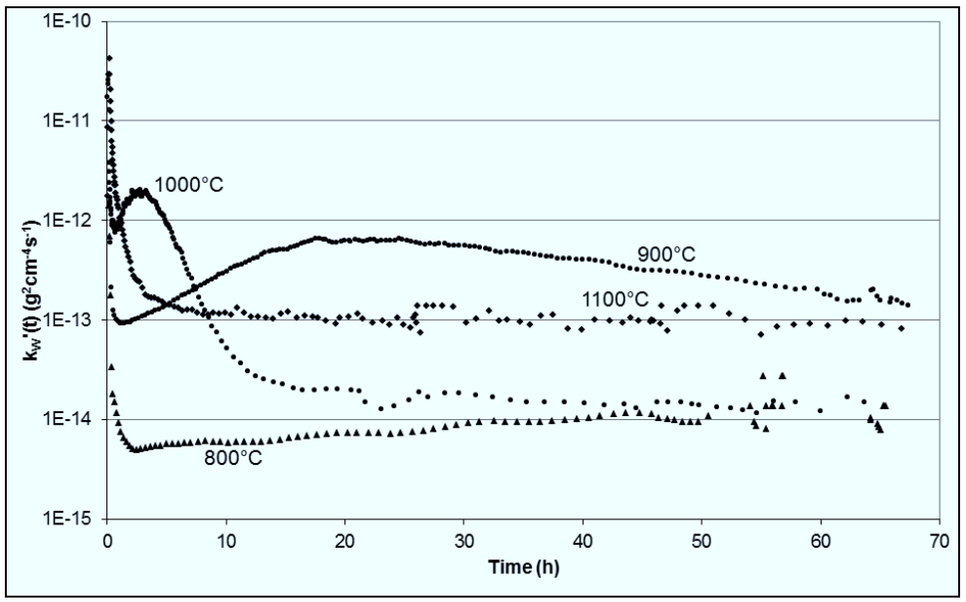

Figure 60: Time dependence of the instantaneous apparent oxidation rate k_W' of Haynes 214 during isothermal oxidation in Ar-20%O_2 for 72 h

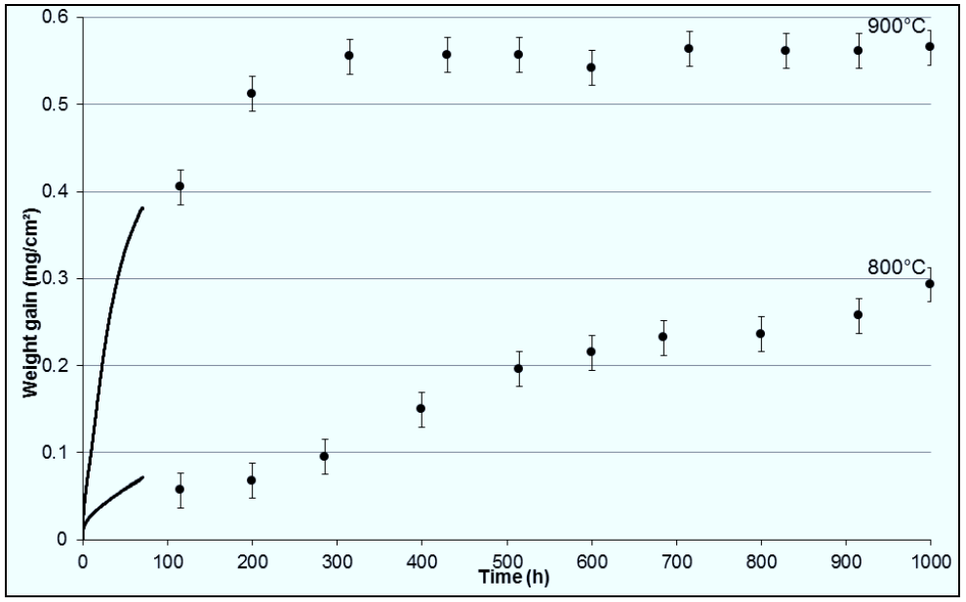

Figure 61: Area specific weight gain during discontinuous oxidation tests up to 1000 h (solid points) compared with TGA results (lines) of Haynes 214 in Ar-20%O_2 at different temperatures

6.2.2.2 Oxide Scale Formation

Figure 62 shows the BSE images of the cross-sections of Haynes 214 after 72 h isothermal oxidation in Ar-20%O_2 at 800-1100°C. At 800°C the surface is covered by external alumina. After oxidation at 900°C the mixed oxide contains in addition aluminum, as measured by EDX-analysis. Optical fluorescence measurements of Cr^{3+} ions in alumina were performed in a number of random locations on the specimen surfaces to obtain more detailed information about the type of Al_2O_3 formed. A typical example of these measurements is shown in Figure 63. The results show that the alumina consisted of α-Al_2O_3 but at 800°C and 900°C significant amounts of metastable alumina (probably θ-Al_2O_3). (Note that the intensity for α is approximately ten times larger than that for an equivalent amount of θ [78]).

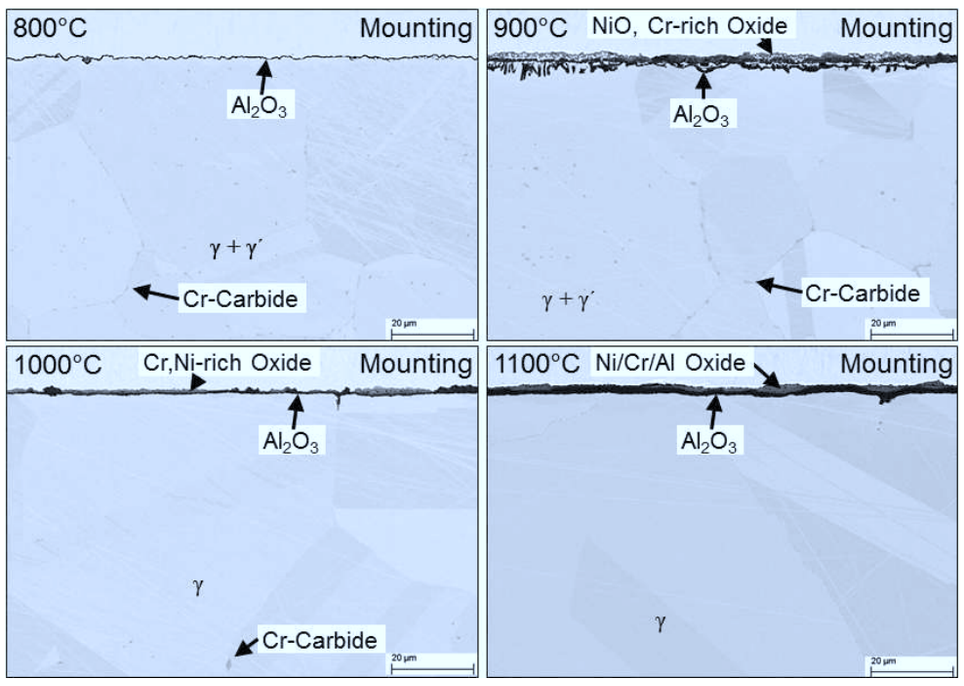

Figure 62: Metallographic cross sections (BSE images) of Haynes 214 after isothermal oxidation in Ar-20%O_2 for 72 h

Apart from obvious differences in oxide thicknesses and composition, the oxide scales of the specimens oxidized for 72 h at 800-1100°C differ in the types of Al_2O_3 formed (see Figure 63). In contrast to 800°C, 900°C and 1000°C, no θ-Al_2O_3 was found after 72 h oxidation at 1100°C. The positions of the R1 and R2 fluorescence lines for Cr^{3+} ions in α-Al_2O_3 differ from those of the stress-free sapphire reference (see Figure 63). This suggests the presence of residual compressive stresses in the oxide scales formed in the investigated test gases. According to literature [79], these stresses consist of extrinsic and intrinsic stresses, arising from a thermal mismatch between oxide scale and alloy during cooling to room temperature

and oxide growth stresses. Calculating the average in-plane stresses of the alumina-based scales, using the procedure described in reference [79], shows that the residual stresses increase with increasing temperature from 2.7 GPa at 800°C to 7.0 GPa at 1100°C. The latter value is in the same range as the stresses determined for a 45Ni-25Cr-25Fe-5Al alloy (6.7±0.6 GPa) after oxidation at the same temperature [79].

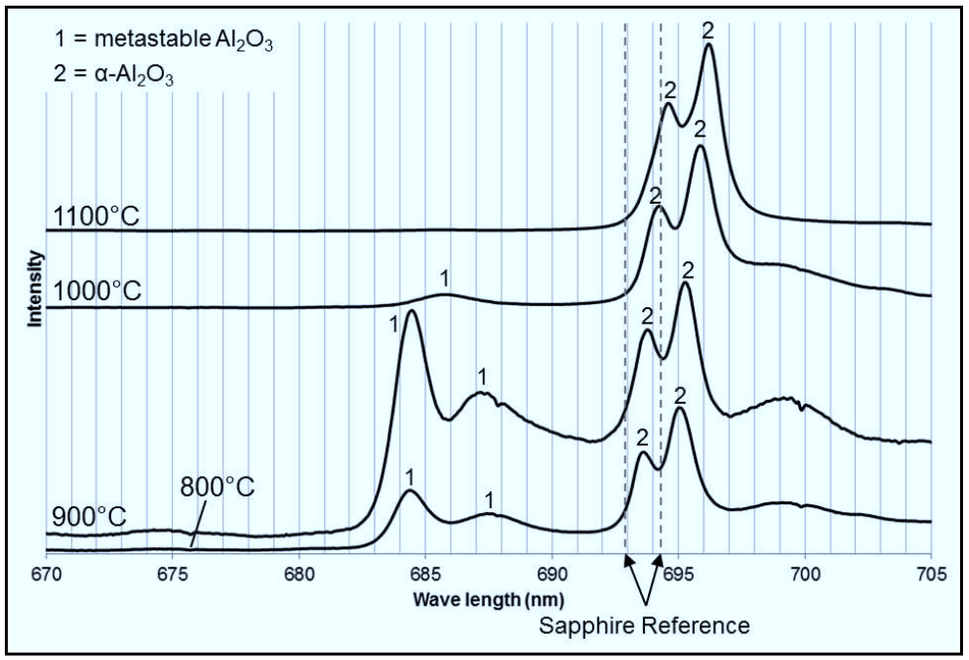

Figure 63: Intensity plots of fluorescence of Cr^{3+} of the oxide surfaces of Haynes 214 after isothermal oxidation in Ar-20%O_2 at different temperatures for 72 h

Beneath mixed oxides scales the formation of internal alumina precipitates was found. Figure 64 shows the BSE images of the cross-sections of Haynes 214 after 8 h, 72 h and 1000 h oxidation at 800°C in Ar-20%O_2. In the specimens oxidized for 8 h and 72 h only a few locations of internal alumina precipitates were observed. The maximum width of the internal oxidation zone (IOZ) after 8 h of oxidation does not exceed 0.5 µm. After 72 h exposure the maximum IOZ width is approximately 1.5 µm. The external mixed oxide of both specimens is Cr-rich with trace amounts of nickel. Extending at 800°C the oxidation time to 1000 h resulted in expansion of the mixed oxide scale areas (Figure 64). The maximum depth of the IOZ after 1000 h oxidation at 800°C is about 5 µm. Formation of internal aluminum oxides results in a volume increase. Consequently, the alloy is locally extruded outwards [31] forming metallic protrusions in the external Cr-rich oxide scales (Figure 64). In the elemental concentration profiles analyzed by GD-OES (Figure 65) a nickel enrichment in combination with a decreased oxygen concentration at a sputter time of 23 s corresponds to the in-scale

metal protrusions. Beneath the IOZ an aluminum concentration of approximately 4.8 at.-% is measured, which implies an aluminum depletion of 4.1 at.-% (Initial Alloy concentration: 9.0 at.-% Al) in this region. A lack of clear borderlines in the diagram between Cr-rich oxide, protrusions, internal Al_2O_3 and alloy arises from lateral inhomogeneity of the oxide scale [82].

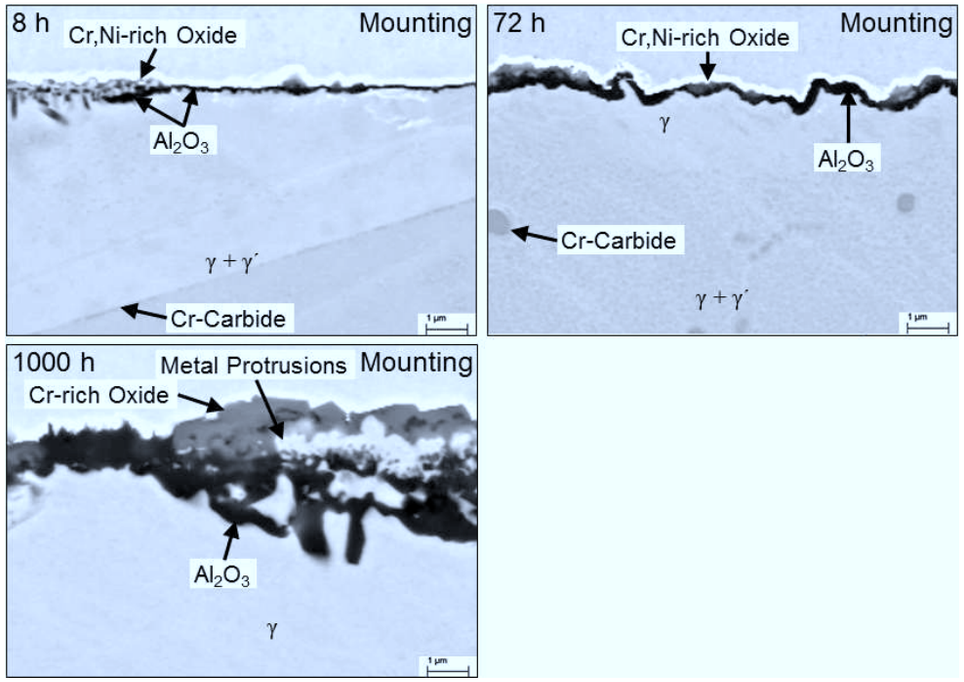

Figure 64: Metallographic cross sections (BSE images) of Haynes 214 after isothermal oxidation in Ar-20%O_2 at 800°C

Figure 66 shows the BSE images of the cross-sections of Haynes 214 after 8 h, 72 h and 1000 h oxidation at 900°C in Ar-20%O_2. The microstructure of the oxide scale formed during 8 h exposure at 900°C is qualitatively similar to that formed during 72 h oxidation at 800°C (compare Figure 64 and Figure 66). The main differences are a more pronounced IOZ and the existence of metallic protrusions in the outer mixed oxide scale. In addition, Al_2O_3 starts to almost completely separate the metallic protrusions from bulk metal after 8 h. Increasing at 900°C the oxidation time to 72 h results in decreasing areas covered by external alumina. In contrast to 800°C, the material exhibits after 72 h exposure at 900°C a thicker outer oxide scale containing NiO, Cr-rich oxide and metal protrusions. Furthermore, the internal aluminum oxides formed during 72 h oxidation at 900°C exhibit two different morphologies (see Figure 62). The first one consists of needle-like precipitates arranged perpendicular to the specimen surface. The second morphology is a virtually continuous inner alumina layer close to the initial specimen surface. After 1000 h oxidation at 900°C the oxide scale consists exclusively of a continuous inner Al_2O_3 layer and an outer oxide mixture, containing NiO and

Cr-rich oxide. In contrast to the 72 h exposure, the outer oxide scale contains no metallic protrusions. This is in agreement with the GD-OES measurement which revealed no Ni enrichment inside the external oxide scale (Figure 67). The thicknesses of both, external oxide and internal alumina layer, vary in thickness between 2-5 µm and 1-2 µm, respectively. The IOZ present in the specimen oxidized for 72 h is virtually completely vanished after 1000 h exposure. The aluminum concentration below the IOZ amounts to approximately 7.4 at.-% (Figure 67), which is 3.3 at.-% higher compared to the specimen oxidized at 800°C (Figure 65).

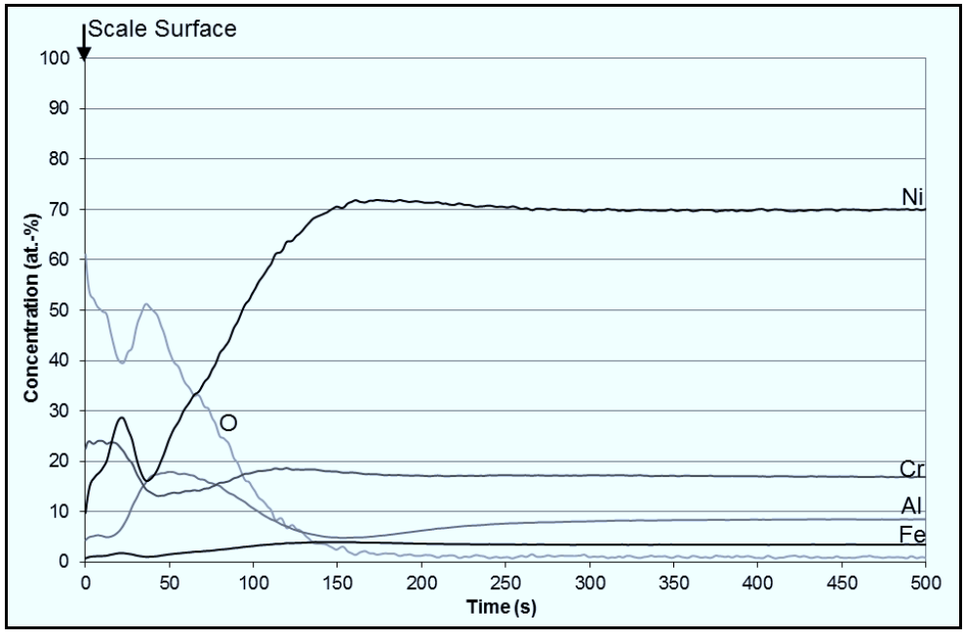

Figure 65: GD-OES depth profiles of Haynes 214 after isothermal oxidation in Ar-20%O_2 at 800°C for 1000 h

After oxidation for 8 h and 72 h at 1000°C and 1100°C, respectively, the external oxide scale is separated from the bulk material by a continuous Al_2O_3 scale (Figure 68, Figure 69). However, after 8 h at 1000°C some internal Al_2O_3 precipitates were found. After 1100°C exposure this was not observed. The external scale present after 8 h oxidation at 1000°C consists of Cr-rich oxide and some NiO randomly distributed in the Cr-rich oxide scale (Figure 68). The EDX mapping of this specimen (Figure 70, Table 7) shows, apart from the formation of NiO, also minor amounts of Fe-containing oxide in the external scale.

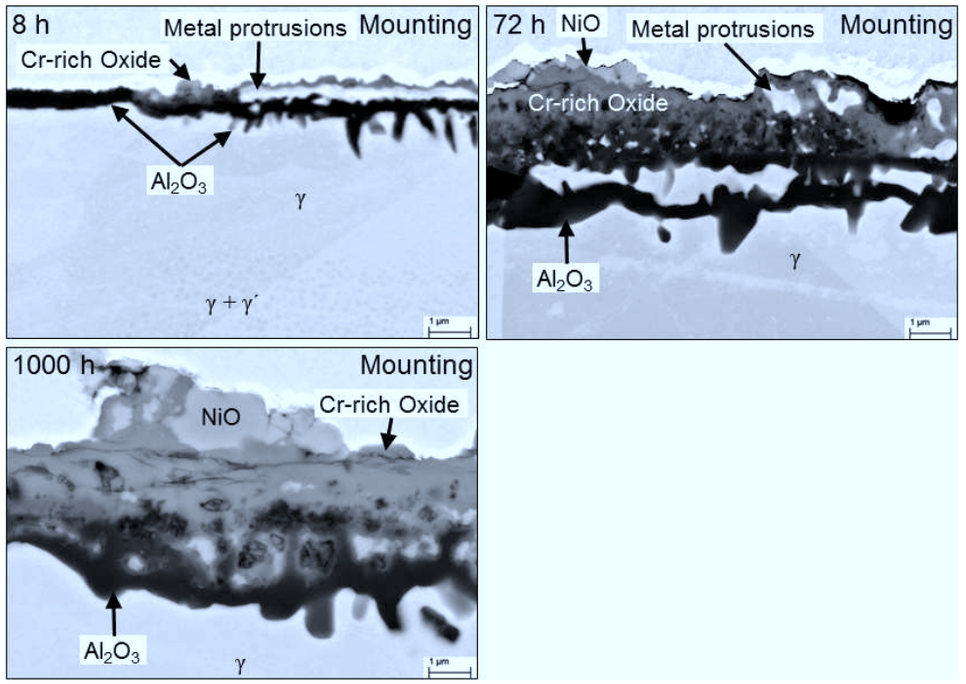

Figure 66: Metallographic cross sections (BSE images) of Haynes 214 after isothermal oxidation in Ar-20%O_2 at 900°C

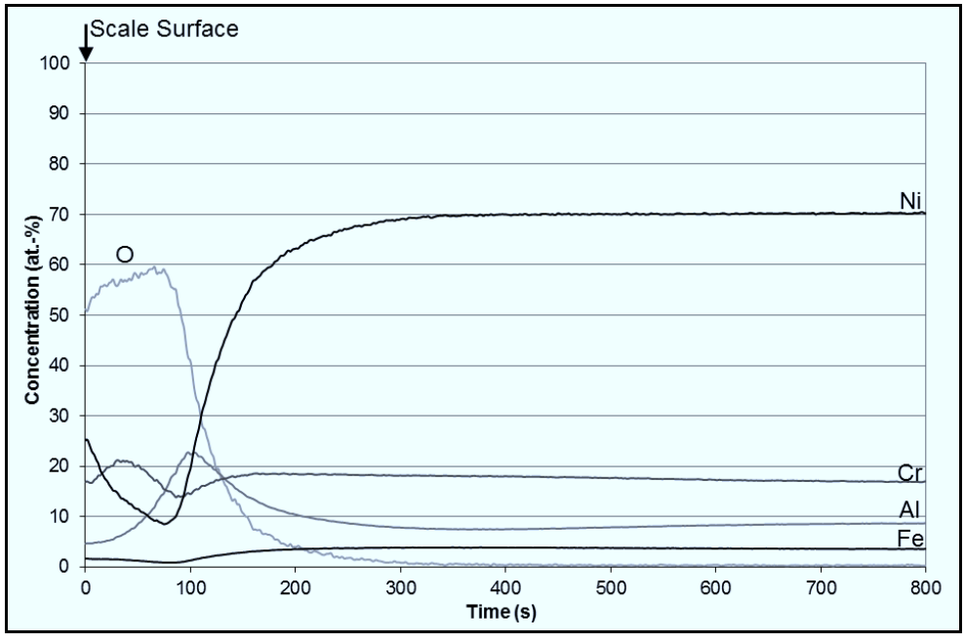

Figure 67: GD-OES depth profiles of Haynes 214 after isothermal oxidation in Ar-20%O_2 at 900°C for 1000 h

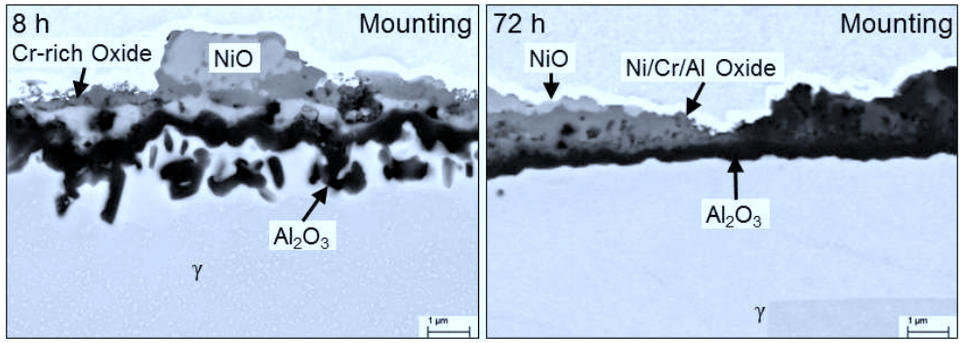

Figure 68: Metallographic cross sections (BSE images) of Haynes 214 after isothermal oxidation in Ar-20%O_2 at 1000°C

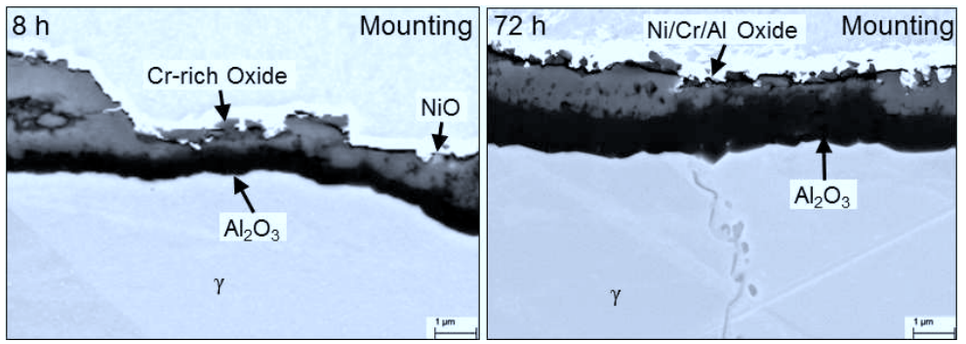

Figure 69: Metallographic cross sections (BSE images) of Haynes 214 after isothermal oxidation in Ar-20%O_2 at 1100°C

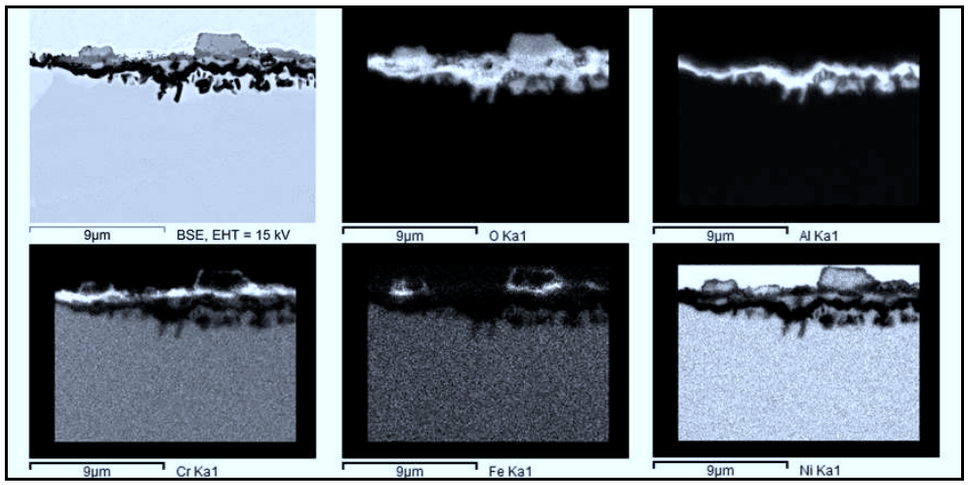

Figure 70: EDX mapping of Haynes 214 after isothermal oxidation in Ar-20%O_2 at 1000°C for 8 h

Chemical Composition (at.-%)					
O	Mg	Al	Cr	Fe	Ni
54.5	0.5	20.4	6.0	0.7	17.8

Table 7: Chemical composition (EDX) of the outer single-phase Ni/Cr/Al-mixed oxide formed on Haynes 214 after isothermal oxidation in Ar-20%O_2 at 1100°C for 72 h (compare Figure 69)

6.2.2.3 Formation of Precipitate Free Zone (PFZ)

Formation and growth of the oxide scale affects the microstructure and the composition of the investigated alloy in the subscale zone. Figure 71 shows a BSE image of the cross-section of Haynes 214 after discontinuous oxidation for 1000 h at 800°C. The alloy matrix consists of γ-phase and finely distributed γ´-precipitates. Beneath the oxide a precipitate free zone (PFZ) is formed which is minimum 4 µm wide. However, the PFZ differs locally in width and is significantly larger in the vicinity of grain boundaries. The composition of the points (a) and (b) in the PFZ (Figure 71), analyzed with EDX, is given in Table 8.

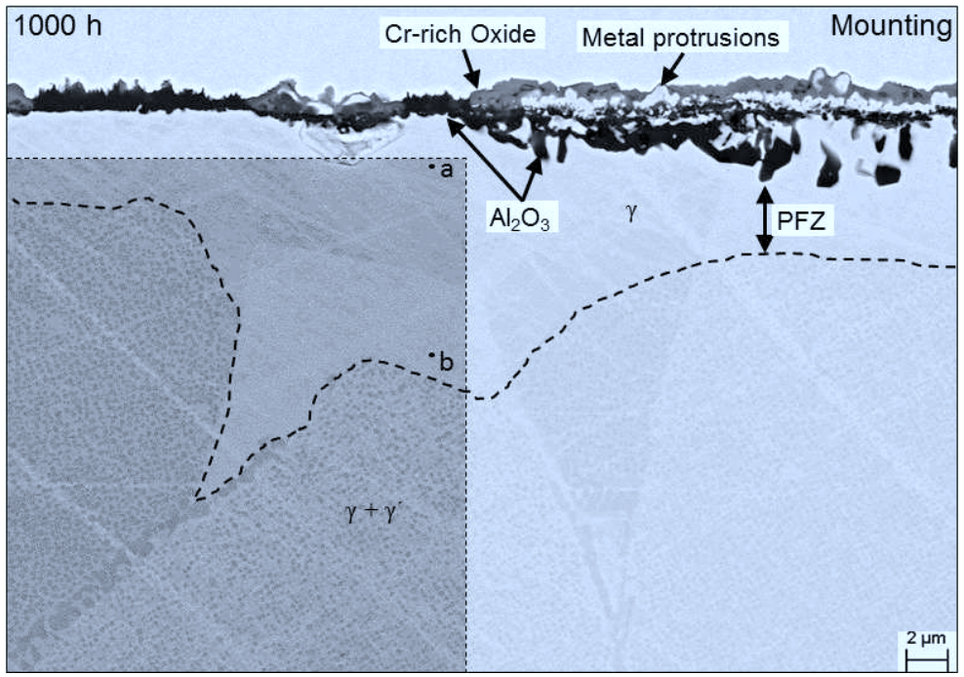

Figure 71: Metallographic cross section (BSE image) and EDX analysis of Haynes 214 after isothermal oxidation in Ar-20%O_2 at 800°C for 1000 h. Lower left part of the figure is shown in increased contrast to illustrate γ´ precipitates, dashed line marks the boundary between γ- and γ+γ´-zones

	Chemical Composition (at.-%)			
Point	Al	Cr	Fe	Ni
a	2.1	20.4	4.2	73.3
b	4.8	19.0	3.9	72.4

Table 8: Chemical Composition of the points marked in Figure 71 analyzed with EDX

The EDX-Analysis of the points (Table 8) marked in Figure 71 reveal an aluminum depletion in the PFZ of 2.7 at.-%. Compared to the bulk concentration (8.9 at.-% Al) EDX analysis of point (b), close to the precipitate containing zone, reveals a total aluminum depletion of 4.1 at.-%, which in good agreement with the value determined by GD-OES (Figure 65). After 1000 h oxidation at 900°C (Figure 72) the PFZ width is increased significantly compared to that after the same exposure time at 800°C and overall larger than 22 µm. In contrast to 1000 h oxidation at 800°C, the EDX-Analysis of the points (a) and (b) (Table 9) marked in Figure 72 indicate that there is no significant depletion of aluminum in the PFZ, as both points reveal an aluminum concentration of approximately 7.2 at.-%.

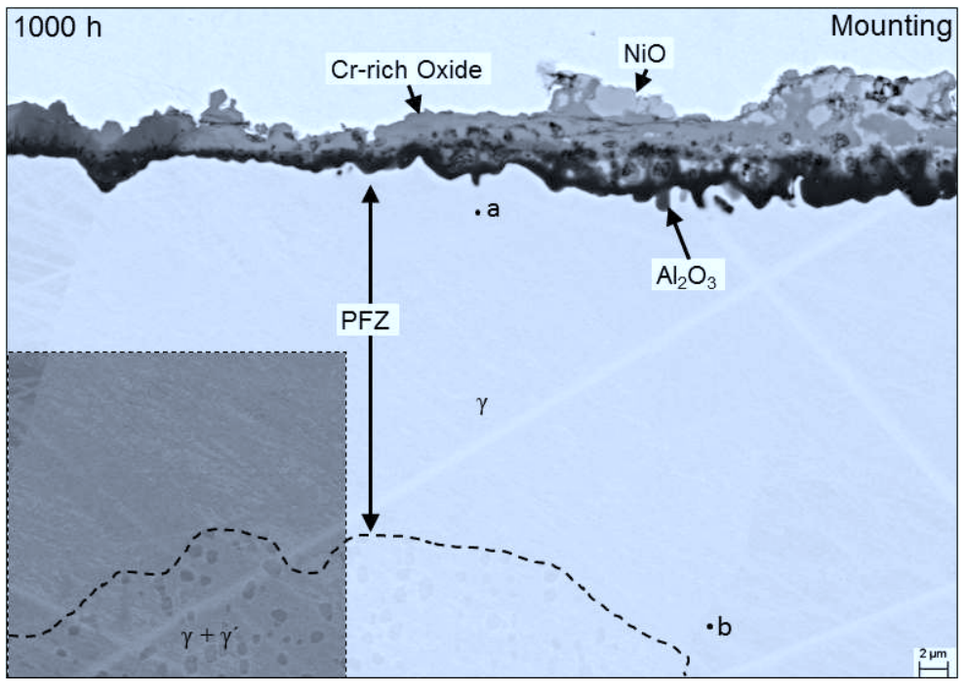

Figure 72: Metallographic cross section (BSE image) and EDX analysis of Haynes 214 after isothermal oxidation in Ar-20%O_2 at 900°C for 1000 h. Lower left part of the figure is shown in increased contrast to illustrate γ´ precipitates, dashed line marks the boundary between γ- and γ+γ´-zones

	Chemical Composition (at.-%)			
Point	Al	Cr	Fe	Ni
a	7.2	17.8	3.5	71.5
b	7.2	18.0	3.8	71.0

Table 9: Chemical Composition of the points marked in Figure 72 analyzed with EDX

The EDX-Analysis of point (b) (Figure 72), close to the precipitate containing zone, showed a similar aluminum concentration (7.2 at.-%) as the corresponding GD-OES measurement (Figure 67, 7.4 at.-%). This results in a total aluminum depletion, compared to the bulk concentration (8.9 at.-%), of 1.5-1.7 at.-%, which is significantly less compared to the 1000 h exposure at 800°C (4.1 at.-% depletion, Table 8). In contrast to 1000 h oxidation at 900°C, the specimen oxidized for 72 h exhibits an aluminum depletion within the PFZ (Figure 73, Table 10). According to the EDX-Analysis this depletion amounts to 1.4 at.-%, whereas the total aluminum depletion, compared to the bulk concentration (8.9 at.-% Al), is 3 at.-%. The latter is twice as high as the aluminum depletion after 1000 h at 900°C. Similar to this, the chromium concentration in the PFZ after 72 h oxidation at 900°C (14.3-14.6 at.-%) is also lower than after 1000 h oxidation (17.8-18.0 at.-%). After 800°C exposure for 1000 h the chromium concentration in the PFZ amounts to 19.0-20.4 at.-% and is even higher than after 1000 h oxidation at 900°C.

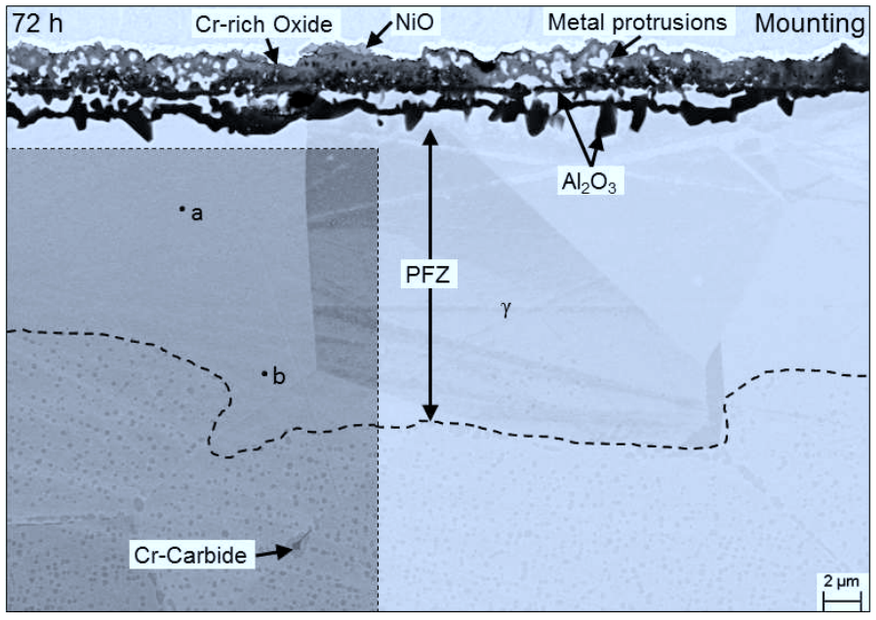

Figure 73: Metallographic cross section (BSE image) and EDX analysis of Haynes 214 after isothermal oxidation in Ar-20%O_2 at 900°C for 72 h. Lower left part of the figure is shown in increased contrast to illustrate γ´ precipitates, dashed line marks the boundary between γ- and γ+γ´-zones

	Chemical Composition (at.-%)			
Point	Al	Cr	Fe	Ni
a	4.5	14.3	3.4	77.8
b	5.9	14.6	3.1	76.4

Table 10: Chemical Composition of the points marked in Figure 73 analyzed with EDX

As the bulk alloy after exposure at 1000°C and 1100°C did not exhibit detectable amounts of γ`-precipitates, i. e. the alloy, including the subscale zone, consisted of solely of γ-phase, apart from very minor amounts of carbides. After 72 h oxidation at both temperatures virtually flat aluminum and chromium concentration profiles were found. However, after 8 h oxidation a minor aluminum depletion was observed. At 1000°C the total aluminum depletion beneath the oxide scale was determined by GD-OES to be 2.1 at.-% and 0.8 at.-% at 1100°C. The minimum aluminum concentrations beneath the oxide layer of the specimens oxidized at 800-1100°C are summarized in Figure 74.

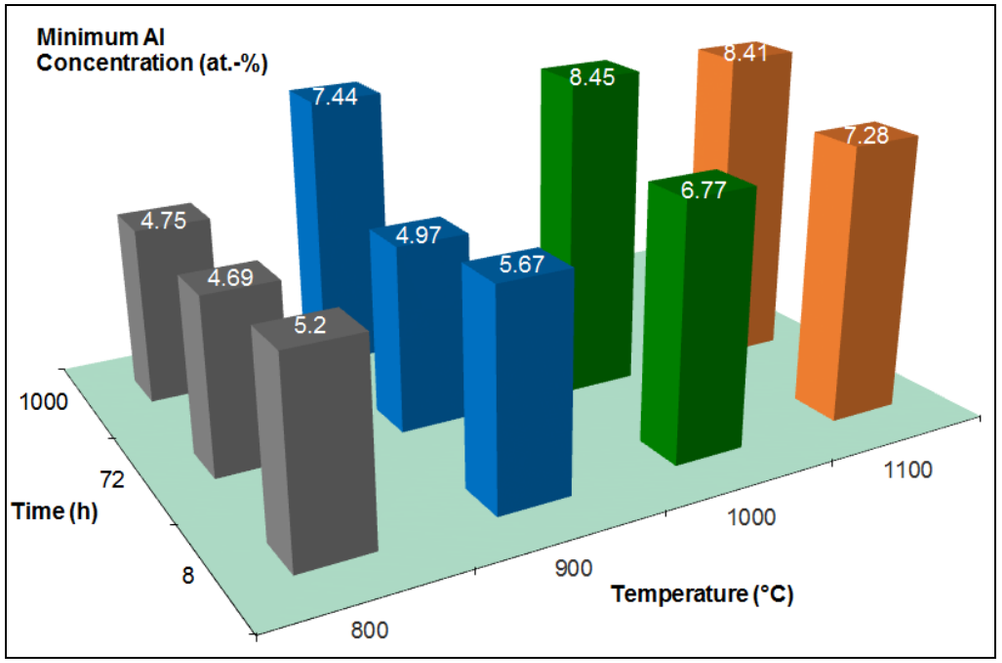

Figure 74: Minimum Al concentrations (At.-%) beneath the oxide layer of Haynes 214 after isothermal oxidation in Ar-20%O_2 at 800-1100°C for up to 1000 h as measured by GD-OES

6.2.3 Discussion of the Oxidation Behavior in Ar-20%O_2

6.2.3.1 Time and Temperature Dependence of the Oxide Scale Morphology

Generally, the oxidation tests for different times at 800-1100°C showed that the oxide scale formation of Haynes 214 is affected by oxidation time and temperature. Some specimens showed internal precipitation of Al_2O_3, whereas others exhibited a continuous protective Al_2O_3 layer.

The main parts of the specimens oxidized at 800°C for 8 h and 72 h were covered by a continuous Al_2O_3 scale and only a few locations of internal alumina precipitates were observed. This is in agreement with the observations of Pint et al [115], who found Haynes 214 to be covered by external Al_2O_3 after 100 h oxidation at this temperature in air and air with 10%H_2O (see Table 11). Extending the oxidation time to 1000 h, however, resulted in the present work in significant propagation of the locations of internal alumina formation. This results in a volume increase and consequently matrix material is locally extruded outwards forming protrusions in the external Cr-rich oxide scales (Figure 64). Despite of the formation of this Cr-rich oxide, the Cr concentration beneath the scale does not exhibit a steep concentration profile in the subscale regions (Figure 65). A small decrease in chromium concentration, analyzed by GD-OES, in the IOZ is only related to the formation of Al_2O_3 precipitates, which decrease the total amount of bulk material related to the overall volume in this region (see also EDX point analysis, Figure 71). This finding is contradictory to numerous findings for other NiCr base alloys [82, 84], which showed a significant chromium depletion. However, for the NiCrAl base alloy 602 CA a behavior similar to that seen here for Haynes 214, oxidized at 800°C for 1000 h, was found [84]. It was illustrated that the flat subscale chromium profiles are related to the thermodynamic interaction of aluminum and chromium in the nickel matrix. The subscale alumina precipitation creates aluminum depletion in a zone deeper into the alloy (see Figure 65). Due to the thermodynamic interaction of aluminum and chromium in the γ-Ni matrix, namely a lower aluminum concentration results in a lower chromium activity [34, 84], this provides an chromium activity gradient and thus an additional driving force for chromium to diffuse from the bulk alloy towards the surface [84]. In case of the present studies on Haynes 214, oxidized at 800°C for 1000 h, the enhanced chromium diffusion towards the metallic protrusions indicates that the protrusions are not separated from the bulk alloy by Al_2O_3. Furthermore, the enhanced chromium diffusion seems to hinder the formation of NiO, as the SEM/EDX (Figure 64) and GD-OES (Figure 65) analysis revealed no significant amounts of this oxide on the surface.

An oxide scale morphology, similar to that of the specimen exposed at 800°C for 1000 h, was found after 8 h oxidation at 900°C (Figure 66). However, the 900°C specimen revealed already after 8 h formation of a dense Al_2O_3 layer near the interface with the alloy which seems to almost completely separate the external metallic protrusions from the bulk alloy and thus prevents the chromium diffusion towards the metallic protrusions. Consequently, after 72 h oxidation at 900°C some of the protrusions are oxidized completely resulting in the formation of NiO, beside Cr-rich oxide (Figure 66). As a result of NiO formation the oxidation rate of the material increases and reaches a local maximum at approximately 20 h (Figure 60), as NiO exhibits a higher oxidation rate than Cr_2O_3 and Al_2O_3 (Figure 13). Figure 62 shows that there still locations with internal Al_2O_3 nodules perpendicular to the surface exist exhibiting a higher amount of non-oxidized metal protrusions and consequently a lower amount of NiO is present compared to the locations where an inner Al_2O_3 layer separates metallic protrusions from the bulk alloy. This illustrates that the transition from internal Al_2O_3 precipitation to an Al_2O_3 layer separating external scale and bulk alloy is a continuous process. Moreover, the laterally growing Al_2O_3 has partially formed in two depths beneath the external scale (Figure 62, Figure 66) and it is difficult to determine whether the upper part is an initially continuous scale or not. However, SEM analysis of the specimen oxidized for 1000 h at 900°C indicates that the inner Al_2O_3 layer separated successfully the external scale from the bulk alloy, whereas some parts of the former upper Al_2O_3 layer become embedded in the oxide scale (Figure 66). The external oxide contains hardly any metal protrusions and significant amounts of NiO are randomly distributed in the Cr-rich oxide. This morphology is a result of the complete oxidation of the metal protrusions, forming first Cr-rich oxide and, after separation from the bulk material by the inner alumina, subsequently NiO. The low weight gain of the specimen oxidized at 900°C (Figure 61) between 300 h and 1000 h indicates that, from approximately 300 h on the metallic protrusions are oxidized completely and the oxide growth is solely governed by the growth of a slow-growing continuous Al_2O_3 layer at the inner scale regions. The theory of different oxidation steps in NiCrAl alloys is described in section 4.3.1.

Similar to the specimen after 1000 h at 900°C the specimen after 8 h at 1000°C showed a continuous Al_2O_3 layer resulting in an external scale of Cr-rich oxide and NiO without any metallic protrusions. However, the metal matrix contains some internal Al_2O_3 precipitates beneath the continuous layer. This indicates the presence of an initial stage of internal Al_2O_3 formation and external Cr-rich oxide formation, similar to the results of the test at 800°C for 1000 h (Figure 64). Subsequently, the transition from internal Al_2O_3 to a continuous Al_2O_3 layer, as found after 8 h oxidation at 1000°C (Figure 68), results in an increased oxidation rate after approximately 3 h (Figure 60) due to NiO formation. This effect was already described for the oxidation test at 900°C for 72 h. After 72 h exposure at 1000°C the oxidation process is qualitatively similar to the 1000 h test at 900°C, governed by slow-growing Al_2O_3, as the

oxidation rate (Figure 60) is in the typical range for α-Al_2O_3 formation [25]. This correlates with results from the literature [36, 115, 116, 117], which showed external Al_2O_3 and the Ni-rich oxide formed during the transient stage. The results of the present study revealed the presence of NiO on top of a single phase Ni/Cr/Al mixed oxide, which might correlate with the $Ni(Cr,Al)_2O_4$ spinel reported in reference [115]. Compared to the results after 8 h, the incorporated NiO, the Cr-rich oxide and some external Al_2O_3 are probably replaced by this spinel phase.

After 8 h oxidation at 1100°C the external scale consists of Cr-rich oxide and NiO on top of a continuous Al_2O_3 layer. In contrast to 1000°C, internal Al_2O_3 precipitates were not observed after 8 h oxidation. This indicates a faster transition from internal Al_2O_3 to the formation of a continuous Al_2O_3 layer at the higher temperature. In a similar manner as for the 1000°C experiments, after 72 h exposure at 1100°C Cr-rich oxide, NiO and some Al_2O_3 are replaced by a single phase Ni/Cr/Al mixed oxide, which is probably $Ni(Cr,Al)_2O_4$.

Source	Test type	Sample type	Temperature (°C)	Gas	Time (h)	Type of oxide scale
Young [36]	Isothermal	0.13 mm thick foils	1100 - 1200	Air	Up to 1000	$Ni(Al,Cr)_2O_4$ and ext. Al_2O_3
Pint [116]	Discontinuous	Foils with different thicknesses	1000 - 1050	Air	Up to 6000	Ext. Al_2O_3 and Ni-rich scale
Bauccio [117]	Burner rig	-	980 - 1205	Air	500, 1000	Al_2O_3 scale
Sporer [118]	Isothermal	Honeycomb foils	1100 - 1200	Air Synth. flue gas	Up to 2600	Ext. Al_2O_3 and $NiCr_2O_4$ spinel
Pint [115]	Isothermal	100 µm thick foils, as-rolled surface finish	800 – 900	Air Air+10%H_2O	100	Thin Al_2O_3 scale
			1000 - 1100			$Ni(Cr,Al)_2O_4$ and Al_2O_3
Lai [119]	Discontinuous	0.127 mm foils, pre-oxidized (1h, 1050°C)	Up to 1250	Air	300	No breakaway (Protective Al_2O_3 scale)

Table 11: Scale formation on Haynes 214 as reported in literature [36, 115, 116, 117, 118, 119]

The results thus show that at all four investigated temperatures the time dependent oxidation processes of Haynes 214 in Ar-20%O_2 seem to be similar, just accelerating with increasing exposure temperature. Therefore, based on the described effects the following mechanism is proposed:

1. Al_2O_3 forms internally and produces metal protrusions. Cr-rich oxide is formed on top of the protrusions

2. Internal Al_2O_3 transforms into continuous layer and separates metal protrusions from the bulk alloy. Protrusions deplete in Cr due to ongoing Cr-oxide formation and after a certain extent of depletion Ni starts to oxidize
3. The metal protrusions are oxidized completely resulting in an external scale consisting of Cr-rich oxide and NiO
4. Cr-rich oxide and NiO react to form a single phase Ni/Cr/Al spinel type mixed oxide (probably $Ni(Cr,Al)_2O_4$)

After 72 h oxidation at 1100°C the specimen shows step 4 of the proposed mechanism, whereas the 1000°C and 900°C specimens are exhibiting steps 3 and 2, respectively. After 1000 h exposure at 800°C the oxide scale of Haynes 214 shows the morphology of step 1, whereby it is unclear whether the material will undergo the other steps at this temperature during longer time of exposure or not. The formation of external Al_2O_3 after 8 h and 72 h cannot be explained by the proposed mechanism. In addition, time and temperature dependent precipitation of γ′ (chapter 6.2.1) might cause deviations from the proposed mechanism.

6.2.3.2 Effect of γ′-Precipitation on Oxidation Behavior

The formation of γ′ affects the Al concentration in the γ-matrix and is therefore expected indirectly to change the oxidation behavior. As rapid cooling during the manufacturing process is done to minimize precipitation, the amount of γ′-precipitates in the as-received condition is extremely small. Quenching prevents the phase formation which would be expected according to thermodynamic equilibrium. The phase equilibria of Haynes 214 as function of temperature can be calculated using ThermoCalc© (Figure 75). The reliability of the Thermocalc calculations obviously depends on the accuracy of the thermodynamic data in the used database TTNI7 [120]. The calculation for Haynes 214 shows up to approximately 750°C the presence of <2 at.-% of Cr-rich $M_{23}C_6$ precipitates, which are replaced at higher temperatures by M_7C_3.

At temperatures below approx. 935°C the alloy is expected to contain γ′-precipitates; the amount increases with decreasing temperature. This agrees with observations from the vacuum exposures at 1000°C (Figure 58), which indicated no γ′-formation at this temperature. The calculations revealed that at approximately 620°C the mole fractions of γ′ and γ are equal, with about 49 at.-% each (2 at.-% $M_{23}C_6$). In addition, a changing amount of γ′ also changes the composition of the γ-matrix as a function of temperature (Figure 76). As the aluminum concentration in γ′-(Ni_3Al) (approximately 25 at.-%) is significantly higher than that in the bulk material (8.9 at.-%), an increasing amount of γ′ will decrease the aluminum concentration in the γ phase. The compositions of the γ-phase in the investigated temperature range calculated with ThermoCalc© are given in Table 12.

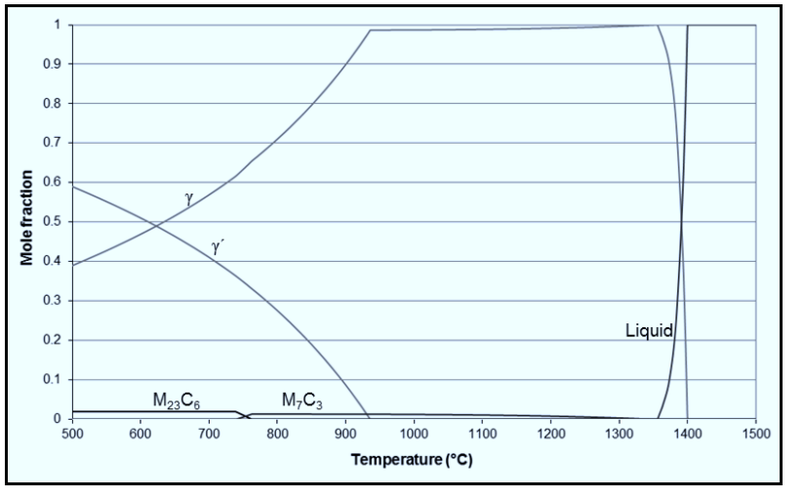

Figure 75: Mole fractions of phases of Haynes 214 calculated with Thermocalc© (Database: TTNI7)

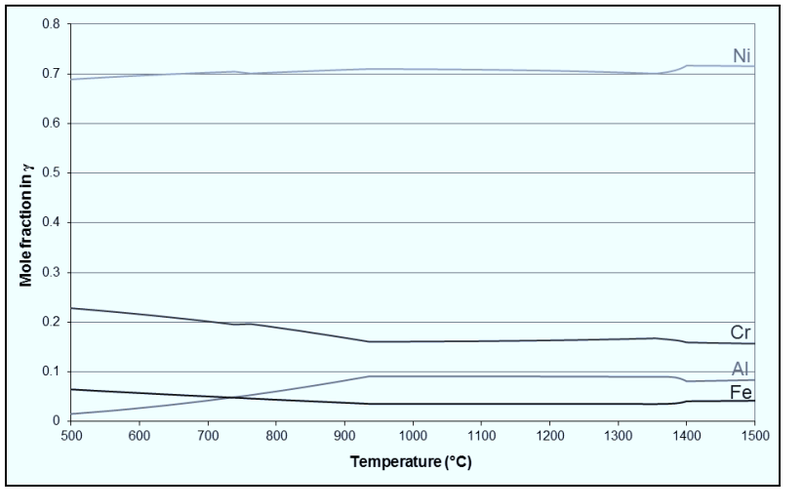

Figure 76: Composition of the γ-phase in chemical equilibrium of Haynes 214 calculated with Thermocalc© (Database: TTNI7). At around 1355°C the solidus temperature and at 1400°C the liquidus temperature is reached

	Chemical Composition (at.-%)				
Temperature	Ni	Cr	Al	Fe	Mn
800°C	70.3	19.0	6.1	4.4	0.2
900°C	70.8	16.9	8.3	3.8	0.2
1000, 1100°C	71.0	16.1	9.1	3.6	0.2

Table 12: Chemical composition of the γ-phase in Haynes 214 calculated with ThermoCalc© (Database: TTNI7)

During high temperature exposure the alloy microstructure may change due to γ´-formation or -dissolution always adjusting to the chemical equilibrium (Figure 75). The formation of a precipitate free zone (PFZ) below the oxide layer (see chapter 4.3) has as consequence that the phase in contact to the oxide is solely γ. This phenomenon is schematically described by Young and Gleeson [121]. Consequently, as the γ composition is dependent on the amount of γ´ (Figure 76), the latter will affect also the oxidation behavior of the material. Important to note is that especially the aluminum concentration in γ in chemical equilibrium changes from 6.1 at.-% at 800°C to 9.1 at.-% at 1000°C and 1100°C.

6.2.3.3 Effect of Aging Treatments on Oxidation Behavior

To investigate possible effects of γ´-precipitation on the oxidation behavior of Haynes 214, oxidation tests on aged specimens were performed to compare the oxide scale morphologies with those of the tests on as-received (solution annealed) specimens (see chapter 6.2.1, 6.2.2). The aging process consisted of 100 h exposure at 800°C in vacuum. This will produce a volume fraction of γ´ which is close to the thermodynamic equilibrium value at this temperature (see chapter 3). The samples were ground to p1200 standard surface finish to achieve the same surface condition as for the oxidation tests on solution annealed material.

6.2.3.3.1 Oxidation Kinetics of Aged Haynes 214

Figure 77 shows the area specific weight gains of the aged specimens of Haynes 214 during isothermal exposure in Ar-20%O_2 at 800-1100°C for 72 h (see section 5.3). The dashed lines illustrate the weight gains of the as-received specimens of Haynes 214 during oxidation under the same experimental conditions shown in Figure 59.

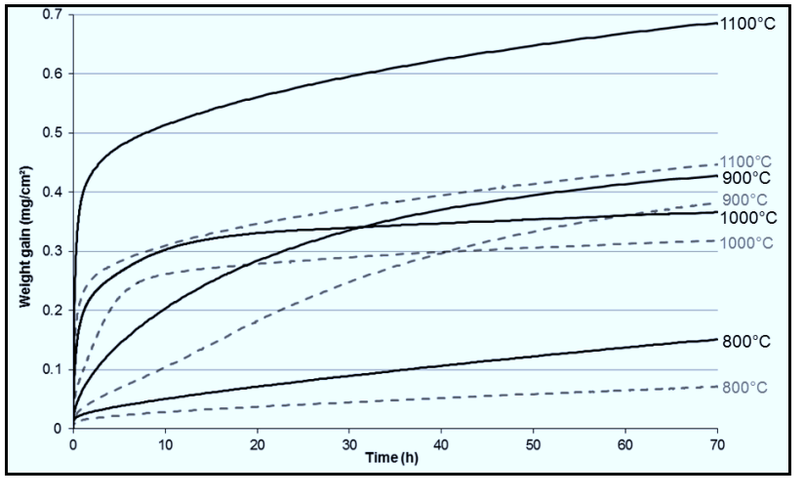

Figure 77: Area specific weight gain during isothermal oxidation of aged Haynes 214 in Ar-20%O_2 at different temperatures (dashed lines indicate, for comparison, the weight changes of the as-received samples, see Figure 59)

For every test temperature the aged material exhibits a higher weight gain than the solution annealed material. The instantaneous apparent parabolic oxidation rate constants for the two specimen types at 800°C show similar time dependence but differ by approximately a factor of 8 (Figure 78). In contrast to the solution annealed specimen the aged specimen exposed at 900°C shows a different time dependence of k_W' but, after the initial oxidation stage, no increase in oxidation rate is found (Figure 78). However, the maximum oxidation rate is similar to that of the solution annealed specimen. During 1000°C exposure the oxidation rate between 2 h and 9 h is smaller for the aged specimen, whereas in the initial stage (t < 2 h) it is higher (Figure 79). The latter is hard to see from Figure 79, but is apparent from the weight gain plots (Figure 77). After approximately 20 h exposure the oxidation rates at 1000°C are similar for both sample types.

After 72 h exposure at 1100°C the aged material exhibits a weight gain which is approximately 50 % higher than that of the solution annealed material. However, this difference is only related to the early stages of oxidation because the oxidation rates after approximately 3-5 h are very similar for both materials (Figure 79). As can be seen from the thermogravimetric analyses (Figure 78) the oxidation rates at 1000°C and 1100°C in the initial stage are higher for the aged compared to the as-received specimens.

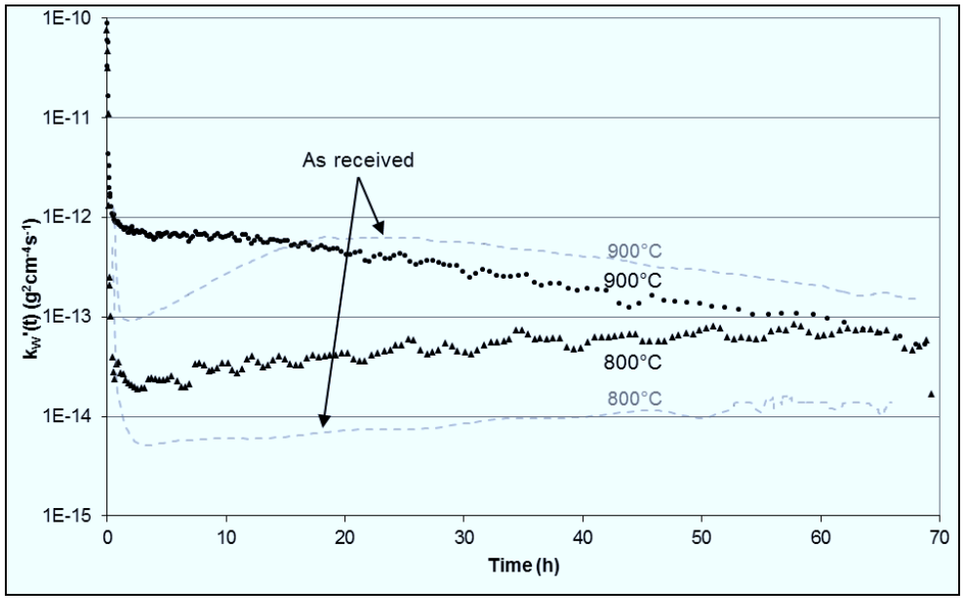

Figure 78: Time dependence of the instantaneous apparent oxidation rate k_W' of aged Haynes 214 during isothermal oxidation at 800-900°C in Ar-20%O_2 for 72 h (dashed lines indicate, for comparison, the oxidation rates of the samples in the as-received condition)

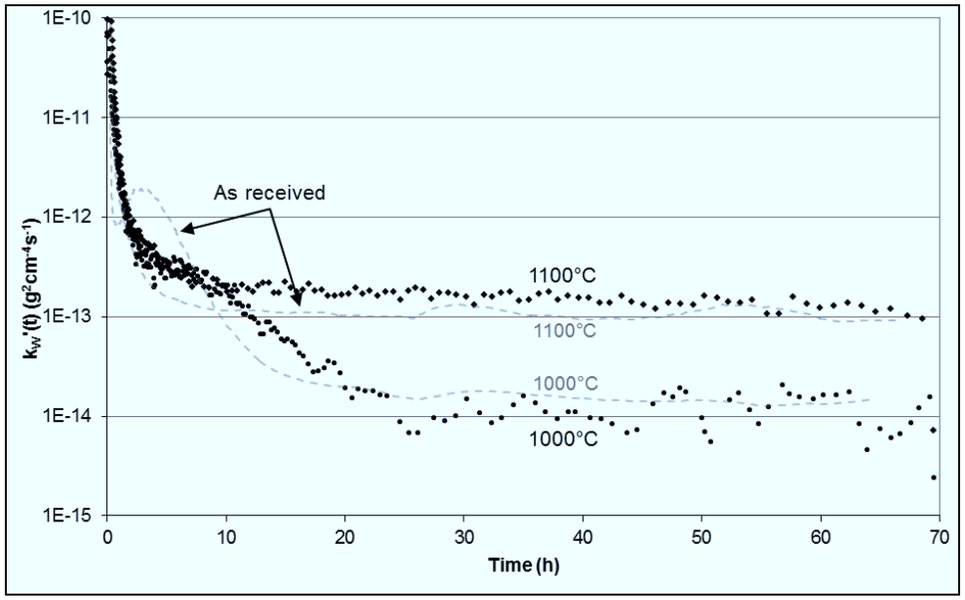

Figure 79: Time dependence of the instantaneous apparent oxidation rate kw' of aged Haynes 214 during isothermal oxidation at 1000-1100°C in Ar-20%O_2 for 72 h (dashed lines indicate, for comparison, the oxidation rates of the samples in the as-received condition)

6.2.3.3.2 Oxide Scale Morphology

Figure 80 shows BSE images of cross sections of solution annealed (as-received) and aged Haynes 214, after oxidation in Ar-20%O_2 at 800°C and 900°C for 72 h, respectively. After 72 h of exposure at 800°C the as-received material exhibits an external Al_2O_3 scale with small amounts of Ni,Cr-rich oxide. However, the aged material forms internal Al_2O_3 and an external Cr-rich oxide. As a result of the volume increase by internal Al_2O_3 formation bulk metal protrusions are located in the external Cr-rich oxide. In contrast to the as-received material, no significant amounts of nickel containing oxide were found. As a result of the increased formation of Cr-rich oxide on the aged sample, the weight gain after 72 h of oxidation is approximately twice as high as for the as-received sample (Figure 77).

In contrast to the 800°C experiments both the as-received and aged specimen, showed after oxidation at 900°C similar oxide scale morphologies (Figure 80). The coarsening rate of γ´ is increasing with increasing temperature (see chapter 3), whereas the equilibrium volume fraction is lower at 900°C (9 at.-%) than at 800°C (29 at.-%), as shown in chapter 5.2. Consequently, the microstructural difference between as-received and aged material is smaller after 72 h exposure at 900°C than at 800°C. More precisely, according to the fact that it lasts approximately 100 h at 800°C to approach thermodynamic equilibrium (see chapter 3), it is

assumed that the microstructure of the as-received material after 72 h oxidation at 900°C shows no significant difference from the aged material.

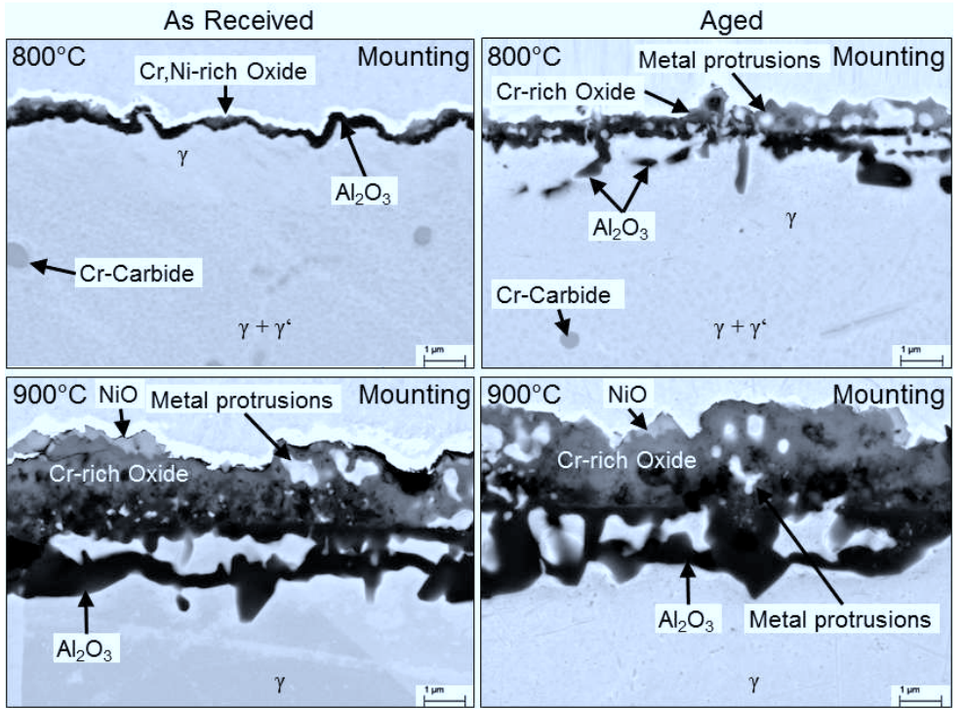

Figure 80: BSE images of cross sections of as-received (left) and aged (right) Haynes 214 after isothermal oxidation at 800°C and 900°C in Ar-20%O_2 for 72 h

Figure 81 compares the BSE images of the cross sections of the solution annealed and aged material oxidized at 1000°C and 1100°C for 72 h respectively. In contrast to 800°C and 900°C, at these temperatures γ´ is not stable according the Thermocalc© calculations (Figure 75). Consequently, the equilibrium Al content in γ is virtually identical to the total bulk Al concentration (9.0 at.-%). Initially present γ´ in the aged specimen is expected to dissolve during the oxidation test.

After 1000°C and 1100°C exposure, respectively, the oxide scale morphologies of the as-received and aged material are similar. The scales of the specimens oxidized at 1000°C consist of single phase Ni/Cr/Al mixed oxide (probably $Ni(Cr,Al)_2O_4$), NiO and a continuous Al_2O_3 layer beneath. After oxidation at 1100°C no NiO is found and the material is solely covered by the single phase Ni/Cr/Al mixed oxide and a continuous inner Al_2O_3 scale. Even though the scale morphologies of the two sample types are similar after oxidation at 1000°C and 1100°C, the oxidation behavior differs clearly in terms of average total oxide scale thickness. This finding correlates with the thermogravimetric measurements (Figure 77). The

higher weight gain of the aged material at 1000°C and 1100°C is a result of the increased formation of Ni,Cr-containing oxide, which exhibits a higher grow rate than Al_2O_3 [25, 31]. A larger amount of this transient Ni,Cr-containing oxide indicates that the formation of a continuous external Al_2O_3 scale is delayed for the aged compared to the as-received material. This is a result of the lower aluminum concentration in the γ-phase of the aged material in the very early stages of the oxidation test (see chapter 6.2.3.2), i. e. before complete dissolution of the γ´ precipitates occurred.

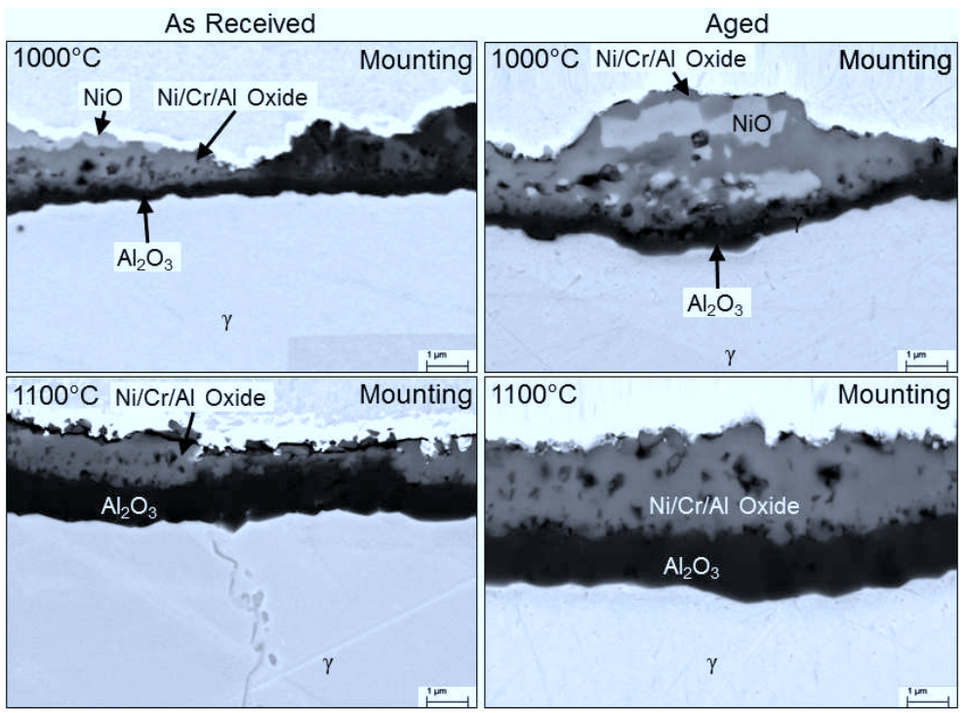

Figure 81: BSE images of cross sections of as-received (left) and aged (right) Haynes 214 after isothermal oxidation at 1000°C and 1100°C in Ar-20%O_2 for 72 h

6.2.3.4 Proposed Oxidation Mechanisms

In chapter 4.3.1 three different mechanisms, describing the oxidation stages of NiCrAl alloys, are shown. Figure 14 shows that all three mechanisms lead to a three-layered oxide structure, as shown in Figure 82. This scale morphology and composition is similar to the proposed oxidation mechanism for Haynes 214, shown in chapter 6.2.3.1. However, in contrast to Figure 82 the results from the present study on Haynes 214 did not reveal a continuous NiO layer above a Cr_2O_3 layer. The material exhibited NiO particles inside the Cr_2O_3 layer, as a result of the oxidation of metal protrusions in the latter (see 6.2.3.1). Furthermore, the final step proposed for the oxidation of Haynes 214 is the formation of a single phase Ni/Cr/Al mixed oxide, which is probably $Ni(Cr,Al)_2O_4$ spinel (see 6.2.3.1). Spinel formation was also

proposed in literature as stated in Figure 82 but in the present findings on Haynes 214 the single phase Ni/Cr/Al mixed oxide was found without any Cr_2O_3 beneath (see 6.2.3.1).

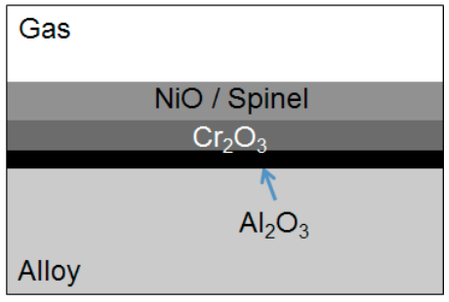

Figure 82: Schematic three-layered oxide structure of NiCrAl alloys formed according to the three mechanisms illustrated in Figure 14 [33, 51, 52]

Beside these differences, the mechanism proposed in the present study for the oxidation of Haynes 214 (6.2.3.1) correlates best with the mechanism from Hu et al [52]. Both approaches suggest the initial formation of internal Al_2O_3, external Cr-Oxide and Ni-rich metal protrusions in between. In the second step of both mentioned mechanisms the internal Al_2O_3 particles form a continuous layer and as a result NiO is formed. The final step from Hu et al [52], however, differs from the mechanism proposed in the present study, as here no formation of a NiO layer (Figure 82) was observed.

All three mechanisms proposed in literature for oxidation of NiCrAl model alloys [33, 51, 52] are based on experiments at or above 1000°C (Giggins et al: 1000 – 1200°C, Nijdam et al and Hu et al: 1100°C). Consequently, the oxidation process of a multi-element material, such as Haynes 214, below 1000°C might not be correct described by the proposed mechanisms. For the mechanism proposed in the present study this is the case for exposures of Haynes 214 below 900°C, as stated in chapter 6.2.3.1. The oxidation tests of as-received specimens of Haynes 214 revealed after 72 h oxidation at 800°C external Al_2O_3, whereas after 1000 h internal Al_2O_3 and external Cr-rich oxide formation were observed, which cannot be described by the proposed mechanism. However, this behavior at 800°C correlates with the first two steps of the mechanism proposed by Nijdam et al [51] (see Figure 14). But as they suggested these steps are based on tests at 1100°C and the present results revealed a different behavior at this temperature, it is not clear if describing the oxidation process at 800°C by this mechanism is correct.

Another way to describe the oxidation behavior of Haynes 214 at 800°C differing from that at higher temperatures might be the correlation of external Al_2O_3 formation with the effect of surface cold work, explained in 6.1.3.3 for the oxidation of alloy 602 CA. It was found that external Al_2O_3 scale formation is promoted by introducing cold work in the specimen surface

prior to exposure by the grinding process (p1200). To proof if this theory holds also for the oxidation of Haynes 214 at 800°C, two Haynes 214 specimens were prepared for 24 h TGA tests in Ar-20%O_2 at 800°C. One specimen was p1200 grit ground, as in the previous experiments, the other was prepared to a mirror like surface using diamond paste. Figure 83 shows that the weight gain of the polished specimen is larger than that of the ground specimen after 24 h oxidation at 800°C. However, the difference between the two specimens with different surface treatment is smaller compared to the corresponding experiments with Alloy 602 CA (see Figure 52).

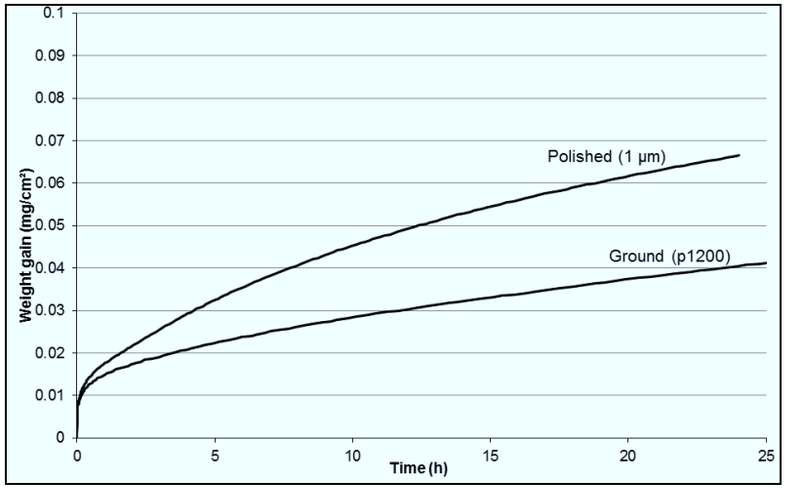

Figure 83: Area specific weight gain during isothermal oxidation of Haynes 214 in Ar-20%O_2 at 800°C showing effect of surface treatment on oxidation kinetics

Figure 84 compares metallographic cross sections of the diamond polished specimen and the p1200 grit ground specimen after 24 h exposure. The external formation of Al_2O_3 is substantially more pronounced for the ground than for the polished specimen. The latter exhibited mainly internal Al_2O_3 precipitates, metal protrusions and external Cr-rich oxide. This is similar to step 2 in the mechanism proposed in chapter 6.2.3.1 for oxidation at temperatures above 800°C.

In contrast to the results of the polished specimen of Alloy 602 CA (Figure 53, b), the polished specimen of Haynes 214 exhibited a few locations where external Al_2O_3 occurred. This correlates with the smaller weight gain of this specimen compared to that of Alloy 602 CA (Figure 52) and might be the result of the higher Al concentration in Haynes 214 (4.46 wt.-%) compared to Alloy 602 CA (2.43 wt.-%). However, the results of the oxidation tests of the polished and ground specimens of Haynes 214 show that the surface cold work promotes also for alloy 214 the formation of external Al_2O_3 at 800°C. Internal oxidation of Al after 72 h oxidation at 900°C (Figure 66) and after 8 h at 1000°C (Figure 68) show that the beneficial

effect of cold work introduced by grinding rapidly vanishes upon heating the specimen to temperatures of 900°C and above in a similar manner as described for Alloy 602 CA (6.1.3.3).

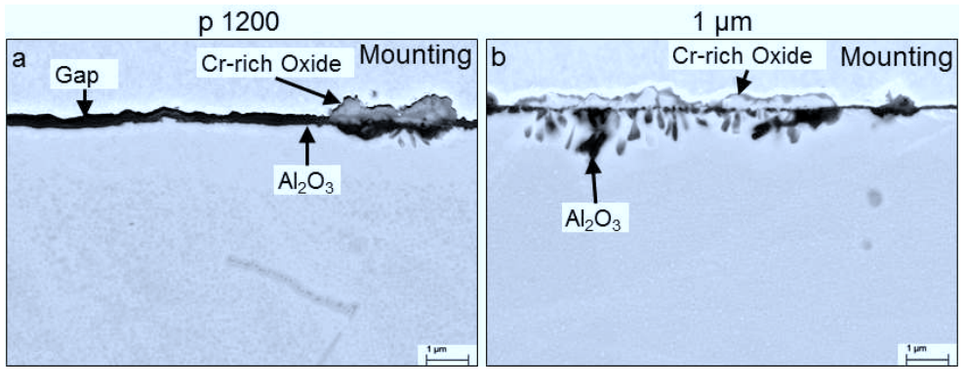

Figure 84: Metallographic cross section (BSE image) of Haynes 214 after isothermal oxidation at 800°C in Ar-20%O_2 for 24 h. a) specimen ground (b) diamond polished prior to exposure

As stated in chapter 6.2.2.2, extending at 800°C the oxidation time of Haynes 214 from 72 h to 1000 h resulted in expansion of the locations of internal Al_2O_3 formation. Thus, obviously the external Al_2O_3 formed after 72 h exposure as a result of the beneficial effect of surface cold work (see above) cannot be maintained for 1000 h at 800°C on Haynes 214. Additional experiments on alloy 602 CA, however, revealed a continuous Al_2O_3 scale after 1000 h oxidation at 800°C in Ar-20%O_2 (Figure 85). This is confusing, as the Al content of Haynes 214 (4.46 wt.-%) is higher compared to that of alloy 602 CA (2.43 wt.-%) and therefore formation and maintenance of an external Al_2O_3 scale is expected to be promoted in comparison to this material.

As shown in chapter 6.2.1 and illustrated in Figure 85 the microstructure of Haynes 214 contains γ´-precipitates in chemical equilibrium at 800°C. This results in an Al concentration in the γ-phase which is lower than the bulk concentration and amounts to 6.1 at.-% (2.9 wt.-%) at 800°C (chapter 6.2.3.2). As stated in chapter 6.2.3.2, the phase in contact with the alloy / oxide interface is solely γ, due to the formation of a subsurface PFZ. Thus, it is proposed that the aluminum content responsible for the maintenance of an existing external Al_2O_3 scale, whose formation was promoted by surface cold work, is the aluminum concentration in the γ-phase and not the bulk concentration (see chapter 6.2.3.2 and ref. [121]). Consequently, as the amount of γ´ in the γ-microstructure increases with increasing exposure time and approaches the chemical equilibrium at 800°C after approximately 100 h (stated in chapter 6.2.1) the tendency of external Al_2O_3 formation decreases at 800°C up to an exposure time of 100 h.

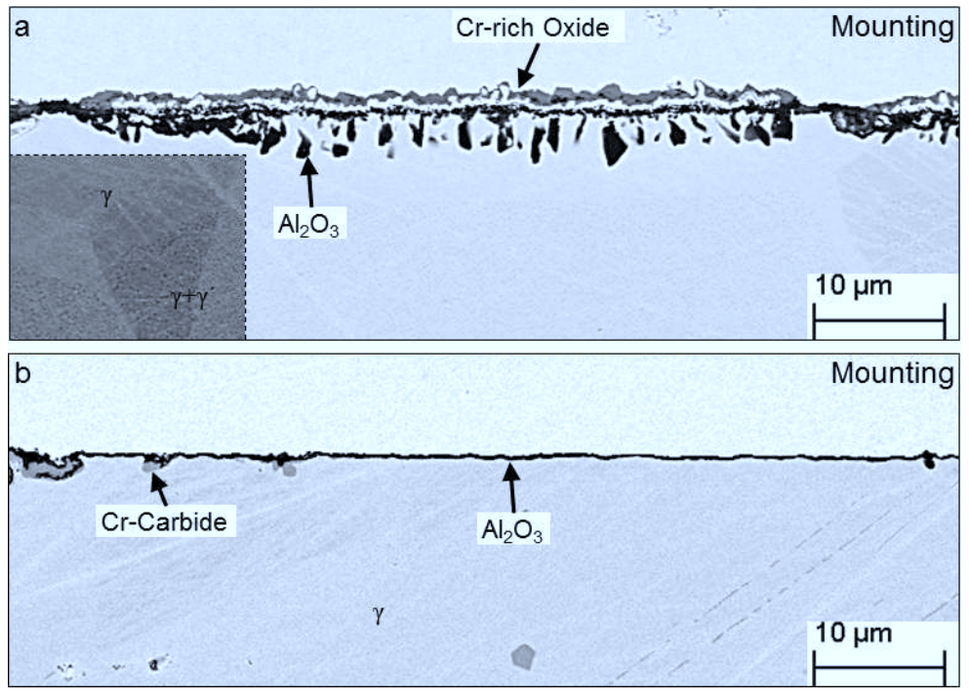

Figure 85: Metallographic cross sections (BSE images) of ground specimens of Haynes 214 (a) and Alloy 602 CA (b) after oxidation in Ar-20%O_2 at 800°C for 1000 h. Lower left part of figure (a) is shown in increased contrast to illustrate γ´ precipitates

This decreased tendency of external Al_2O_3 formation by γ´-precipitation in Haynes 214 was observed in oxidation tests on aged specimens of Haynes 214, described in chapter 6.2.3.3. Compared to the experiments on as-received material (chapter 6.2.2.2), the starting Al concentration in the γ-phase of the aged specimens was approximately 6.1 at.-% (2.9 wt.-%), as they were aged at 800°C. As a result, at all four test temperatures the aged specimens exhibited after 72 h exposure a higher weight gain than the specimens in the as-received condition (chapter 6.2.3.3). After oxidation at 800°C the amount of internal Al_2O_3 formation was significantly higher for the aged specimen compared to the as-received specimen of Haynes 214. The aged specimen revealed after 72 h of oxidation at 800°C a similar oxide scale morphology as the as-received specimen exposed for 1000 h (6.2.2.2). This indicates that the increased amount of internal Al_2O_3 precipitates formed after 1000 h oxidation compared to 72 h exposure is a result of the formation of γ´-precipitates. In contrast to aged Haynes 214, Alloy 602 CA in as-received condition exhibited after 1000 h oxidation at 800°C a continuous Al_2O_3 scale, although the aluminum content in the γ-phase of aged Haynes 214 (2.9 wt.-%) is still higher than in Alloy 602 CA (2.43 wt.-%), which only consists of γ and Cr-carbides (chapter 6.1). This shows that, despite the formation of γ´, also the concentration of other alloying constituents (especially Cr), beside Al, obviously affects the formation of an external Al_2O_3 scale. Chapter 7 will later focus on this effect.

Beside the difference in the amount of internal Al_2O_3 formation between as-received and aged material of alloy 214 at 800°C, also differences in oxide scale thickness at higher temperatures show the effect of γ´-precipitation. At 1000°C and 1100°C respectively the phases present in the oxide scales of the as-received and aged specimens are very similar. However, the aged specimens revealed a thicker layer of Cr- and Ni-containing transient oxides as the formation of a continuous Al_2O_3 layer is delayed (see chapter 6.2.3.3). This is a result of the lower aluminum content in the γ-matrix in the very early stages of oxidation. As γ´ is not stable at 1000-1100°C and will thus dissolve during ongoing oxidation (see chapter 6.2.3.3) the aluminum concentration in the γ-phase increases.

The following mechanism, shown in Figure 86, is proposed to describe the oxidation behavior of Haynes 214 at 800-1100°C, based on:

- The oxidation steps proposed in chapter 6.2.3.1 for the oxidation behavior of Haynes 214 at 900-1100°C
- The mechanism by Hu et al [52] determined by oxidation tests on a Ni-Cr-Al model alloy at 1100°C
- The effect of surface cold work promoting external Al_2O_3 formation at 800°C
- The effect of γ´-precipitation decreasing the tendency to external Al_2O_3 formation

At 800°C (left part of Figure 86) the cold-work introduced by specimen grinding promotes external alumina formation (step 1), due to a high density of grain boundaries in the surface near region. Thereby the difference between grain and grain boundary diffusion is far more pronounced for substitutionally dissolved elements, such as e. g. Al in γ-Ni, than for interstitially dissolved elements, like oxygen [102]. After a certain time γ´-precipitation decreases the Al concentration in γ (see section 6.2.3.3) and increases the tendency to internal Al_2O_3 formation in combination with extruding metal protrusions and Cr-rich oxide formation (step 2). At 900°C and above (right part of Figure 86) the beneficial effect of specimen grinding vanishes rapidly due to faster recrystallization. Consequently, initially internal Al_2O_3 formation is more promoted compared to 800°C (step 1), although the amount of γ´-precipitates is significantly lower in this temperature range (900-1100°C). After a certain time impingements of internal Al_2O_3 rods at random sites of the oxidation front (IOZ / PFZ interface) lead to the formation of Al_2O_3 film sections and lateral Al diffusion from this impingement sites to neighboring precipitates isolates the internal oxidation zone (IOZ) from the bulk alloy [101] (step 2). A continuous Al_2O_3 layer is formed which suppresses outward Cr diffusion and consequently NiO starts to form in random locations until all metal protrusions are oxidized (step 3). After longer times a single-phase Ni/Cr/Al mixed oxide is formed (step 4).

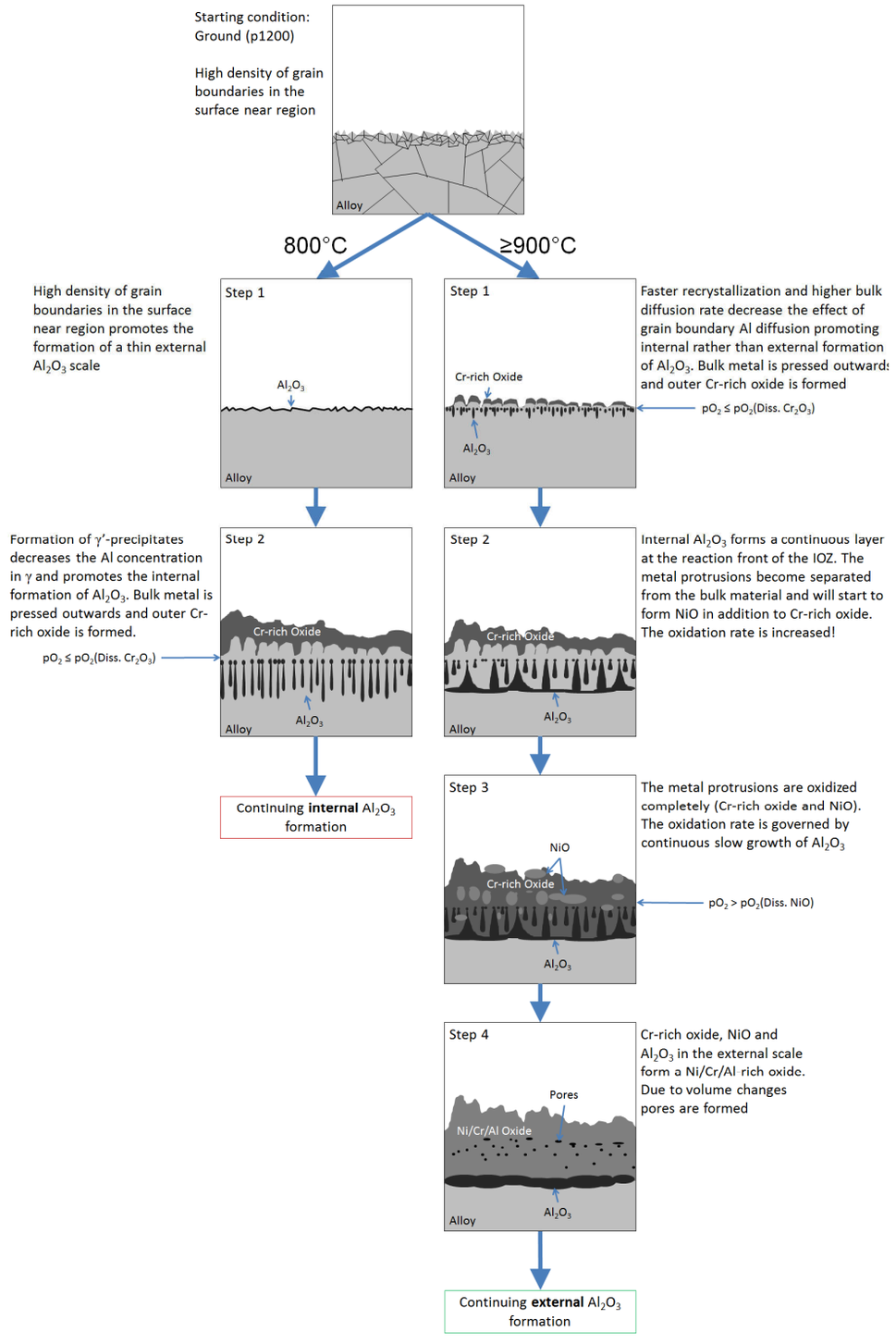

Figure 86: Proposed oxidation mechanism of Haynes 214 based on the presented results

6.2.4 Behavior of Haynes 214 in H_2O-Containing Gases Compared with Ar-20%O_2

6.2.4.1 Behavior in Ar-7%H_2O

Figure 87 shows the area specific weight gains of as-received Haynes 214 during isothermal exposure at 800°C, 900°C, 1000°C and 1100°C in Ar-7%H_2O. In addition, the area specific weight gains in Ar-20%O_2 which were already presented before (Figure 59) are shown here again for easier comparison and better readability of the text (Figure 88). After 72 h oxidation at 800°C and 1100°C the weight gain of Haynes 214 is higher in Ar-7%H_2O than in Ar-20%O_2. However, at 900°C and 1000°C the weight gain after the 72 h exposure is higher in Ar-20%O_2 than in Ar-7%H_2O. Especially, the time dependent slopes of the curves substantially differ in the two environments at 900°C and 1000°C. At 800°C the time dependent slopes in the two gases are very similar.

As in Ar-20%O_2, the oxidation kinetics of the material exposed in Ar-7%H_2O at the four test temperatures could not be described using the classical parabolic rate description, shown in equation (17). Therefore Figure 89 shows the instantaneous, apparent parabolic rate constant (k_w') for the exposure in Ar-7%H_2O as function of time, calculated using the procedure described in reference [113, 114] and appendix B. After the initial oxidation stage, virtually constant k_w'-values were found for the tests at 800°C, 1000°C and 1100°C. However, the oxidation rate of the 900°C specimen decreases at $t > 5$ h with increasing exposure time. In Ar-20%O_2 at 900°C a similar decrease was observed at $t > 25$ h (Figure 60), but due to an initial ($t < 25$ h) increase in oxidation rate, the k_w'-values obtained in Ar-20%O_2 are significantly higher than in Ar-7%H_2O at 900°C.

Figure 90 and Figure 91 show BSE images of the cross sections of Haynes 214 after isothermal exposure in Ar-7%H_2O for 72 h. At 800°C the material is partly covered by an external Al_2O_3 scale and exhibits in other locations internal Al_2O_3 precipitates, metal protrusions and external Cr-rich oxide. This oxide scale morphology is similar to that described and discussed in chapter 6.2.2.2 for the oxidation in Ar-20%O2 at 800°C.

After oxidation at 900°C a similar morphology was found, however, compared to 800°C the tendency to formation of an internal Al_2O_3 layer, rather than separated internal precipitates, seems to be more pronounced at 900°C. This type of internal Al_2O_3 layer formation was also observed after 72 h oxidation in Ar-20%O_2 at this temperature (see 6.2.2.2). In contrast to the oxide scale formed in Ar-20%O_2, the amount of NiO formed after 72 h is lower after oxidation in Ar-7%H_2O. This explains why the weight gain after 72 h oxidation in Ar-7%H_2O (Figure 87) is lower than in Ar-20%O_2 (Figure 88).

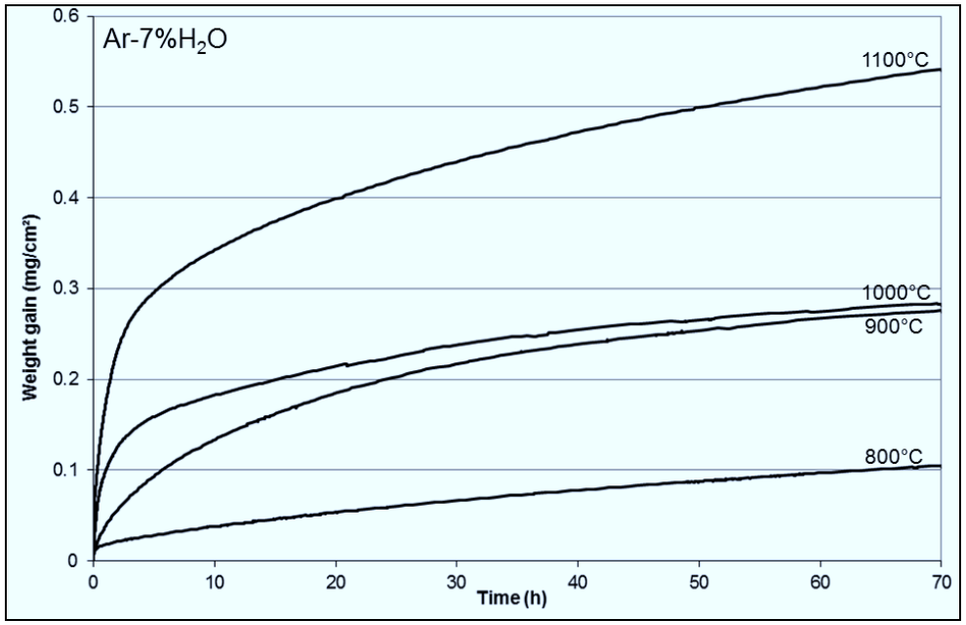

Figure 87: Area specific weight gain during isothermal oxidation of Haynes 214 in Ar-7%H_2O at different temperatures

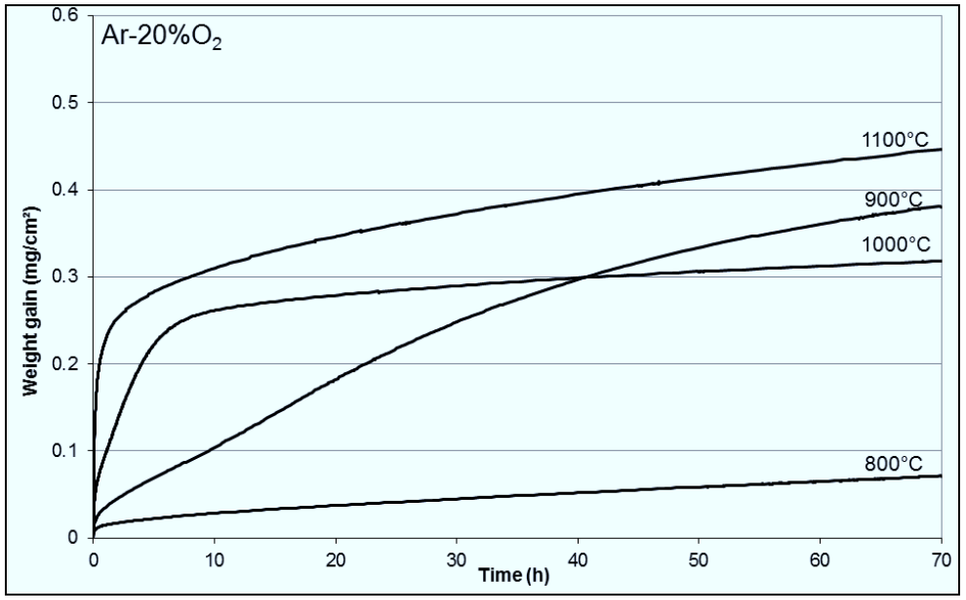

Figure 88: Area specific weight gain during isothermal oxidation of Haynes 214 in Ar-20%O_2 at different temperatures (already shown in Figure 59)

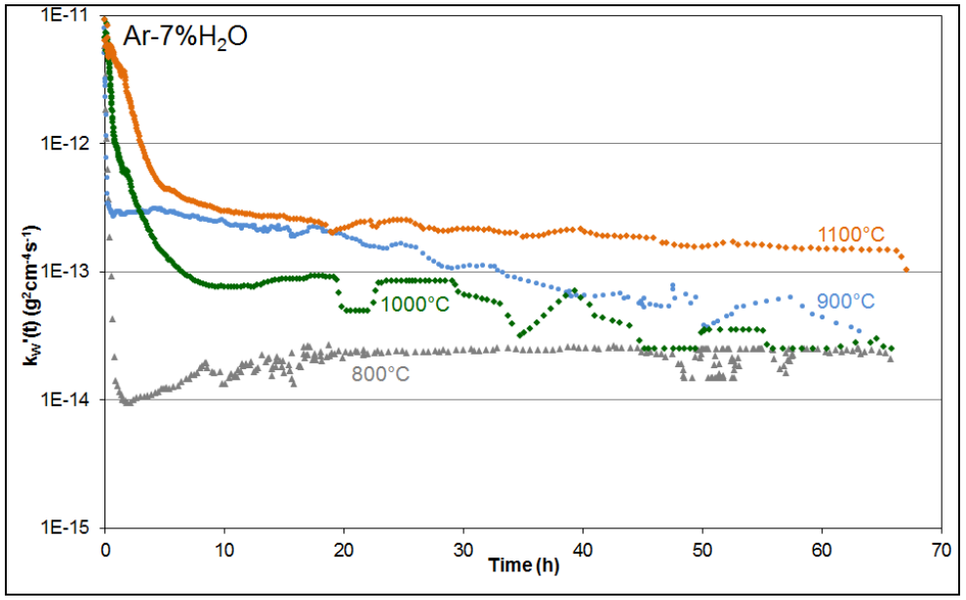

Figure 89: Time dependence of the instantaneous apparent parabolic rate constant kw' of Haynes 214 during isothermal oxidation in Ar-7%H_2O for 72 h

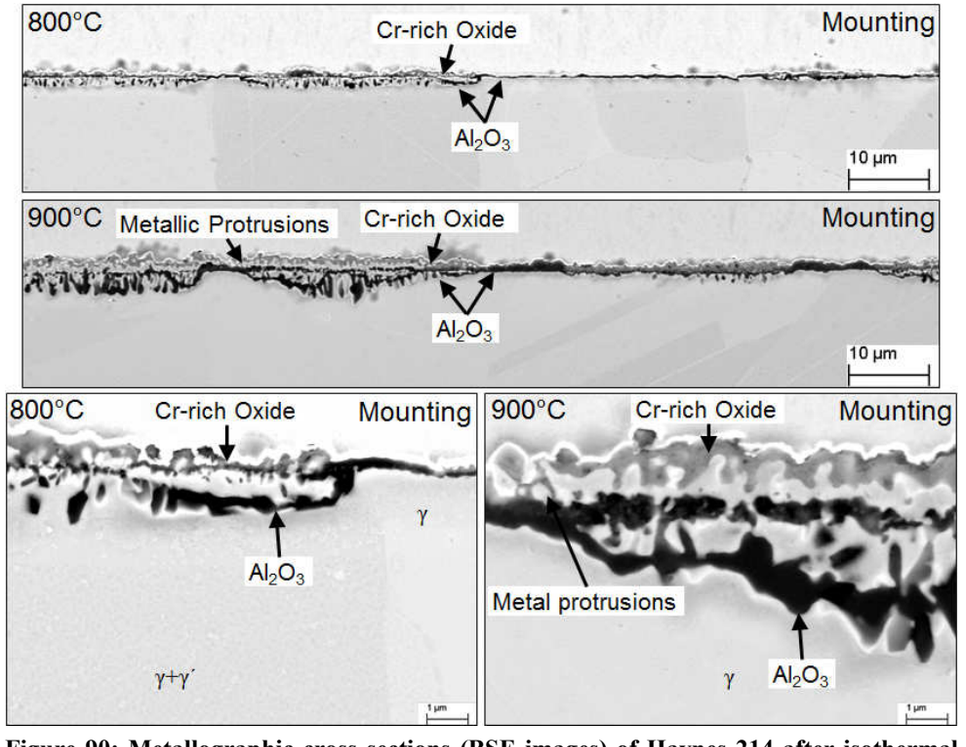

Figure 90: Metallographic cross sections (BSE images) of Haynes 214 after isothermal oxidation at 800°C and 900°C in Ar-7%H_2O for 72 h

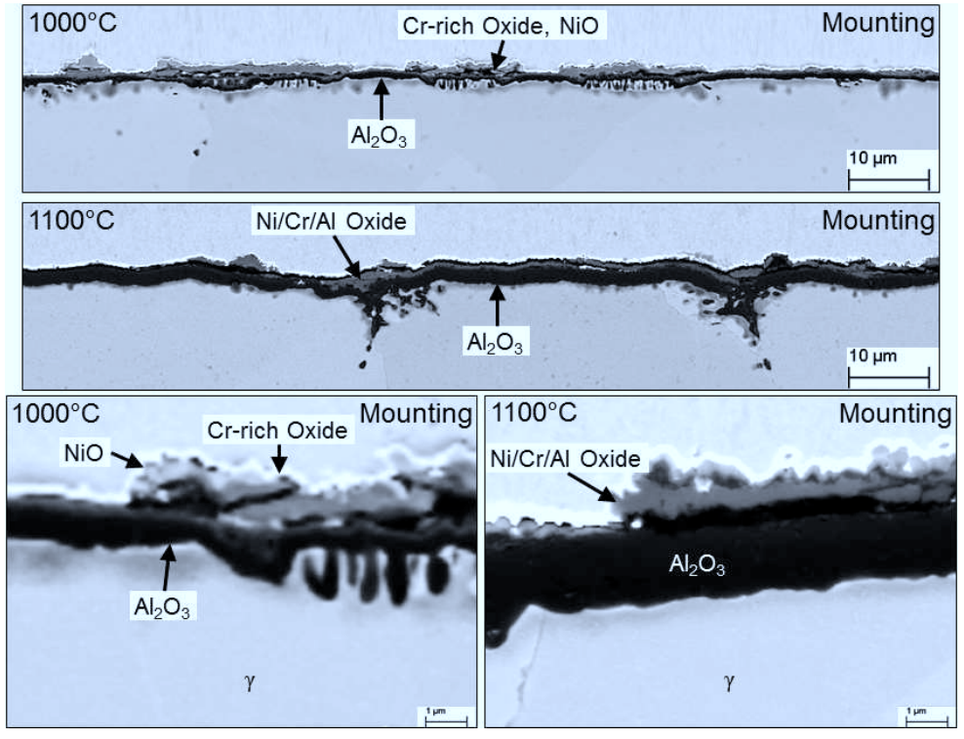

Figure 91: Metallographic cross sections (BSE images) of Haynes 214 after isothermal oxidation at 1000°C and 1100°C in Ar-7%H_2O for 72 h

After 72 h exposure at 1000°C and especially 1100°C in Ar-7%H_2O the material is covered by a continuous Al_2O_3 layer. In contrast to 1100°C, at 1000°C some internal Al_2O_3 precipitates were still found beneath the continuous layer. In Ar-20%O_2 at 1000°C internal Al_2O_3 precipitates were only found after 8 h oxidation, whereas after 72 h exposure no internal precipitates were observed. Similar to the results in Ar-20%O_2, the external scale formed in Ar-7%H_2O after 72 h oxidation at 1000°C contains a Cr-rich oxide and NiO, whereas at 1100°C a single-phase Ni/Cr/Al mixed oxide is present, which is confirmed by SNMS measurement (Figure 92). At 1000°C and especially at 1100°C the k_w'-values in the early stages of oxidation in Ar-7%H_2O are larger than those in Ar-20%O_2. Thus the higher weight gain after 72 h oxidation in Ar-7%H_2O (Figure 87, Figure 88) is mainly related to differences in the early oxidation stages. Interesting to note is that the external Ni/Cr-rich layer tends to spall during specimen cooling after the end of the exposure (Figure 91).

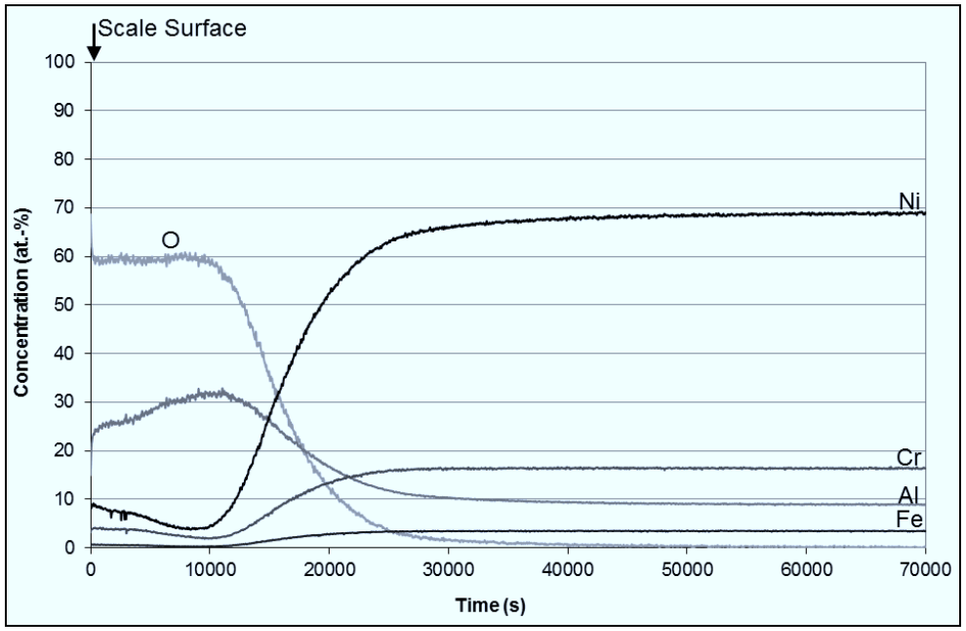

Figure 92: SNMS depth profiles of Haynes 214 after isothermal oxidation in Ar-7%H_2O at 1100°C for 72 h

6.2.4.2 Behavior in Ar-4%H_2-7%H_2O

Figure 93 shows the area specific weight gains of Haynes 214 during isothermal exposure at 800°C, 900°C, 1000°C and 1100°C in Ar-4%H_2-7%H_2O. In addition, the area specific weight gains obtained in Ar-20%O_2 (Figure 59) are shown again for comparison and better readability (Figure 94). The weight gain in Ar-4%H_2-7%H_2O increases with increasing exposure temperature but is at every temperature lower than the corresponding weight gain in Ar-20%O_2 (Figure 88) and Ar-7%H_2O (Figure 87). The weight gain in Ar-4%H_2-7%H_2O at 900°C temporarily slightly exceeds the one at 1000°C (17 h < t < 62 h), whereas the weight gain during oxidation in Ar-20%O_2 at 900°C exceeded that at 1000°C at t > 42 h (Figure 88) and is after 72 h oxidation more than 0.2 mg/cm² higher than that of Ar-4%H_2-7%H_2O. This correlates with the oxidation rate k_w' obtained in Ar-20%O_2 which is at t > 25 h more than one order of magnitude higher compared to Ar-4%H_2-7%H_2O (Figure 95). In contrast to Ar-20%O_2 an initial increase in oxidation rate was not observed for Ar-4%H_2-7%H_2O at 900°C, similar as described for Ar-7%H_2O (Figure 89). The oxidation rates at 1000°C and 1100°C are quite similar in Ar-4%H_2-7%H_2O and Ar-20%O_2 and the differences in weight gain after 72 h oxidation between Ar-4%H_2-7%H_2O and Ar-20%O_2 are virtually exclusively related to the early stages of oxidation (Figure 60, Figure 95). In contrast to this, the oxidation rate at 800°C is lower in Ar-4%H_2-7%H_2O compared to Ar-20%O_2 and this very low oxidation rate is the reason for the high fluctuating k_w'-values at 800°C (Figure 95); i. e. the weight gain rates are near the sensitivity limit of the TGA system.

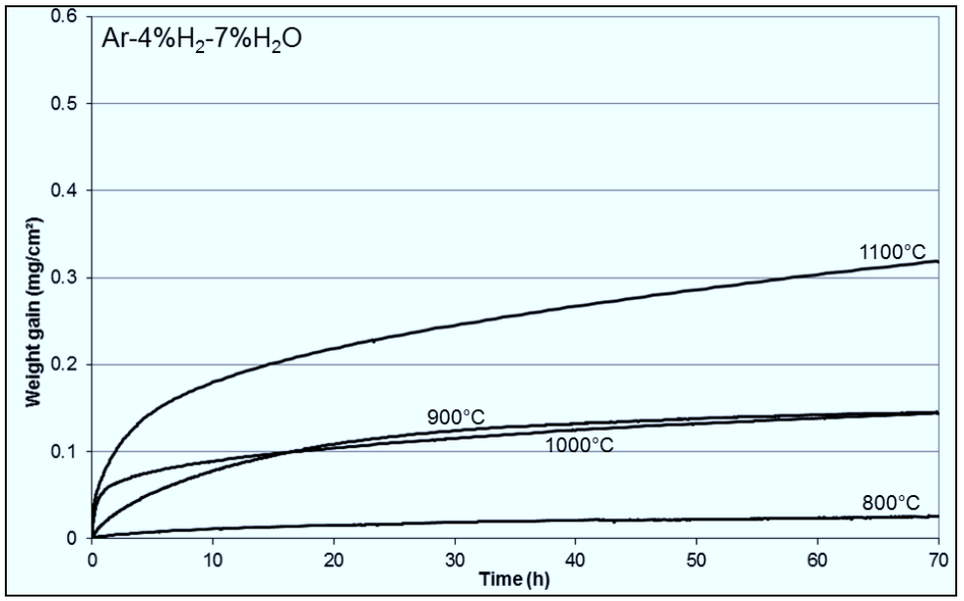

Figure 93: Area specific weight gain during isothermal oxidation of Haynes 214 in Ar-4%H_2-7%H_2O at different temperatures

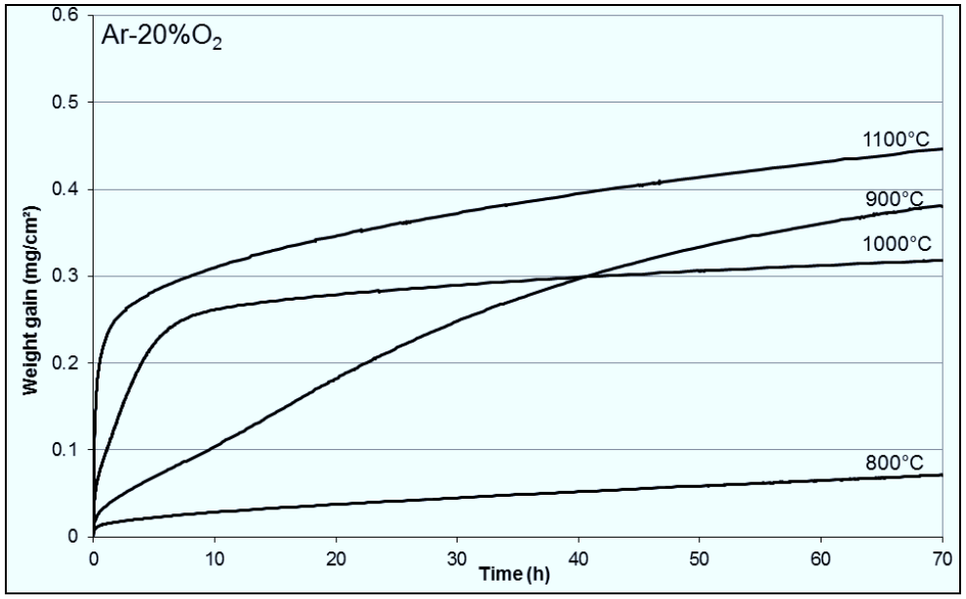

Figure 94: Area specific weight gain during isothermal oxidation of Haynes 214 in Ar-20%O_2 at different temperatures (already shown in Figure 59)

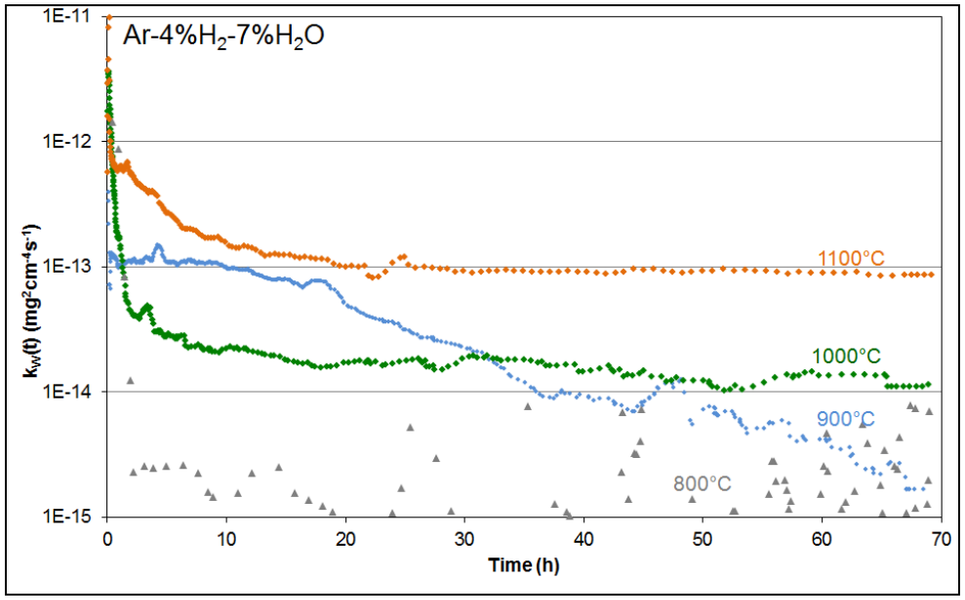

Figure 95: Time dependence of the instantaneous apparent parabolic rate constant kw' of Haynes 214 during isothermal oxidation in Ar-4%H_2-7%H_2O for 72 h

Figure 96 and Figure 97 show BSE images of the cross sections of Haynes 214 after 72 h oxidation in Ar-4%H_2-7%H_2O at 800°C, 900°C, 1000°C and 1100°C. As already described before (chapter 6.1.2.2), the equilibrium oxygen partial pressure of this test gas in this temperature range is lower than the dissociation pressure of NiO (see Figure 10). Consequently, NiO is not stable under the prevailing test conditions.

After oxidation at 800°C the specimen is mainly covered by an external Al_2O_3 scale. The number of locations where internal Al_2O_3 precipitates, metal protrusions and Cr-rich oxide were found is smaller than in Ar-20%O_2 (Figure 62) and Ar-7%H_2O (Figure 91). This explains the higher weight gain in the two latter gases (Figure 87, Figure 93, Figure 94).

After exposure at 900°C the number of locations of internal Al_2O_3, metal protrusions and Cr-rich oxide is again lower in Ar-4%H_2-7%H_2O (Figure 96) than in Ar-20%O_2 (Figure 62) and Ar-7%H_2O (Figure 91). Similar to the result at 900°C in Ar-7%H_2O, no NiO was found after oxidation in Ar-4%H_2-7%H_2O, which results in a weight gain which is significantly lower than that in Ar-20%O_2 (Figure 94).

The material exhibits after exposure in Ar-4%H_2-7%H_2O at 900°C more locations of internal Al_2O_3, metal protrusions and external Cr-rich oxide than after 800°C. After oxidation at 1000°C and 1100°C the amount of external Cr-rich oxide in Ar-4%H_2-7%H_2O is significantly lower than after the tests in Ar-20%O_2 (Figure 62) and Ar-7%H_2O (Figure 91). In contrast to

Ar-7%H_2O and Ar-20%O_2, no NiO was found in Ar-4%H_2-7%H_2O. Consequently, the external oxide after the 1000°C test consists only of Cr-rich oxide and of a single phase Cr/Al mixed oxide after 1100°C exposure. In contrast to the tests in Ar-7%H_2O and Ar-20%O_2, the scales formed at 1000°C and 1100°C in Ar-4%H_2-7%H_2O exhibited metal protrusions, as a result of the fact that NiO is not stable in this low pO_2 gas. As the growth rate of NiO is higher than that of Cr_2O_3 (see Figure 13), the absence of NiO resulted in a decreased weight gain of the specimens exposed in Ar-4%H_2-7%H_2O (Figure 93) compared to those in Ar-7%H_2O (Figure 87) and Ar-20%O_2 (Figure 94).

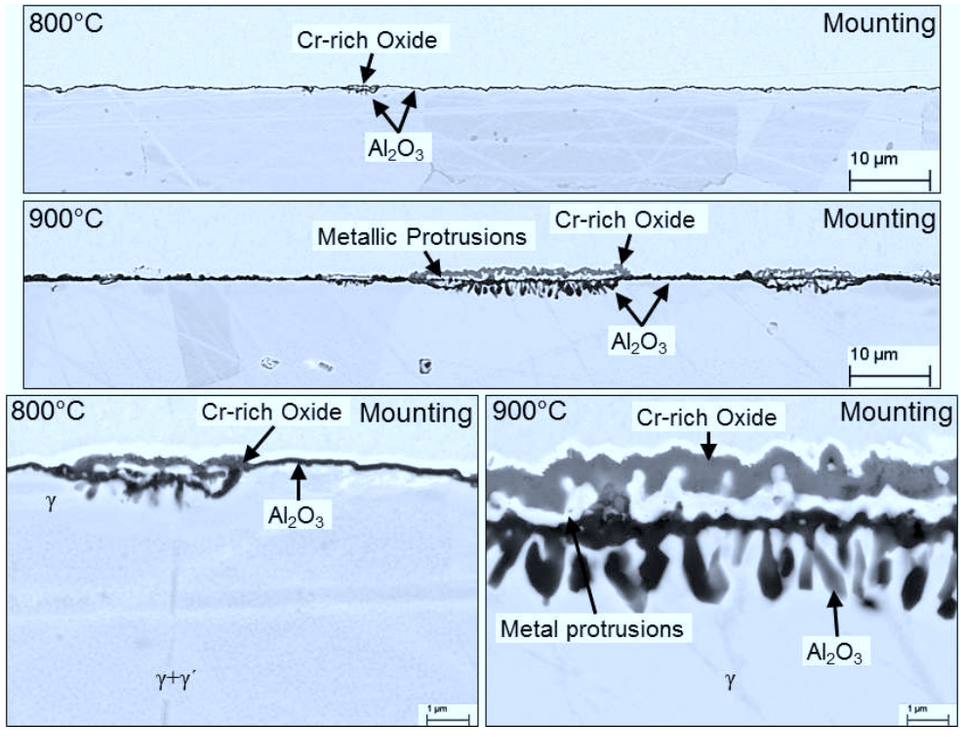

Figure 96: Metallographic cross sections (BSE images) of Haynes 214 after isothermal oxidation at 800°C and 900°C in Ar-4%H_2-7%H_2O for 72 h

Another finding after the oxidation in Ar-4%H_2-7%H_2O was the presence of nickel particles at the oxide surface, exemplarily shown for the 1000°C and 1100°C exposures in Figure 98. These were mainly found in areas where also Cr-rich oxide nodules were present. The nickel particles are believed to result from the not oxidized metal protrusions formed in this test gas. After oxidation at 1000°C approximately 1 µm large nickel particles are formed in the vicinity of the Cr-rich oxide and in addition very fine particles were found on areas covered by Al_2O_3. In contrast to 1000°C, these fine nickel particles were not found on Al_2O_3 after 1100°C exposure and the particles in the vicinity of the Cr-rich oxide are significantly larger

compared to those at 1000°C (Figure 98). Nickel particles on the oxide surface were also found for Alloy 602 CA oxidized in Ar-4%H_2-7%H_2O and were discussed in section 6.1.3.3.

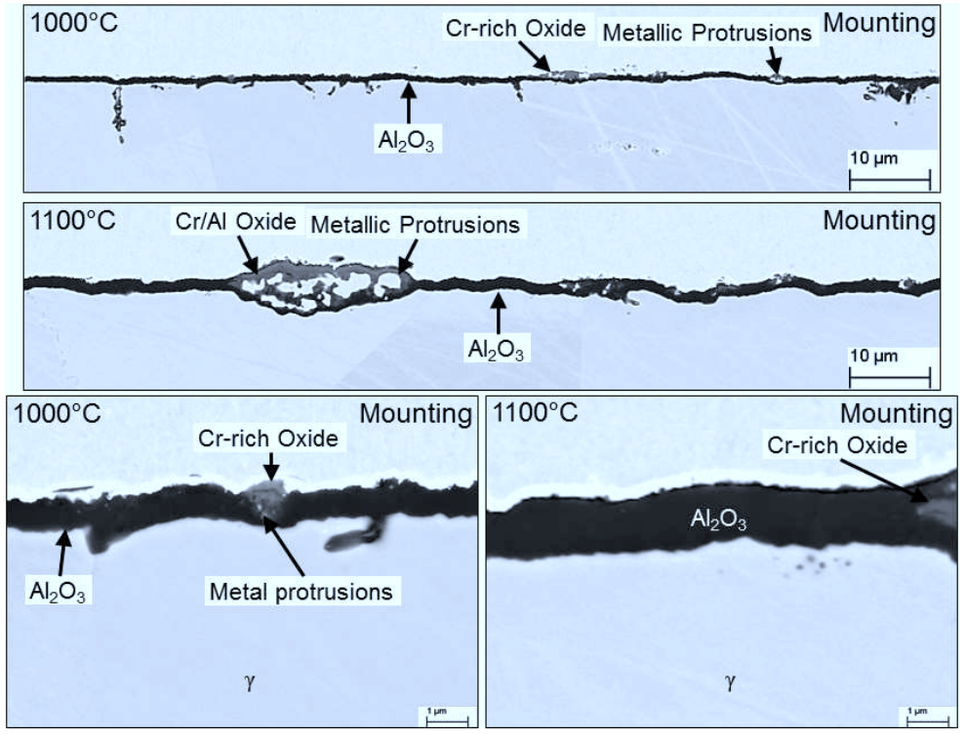

Figure 97: Metallographic cross sections (BSE images) of Haynes 214 after isothermal oxidation at 1000°C and 1100°C in Ar-4%H_2-7%H_2O for 72 h

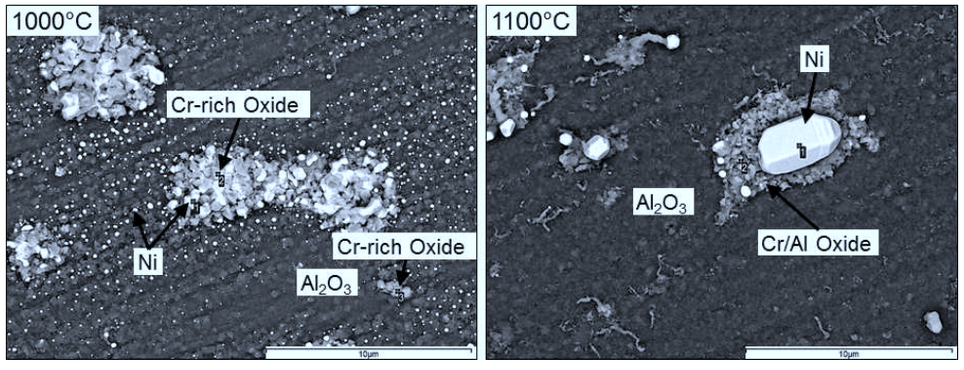

Figure 98: Secondary electron (SE) image of surface oxide morphology for Haynes 214 after isothermal oxidation at 1000°C (left) and 1100°C (right) in Ar-4%H_2-7%H_2O for 72 h

6.2.4.3 Behavior in Ar-20%O_2-7%H_2O

Figure 99 shows the area specific weight gains of Haynes 214 during isothermal exposure at 800°C, 900°C, 1000°C and 1100°C in Ar-20%O_2-7%H_2O. In addition, the area specific weight gains in Ar-20%O_2 (Figure 59) are shown again for easier comparison and better readability (Figure 100). At 1000°C and 1100°C the weight gains of Haynes 214 after 72 h oxidation are higher in Ar-20%O_2-7%H_2O than in Ar-20%O_2. However, the kinetics at 1000°C and 1100°C in Ar-20%O_2-7%H_2O (Figure 99) seem to be more similar to those in Ar-20%O_2 (Figure 100) than those in Ar-7%H_2O or Ar-4%H_2-7%H_2O (Figure 87, Figure 93). During 1000°C exposure the k_w'-value of Haynes 214 is higher in Ar-20%O_2-7%H_2O (Figure 101) than in Ar-20%O_2 (Figure 60). At 1100°C the oxidation rate is steadily decreasing, whereas in Ar-20%O_2 at approximately t > 10 h it is virtually constant. This results in a lower oxidation rate after 72 h exposure in Ar-20%O_2-7%H_2O compared to Ar-20%O_2 at 1100°C. However, due to a higher oxidation rate in the early stages of oxidation at 1000°C and 1100°C in Ar-20%O_2-7%H_2O the weight gains after 72 h are higher compared to Ar-20%O_2. In contrast to 1000°C and 1100°C, the specimens exposed in Ar-20%O_2-7%H_2O at 800°C and 900°C exhibited lower weight gains than those exposed in Ar-20%O_2. At 900°C the oxidation rate in the early stage of oxidation is higher in Ar-20%O_2-7%H_2O, but due a steady increase up to t = 25 h the oxidation rate in Ar-20%O_2 is slightly higher than that obtained for Ar-20%O_2-7%H_2O at approximately t > 15 h.

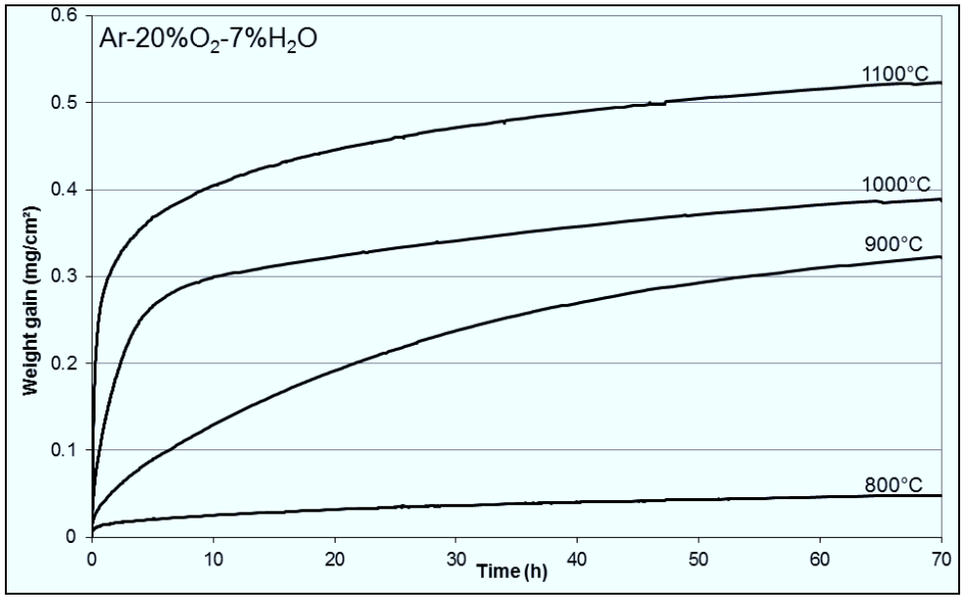

Figure 99: Area specific weight gain during isothermal oxidation of Haynes 214 in Ar-20%O_2-7%H_2O at different temperatures

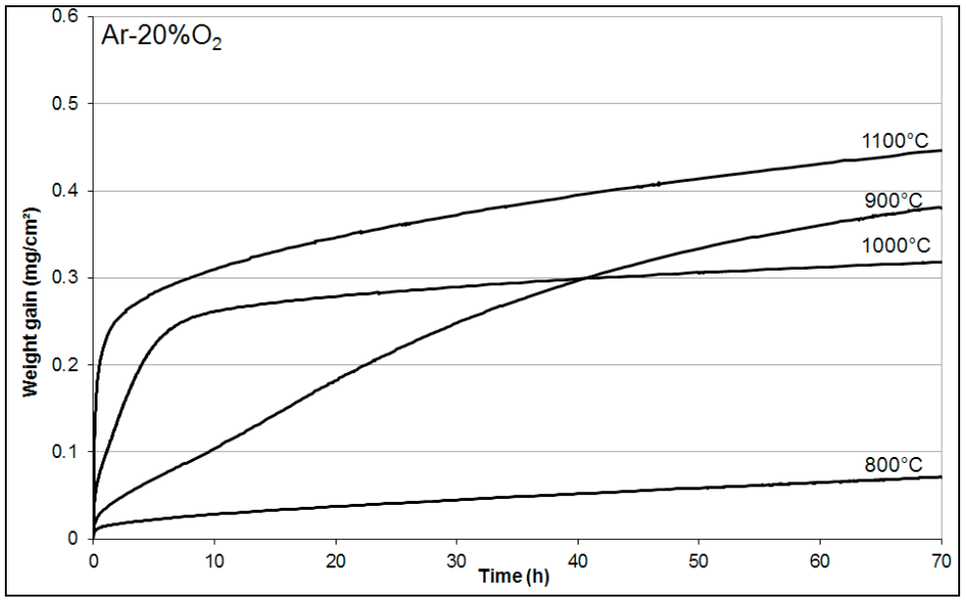

Figure 100: Area specific weight gain during isothermal oxidation of Haynes 214 in Ar-20%O_2 at different temperatures (already shown in Figure 59)

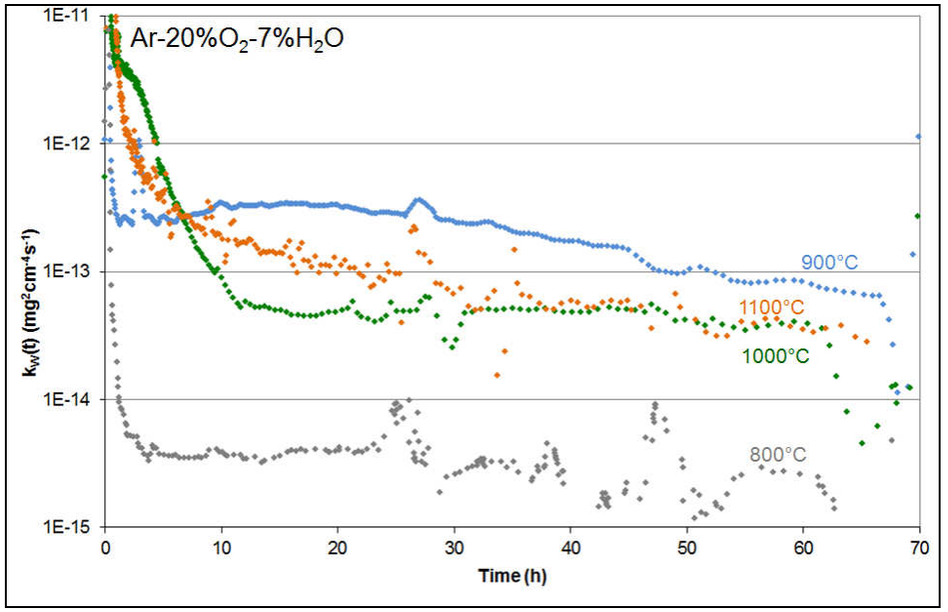

Figure 101: Time dependence of the instantaneous apparent oxidation rate kw' of Haynes 214 during isothermal oxidation in Ar-20%O_2-7%H_2O for 72 h

Figure 102 and Figure 103 show BSE images of cross sections of Haynes 214 after 72 h isothermal exposure in Ar-20%O_2-7%H_2O at 800°C, 900°C, 1000°C and 1100°C. As

illustrated in Figure 10 the equilibrium oxygen partial pressure in this test gas is virtually equal to that in Ar-20%O_2 (0.2 bar) and thus significantly higher than that in Ar-7%H_2O and Ar-4%H_2-7%H_2O.

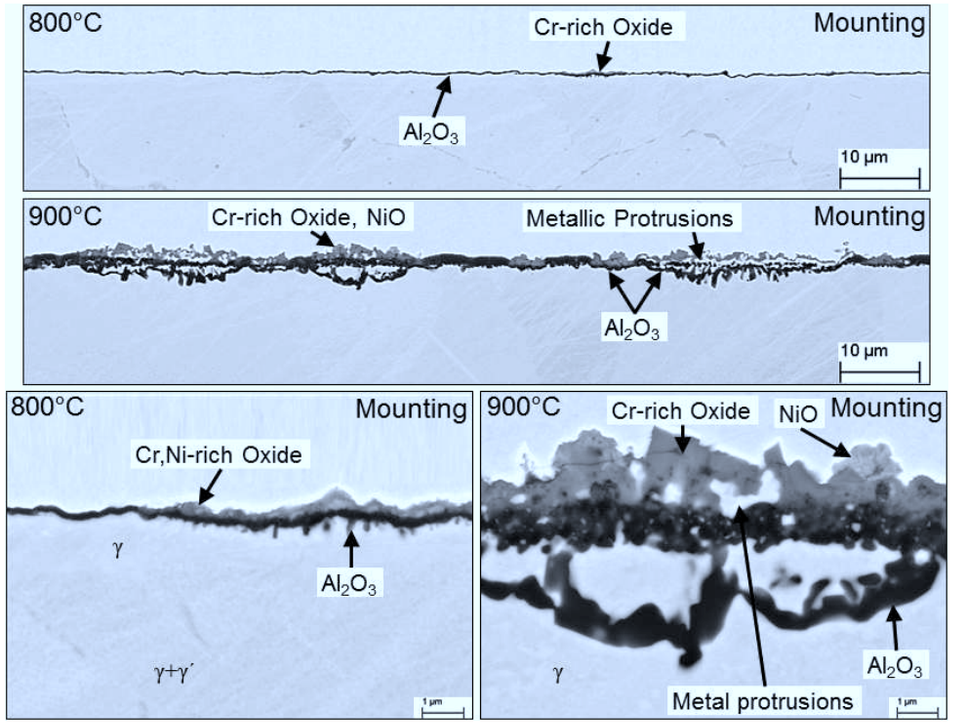

Figure 102: Metallographic cross sections (BSE images) of Haynes 214 after isothermal oxidation at 800°C and 900°C in Ar-20%O_2-7%H_2O for 72 h

After oxidation at 800°C the specimen is mainly covered by an external Al_2O_3 scale, similar to that found in Ar-20%O_2 (Figure 64). The weight gain is higher than in the exposure in Ar-4%H_2-7%H_2O but slightly lower than in Ar-7%H_2O and Ar-20%O_2. A higher weight gain can be the result of a higher amount of Cr- and/or Ni-containing oxides, as these exhibit a higher oxidation rate than Al_2O_3 (Figure 13). However, at 800°C the weight gain difference between the test gases after 72 h oxidation is quite small compared to the tests at higher temperatures.

After 900°C oxidation in Ar-20%O_2-7%H_2O the external scale contains NiO, as also found for 72 h exposure in Ar-20%O_2 (Figure 66) at this temperature. However, the weight gain after 72 h oxidation in Ar-20%O_2-7%H_2O (Figure 99) is lower compared to Ar-20%O_2 (Figure 100), but slightly higher compared to Ar-7%H_2O (Figure 90). The amount of internal Al_2O_3 precipitates, metal protrusions and Cr-rich oxide formed in Ar-20%O_2-7%H_2O is in a similar range as observed in Ar-7%H_2O.

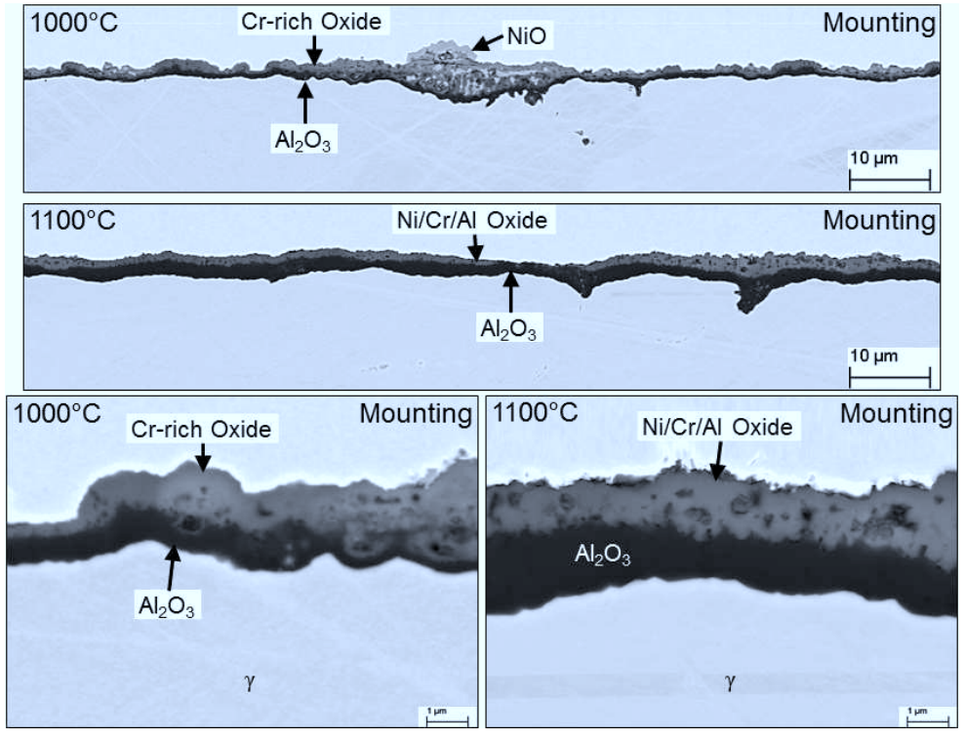

Figure 103: Metallographic cross sections (BSE images) of Haynes 214 after isothermal oxidation at 1000°C and 1100° C in Ar-20%O_2-7%H_2O for 72 h

After 72 h exposure at 1000°C in Ar-20%O_2-7%H_2O Haynes 214 exhibited a higher weight gain compared to Ar-20%O_2 and the other H_2O-containing gases. This correlates with the larger amounts of Cr-rich oxide and NiO found in the external scale formed in the first mentioned gas (Figure 103). Similar as described for the 1000°C test in Ar-20%O_2, NiO is randomly distributed in the Cr-rich oxide scale. After 1100°C oxidation a single phase Ni/Cr/Al mixed oxide above a continuous Al_2O_3 layer is formed, similar to the results from the tests in Ar-20%O_2 (Figure 69) and Ar-7%H_2O (Figure 91) at this temperature. GD-OES analysis of the specimen exposed in Ar-20%O_2-7%H_2O (Figure 104) revealed a composition of the external mixed oxide very similar to that formed in Ar-20%O_2 (Figure 105), whereas in Ar-7%H_2O (Figure 92) the measured concentration is different. This difference is probably related to oxide spallation in case of Ar-7%H_2O.

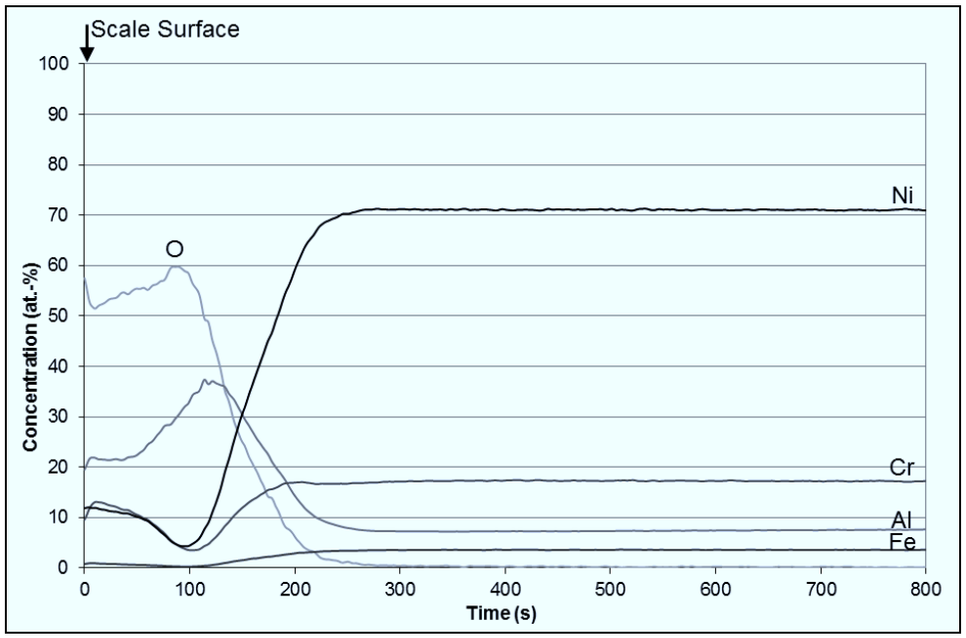

Figure 104: GD-OES depth profiles of Haynes 214 after isothermal oxidation in Ar-20%O_2-7%H_2O at 1100°C for 72 h

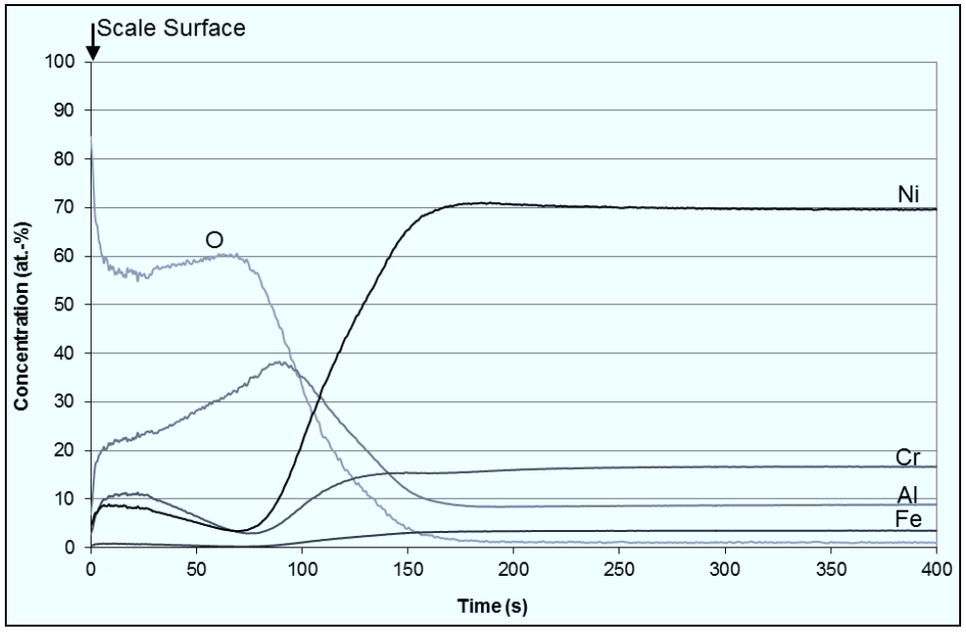

Figure 105: GD-OES depth profiles of Haynes 214 after isothermal oxidation in Ar-20%O_2 at 1100°C for 72 h

6.2.5 Discussion of the Behavior in H_2O-containing Gases Compared to Ar-20%O_2

General Remarks

The investigations in the H_2O-containing atmospheres revealed that after 72 h exposure at 800°C and 900°C differences in area specific weight gain resulted mainly from different numbers of locations of internal Al_2O_3 precipitates accompanied by metal protrusions and Cr-rich oxide. The smaller their amount is, the lower is the area specific weight gain. At 900°C only the specimens exposed in Ar-20%O_2-7%H_2O and Ar-20%O_2 formed significant amounts of NiO. The test in Ar-7%H_2O revealed hardly any formation of NiO and in Ar-4%H_2-7%H_2O this is not thermodynamically stable. The formation of Cr-rich oxide and NiO seems to be in contradiction with literature results which revealed for 800-900°C on Haynes 214 the formation of a thin Al_2O_3 layer after 100 h oxidation in Air-10%H_2O [115], as shown in Table 11. The reason for this difference may be related to different sample preparation methods prior to exposure. As described in section 6.2.3.4, surface cold work introduced by specimen grinding promotes the formation of an external Al_2O_3 layer on Haynes 214 at 800°C; a ground specimen (p1200) exhibited a larger tendency to external Al_2O_3 formation than a polished one (1 µm diamond paste). In reference [115] as-rolled specimens were used for the oxidation tests. As cold rolling introduces substantial amounts of cold work, the tendency to external Al_2O_3 formation of these specimens might be even higher than that of the ground specimens used in the present study. This would explain the formation of an external Al_2O_3 scale observed in [115], whereas the present experiments revealed significant amounts of internal Al_2O_3 precipitates along with formation of external Cr-rich oxide. However, further studies are required to verify this assumption.

Oxidation at 800°C

After 72 h exposure at 800°C the highest weight gain was found in Ar-7%H_2O in agreement with the observed larger amount of locally occurring internal oxidation of aluminum. Thus, the tendency for external Al_2O_3 formation is in this test gas lower than in all other investigated gases. The effect of H_2O promoting the internal oxidation of Al was already reported in literature by several authors for the oxidation of Fe-base borderline alumina forming alloys [122, 123, 124] and FeCr alloys [41]. Quadakkers et al proposed for the latter alloys the following mechanism [41]:

- Hydrogen released by oxidation diffuses into the alloy
- Interstitial hydrogen enlarges the alloy lattice
- Oxygen solubility and/or oxygen diffusion into the alloy increases
- Tendency for internal oxidation of Al increases

Assuming this mechanism to be correct also for Ni-base alumina forming alloys, such as Haynes 214, would explain the higher number of internal Al_2O_3 precipitates formed in Ar-7%H_2O at 800°C compared to Ar-20%O_2 and the resulting higher k_W'-values in Ar-7%H_2O (Figure 89) compared to all other investigated test gases (Figure 60, Figure 95, Figure 101). As the mechanism is based on the release of hydrogen, it is expected not to affect the oxidation in Ar-20%O_2-7%H_2O, due to the presence of O_2. This correlates with the fact that the weight gain and corresponding k_W'-values in the latter test gas are lower than in Ar-7%H_2O and in a similar range as obtained for the oxidation test in Ar-20%O_2 (Figure 59). Thus, the amount of internal Al_2O_3 precipitates is similar in the two O_2-containing gases (Figure 64, Figure 102), whereas it is significantly higher in Ar-7%H_2O (Figure 90).

Concerning oxidation in Ar-4%H_2-7%H_2O, the increased amount of H_2 present in this test gas, might promote the effect proposed by Quadakkers et al [41] in comparison to Ar-7%H_2O. However, the area specific weight gain in this test gas and the corresponding k_W'-values are lower compared to those in Ar-7%H_2O. Furthermore, also the tests in Ar-20%O_2-7%H_2O and Ar-20%O_2 revealed higher k_W'-values than obtained for Ar-4%H_2-7%H_2O. This correlates with results from Young et al [114], which showed that the k_W'-values of an Al_2O_3-forming FeCrAlY alloy are smaller in Ar-4%H_2-7%H_2O than in Ar-20%O_2 in the temperature range 1200 – 1300°C. The authors pointed out, that due to a much lower oxygen partial pressure in Ar-4%H_2-7%H_2O (see Figure 10) the gradient in oxygen chemical potential across the oxide scale is smaller compared to Ar-20%O_2 [114]. Consequently, the growth rate of external Al_2O_3 is lower in Ar-4%H_2-7%H_2O than in the test gases with higher pO_2. However, as especially seen in Figure 95, the weight gain rates at 800°C are so small that they are near the sensitivity limit of the used TGA facility and therefore the relative differences in k_W'-values should be taken with some care.

Oxidation at 900°C

As shown in section 6.2.2 and 6.2.4, after 72 h oxidation at 900°C only the specimens exposed in Ar-20%O_2 and Ar-20%O_2-/%H_2O exhibited significant amounts of NiO in the oxide scale. The oxidation mechanism for Haynes 214 proposed for Ar-20%O_2 in chapter 6.2.3.4 leads to the conclusion that the presence of NiO in the external scale indicates a change from step 2 to step 3 in the schematic presentation in Figure 86. Assuming this oxidation mechanism to be applicable also for the oxidation in wet gases, would mean that this change (step 2 to step 3) matches to the specimens exposed for 72 h at 900°C in Ar-20%O_2 and Ar-20%O_2-7%H_2O, whereas the specimen exposed in Ar-7%H_2O still shows after 72 h oxidation step 2, i. e. without any detectable amounts of NiO. This may be related to the proposed effect of H_2O in the absence of intentionally added O_2, promoting the internal oxidation of aluminum, described above for the 800°C oxidation. It can, however, not be concluded from the present 72 h results whether the change from step 2 to step 3 is suppressed

or solely delayed by the presence of H_2O. In the latter case this would imply that, during exposure in Ar-7%H_2O, the change from step 2 to step 3 which did not occur up to 72 h, may occur after longer exposure times. Another factor affecting the formation of NiO is the oxygen partial pressure in the test gas. In literature [83] a lower pO_2, in a test gas in which NiO is stable, was reported to decrease the oxidation rate of nickel in NiCr alloys, which promoted the formation of a protective Cr_2O_3 scale. The growth rate of NiO in Ar-7%H_2O was reported to be similar to that of Cr_2O_3 [83], although in high pO_2 gases, such as Ar-20%O_2 or Ar-20%O_2-7%H_2O, it is approximately one order of magnitude higher (Figure 13). This implies that a decrease in pO_2 can decrease the amount of formed NiO and thus affect the change from step 2 to step 3. In case of oxidation in Ar-4%H_2-7%H_2O a change from step 2 to step 3 cannot be identified by NiO formation, as NiO is not thermodynamically stable in this test gas.

Oxidation at 1000°C and 1100°C

After 72 h exposure at 1000°C the oxide scales of the specimens exposed in Ar-7%H_2O, Ar-20%O_2-7%H_2O and Ar-20%O_2 do not contain metal protrusions, as found after 900°C oxidation. The initially formed protrusions are oxidized completely and thus the external Cr-rich oxide scale contains NiO, as described by the proposed mechanism for the oxidation of Haynes 214 in Ar-20%O_2 (Figure 86, step 3). In addition, beneath that outer scale a continuous Al_2O_3 layer was formed. In contrast to the exposures in the two O_2 containing test gases, some internal Al_2O_3 precipitates were found after 72 h oxidation in Ar-7%H_2O beneath the semi-continuous Al_2O_3 layer. Due to the fact that NiO is not thermodynamically stable in Ar-4%H_2-7%H_2O in the investigated temperature range (see Figure 10), the oxide scale after 72 h oxidation at 1000°C and 1100°C in this test gas still contains metal protrusions within the external Cr-rich oxide. As shown in section 6.2.4.2, the amount of Cr-rich oxide formed at 1000°C and 1100°C in Ar-4%H_2-7%H_2O is significantly smaller compared to the other H_2O-containing gases and Ar-20%O_2. However, in literature Cr_2O_3 on NiCr-base alloys is reported to exhibit a higher growth rate in Ar-4%H_2-7%H_2O than in Ar-20%O_2 at 1050°C [90]. It is proposed that the effect of a smaller amount of Cr-rich oxide in Ar-4%H_2-7%H_2O in the present study on Haynes 214 is related to a faster formation of a continuous Al_2O_3 layer and not to the Cr_2O_3 growth rate. As no NiO is formed and the amount of Cr-rich oxide is significantly smaller in Ar-4%H_2-7%H_2O than in the other investigated test gases, the area specific weight gain after 72 h oxidation in that gas is lower than in the other test gases (Figure 59, Figure 87, Figure 93, Figure 99).

Another interesting finding is the presence of nickel particles on the oxide surface of Haynes 214 exposed in Ar-4%H_2-7%H_2O, exemplarily shown for 1000°C and 1100°C oxidation in Figure 98. These particles result from metallic protrusions formed as a result of internal Al_2O_3 formation in the initial oxidation stage, as described in chapter 6.2.3.1 for the oxidation in Ar-

20%O_2. In the latter atmosphere the Ni-rich particles become subsequently oxidized, bit they remain in metallic form during exposure in Ar-4%H_2-7%H_2O due to the low equilibrium oxygen partial pressure in this gas (Figure 10). Nickel particles on the oxide surface were also observed for the oxidation of alloy 602 CA in this atmosphere (Figure 35). Their presence on the oxide surface is probably based on the following points:

- Internal Al_2O_3 formation results in a volume increase in the alloy and metallic protrusions are formed (see chapter 6.2.3.1)
- NiO is not stable in Ar-4%H_2-7%H_2O
- The rate of extrusion of mainly metallic nickel is proposed to be faster than the formation of Cr-rich oxide overgrowing the metal protrusions

These effects might result in an extrusion of mainly metallic nickel after a critical Cr-consumption through the external Cr-rich oxide. Consequently, metallic particles containing mainly nickel are found on the oxide surface after exposure in Ar-4%H_2-7%H_2O (Figure 98).

After 72 h oxidation at 1100°C the weight gain in Ar-4%H_2-7%H_2O is lower than in the other investigated test gases (Figure 59, Figure 87, Figure 93, Figure 99), similar to the results at 1000°C. This is the result of the fact that NiO is not stable in that atmosphere and that the amount of external Cr containing oxide is lower than in the other test gases (see Figure 62, Figure 90, Figure 96, Figure 102). The weight gain differences after 72 h are thus mainly related to differences in the transient state of oxidation as at 1000°C and 1100°C Cr- and Ni-containing oxides were only formed until a continuous Al_2O_3 layer had developed.

In Ar-7%H_2O and Ar-20%O_2-7%H_2O the continuous Al_2O_3 layer is partly covered by a single phase Ni/Cr/Al mixed oxide, which is probably $Ni(Cr,Al)_2O_4$ spinel, similar as described for the oxidation in Ar-20%O_2 (see chapter 6.2.3.1). In contrast to this, the single phase mixed oxide formed in Ar-4%H_2-7%H_2O at 1100°C contains no nickel. Regarding the oxidation mechanism for Haynes 214 proposed in chapter 6.2.3.4, this indicates that step 4 in the mechanism (Figure 86) might never be reached by the material during exposure in Ar-4%H_2-7%H_2O in the investigated temperature range. However, the specimens exposed in Ar-7%H_2O and Ar-20%O_2-7%H_2O for 72 h at 1100°C exhibit the oxide scale morphology shown in step 4 (Figure 86).

7 Effects of Alloy Composition Variation

A limited number of investigations on the NiCrAl containing alloy Haynes 224 were carried out in addition to the presented studies. This was done to estimate weather the mechanisms proposed in the previous sections, may be transferred to another NiCrAl alloy. The chemical composition, determined in the same way as described in chapter 5.1, is given in Table 13.

	Ni	Cr	Al	Fe	Ti	Mn	Co	Si	Mo	C	Zr	Y	B
Haynes 224	47.6	20.4	3.89	28.2	0.14	0.051	0.047	0.041	<0.01	0.1843	0.071	0.061	<0.01

Table 13: Analyzed chemical composition of Haynes alloy 224 in wt.-%

Alloy 224 differs from the other studied alloys in that it contains Al- and Cr-contents between those of 214 and 602 CA. The Fe-content is substantially higher than that of 602 CA and 214; this exhibits an adverse effect on the stability of the γ´-phase found in alloy 214 (Figure 106). Using the tests in Ar-7%H_2O as example, Figure 107 shows that, despite a lower Al-content (3.89 wt.-%) than Haynes 214 (4.46 wt.-%), Haynes 224 exhibited after 72 h oxidation at 800 – 1100°C formation of a continuous Al_2O_3 layer with variable amounts of (locally present) Cr-rich transient oxide (Figure 107). The instantaneous k_W' showed at all temperatures values which slightly decrease with increasing time (Figure 108).

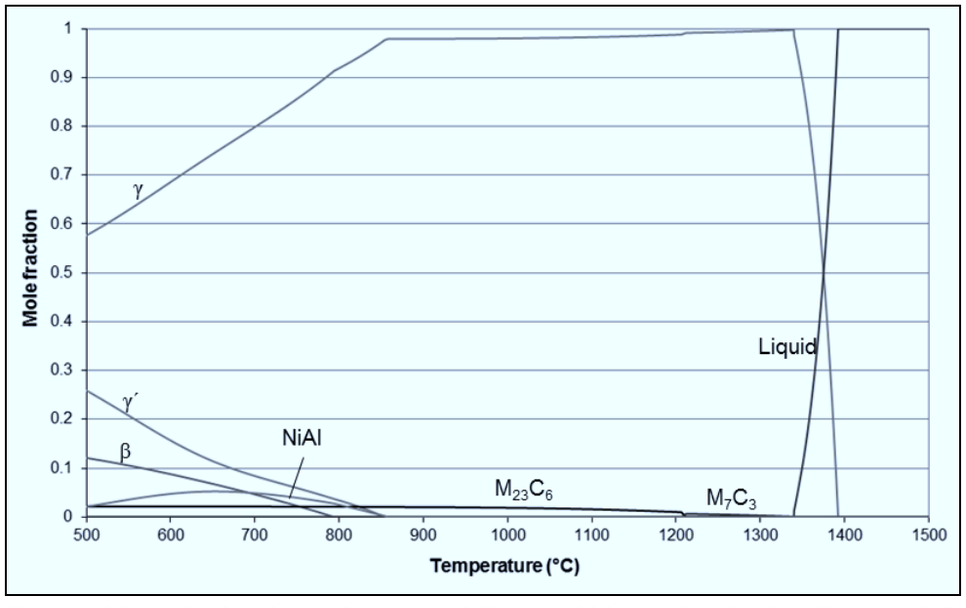

Figure 106: Mole fractions of phases of Haynes 224 calculated with Thermocalc© (Database: TTNI7)

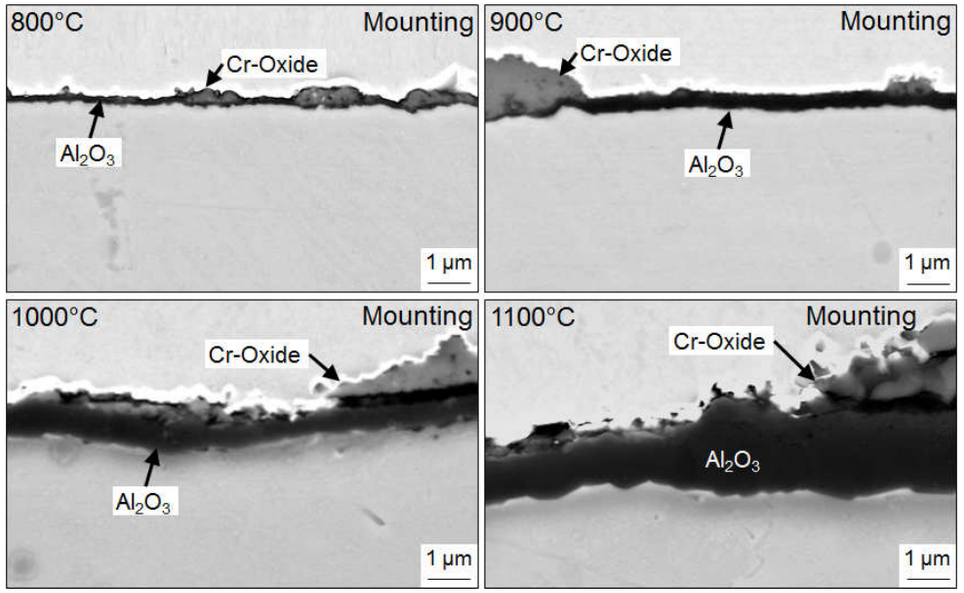

Figure 107: Metallographic cross sections (BSE images) of Haynes 224 after isothermal oxidation in Ar-7%H_2O for 72 h

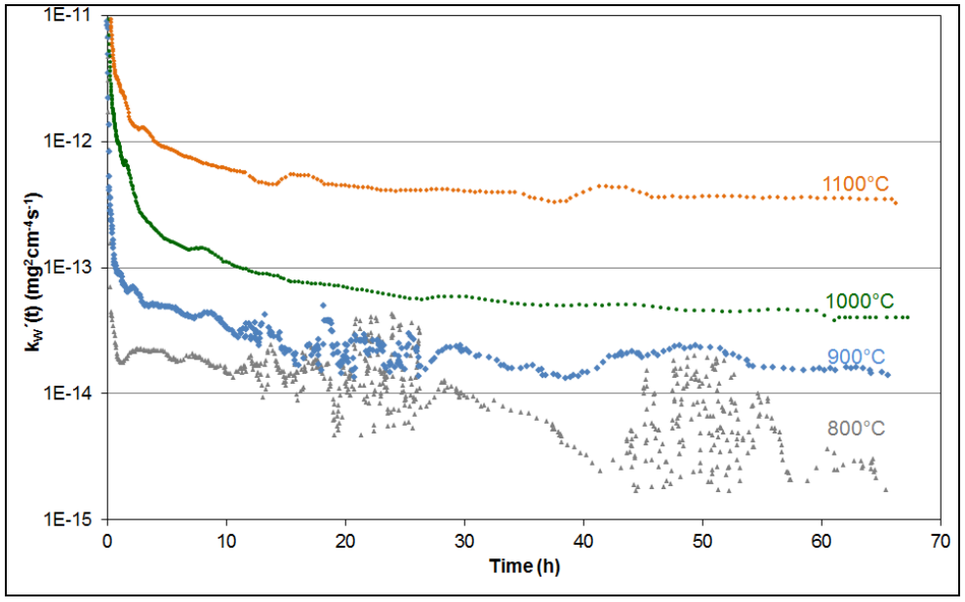

Figure 108: Time dependence of the instantaneous apparent parabolic rate constant kw' of Haynes 224 during isothermal oxidation in Ar-7%H_2O for 72 h

External alumina scale formation at all test temperatures was not only found in Ar-7%H_2O but also in the other test gases used, i. e. Ar-20%O_2 and Ar-4%H_2-7%H_2O (Figure 109). The fact that the tendency to external Al_2O_3 formation is higher for Haynes 224 than for Haynes

214 illustrates that not only the alloy aluminum concentration is crucial for the formation and maintenance of an external Al_2O_3 scale. Different concentrations of other elements, in particular chromium (20.4 wt.-%) and iron (28.2 wt.-%) will produce a microstructure different from Haynes 214, especially at the lower temperatures. It is proposed that the higher Cr-content in combination with a lower amount of Al-rich γ´-precipitates in Haynes 224 is the reason for the increased tendency to external Al_2O_3 formation. Additionally, the formation of Ni-containing oxide in the external scale of Haynes 224 was found to be less pronounced compared to Haynes 214. SNMS measurements on Haynes 224 after 72 h exposure in Ar-7%H_2O at 1100°C revealed a Ni-content in the external oxide scale of less than 3.5 at.-% (Figure 110), which is significantly lower compared to the corresponding measurement on Haynes 214 (8.8 at.-%, Figure 92).

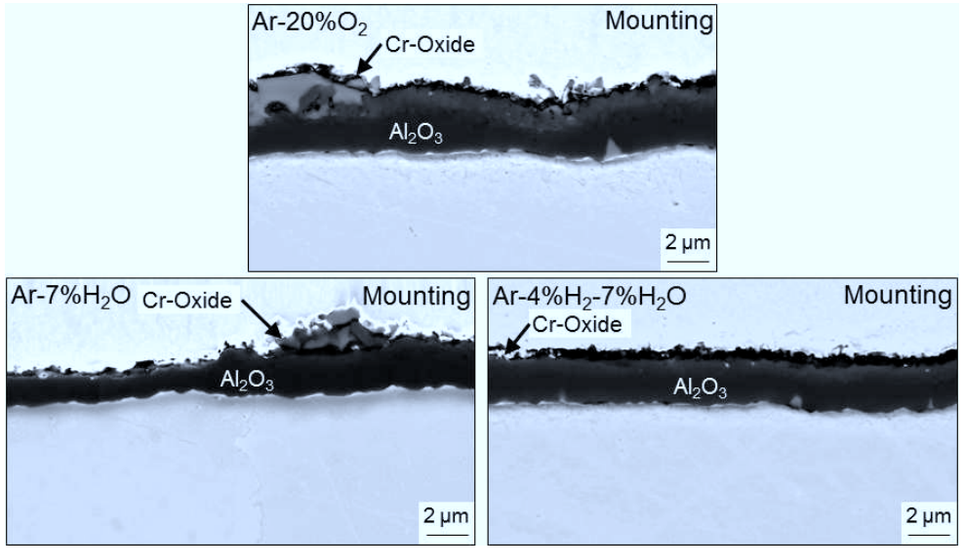

Figure 109: Metallographic cross sections (BSE images) of Haynes 224 after isothermal oxidation at 1100°C in Ar-20%O_2, Ar-7%H_2O and Ar-4%H_2-7%H_2O for 72 h

To determine effects of alloy composition on the oxide scale formation oxidation maps can be used. Figure 111 shows isothermal oxidation maps for ternary NiCrAl alloys at 1000°C in which the two alloys extensively investigated in the present study and Haynes 224 are inserted according to their Cr- and Al-contents. The graphical presentation relates to a graph proposed by Giggins and Pettit [33]. As far as known to the author, no accompanying diagrams for 800°C or 900°C are available. As only Cr and Al are considered, this is only a rough estimation as effects of other alloying elements, such as e. g. Fe, are not considered. In addition, the effect of alloy microstructure, as described above, and the effect of surface cold work, as described in section 6.1.3.3, on the oxidation behavior are not taken into account in the diagrams.

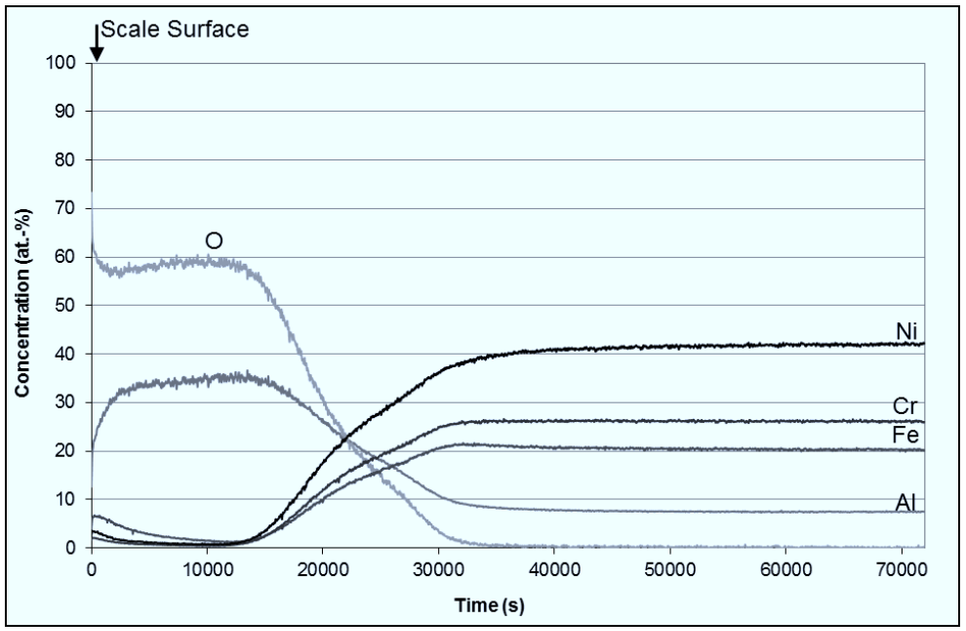

Figure 110: SNMS depth profiles of Haynes 214 after isothermal oxidation in Ar-7%H_2O at 1100°C for 72 h

However, the classification of Alloy 602 CA in group II (External layer of Cr_2O_3 and internal oxidation of Al) in the oxidation maps (Figure 111) correlate well with the experiments presented in the prevailing investigation. The oxidation maps (Figure 111) relate to 1000°C, i. e. a temperature at which the positive effect of surface cold work by specimen grinding was shown to be not effective on alumina scale formation (section 6.2.3.4). However, the positive effect of surface cold work at 800°C, described in section 6.1.3.3, will shift the line below the composition of Alloy 602 CA for this temperature, as seen from the results in section 6.1.2.2.

Another important factor which can affect the oxidation behaviour is the test atmosphere. As pointed out for Alloy 602 CA and Haynes 214 the oxide scale morphology is affected by H_2O in the test gas. However, no significant change from external to internal formation of Al_2O_3, namely from group III to group II in the oxidation map, like presented in literature for NiCrAl alloys with substantially lower Cr content [67, 68] was found for the two materials. This is probably based on the fact that H_2O additions mainly shift the boundary of group I and III towards group III in the oxidation maps but do not substantially affect the boundary of group II and III (see Figure 111, b). Thus, the formation of a protective Al_2O_3 layer on NiCrAl alloys with a Cr-content of 16 wt.-% or more, like in the materials investigated in the present study, seems not to be significantly affected by H_2O-additions in the test atmosphere.

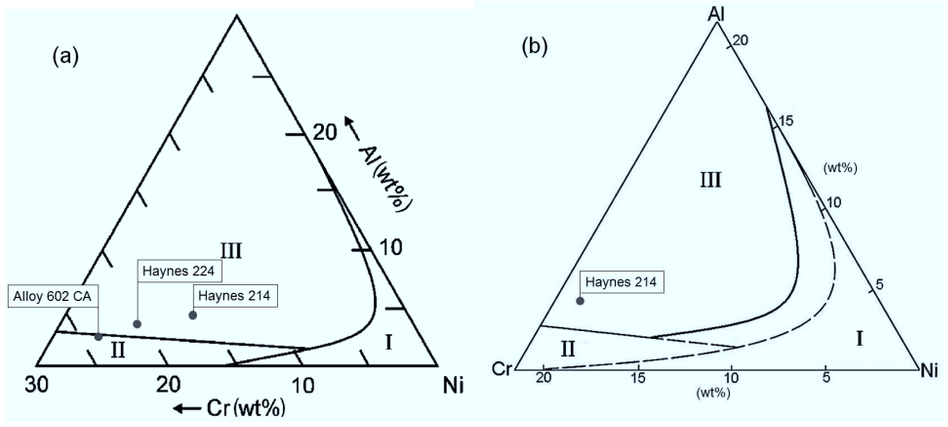

Figure 111: Oxidation maps of Ni-Cr-Al ternary alloys at 1000°C [25, 33, 68]

a) Oxidation of 600 grit ground specimens in 0.1 atm O_2 [25, 33]

b) Oxidation of rolled specimens in Air (dashed lines) and Air+30%H_2O (solid lines) [68]

Group designations: I = External layer of NiO + internal Cr and/or Al oxides

II = External layer of Cr_2O_3 and internal precipitation of Al_2O_3

III = External layer of Al_2O_3

Further it is important to note, that alloy 224 is located nearer to the borderline between area II and area III in Figure 111 (a) than alloy 214. Consequently, 214 should more easily form an external Al_2O_3 scale than 224. In the present studies this was found not to be the case, especially at the lower temperatures, i. e. 800°C and 900°C. This may be related to the fact that the effect of Cr content on external Al_2O_3 scale formation is not completely correctly described by the oxidation map in Figure 111. Another explanation may be that the high Fe content in alloy 224 destabilizes the γ′-phase. Based on the considerations in section 6.2.3.2 this should be beneficial for external Al_2O_3 scale formation.

8 Considerations Related to Material Geometry and Oxidation Behavior

As stated in section 1, a porous metallic substrate is needed as support structure for the gas separation membranes being permeable for the different process gases. However, the present studies were focussed on the oxidation behavior of flat specimens of the NiCrAl-base alloys 602 CA, 214 and 224, because this allowed the use of a number of analysis techniques for studying the oxidation mechanisms which could not be applied if porous materials would have been used.

For discussing possible effects of specimen geometry on its oxidation behavior the porous metallic substrate is assumed to consist of spheres with a diameter in the range of 10 – 15 µm [125]. The formation of oxides on the sphere surfaces will be similar to that of flat specimens. For instance, experiments on porous Haynes 214 revealed the formation of the same types of oxides as found in the present study for flat alloy sheets in the same temperature range [126]. However, a fundamental difference in oxidation behavior is related to the different volume to surface ratio of spherical particles compared to flat rectangular specimens [32]. As this ratio is lower for spherical particles, the Al-reservoir is smaller compared to that of the rectangular geometry [32]. Consequently, as the formation of a protective Al_2O_3 layer is crucial for the operation of the material as support structure for the ceramic membranes (see section 1), depletion of Al by Al_2O_3 formation is more crucial for spherical particles than for flat specimens if particle diameter is considered equal to that of the thickness of the flat specimen. Starting with a material which initially forms an external alumina scale, the transition from external to internal formation of Al_2O_3 after long time due to severe Al-depletion (described in chapter 4.3.4), namely end of life of the substrate-membrane system, will occur earlier in spheres than in flat rectangular specimens of the same diameter. This time limit is extensively treated in literature and called “time to breakaway oxidation” [25, 31, 32, 36].

The effect of specimen geometry on occurrence of breakaway can be estimated for FCC materials with the following formula [127]:

$$t_B = {d_{sheet}}^2 \times \left[\left(\frac{(C_0 - C_B) \times \rho}{200 \times \mu} \right)^2 \times \frac{1}{2 \times k_W} - \frac{2.5 \times 10^{-5}}{D} \right] \tag{55}$$

t_B = Time to breakaway $[s]$

d_{sheet} = Sheet diameter $[cm]$

C_0 = Initial concentration of the scale forming element $[wt.-\%]$

C_B = Breakaway concentration of the scale forming element $[wt.-\%]$

ρ = Density of the alloy $[mg/cm^3]$

μ = Metal / oxide mass ratio (Al_2O_3: 1.125)

k_W = Parabolic rate constant in respect to area specific weight gain $[mg^2/cm^4 \times s]$

D = Diffusivity of the scale forming element $[cm^2/s]$

Equation (55) is only valid for flat sheets of infinite length and width [127]. Calculations of t_B for BCC alloys [32] revealed a factor to take into account geometries deviating from a flat sheet to replace d_{sheet} in the formula. For spherical particles this factor can be derived to be [32]:

$$f = 2 \times \frac{V_{Sphere}}{A_{Sphere}} = \frac{1}{3} \times d_{Sphere} \tag{56}$$

d_{sphere} = Sphere diameter $[cm]$

Thus from combining equation (55) and (56) it follows that for ideal parabolic oxidation the time to breakaway of a spherical particle is 9 times smaller compared to that of a flat sheet with the same diameter.

Beside the smaller Al-reservoir in case of spherical particles, also the formation of precipitates, such as e. g. γ′, will be affected by sample geometry. For Haynes 214 after 72 h oxidation at 900°C the precipitate free zone (PFZ) amounts approximately to 12 µm, which means that a spherical particle of this material with a diameter up to 24 µm will be after 72 h at 900°C single-phase γ without any γ′-precipitates. However, at 800°C, where the formation of γ′-precipitates was found to be crucial for the oxidation mechanism of Haynes 214 (see section 6.2.3.4), the mean PFZ width after 1000 h is only approximately 4 µm. If all γ′-precipitates are dissolved the Al-depletion in the γ-phase will be higher than for the flat sheets shown in this work and the Al-reservoir effect, as explained above, will affect oxidation. Consequently, as long as γ′-precipitates are present in the metal matrix of spherical alloy 214 particles the oxidation mechanism will probably be similar to that proposed for sheets (see section 6.2.3.4). However, at 1000°C and 1100°C where no γ′-precipitates are formed only the consumption of the Al-reservoir affects the transition from external to internal Al_2O_3 formation.

In case of alloy 602 CA similar considerations will be applicable for oxidation at 800°C. However, it should be borne in mind that the external alumina formation was positively

affected by surface grinding. It is thus expected that this factor promoting external alumina formation will not be adaptable for spherical particles. In case of external chromia and internal alumina formation (as found in the present study at 900 – 1100°c for alloy 602 CA) it is expected that the oxidation behavior for plate and particle will not fundamentally differ. However, the kinetics of internal oxidation will after a given exposure time be affected by specimen geometry because the growth of the internal oxidation zone (IOZ) is expected to cease after a critical depletion of Al has occurred in a particle with a small diameter.

These considerations show that the absolute value for which the change from external to internal alumina formation occurs is expected to be quantitatively different for a sphere compared to that of the flat rectangular specimens investigated in the prevailing work. However, it is believed that the major findings in the present study with respect to effect of alloy composition, temperature and gas composition on external and internal scale formation will not fundamentally change if different sample geometries are considered.

9 Summary and Conclusion

The following NiCrAl base alloys were investigated in respect to oxidation behavior in different test gases to study the oxidation mechanisms of potentially suitable materials for metallic support structures for gas separation membranes:

- Alloy 602 CA
- Haynes 214

Alloy 602 CA has a higher Cr- but lower Al-content than Haynes 214. The present studies were focused on the temperature range 800 – 1100°C whereby main emphasis was put on studying conditions for external alumina scale formation in different types of environments.

The oxidation studies using the Ni-base alloy 602 CA revealed formation of an external alumina scale during isothermal oxidation at 800°C. Temperature increase resulted in formation of heterogeneous oxidation products consisting of an external chromia scale beneath which aluminum was internally oxidized. The external chromia scales formed at higher temperatures showed higher growth rates and exhibited less void and crack formation in Ar-H_2O and Ar-H_2-H_2O than in Ar-O_2(H_2O). The results thus indicate that the differences in growth rate and morphology of the chromia are more affected by pO_2 than by presence of water vapor. The effects of pO_2 on chromia growth rate and morphology were qualitatively similar but less pronounced than previously described for binary NiCr model alloys. This difference is likely related to the effect of titanium incorporation into the chromia scale and the effect of metallic nodules which protrude outwardly into the chromia scales on alloy 602, the latter occurring independently of the test gas used.

Incorporation of titanium in the scale differs between the three test atmospheres. This can qualitatively be explained by the effect of equilibrium oxygen partial pressure on titanium solubility in titanium doped chromia.

The tendency for external alumina scale formation on Alloy 602 CA decreased with increasing temperature. This trend was found in all test gases used. Even changes in equilibrium oxygen partial pressures by several orders of magnitude did not substantially affect this temperature dependence from external to internal alumina scale formation. It was found that the effect of temperature on external alumina scale formation was substantially affected by the surface treatment of the specimen. Cold work introduced by this treatment up to a depth of a few micrometers provided rapid diffusion paths promoting external alumina formation; this effect was retained for long time at 800°C but was lost at higher temperatures due to rapid recrystallization. Different gas compositions resulted in differences in growth rate of the external chromia scales at the higher temperatures and should thus indirectly affect the

critical aluminum content for obtaining external scale formation. However, these differences in dry and various wet environments were small compared to literature data on oxidation of NiCrAl alloys with substantially lower chromium contents than present in Alloy 602 CA.

Oxidation studies in Ar-20%O_2 on Haynes 214 showed that the formation of an external Al_2O_3 scale on that material strongly depends on exposure time and temperature, as described in chapter 6.2.3.4. Similar to the experiments on Alloy 602 CA, also the oxidation tests on Haynes 214 revealed at 800°C an oxide scale formation affected by surface cold work prior to exposure. Also here the latter effect provides rapid diffusion paths in the surface near region thus promoting the formation of an external Al_2O_3 scale during 800°C exposure. However, in contrast to Alloy 602 CA, the external Al_2O_3 formed after 72 h exposure due the beneficial effect of surface cold work cannot be maintained during exposure for 1000 h at 800°C on Haynes 214. Consequently, the extent of locally formed internal Al_2O_3 precipitates accompanied by external Cr-rich oxide is significantly higher after 1000 h than after 72 h exposure.

In addition to small amounts of Cr-rich carbides, found at 800-1100°C, the matrix of Haynes 214 contains in chemical equilibrium at 800°C and 900°C γ´-precipitates. However, due to the formation of a precipitate free zone (PFZ) the phase in contact with the alloy / oxide interface is solely γ-Ni matrix, of which the Al-concentration is lower than the bulk concentration. It is therefore proposed that the Al-content responsible for the maintenance of an existing external Al_2O_3 scale, the formation of which was promoted by surface cold work, is the Al-concentration in the γ-phase and not the overall Al-concentration. The Al-concentration in the γ-phase decreases with increasing amount of γ´. Consequently, as the amount of γ´ in the γ-matrix increases with increasing exposure time the tendency of external Al_2O_3 formation decreases until the chemical equilibrium is reached. It is proposed that for the exposure at 800°C in Ar-20%O_2 the formation of γ´-precipitates results in an increased tendency for formation of internal Al_2O_3 precipitates and accompanying external Cr-rich oxide after 1000 h of oxidation, different from the 72 h exposure (Figure 86).

For the oxidation of Haynes 214 at 900-1100°C in Ar-20%O_2 the oxidation differs from that at 800°C (Figure 86). Similar to Alloy 602 CA rapid recrystallization eliminates the effect of surface cold work on external Al_2O_3 formation. As a result internal Al_2O_3 precipitates and external Cr-rich oxide are initially formed (step 1, Figure 86). Due to the volume increase by internal oxidation of Al, metal protrusions are found in the external Cr-rich oxide, in a similar manner as described for Alloy 602 CA. Subsequent formation of a continuous internal Al_2O_3 layer at the reaction front of the internal oxidation zone (IOZ) changes the oxidation process. The continuous layer separates the metal protrusions from the bulk alloy. Due to ongoing Cr-oxide formation the protrusions deplete in Cr and after a certain extent of depletion Ni starts

to oxidize (step 2, Figure 86) until finally complete oxidation of the protrusions occurred and the oxide scale consists of Cr-rich oxide, NiO, some Al_2O_3 particles and a continuous Al_2O_3 layer beneath (step 3, Figure 86). Finally, Cr-rich oxide, NiO and Al_2O_3 particles start to react forming a single phase Ni/Cr/Al spinel type oxide (step 4, Figure 86).

Exposure of specimens of Haynes 214 in different H_2O containing gases revealed an increased tendency to internal oxidation of Al in Ar-7%H_2O. A mechanism from literature, which is based on hydrogen diffusion into the alloy, was proposed to describe this effect of H_2O without intentionally added O_2. In addition, it was proposed that a decreased pO_2 in the test gas will decrease the growth rate of Al_2O_3 and result in lower k_W'-values. These two effects result in deviations from the mechanism proposed for the oxidation of Haynes 214 in Ar-20%O_2, described above. Thus, the number of areas showing internal Al_2O_3 precipitates and external Cr-rich oxide found after oxidation in Ar-7%H_2O were higher than after exposure in Ar-20%O_2. Furthermore, oxidation tests in Ar-4%H_2-7%H_2O revealed the formation of an oxide scale containing no NiO, as this oxide is not thermodynamically stable in the mentioned test gas. Consequently, the area specific weight gain in Ar-4%H_2-7%H_2O was lower compared to that in the other test gases. Internal Al_2O_3 formation and the fact that NiO is not stable under these conditions are proposed to lead to the observed Ni-rich particles on the oxide surface of the specimens exposed in Ar-4%H_2-7%H_2O, resulting from metal protrusions. As a result of the fact that NiO is not formed in this gas, the single phase outer mixed oxide contains after 72 h at 1100°C no Ni. This is another difference with the mechanism proposed for the oxidation of Haynes 214 in Ar-20%O_2, which showed, similar to the results in Ar-7%H_2O and Ar-20%O_2-7%H_2O, the formation of a single phase Ni/Cr/Al mixed oxide in the final step (step 4, Figure 86).

Comparing the oxidation behavior of Alloy 602 CA and Haynes 214 shows that during 800°C exposure Alloy 602 CA formed a protective external Al_2O_3 scale up to 1000 h due to the beneficial effect of surface cold work while Haynes 214 showed initially (72 h) external Al_2O_3 formation but after 1000 h exposure significant internal oxidation of aluminum due to the formation of γ´-precipitates at this temperature. It is suggested that the aluminum bulk alloy concentration in the γ-phase is crucial for the formation of an Al_2O_3 layer and not primarily bulk concentration. However, even when considering the γ´ formation at 800°C in Haynes 214 the aluminum concentration in the γ-phase (2.9 wt.-%) is still slightly higher than the bulk concentration in Alloy 602 CA (2.43 wt.-%), forming no γ´ in the investigated temperature range. Thus, beside γ´-precipitation and aluminum content, also the concentration of other alloying elements, e. g. Cr and Fe, can affect the formation of an external Al_2O_3 scale.

In contrast to the behavior at 800°C, Alloy 602 CA exhibited at 900 – 1100°C internal Al_2O_3 precipitates, the amount of which increases with increasing exposure temperature, whereas Haynes 214 formed after initial internal oxidation of aluminum a continuous inner Al_2O_3 layer when exposed in Ar-20%O_2. The higher concentration of aluminum in combination with the lower or zero amount of γ′ in the temperature range 900 – 1100°C is believed to promote the formation of a continuous Al_2O_3 layer on Haynes 214.

Additional oxidation experiments on Haynes 224 with a lower Al- but higher Cr- and Fe-content than Haynes 214 revealed after 72 h oxidation at 800 – 1100°C always formation of a continuous Al_2O_3 layer with different amounts of Cr-rich transient oxide. It is proposed that the higher Cr content in combination with a lower amount of Al-rich γ′-precipitates in Haynes 224 (due to the high Fe-content) is the reason for the increased tendency to external Al_2O_3 formation. Similar to the investigated alloys 602 CA and Haynes 214, Haynes 224 did not show a significant change from external to solely internal formation of Al_2O_3 by H_2O additions, like described in literature for other types of NiCrAl base alloys. The results indicate that this is related to the fact that in the alloys studied here, the Cr-content (≥ 16 wt.-%) is substantially higher compared to the alloys for which in literature a substantial effect of water vapor on external alumina formation was described.

For discussing possible effects of specimen geometry on its oxidation behavior the porous metallic substrate, needed as support structure for gas separation membranes, is assumed to consist of spheres. These considerations showed that the absolute value for which the change from external to internal alumina formation occurs is expected to be quantitatively different for a sphere compared to that of the flat rectangular specimens investigated in the prevailing work. However, it is believed that the major findings in the present study with respect to effect of alloy composition, temperature and gas composition on external and internal scale formation will not fundamentally change if different sample geometries are considered.

10 References

1 International Energy Agency
Key World Energy Statistics 2014
IEA Publications (2014)

2 BP Statistical Review of World Energy June 2015
www.bp.com/statisticalreview
64rd Edition, BP (2015)

3 International Energy Agency
CO_2 Emissions From Fuel Combustion Highlights
2014 Edition, IEA Publications (2014)

4 S. Arrhenius
On the Influence of Carbonic Acid in the Air upon Temperature of the Ground
Philosophical Magazine and Journal of Science, 5th Series, 237-276 (1896)

5 G. S. Callendar
The Artificial Production of Carbon Dioxide and Its Influence on Climate
Quartely Journal, Royal Meteorological Society, Vol. 66, 395-400 (1940)

6 International Energy Agency
Technology Roadmap Carbon Capture and Storage
IEA Publications (2013)

7 International Energy Agency
Technology Roadmap High-Efficiency, Low-Emissions, Coal-Fired Power Generation
IEA Publications (2012)

8 International Energy Agency
CCS Retrofit Analysis of the Globally Installed Coal-fired Power Plant Fleet
IEA Publications (2012)

9 International Energy Agency
Global Action to Advance Carbon Capture and Storage A Focus on Industrial Applications
IEA Publications (2013)

10 W. Heidug
Joint IEA-OPEC workshop on CO_2-enhanced oil recovery with CCS
IEA-OPEC CO_2-EOR Kuwait Workshop (2012)

11 Y. Xing
Development of Thin Film Oxygen Transport Membranes on Metallic Supports
Schriften des Forschungszentrums Jülich, Energy and Environment, Vol. 130 (2011)

12 Y. Xing, S. Baumann, D. Sebold, M. Rüttinger, A. Venskutonis, W. A. Meulenberg, D. Stöver
Chemical Compatibility Investigaton of Thin-Film Oxygen Transport Membranes on Metallic Substrates
Journal of the American Ceramic Society, Vol. 94 (3), 861-866 (2010)

13 V. Sebastián, I. Kumakiri, R. Bredesen, M. Menéndez
Zeolite membrane for CO_2 removal: Operating at high pressure
Journal of Membrane Science, Vol. 292, 92-97 (2007)

14 L. Zhao, E. Riensche, R. Menzer, L. Blum, D. Stolten
A parametric study of CO_2/N_2 gas separation membrane processes for post-combustion capture
Journal of Membrane Science, Vol. 325, 284–294 (2008)

15 B. Belaissaoui, E. Favre
Membrane Separation Processes for Post-Combustion Carbon Dioxide Capture: State of the Art and Critical Overview
Oil & Gas Science and Technology, Vol. 69, No. 6, 1005-1020 (2014)

16 T. van Gestel, D. Sebold, F. Hauler, W. A. Meulenberg, H. P. Buchkremer,
Potentialities of microporous membranes for H_2/CO_2 separation in future fossil fuel power plants: Evaluation of SiO_2, ZrO_2, Y_2O_3–ZrO_2 and TiO_2–ZrO_2 sol–gel membranes
Journal of Membrane Science, Vol. 359, 64–79 (2010)

17 Z. P. Shao, W. S. Yang, Y. Cong, H. Dong, J. H. Tong, G. X. Xiong
Investigation on the Permeation Behaviour and Stability of a $Ba_{0,5}Sr_{0,5}Co_{0,8}Fe_{0,2}O_{3-\delta}$ Oxygen Membrane
Journal of Membrane Science, Vol. 172, 177-88 (2000)

18 K. Watanabe, M. Yuasa, T. Kida, K. Shimanoe, Y. Teraoka, N. Yamazoe
Preparation of oxygen evolution layer/$La_{0,6}Ca_{0,4}CoO_3$ dense membrane/porous support asymmetric structure for high-performance oxygen permeation
International Journal of Advanced Science and Technology, Vol. 72, 93-8 (2010)

19 H. Jiang, H. Wang, F. Liang, S. Werth, T. Schiestel, J. Caro
Zersetzung von Lachgas in die Elemente mit In-situ Entfernung des Sauerstoffs durch eine Perowskitmembran
Angewandte Chemie, Int. Ed. 48 (2009)

20 R. Kriegel
Energiebedarf von Sauerstoffmembrananlagen
Frauenhofer IKTS, Jahresberichte (2013)

21 K. Brands
Entwicklung und Charakterisierung eines metallischen Substrates für nanostrukturierte keramische Gastrennmembranen
Forschungszentrum Jülich, Energy & Environment, Vol. 72 (2010)

22 J. Stubbles
The Basic Oxygen Steelmaking (BOS) Process
American Iron and Steel Institute (2015)

23 NESTEC Inc.
Description of Thermal Oxidizers
NESTEC Inc., Douglasville, PA, US

24 T. van Gestel, D. Sebold, W. A. Meulenberg, M. Bram, H. Buchkremer
Manufacutring of new nano-structured ceramic-metallic composite microporous membranes consisting of ZrO_2, Al_2O_3, TiO_2 and stainless steel
Solid State Ionics, Vol. 179, 1360-1366 (2008)

25 N. Birks, G. H. Meier, F. S. Pettit
Introduction to the High-Temperature Oxidation of Metals
Cambridge University Press, 2nd Edition (2006)

26 M. J. Donachie, S. J. Donachie
Superalloys - A Technical Guide
ASM International (2002)

27 J. R. Davis
ASM Specialty Handbook: Heat-Resistant Materials
ASM International (1999)

28 J. L. Smialek, N. S. Jacobson
Oxidation of High-Temperature Aerospace Materials
High Temperature Materials and Mechanisms, CRC Press (2014)

29 A. S. Kanna, W. J. Quadakkers, X. Yang, H. Schuster
On the Mechanism of the Oxidation of NiCrAl-Base Alloys in Air and Air Containing Sulphur Dioxide
Oxidation of Metals, Vol. 40, 275-294 (1993)

30 R. C. Reed
The Superalloys Fundamentals and Applications
Cambridge University Press (2006)

31 D. Young
High Temperature Oxidation and Corrosion of Metals
Elsevier Corrosion Series, Vol. 1 (2008)

32 I. Gurappa, S. Weinbruch, D. Naumenko, W. J. Quadakkers
Factors governing breakaway oxidation of FeCrAl-based alloys
Materials and Corrosion, Vol. 51, 224-235 (2000)

33 C. S. Giggins, F. S. Pettit
Oxidation of Ni-Cr-Al Alloys Between 1000° and 1200°C
Journal of the Electrochemical Society, Solid State Science, Vol. 118, No. 11, 1782-1790 (1971)

34 N. C. Oforka, B. B. Argent
Thermodynamics of Ni-Cr-Al Alloys
Journal of the Less-Common Metals, Vol. 114, 97-109 (1985)

35 T. J. Nijdam, N. M. van der Pers, W. G. Sloof
Oxide phase development upon high temperature oxidation of γ-NiCrAl alloys
Materials and Corrosion, Vol. 57, No. 3, 269-275 (2006)

36 D. J. Young, A. Chyrkin, J. He, D. Naumenko, D. Grüner, W. J. Quadakkers
Slow Transition from Protective to Breakaway Oxidation of Haynes 214 Foil at High Temperature
Oxidation of Metals, 79, 405-427 (2013)

37 C. T. Sims, N. S. Stoloff, W. C. Hagel
Superalloys II – High-Temperature Materials for Aerospace and Industrial Power
John Wiley and Sons (1987)

38 P. Kofstad
High Temperature Corrosion
Elsevier Applied Science Publishers Ltd. (1988)

39 W. Schatt
Einführung in die Werkstoffwissenschaften
Deutscher Verlag Für Grundstoffindustrie, Vol. 7 (1991)

40 G. Y. Lai
High Temperature Corrosion and Materials Applications
ASM International (2007)

41 W. J. Quadakkers, J. Zurek
Oxidation in Steam and Steam/Hydrogen Environments
Shreir's Corrosion Vol. 1, 407-456, Amsterdam (2010)

42 H. T. J. Ellingham
Reducibility of Oxides and Sulphides in Metallurgical Processes
Journal of Society of Chemical Industry, Transactions and Communications, 125-160 (1944)

43 H. L. Tuller, S. R. Bishop
Point Defects in Oxides: Tailoring Materials Through Defect Engineering
Annuual Review of Materials Research, Vol. 41, 369-398 (2011)

44 A. S. Kanna
High Temperature Oxidation and Corrosion
ASM International, No. 06949G (2002)

45 J. Maier
Ionic conduction in space charge regions
Prog. Solid State Chemistry, Vol. 23, 171-263 (1995)

46 W. Zhao, Z. Li, B. Gleeson
A New Kinetics-Based Approach to Quantifying the Extent of Metastable → Stable Phase Transformation in Thermally-Grown Al_2O_3 Scales
Oxidation of Metals, Vol. 79, 361-381 (2013)

47 E. N'Dah, A. Galerie, Y. Wouters, D. Goossens, D. Naumenko, V. Kochubey, W. J. Quadakkers
Metastable alumina formation during oxidation of FeCrAl and its suppression by surface treatments
Materials and Corrosion, Vol. 56, No. 12, 843-847 (2005)

48 H. J. Grabke, M. W. Brumm, B. Wagemann
The oxidation of NiAl
Materials and Corrosion, Vol. 47, 675-677 (1996)

49 F. Gesmundo, P. Castello, F. Viani, J. Philibert
An Approximate Treatment of the Transient State in the Oxidation of Binary Alloys Forming the Most-Stabel Oxide. Part II: Single-Phase Alloys in Systems with a Solubility Gap
Oxidation of Metals, Vol. 47, 525-550 (1997)

50 F. Gesmundo, M. Pereira
The Transient State in the Oxidation of Binary-Alloys Forming the Most-Stable Oxide – A Numercial Solution
Oxidation of Metals, Vol. 47, 507-524 (1997)

51 T. J. Nijdam, L. P. H. Jeurgens, W. G. Sloof
Promoting exclusive α-Al_2O_3 growth upon high-temperature oxidation of NiCrAl alloys: experiment versus model predictions
Acta Materialia, Vol. 53, 1643-1653 (2005)

52 L. Hu, D. B. Hovis, A. H. Heuer
Transient Oxidation of a γ-Ni-28Cr-11Al Alloy
Oxidiation of Metals, Vol. 73, 275-288 (2010)

53 J. L. Meijering
Internal Oxidation in Alloys
Advances in Material Research, Vol. 5, 1-83 (1971)

54 R. A. Rapp
Kinetics, microstructures and mechanism of internal oxidation-its effect and prevention in high temperature alloy oxidation
Corrosion, Vol. 21, 382-401 (1965)

55 D. L. Douglass
A Critique of Internal Oxidation in Alloys During the Post-Wagner Era
Oxidation of Metals, Vol. 44, 81-111 (1995)

56 C. Wagner
Theoretical Analysis of the Diffusion Processes Determining the Oxidation Rate of Alloys
Journal of the Electrochemical Society, Vol. 99, No.10, 369-380 (1952)

57 C. Wagner
Reaktionstypen bei der Oxydation von Legierungen
Zeitschrift für Elektrochemie, Vol. 63, No.7, 772-782 (1959)

58 A. Fick
Über Diffusion
Annalen der Physik, Vol. 170, 1, 59-86 (1855)

59 V. A. Lashgari
Internal and external Oxidation of Manganese in Advanced High Strength Steels
PhD Thesis, Delft University of Technology, The Netherlands (2014)

60 J. A. Nesbitt
Predicting the Minimum Al Concentrations for Protective Scale Formation on Ni-Base Alloys
Journal of the Electrochemical Society, Vol. 136, No. 5, 1551-1517 (1989)

61 F. Maak
Zur Auswertung von Messungen der Schichtdickne binärer Legierungen mit innerer Oxydation bei gleichzeitiger äußerer Oxydation
Zeitschrift für Metallkunde, Vol. 52, 545-546 (1961)

62 A. Sieverts
Die Aufnahme von Gasen durch Metalle
Zeitschrift für Metallkunde, Vol. 21, 37-46 (1929)

63 J.-W. Park, C. J. Altstetter
The Diffusion and Solubility of Oxygen in Solid Nickel
Metallurgical Transactions A, Vol. 18A, 43-50 (1987)

64 J. H. Swisher, E. T. Turkdogan
Solubility, Permeability and Diffusivity of Oxygen in Solid Iron
Trans. AIME, 239, 426-431 (1968)

65 R. A. Rapp
The Transition from Internal to External Oxidation and the Formation of Interruption Bands in Silver-Indium Alloys
Acta Metallurgica, Vol. 9, 730-741 (1961)

66 W. Zhao, Y. Kang, J. M. Alvarado Orozco, B. Gleeson
Quantitative Approach for Determining the Critical Volume Fraction for the Transition from Internal to External Oxidation
Oxidation of Metals, Vol. 83, 187-201 (2015)

67 W. Zhao, B. Gleeson
Steam Effects on the Oxidation Behaviour of Al_2O_3-Scale Forming Ni-Based Alloys
Oxidation of Metals, Vol. 79, 613-625 (2013)

68 W. Zhao, B. Gleeson
Assessment of the Detrimental Effects of Steam on Al_2O_3-Scale Establishment
Oxidation of Metals, published online 24.02.2015

69 W. J. Quadakkers, D. Naumenko, E. Wessel, V. Kochubey, L. Singheiser
Growth Rates of Alumina Scales on Fe-Cr-Al Alloys
Oxidation of Metals, Vol. 61, 17-37 (2004)

70 https://www.bruker.com/products/x-ray-diffraction-and-elemental-analysis/handheld-xrf/how-xrf-works.html
Bruker Corporation, accessed at 18.11.2015

71 L. Reimer
Scanning Electron Microscopy
Springer Series in Optical Sciences (1998)

72 http://synchrotron.royalsociety.org.nz/science/techniques/
NZ Synchrotron Group Ltd., accessed at 18.11.2015

73 P. Moeck
http://web.pdx.edu/~pmoeck/phy381/Topic5a-XRD.pdf
Portland State University, Department of Physics, accessed at 18.11.2015

74 http://www.metalle.uni-bayreuth.de/de/download/teaching_downloads/Prakt_Materialcharakterisierung_H4a/Prakt_H4a_GDOES.pdf
University of Bayreuth, accessed at 18.11.2015

75 J.-P. Pfeifer, H. Holzbrecher, W. J. Quadakkers, W. Speier
Quantitative analysis of oxide films on ODS-alloys using MCs^+-SIMS and e-beam SNMS
Journal of Analytical Chemistry, Vol. 346, 186-191 (1993)

76 W. J. Quadakkers, A. Elschner, W. Speier, H. Nickel
Composition and growth mechanisms of alumina scales on FeCrAl-based alloys determined by SNMS
Applied Surface Science, Vol. 52, 271-287 (1991)

77 L. Niewolak, D. Naumenko, E. Wessel, L. Singheiser, W. J. Quadakkers
Optical fluorescence spectroscopy for identification of minor oxide phases in alumina scales grown on high temperature alloys
Materials Characterization, Vol. 55, 320-331 (2005)

78 V. K. Tolpygo, D. R. Clarke
Microstructural Study of the Theta-Alpha Transformation in Alumina Scales Formed on Nickel-Aluminides
Materials at High Temperatures 17, 59-70 (2000)

79 D. M. Lipkin, D. R. Clarke
Measurement of the Stress in Oxide Scales Formed by Oxidation of Alumina-Forming Alloys
Oxidation of Metals, Vol. 45, 267-280 (1996)

80 M. Subanovic
Einfluss der Bondcoatzusammensetzung und Herstellungsparameter auf die Lebensdauer von Wärmedämmschichten bei zyklischer Temperaturbelastung
Schriften des Forschungszentrums Jülich, Energy & Environment, Vol. 42 (2009)

81 G. Böhm, M. Kahlweit
Über die innere Oxydation von Metalllegierungen
Acta Metallurgica, Vol. 12, 641-648 (1964)

82 J. Zurek, D. J. Young, E. Essuman, M. Hänsel, H. J. Penkalla, L. Niewolak, W. J. Quadakkers
Growth and adherence of chromia based surface scales on Ni-base alloys in high- and low-pO_2 gases
Materials Science and Engineering A, Vol. 477, 259-270 (2008)

83 E. Essumann, G. H. Meier, J. Zurek, M. Hänsel, T. Norby, L. Singheiser, W. J. Quadakkers
Protective and non-protective scale formation of NiCr alloys in water vapour containing high- and lowpO_2 gases
Corrosion Science, Vol. 50, 1753-1760 (2008)

84 A. Chyrkin, W. G. Sloof, R. Pillai, T. Galiullin, D. Grüner, L. Singheiser, W. J. Quadakkers
Modelling compositional changes in nickel base alloy 602 CA during high temperature oxidation
Materials at High Temperatures, Vol. 32, Issue 1-2, 102-112 (2015)

85 R. Pillai, H. Ackermann, H. Hattendorf, S. Richter
Evolution of carbides and chromium depletion profiles during oxidation of Alloy 602 CA
Corrosion Science, Vol. 75, 28-37 (2013)

86 R. Pillai, H. Ackermann, K. Lucka
Predicting the depletion of chromium in two high temperature Ni alloys
Corrosion Science 69, 181-190 (2013)

87 H. Ackermann, G. Teneva-Kosseva, H. Köhne, K. Lucka, S. Richter, J. Mayer
Oxide scale formation on Al containing Ni-Cr-based high temperature alloys during application as flame tube material in recirculation oil burners
Materials and Corrosion 59, No.5, 380-388 (2008)

88 W. J. Quadakkers
High Temperature Corrosion in the Service Environments of a Nuclear process Heat Plant
Mat. Sci. Eng. 87, 107 – 112 (1987)

89 P. J. Ennis, W. J. Quadakkers
Corrosion and Creep of Nickel-Base Alloys in Steam Reforming Gas
High Temperature Alloys - Their Exploitable Potential, Elsevier Applied Science, 465-474 (1987)

90 E. Essuman, G. H. Meier, J. Zurek, M. Hänsel, L. Singheiser, T. Norby, W. J. Quadakkers
Effect of oxygen partial pressure on the oxidation behaviour of an yttria dispersion strengthened NiCr-base alloy
J. Mater. Sci., 43, 5591-5598 (2008)

91 C. García-Rosales, H.A. Schulze, A. Naoumidis, H. Nickel
Influence of Oxygen Partial Pressure on the Quasi-Ternary System Cr─Mn─Ti Oxide
Journal of the American Ceramic Society, 76 (11), 2869–2878 (1993)

92 Holt, P. Kofstad
Electrical conductivity of Cr_2O_3 doped with TiO_2
Solid State Ionics 117, 21-25 (1999)

93 W. J. Quadakkers
Method for Coating a Metallic Nickel-containing Material with a Nickel Catalyst, WO 2004087312 A1, priority date March 31, 2003

94 U. Brill
Neue warmfeste und korrosionsbeständige Nickel-Basis-Legierung für Temperaturen bis zu 1200°C
Metall, 8, 778-782 (1992)

95 M. Stanislowski, E. Wessel, T. Markus, L. Singheiser, W. J. Quadakkers
Chromium vaporization from alumina-forming and aluminized alloys
Solid State Ionics 179, 2406-2415 (2008)

96 V. V. Joshi, A. Meier, J. Darsell, P. Nachimuthu, M. Bowden, K. S. Weil
Short-Term Oxidation Studies on Nicrofer-6025 HT in Air at Elevated Temperatures for Advanced Coal Based Power Plants
Oxidation of Metals 79, 383-404 (2013)

97 M. Stanislowski, J. Froitzheim, L. Niewolak, W. J. Quadakkers, K. Hilpert, T. Markus, L. Singheiser
Reduction of chromium vaporization from SOFC interconnectors by highly effective coatings
Journal of Power Sources 164, 578-589 (2007)

98 G. Teneva-Kosseva, H. Ackermann, H. Köhne, M. Spähn, S. Richter, J. Mayer
Service conditions and their influenceon oxide scale formation on metallic high temperature alloys for application in innovative combustion processes
Materials and Corrosion 57, No.2, 122-127 (2006)

99 I. A. Kvernes, P. Kofstad
The Oxidation Behavior of Some Ni-Cr-Al Alloys at High Temperatures
Metallurgical Transactions, Vol. 3, 1511-1519 (1972)

100 T. Gheno, G. H. Meier, B. Gleeson
High Temperature Reaction of MCrAlY Coating Compositions with CaO Deposits
Oxidation of Metals, 84, 185-209 (2015)

101 H. M. Hindam, W. W. Smeltzer
Growth and Microstructure of α-Al_2O_3 on Ni-Al Alloys: Internal Precipitation and Transition to External Scale
J. Electrochem. Soc., Vol. 127, No.7 (1980)

102 S. Leistikow, I. Wolf, H. J. Grabke
Effects of cold work on the oxidation behavior and carburization resistance of Alloy 800
Werkstoffe und Korrosion 38, 556-562 (1987)

103 R. W. Cahn, P. Haasen
Physical Metallurgy
Elsevier Ltd., Fourth Edition (1996)

104 R. Bürgel, P. D. Portella, J. Preuhs
Recrystallization in Single Crystals of Nickel Base Superalloys
Superalloys 2000, TMS (2000)

105 M. C. Maris-Sida, G. H. Meier, F. S. Pettit
Some Water Vapor Effects during the Oxidation of Alloys that are α-Al_2O_3 Formers
Metallurgical and Materials Transactions A, Vol. 34A, 2609-2619 (2003)

106 F. Gesmundo, F. Viani
Transition from Internal to External Oxidation for Binary Alloys in the Presence of an Outer Scale
Oxidation of Metals, Vol. 25, 269-282 (1986)

107 G. R. Holcomb
Chromia Evaporation in Advanced Ultra-Supercritical Steam Boilers and Turbines
Thermodynamics – Kinetics of Dynamic Systems, 205-226 (2011)

108 D. Caplan, M. Cohen
The Volatilization of Chromium Oxide
Journal of the Electrochemical Society, Vol. 108, No.5, 438-442 (1961)

109 M. Michalik, M. Hänsel, J. Zurek, L. Singheiser and W.J. Quadakkers
Effect of water vapour on growth and adherence of chromia scales formed on Cr in high and low pO_2-environments at 1000 and 1050°C
Materials at High Temperatures, 22(3/4), 213–221 (2005)

110 N. P. Bansal, P. Singh, S. Widjaja, D. Singh
Advances in Solid Oxide Fuel Cells VII
Ceramic Engineering and Science Proceedings, Vol. 32, Issue 4 (2011)

111 Haynes International
Haynes ® 214® alloy
Alloy Brochure, www.haynesintl.com/pdf/h3008.pdf

112 DIN EN ISO 643:2003
Mikrophotographische Bestimmung der scheinbaren Korngröße
Normenausschuss Materialprüfung DIN (2003)

113 D. Monceau, B. Pieraggi
Determination of Parabolic Rate Constants from a Local Analysis of Mass-Gain Curves
Oxidation of Metals, Vol. 50, 477-493 (1998)

114 D. J. Young, D. Naumenko, L. Niewolak, E. Wessel, L. Singheiser, W. J. Quadakkers
Oxidation kinetics of Y-doped FeCrAl-alloys in low and high pO_2 gases
Materials and Corrosion 61, No. 10, 838-844 (2010)

115 B. A. Pint, K. L. More, P. F. Tortorelli
The Effect of Water Vapor on Oxidation Performance of Alloys Used in Recuperators
Oak Ridge National Laboratory (2002)

116 B. A. Pint, B. N. Anderson, W. J. Matthews, C. M. Waldheim, W. Treece
Evaluation of NiCrAl Foil for a Concentrated Solar Power Application
ASME Turbo Expo 2013, Vol. 4, GT2013-94939 (2013)

117 M. Bauccio
ASM Metals Reference Book Third Edition
ASM International (1993)

118 D. Sporer, D. Fortuna
Braze Materials for Brazing Seal Honeycomb: Trends, Challenges and a Market Outlook
5th International Brazing and Soldering Conference (2012)

119 G. Y. Lai
High Temperature Corrosion and Materials Applications
ASM International (2007)

120 Private Communication A. Jansson
Thermo-Calc Software, Sweden (January 2013)
121 D. Young, B. Gleeson
Alloy phase transformations driven by high temperature corrosion processes
Corrosion Science 44, 345-357 (2002)
122 W. E. Boggs
The Oxidation of Iron-Aluminum Alloys from 450° to 900°C
Journal of the Electrochemical Society, 118(6), 906-913 (1971)
123 S. Hayashi, T. Narita
Competitive Effect of Water Vapor and Oxygen on the Oxidation of Fe-5wt.&Al Alloy at 1073 K
Oxidation of Metals, 56(3), 251-270 (2001)
124 T. Malkow, W. J. Quadakkers, L. Singheiser, H. Nickel
Investigations of the long term behaviour of high temperature fuel cell (SOFC) metallic interconnector materials with respect to compatibility with cathode-side contact layers
Report Forschungszentrum Jülich, Jül-3589, ISNN 0944-2952 (1998)
125 Y. Xing, S. Baumann, S. Uhlenbruck, M. Rüttinger, A. Venskutonis, W. A. Meulenberg, D. Stöver
Development of a metallic/ceramic composite for the deposition oft hin-film oxygen transport membranes
Journal of the European Ceramic Society, Vol. 33, 287-296 (2013)
126 Y. Wang, Y. Liu, H. Tang, W. Li
Oxidation behaviors of porous Haynes 214 alloy at high temperatures
Materials Characterization, Vol. 107, 283-292 (2015)
127 D. Young, A. Chyrkin, W. J. Quadakkers
A Simple Expression for Predicting the Oxidation Limited Life of Thin Components Manufactured from FCC High Temperature Alloys
Oxidation of Metals, Vol. 77, 253-264 (2012)

Appendix A – Buoyancy Effect

To calculate correctly the area specific weight gain as a function of time from thermogravimetric measurements the buoyancy effect has to be considered. It states that when a body is immersed in a fluid, the fluid exerts an upward force on the body equal to the weight of the fluid which is displaced by the body [A1]. The weight of the displaced fluid, namely the test gas, around the body, namely the specimen, can be determined by its density and the volume of the specimen. As the volume is assumed to be constant and the density decreases with increasing test temperature, the weight of the displaced gas is lower at higher temperatures. The weight gain difference caused by the change in buoyancy during specimen heating can be calculated by the following equation:

$$\Delta m_A = \frac{\left(\rho_{gas,T1} - \rho_{gas,T2}\right) \cdot V_{Sample}}{A_{Sample}} \tag{A1}$$

Δm_A = Area specific weight gain difference caused by buoyancy effect $\left[mg / cm^2\right]$

$\rho_{gas,T1}$ = Density of the respective gas environment at temperature T_1 $\left[mg / cm^3\right]$

$\rho_{gas,T2}$ = Density of the respective gas environment at temperature T_2 $\left[mg / cm^3\right]$

V_{Sample} = Volume of the sample $\left[cm^3\right]$

A_{Sample} = Surface area of the sample $\left[cm^2\right]$

By assuming the gas to act according to the ideal gas law [A2], the density of the gas can be determined by:

$$\rho_{gas} = \frac{M_{gas}}{v_{gas}} = \frac{M_{gas} \cdot p_0}{R \cdot T} \tag{A2}$$

M_{gas} = Molar mass of the respective gas $\left[g / mole\right]$

v_{gas} = Molar volume of the respective gas $\left[m^3 / mole\right]$

p_0 = Standard pressure $= 1.01325 \cdot 10^5 \frac{N}{m^2}$

R = Ideal gas constant $= 8.314 J / mol \cdot K$

T = Temperature K

By combining equations A1 and A2 it follows for the weight gain difference between T_1 and T_2 caused by the buoyancy effect:

$$\Delta m_A = \frac{M_{gas} \cdot p_0 \cdot V_{Sample}}{R \cdot A_{Sample}} \cdot \left(\frac{1}{T_1} - \frac{1}{T_2}\right) \tag{A3}$$

This weight difference of the gas displaced by the specimen between room temperature (T_1 = 20°C) and the respective test temperature (T_2) has to be subtracted from the weight gain data recorded during the high temperature TG experiments.

References

A1 R. F. Speyer
Thermal Analysis of Materials
Marcel Dekker Inc. (1994)

A2 D. Winterbone, A. Turan
Advanced Thermodynamics for Engineers 2nd Edition
Elsevier Ltd. (2015)

Appendix B – Instantaneous Oxidation Rate Constant

Ideal parabolic oxidation can be described by equation (15), including the parabolic rate constant k_W, which is independent of time [B1]. However, only a limited number of metals and alloys show ideal parabolic behavior [B2] and thus for most materials the apparent parabolic rate constant is a function of exposure time [B3]. Consequently, an instantaneous apparent parabolic rate constant k_W' is commonly used to describe non-parabolic oxidation kinetics. This can be determined by numerical differentiation either of a $\Delta m^2(t)$ - or $\Delta m(t^{1/2})$ -plot (see equation (17)). As in the literature it is shown that in many cases the $\Delta m(t^{1/2})$ -plot allows a more accurate determination of the instantaneous oxidation rate k_W' [B2]. The value of k_W' is derived in the following manner [B4]:

$$\Delta m^2 = 2 \times k_W' \times t \tag{17}$$

$$\Rightarrow \Delta m = \left(2 \times k_W' \times t\right)^{1/2} \tag{B1}$$

$$\Rightarrow \frac{d(\Delta m)}{d\left(t^{1/2}\right)} = \left(2 \times k_W'\right)^{1/2} \tag{B2}$$

$$\Rightarrow k_W' = \frac{1}{2} \times \left[\frac{d(\Delta m)}{d\left(t^{1/2}\right)}\right]^2 \tag{B3}$$

k_W' = Instantaneous apparent parabolic rate constant $\left[mg^2/cm^4 \times s\right]$

By using this procedure for deriving k_W', the oxidation kinetics of alumina growth on Fe-Cr-Al alloys is reported in the literature to be sub-parabolic [B4]. In addition, for the formation of NiO on pure Ni below 1000°C it is found that the oxidation kinetics show a sub-parabolic behavior, too [B5, B6]. Such deviations from ideal parabolic behavior cannot be determined from stand $\Delta m^2(t)$ - or $\Delta m(t^{1/2})$ -plots [B4]. Consequently, the calculation and plotting of the instantaneous apparent parabolic rate constant k_W' as a function of time, like described, is indispensable.

References

B1 D. Young
High Temperature Oxidation and Corrosion of Metals
Elsevier Corrosion Series, Vol. 1 (2008)

B2 B. Pieraggi
Calculations of Parabolic Reaction Rate Constants
Oxidation of Metals, Vol. 27, 177-185 (1987)

B3 D. Monceau, B. Pieraggi
Determination of Parabolic Rate Constants from a Local Analysis of Mass-Gain Curves
Oxidation of Metals, Vol. 50, 477-493 (1998)

B4 W. J. Quadakkers, D. Naumenko, E. Wessel, V. Kochubey, L. Singheiser
Growth Rates of Alumina Scales on Fe-Cr-Al Alloys
Oxidation of Metals, Vol. 61, 17-37 (2004)

B5 R. Peraldi, D. Monceau, B. Pieraggi
Correlations between Growth Kinetics and Microstructure for Scales Formed by High-Temperature Oxidation of Pure Nickel, II. Growth Kinetics
Oxidation of Metals, Vol. 58, 275-295 (2002)

B6 A. Atkinson, R. I. Taylor, A. E. Hughes
A quantitative demonstration of the grain boundary diffusion mechanism for the oxidation of metals
Philosophical Magazine A, Vol. 45, 823-833 (1982)

Band / Volume 304
Thermo-mechanical Properties of Mixed Ionic-Electronic Conducting Membranes for Gas Separation
V. K. Stournari (2016), 167 pp
ISBN: 978-3-95806-117-0

Band / Volume 305
Untersuchungen zu suspensionsplasmagespritzten Wärmedämmschichtsystemen
N. Schlegel (2016), X, 136 pp
ISBN: 978-3-95806-118-7

Band / Volume 306
Laser processing for the integrated series connection of thin-film silicon solar cells
B. Turan (2016), xii, 188 pp
ISBN: 978-3-95806-119-4

Band / Volume 307
Development and Application of a Multiscale Model for the magnetic Fusion Edge Plasma Region
F. Hasenbeck (2016), 190 pp
ISBN: 978-3-95806-120-0

Band / Volume 308
Emissions of Biogenic Volatile Organic Compounds and Ozone Balance under Future Climate Conditions
C. Wu (2016), VI, 105 pp
ISBN: 978-3-95806-121-7

Band / Volume 309
Computerunterstützte Auslegung eines Brennstoffzellen-Batterie-Hybridsystems für die Bordstromversorgung
C. Krupp (2016), iii, 207 pp
ISBN: 978-3-95806-124-8

Band / Volume 310
Influence of H_2O, HCl and H_2S on the Release and Condensation of Trace Metals in Gasification
M. Benito Abascal (2016), XIX, 172 pp
ISBN: 978-3-95806-125-5

Band / Volume 311
Mechanical and Thermochemical Properties of Nano-structured Membranes for Gas Separation in Fossil-fired Power Plants
J. Zhang (2016), II, 134 pp
ISBN: 978-3-95806-126-2

Schriften des Forschungszentrums Jülich
Reihe Energie & Umwelt / Energy & Environment

Band / Volume 312
Development of Embedded Thermocouple Sensors for Thermal Barrier Coatings (TBCs) by a Laser Cladding Process
Y. Zhang (2016), II, 108 pp
ISBN: 978-3-95806-129-3

Band / Volume 313
Streamwater transit time distributions at the catchment scale: constraining uncertainties through identification of spatio-temporal controls
M. Stockinger (2016), XIX, 161 pp
ISBN: 978-3-95806-131-6

Band / Volume 314
Entwicklung eines metallbasierten Substratkonzepts für energieeffiziente Gastrennmembranen
J. A. Kot (2016), xi, 201 pp
ISBN: 978-3-95806-134-7

Band / Volume 315
Langzeitbeobachtung der Dosisbelastung der Bevölkerung in radioaktiv kontaminierten Gebieten Weißrusslands - Korma-Studie II (1998 – 2015) -
P. Zoriy, H. Dederichs, J. Pillath, B. Heuel-Fabianek, P. Hill, R. Lennartz (2016), ca 104 pp
ISBN: 978-3-95806-137-8

Band / Volume 316
Oxidation Mechanisms of Metallic Carrier Materials for Gas Separation Membranes
M. Schiek (2016), 148 pp
ISBN: 978-3-95806-138-5

Weitere ***Schriften des Verlags im Forschungszentrum Jülich*** unter
http://wwwzb1.fz-juelich.de/verlagextern1/index.asp

Energie & Umwelt
Energy & Environment

316

Oxidation Mechanisms of Metallic Carrier Materials

Martin Schiek

Member of the Helmholtz Association

Oxidation Mechanisms of Metallic Carrier Materials for Gas Separation Membranes

Martin Schiek

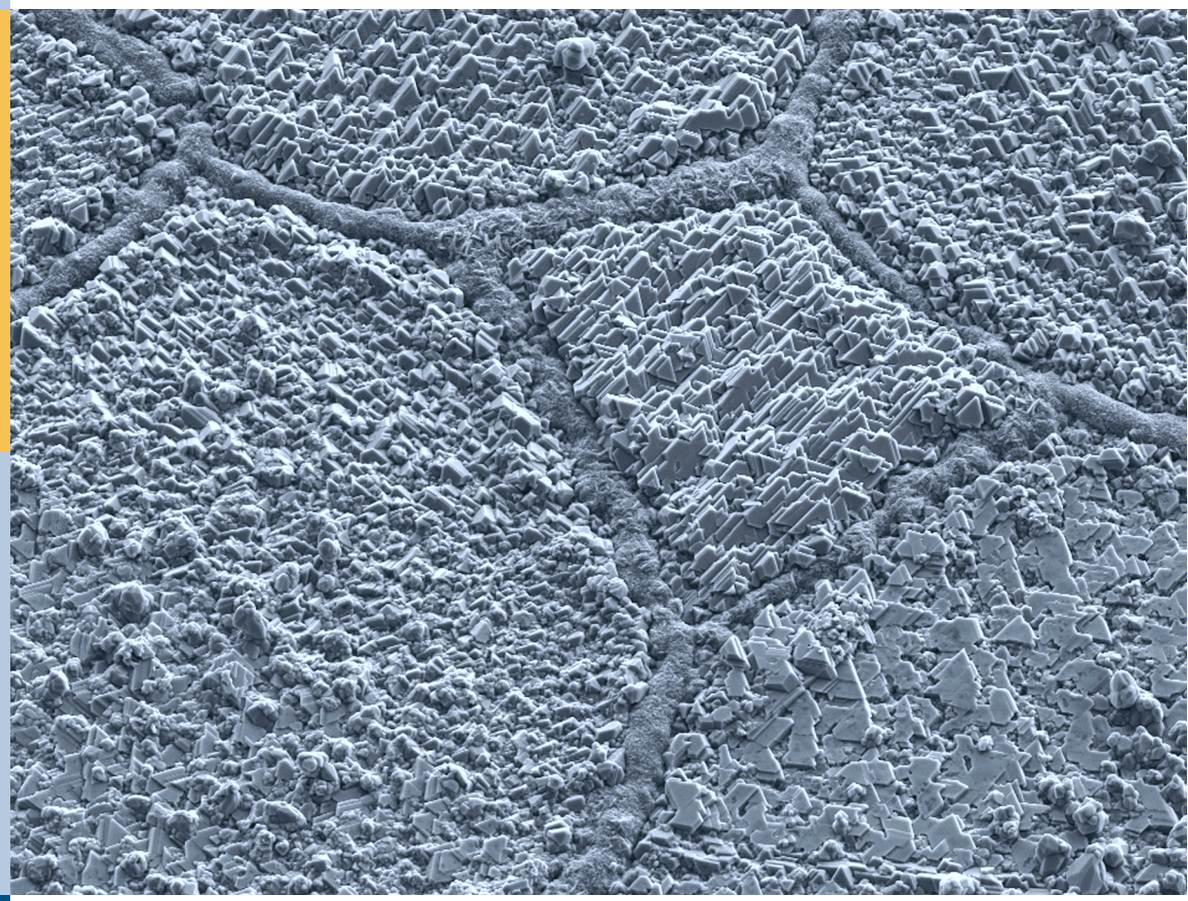

Energie & Umwelt /
Energy & Environment
Band / Volume 316
ISBN 978-3-95806-138-5

JÜLICH
FORSCHUNGSZENTRUM

Energie & Umwelt /
Energy & Environment
Band / Volume 316
ISBN 978-3-95806-138-5

JÜLICH
FORSCHUNGSZENTRUM